Photofragment Velocity-map Imaging of Organic Molecules

Sara H. Gardiner

Wolfson College

University of Oxford

A thesis submitted for the degree of

Doctor of Philosophy

Michaelmas 2013

Sara H. Gardiner
Photofragment Velocity-map Imaging of Organic Molecules

DPhil thesis, Michaelmas Term 2013
Supervisor: Dr Claire Vallance
Examiners: Professor Tim Softley and Dr Matt Costen

University of Oxford
Chemistry Research Laboratory
12 Mansfiled Road, Oxford, United Kingdom, OX1 3TA

Abstract

Photofragment velocity-map imaging (VMI) has generally been employed to investigate the photodissociation dynamics of relatively small molecular systems (< 5 atoms). The work reported in this thesis focuses on the application of this technique for the investigation of the unimolecular photodissociation of larger chemical systems, which are of interest to a broad cross section of the chemical community. Typically, VMI studies involve state-selective detection of one particular fragmentation product, and so are often limited to the investigation of a single dissociation channel. By employing vacuum ultra-violet (VUV) photoionization, we are able to detect most, if not all of the fragments resulting from the dissociation of a neutral species, with 'universal' ionization being achieved in the ideal case when the fragment ionization energies are all lower than the VUV photon energy. This capability becomes particularly important when investigating larger systems, since these often display complex dynamics with multiple competing fragmentation pathways. Our approach allows us to investigate the different photofragmentation processes occurring for a particular system, to evaluate the relative importance of the active dissociation channels, and to gain insight into the energy partitioning amongst the fragments.

A study of the UV photodissociation of two neutral alkyl iodide molecules demonstrates the first use in our laboratory of 'universal' ionization in combination with VMI. Studies into the photofragmentation processes resulting from 193 nm photoexcitation of neutral N,N-dimethylformamide, a small-molecule model for a peptide bond, and a number of neutral cyclic alkenes, which undergo the retro-Diels-Alder reaction, are also presented. The remaining studies presented in this thesis have investigated the photofragmentation processes of *ionic* species, generated by means of VUV photoionization. In the case of *ion* dissociation each fragmentation channel necessarily produces one charged species, which may be detected using the VMI technique. Therefore, such studies provide an insight into all of the active channels. An in-depth VMI study of the UV photodissociation of two ethyl halide cations is presented, which demonstrates the successful investigation of the multiple photofragmentation pathways of these ionic species. The remainder of the cation photodissociation studies are of relevance to a number of common processes known to occur in mass spectrometry, including the McLafferty rearrangement, the retro-Diels-Alder reaction, and 'peptide' bond fragmentation. By velocity-map imaging the products of these reactions, further information is obtained concerning these dissociation processes, which are no doubt of interest to the wider chemical community.

This work forms part of the velocity-map imaging mass spectrometry (VMImMS) project. VMImMS involves imaging each of the fragmentation products that result from dissociation of a parent molecule of interest, with the aim of increasing the amount of information that can be obtained from a mass-spectrometry-type experiment. The work presented in this thesis demonstrates that VMImMS allows us to unravel details of the dissociation dynamics of both neutral and ionic species, and is potentially a powerful technique for investigating the fragmentation processes of increasingly complex systems.

Darkness cannot drive out darkness; only light can do that.

Martin Luther King, Jr.

To my family

Acknowledgements

I feel truly privileged to have been able to undertake my DPhil in the Vallance group lab. When I look back on my time as a DPhil student, it feels as though the years went by in a nanosecond, but, in some ways, it feels like a lifetime has passed. I believe I have developed in many ways, as a person (hopefully for the better), as an experimentalist, and (more recently) as a writer/editor (though this excessive use of parentheses works to nullify that last point). So many of the experiences I have had over this time will stay with me for life. I would like to take this opportunity to thank all those who have crossed my path as I have journeyed along this road. Now, three years later, I have arrived at my destination, and it would not have been possible without each and everyone of you. I have been remarkably fortunate to work with so many incredible people, though there are a few people who should receive a particular thank-you.

Firstly, I would like to thank my supervisor, Dr Claire Vallance. Without her foresight, dedication, and ambition none of this research would have even been conceived. During my Part II and throughout my DPhil, her enthusiasm, innovativeness, and determination often kept me going when I would have otherwise lost hope. She has always encouraged me to give talks, present posters, and attended conferences, from which I have benefitted greatly. I very much appreciate the numerous meetings and scientific discussions that we have had, particularly over the last few months. I am sure it is a great pleasure (and a relief) for her, as it is for me, to see this thesis come to fruition.

I will forever be indebted to Dr Laura Lipciuc for showing me the ropes of VMI back when I was a Part II student, and continuing my scientific education throughout my DPhil. Although her direct nature and criticism of my colour schemes took a while to get used to, her passion for experiment was truly inspiring from the beginning. Though it wasn't all science with Laura - I will always have fond memories of the times we spent drinking wine, and discussing everything under the sun. Since it is quite apt for this thesis, I would like to pass on a little gem of wisdom that Laura once shared with me, "A wise woman once said, 'You have to start small before you can go big.'."

The Vallance group lab has gone through many changes since I joined four years ago as a Part II student. The VMI apparatus saw an upgrade with the addition of multiple lasers, not to mention the VUV cell, three new rigs were built, and of course we have said goodbye and hello to a number of postdocs and students. It's odd to think that I might now be classified as the 'granny' of the lab, and that some of the most recent members might not remember

the days when Cathy and Bobby used to hide behind their respective laser shields. Though I hope Dean will keep the stories going for a few years to come. I would like to thank the cavity side of the lab, particularly Dean, Mathijs and Yatu, for their humour and great company. Thank you to Bobby and Cathy for their friendship, particularly during the Part II to DPhil transition. Bobby's dry Scottish humour and my conversations with Cathy always lifted my spirits. I can't move on without saying how much I appreciated the occasions I spent with Cathy, Cara and Notty - thank-you the Crushworths. Thank you to Ed, who, jointly with Laura, constructed the VMI apparatus. When in doubt as to the whereabouts of something in the lab, Ed was the man to go to. On the imaging side of the lab, I would also like to thank Cécilia, James, Jason, Simon, Gabi, and Eyad. I have learnt a great deal over the last few years, and it is in part due to each and everyone of you.

Throughout my time at Oxford, and through the many conferences and network meetings that I have been fortunate enough to attend, I have been privileged in meeting some truly excellent scientists. I would like to thank all those researchers with whom I have discussed my own science and theirs, from fellow students right through to the most senior academics. It is always enlightening to see your own work through someone else's eyes. The Oxford-Bristol program grant lead to a particularly fruitful collaboration with the Bristol Laser group. I would like to thank Tolga Karsili and Professor Mike Ashfold for the time and effort that they have spent working on the EtX^{+} and DMF systems. I would also like to sincerely thank Professor Tim Softley and Dr Matt Costen for agreeing to examine this thesis.

The VMI apparatus was newly constructed when I began work in the Vallance group lab. It underwent various modifications, and as with all experiments experienced several technical faults over the course of time. Without the hard work of the gentlemen in PTCL workshops and electronics, as well as CRL and PTCL lab services, the last few years would have been a much rougher road. Thank you to all of them for ensuring that work got back on track in as timely a fashion as possible. Furthermore, the course of this DPhil would not have run so smoothly without the efforts of many of the administrative staff, from those in the Finance Department through to those in Stores. I would like to extend my utmost gratitude to the admin staff for the time they spent processing orders and dealing with queries. In particular, I would like to thank Bosa Petrovic for always ensuring the finance side of things was in order. Special thanks also go to the Chemistry IT department for their assistance over the last few years.

I gratefully acknowledge studentship and project funding from the ERC.

Anyone who has tackled a significant life challenge will know that we, as human beings, are not built to be isolated entities. We all need our support networks. The completion of this DPhil has been both an academic, professional, and personal challenge. I have already acknowledged the numerous people who have made up my academic and professional support network. However, I would like to finish these acknowledgements on a much more personal note.

Thank you to my friends, family and honourary family. Whether you've been just around the corner, or on the other side of the world, I've felt an incredible amount of support and encouragement. Without you all I would not have been able to complete this journey. You all know who you are. Though there are a few people to whom I should give a particularly big thank you.

Kham, Sally, Ross, Sam, Jess and Chris thank you all for the motivation and encouragement, friendship, and generosity you have shown me over the last few years.

Lucy, thank you for being the best HS.

Lizzie, thank you for always looking on the bright side and helping me do the same.

Alice, thank you for shooing away all my worries.

Eva, thank you for your wisdom.

David, thank you for bringing light and colour into my life and this thesis.

Auntie Jen, your strength is inspirational. Thank you for the time we have recently spent together, the stories you have shared with me and for your positive vibes.

Uncle Dave, you are truly a fountain of knowledge. Thank you for bringing the family together and for encouraging us all to make the most of the opportunities we have.

Double trouble, Charles, it just hasn't been the same around here without you, but even from more than 8000 km away you still manage to make me smile. Thanks bro.

A wise man once told me, "Every day above the ground is a good day." He has done everything in this power to ensure this has been the case for me. Dad, thank you.

A wise woman once told me, "This too shall pass." She has always been there for me, every step of the way. Mum, thank you.

Contents

List of Figures

List of Tables

List of Abbreviations

μs	microsecond, 10^{-6} seconds
D_0	bond dissociation energy
E_{av}	photofragment available energy
E_{elec}	electronic
E_{int}	internal energy
E_{rot}	rotational
E_T	total translation energy release
E_t	translational energy release of a particular fragment
E_{vib}	vibrational
1D	one dimensional
2D	two dimensional
3D	three dimensional
m/z	mass-to-charge ratio
CCD	charge coupled device
CI	conical intersection
DMF	N,N-dimethylformamide
fs	femtosecond, 10^{-15} seconds
hν	photon energy (where h is Plank's constant and μ is the frequency of the light)
IE	ionization energy
IP	ionization potential
IR	infrared
LIF	laser-induced fluorescence
MB	molecular beam
MCP	microchannel plate
MPI	multiphoton ionization
MS	mass spectrometry
ns	nanosecond, 10^{-9} seconds
PEC	potential energy curve
PEPICO	imaging photoelectron photoion coincidence specroscopy
PES	potential energy curve surface
PImMS	Pixel Imaging Mass Spectrometry
PMT	photomultiplier tube
ps	picosecond, 10^{-12} seconds

PTS	photofragment translational spectroscopy
REMPI	resonantly-enhanced multi-photon ionization
SHG	second harmonic generation
SPI	single photon ionization
THG	third harmonic generation
TOF	time-of-flight
TOF-MS	time-of-flight mass spectrum
TS	transition state
UV	ultra-violet
UVPD	Ultra-violat photodissociation
VMI	velocity-map imaging
VMImMS	Velocity-map Imaging Mass Spectrometry
VUV	vacuum ultra-violet

1

Introduction

Contents

The fragmentation of a chemical bond is one of the most fundamental processes in chemistry. In the first part of this chapter, Section 1.1, a few general dissociation mechanisms will be introduced, along with a number of fundamental concepts related to fragmentation events.

In the case of a unimolecular reaction $(\mathrm{AB} \rightarrow \mathrm{A} + \mathrm{B})$, with the aid of modern investigative techniques it is possible to determine not only *that* the bond dissociates but also *how* it does so; dynamical information about elementary chemical processes can be obtained. However, how a particular dissociation process evolves will depend on how it is initiated, and what we can learn about the event will be influenced by how the result of the event is

detected. Therefore, as will be discussed further in Section 1.2.1, the primary concerns in any photodissociation study are (i) how to initiate a fragmentation event, and (ii) how to detect the result of such an event.

Fragmentation processes are amenable to study by a wide range of methods, and the choice of which to employ is obviously dependent on what we wish to learn about the fragmentation. A number of questions can be posed when considering the possible outcome of a photofragmentation event, for example

1. What are the fragment identities?
2. How is the energy available to the fragments partitioned?
3. Which electronic states are involved?
4. Does the fragmentation result in product alignment?
5. Are there multiple pathways involved, and, if so, what is the relative importance of each pathway?

The aim of any photofragmentation study is to answer as many of these questions as possible, and, in doing so, come to a deeper understanding of the dissociation process. These questions, the types of information required in order to answer them, and the methods which are commonly used to obtain such information will be discussed in Section 1.2. As will become clear, several experimental techniques, which will merely be outlined in Section 1.2, have been key to the advancement of knowledge in the field of photodissociation. A more detailed overview, particularly of some of the earlier work performed in the area of photodissociation dynamics, can be found in reviews by Simons [1], Butler et al. [2] and Sato [3]. The technique that has been employed for the work described in this thesis, velocity-map imaging (VMI), will be covered in more detail in Section 1.3.

The central theme of this thesis is the investigation of the photodissociation dynamics of polyatomic systems. A number of photofragment imaging studies of such molecular systems will be presented. The motivation behind this work will be discussed in Section 1.4, and the studies themselves will be laid out on a chapter-by-chapter basis in Section 1.5.

1.1 Photofragmentation: mechanisms and fundamental concepts

1.1.1 Photodissociation mechanisms

The work presented in this thesis includes photofragmentation studies of both neutral and ionic species. There exist a multitude of different dynamical processes that may result in the dissociation of a chemical bond within such species. The study of photodissociation dynamics enables us to analyse the behaviour of molecules in different excited states, such as those that will be presented here. The schematic potential energy curves shown in Figures 1.1 and 1.2 illustrate a number of general photodissociation mechanisms, which are relevant to neutral and ion photofragmentation processes, respectively.

As shown in Figure 1.1 (a), one of the simplest dissociation mechanisms for neutral species involves excitation of the molecule to an unbound excited electronic state, following absorption of a photon of energy $h\nu_a$. Fast direct dissociation results and the internuclear distance increases until two distinct product fragments are formed.

In contrast, if the initial excitation results in population of a bound region of an excited electronic state, as shown in Figure 1.1 (b), the molecule will be trapped there. Overlap of the vibrational wave functions of the ground state and excited state may facilitate internal conversion (IC) back down to the ground state. The vibrationally hot ground state can then dissociate to form the individual fragmentation products.

Figure 1.1 (c) depicts another case in which the molecule is excited to a bound region of a higher lying electronic state. However, in this case, the photon energy ($h\nu_c$) exceeds the energy of the barrier to dissociation and the mechanism proceeds over the barrier. In the case illustrated, the products formed lie at a higher energy than the products that result from the mechanism shown in Figure 1.1 (b).

Figure 1.1 (d) illustrates a predissociation mechanism, one in which the molecule is initially excited to a bound state, then crosses to an unbound state, and dissociates to form the fragmentation products.

The ion dissociation mechanisms shown in Figure 1.2 reflect those of the neutral shown in Figure 1.1, except that, in the case of the ion, the dissociation occurs above the ionization potential (IP). Figure 1.2 (a) displays two possible photon absorption schemes. The first involves single photon ($h\nu_a$) excitation of the ground state neutral to an unbound electronic state of the ion. The second process proceeds via initial population of the ion ground

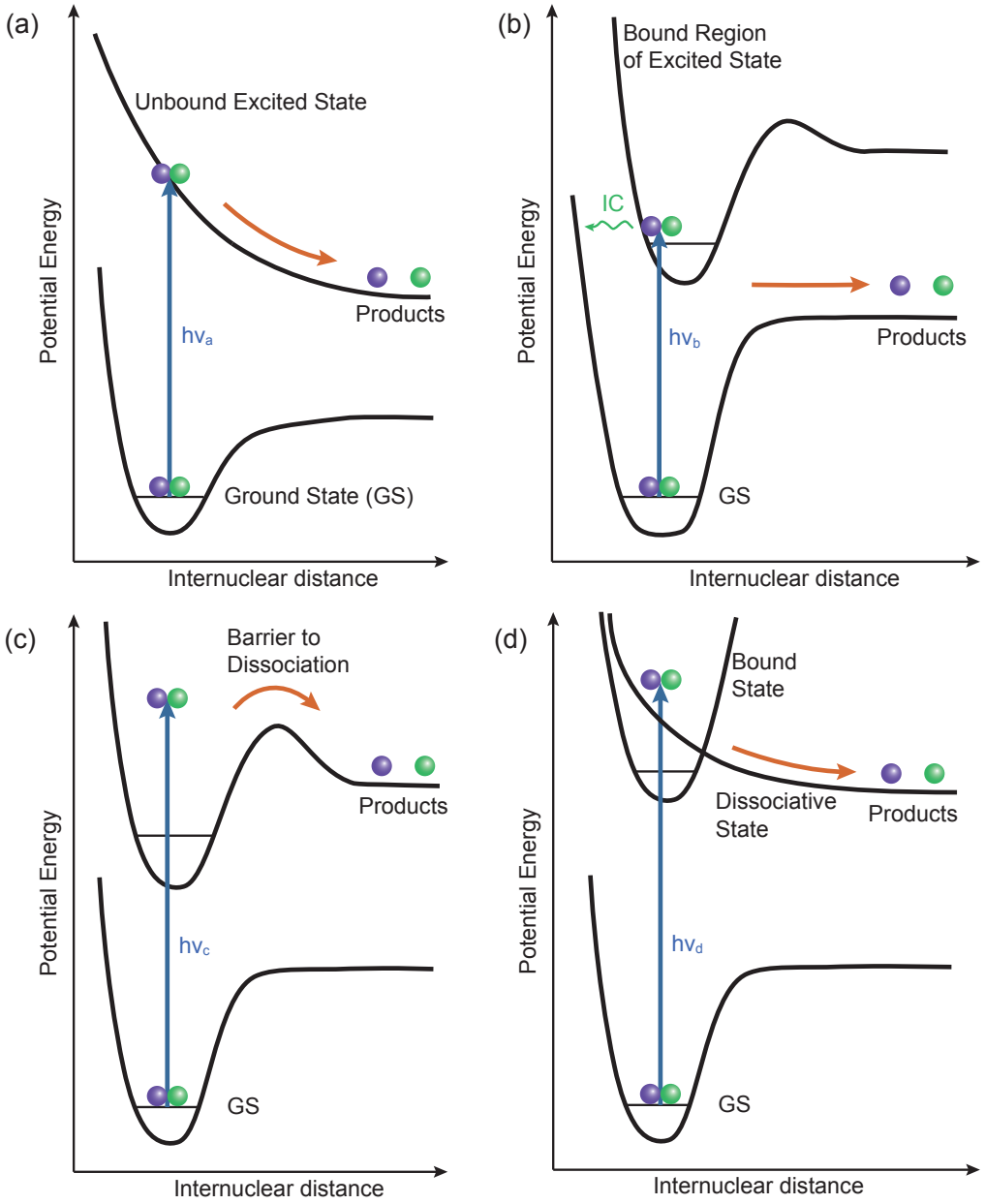

Figure 1.1: Schematic potential energy curves relevant to the photofragmentation of neutral species. Four photodissociation mechanisms are illustrated: (a) excitation to an unbound excited state, (b) excitation to a bound state, followed by internal conversion, (c) dissociation over a barrier, and (d) a predissociation mechanism, each of which is discussed in more detail within the text. In each scheme only those product fragments which result from the dynamical process of interest have been depicted.

state, following absorption of $h\nu_1$, which can then absorb an additional photon, $h\nu_2$ and dissociate along the unbound state to form the products, as shown.

The ionization potentials of most species are on the order of several electron volts (6-10 eV). Therefore, for single-photon dissociative ionization, and even single-photon ionization, a high energy photon in the ultraviolet (UV) or vacuum-ultraviolet (VUV) range is required to exceed the ionization potential (and dissociation limits). As a result, such a single-photon mechanism is not easily achieved, since it is often not easy to produce UV and VUV laser light efficiently and with high enough intensity. Often a multiphoton ionization process is employed, in which multiple photons of lower energy are absorbed in order to exceed the ionization potential. However, the apparatus employed for the work presented in this thesis incorporates a VUV photon source, which produces 118 nm light (see Section 2.4.2). This ensures that formation and dissociation of ionic species can be achieved through sequential absorption of two photons, as depicted in Figure 1.2 (a). In some cases single-photon dissociative ionization is achievable even with the available 10.49 eV photon energy.

The mechanisms in Figure 1.2 (b) and Figure 1.2 (c) may also involve a multiphoton process with initial ionization. However, for simplicity only the one-photon excitation is depicted. Figure 1.2 (b) involves internal conversion from a bound excited state of the ion to the ground state of the ion and results in dissociation of the vibrationally excited parent ion. Figure 1.2 (c) involves dissociation over a barrier. Predissociation mechanisms, as shown in Figure 1.2 (d), can also occur for ions.

Direct dissociation processes, e.g. Figure 1.1 (a) and Figure 1.2 (a), are termed 'impulsive'. Following excitation to a dissociative state, the dissociation occurs rapidly, generally on a timescale on the order of tens to hundreds of femtoseconds (10^{-15} s). A significant portion of the energy in excess of the bond dissociation energy, i.e. the energy available to the fragments following dissociation, can be expected to be released as translational energy. In other words, the available energy is partitioned in a non-statistical manner. In contrast, dissociation mechanisms which involve internal conversion processes, e.g. Figure 1.1 (b) and Figure 1.2 (b), or proceed over a barrier, e.g. Figure 1.1 (c) and Figure 1.2 (c), occur on a much slower timescale, on the order of picoseconds (10^{-12} s), or even nanoseconds (10^{-9} s). These timescales allow for redistribution of the available energy among all of the internal degrees of freedom of the parent molecule before dissociation. Therefore, these slower processes generally result in a fairly statistical distribution of the available energy across the degrees of freedom of the fragmentation products. The timescale of predissociation mechanisms, e.g. Figure 1.1 (d) and Figure 1.2 (d), is generally dependent

on the coupling between the bound and dissociative states. If the transfer of population to the unbound state is efficient, then the dissociation process will proceed on a shorter timescale than if it is not.

1.1.2 Energy redistribution

Any neutral photolysis event, including those presented in Section 1.1.1, may be represented by the general two-step reaction equation

$$\mathrm{AB} + \mathrm{h}\nu \rightarrow \mathrm{AB}^{*} \rightarrow \mathrm{A}(v', j') + \mathrm{B}(v', j') \tag{1.1}$$

When a molecule (for example AB in the above equation, where A-B may be polyatomic) absorbs a photon, of energy $\mathrm{h}\nu$, it is promoted to an excited state (AB^{*}). The molecule then dissociates to yield the fragmentation products, in this case, the A and B co-fragments. These fragments are formed in particular internal quantum states, which are represented by the vibrational, v', and rotational, j', quantum numbers.

In the case of dissociative ionization, the process may be represented as

$$\mathrm{AB} + \mathrm{nh}\nu \rightarrow \mathrm{AB}^{+(*)} + e^{-} \rightarrow \mathrm{A}^{+}(v', j') + \mathrm{B}(v', j') + e^{-} \tag{1.2}$$

where photoexcitation results in loss of an electron, e^{-}, and on dissociation either the A or B fragment may carry the positive charge.

When any fragmentation event occurs, both energy and momentum must be conserved. In addition to the internal energy of the parent molecule, E_{int}, in the case of photofragmentation, a fixed amount of energy is provided by the photon, and a certain amount of energy (D_0) is required to dissociate the bond. Therefore, the dissociation event yields a precise amount of energy, E_{av}, which is available to the photofragments. This is simply the difference between the energy of the excited parent species (i.e. the sum of the initial excitation of the parent molecule, E_{int}, and the energy provided by the photon, $\mathrm{h}\nu$) and the energy required to break the bond, D_0.

$$E_{\mathrm{av}} = \mathrm{h}\nu + E_{\mathrm{int}} - D_0 \tag{1.3}$$

The available energy can be released into translation, E'_{T}, and internal excitation, E'_{int}, of the fragments.

$$E_{\mathrm{av}} = E'_{\mathrm{T}} + E'_{\mathrm{int}} \tag{1.4}$$

The individual translational energies, E'_{t}, of atomic and molecular fragments, as well as any ejected electrons, will contribute to E'_{T}. E'_{int}, which is the sum of the internal energies of

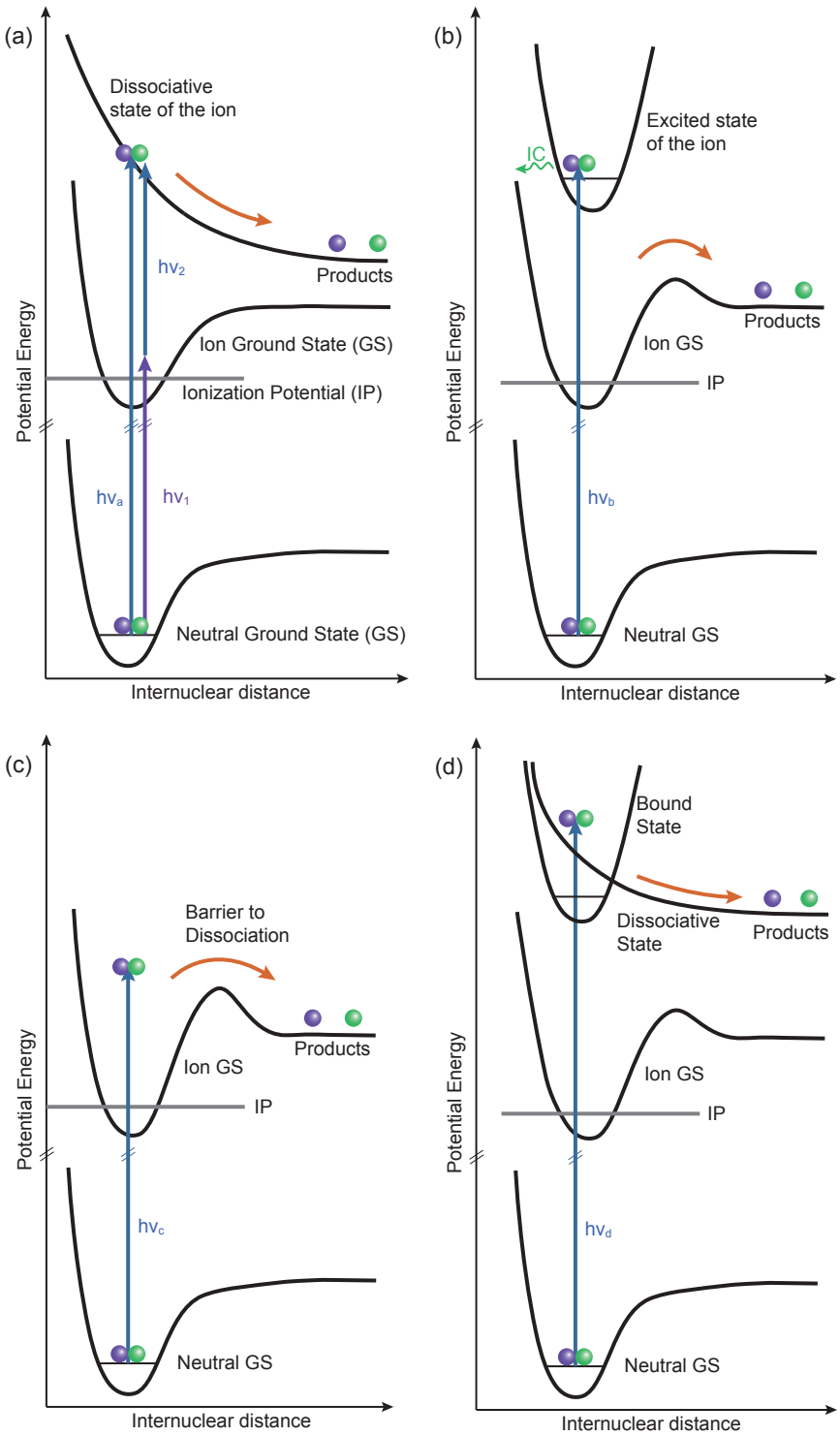

Figure 1.2: Schematic potential energy curves relevant to ion dissociation. Four photodissociation mechanisms are illustrated: (a) excitation to an unbound excited state, (b) excitation to a bound state, followed by internal conversion, (c) dissociation over a barrier, and (d) a predissociation mechanism, each of which is discussed in more detail within the text.

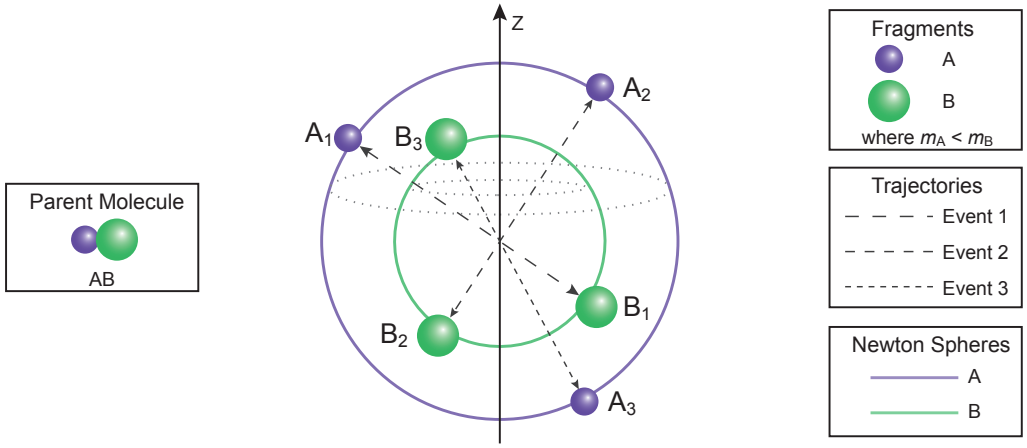

Figure 1.3: A pair of Newton spheres, created in the unimolecular reaction of AB to form fragments A and B ($m_A < m_B$). Three events are shown. (Adapted from Figure 2.1 from reference [4])

the individual fragments, is distributed amongst the rotational, E'_{rot}, vibrational, E'_{vib}, and electronic, $E'_{\text{electronic}}$, energy of the fragments.

$$E'_{\text{int}} = E'_{\text{rot}} + E'_{\text{vib}} + E'_{\text{electronic}} \tag{1.5}$$

As a result of energy conservation, for a given photon energy, hν, and given product internal energies, the photofragment translational energies, and therefore their velocities, are well defined. Co-fragments formed with a specific amount of internal energy, E'_{int}, have a total translational energy, E'_{T}, reflective of the energy partitioning given by Equation (1.4). For a particular E_{av}, co-fragments formed with greater E'_{int} will have less E'_{T} and vice versa.

1.1.3 Newton spheres

Product scattering is often discussed in terms of 'Newton spheres' for each quantum state-resolved fragment. A photofragmentation event results in photofragments on the surfaces of a series of expanding spheres, one for each product quantum state, with their origin at the interaction region. The radius of the sphere is directly proportional to the speed of the fragment, while the position of an individual fragment on the sphere is determined by its scattering angle. The distribution of Newton spheres, and the distribution of fragments on the surface of each Newton sphere, is determined by the detailed dynamics of the fragmentation process under study.

As an illustration, consider the fragmentation of a *diatomic* molecule (AB, where A and B are atoms), which absorbs a given photon energy, $h\nu$, and has a bond dissociation

energy, D_0. For this example assume that there is no internal energy in the parent diatomic molecule, since this could potentially lead to multiple Newton spheres in the products.

The available energy, E_{av} is released into translation and electronic excitation of the atomic fragments.

$$E_{\text{av}} = E'_{\text{T}} + E'_{\text{electronic}} \tag{1.6}$$

The atomic fragments have no vibrational or rotational degrees of freedom. As will be discussed further in Section 1.2.3, if it is assumed that the atoms are formed in their electronic ground states, conservation of momentum determines the partitioning of the translational energy according to the relative masses of the atomic fragments. As shown schematically in Figure 1.3, fragmentation of a diatomic molecule (AB) therefore results in the formation of a pair of Newton spheres, one for each atomic fragment, since the radii of the spheres depend only on the fragment masses. Figure 1.3 shows the case where $m_{\text{A}} < m_{\text{B}}$. Fragment A, which has the lower mass, obtains a greater fraction of the total translational energy through momentum conservation and, therefore, the radius of the Newton sphere for A (shown in purple) is greater than that for B (shown in green).

Three individual fragmentation events are depicted in Figure 1.3. As a result of the conservation of momentum, the A and B atomic fragments scatter in opposite directions. The distribution of photofragments on the surface of the Newton spheres can either be isotropic or anisotropic. The angular distributions can be indicative of the directionality and timescale of the photofragmentation, which will be discussed further in Section 1.2.4.

The concept of Newton spheres is not limited to the fragmentation of diatomic molecules. However, when considering larger systems, the vibrational and rotational excitations of polyatomic fragments need to be taken into account, since they yield numerous additional Newton spheres. For example, when a triatomic molecule dissociates (e.g. $\text{ABC} \rightarrow \text{A} + \text{BC}$), the diatomic fragment, BC, may be formed in a large number of vibrational or rotational states, leading to a correspondingly larger number of possible Newton spheres for the fragments. The work discussed in this thesis focuses on the photofragmentation of polyatomic molecules, for which many possible Newton spheres are created.

1.2 Photodissociation Studies

1.2.1 Pump-probe techniques

As mentioned, two primary concerns in any investigation of a fragmentation process are (i) how to effect a fragmentation event, and (ii) how to detect the result of such an event. Pump-probe techniques cover both of these considerations: the 'pump' step initiates a dissociation event, and the 'probe' step ensures detection of the nascent photofragments.

(i) Pump Step: Originally, flash photolysis, using a short-pulsed light source such as a flash-lamp, was employed to achieve photofragmentation of a parent molecule. Some of the most notable pump-probe work using flash photolysis was carried out by Norrish and Porter [5], who in 1967 were awarded (half) a Nobel prize for their early work in the field of fast chemical reactions.

Following the development of pulsed laser technology, an ultraviolet (UV) or infrared (IR) laser pulse, with a duration ranging from the nanosecond down to the femtosecond time regime, is now commonly employed to achieve dissociation. This proves effective since the photon energy of UV light generally exceeds most bond dissociation energies. It should be noted that light from the infra-red (IR) through to the extreme ultraviolet (XUV) energy range is employed to investigate other molecular phenomena, ranging from molecular vibrational excitation through to photoionization and high-harmonic generation [6–8].

(ii) Probe Step: A number of detection methods have been employed over the years. For example, the system may be probed by spectroscopic methods, e.g. laser-induced fluorescence (LIF) [9] and/or Doppler spectroscopy [10], or ionization of the nascent fragments. Investigative techniques that employ ionization detection methods include resonantly-enhanced multiphoton ionization (REMPI), time-of-flight mass spectrometry (TOF-MS) [11], photofragment translational spectroscopy (PTS) [12], core-extraction [13], and velocity-map imaging (VMI). Ionization has proved to be a particularly useful probe step, since a range of charged-particle detectors are available, including, but not limited to, microchannel plates (MCPs) and delay-line detectors [14]. Ionization can be achieved either by electron bombardment, which involves transfer of energy through collision of high-energy electrons with the fragment, or via photoionization. There are a range of photoionization methods which are commonly employed, including single photon ionization (SPI), multiphoton ionization (MPI), and resonantly-enhanced multiphoton ionization (REMPI). SPI can be achieved when the energy of a single photon exceeds the ionization potential of the fragment of interest, whereas MPI involves successive absorption of a number of photons until the total

energy absorbed exceeds the ionization potential. This method generally requires a much higher photon density compared to SPI. REMPI achieves ionization via excitation to an intermediate electronic state of the nascent fragment, with subsequent ionization from this state, and allows state-selective detection of the photofragments. Such a method is more efficient than MPI since the absorption cross section significantly increases when the energy of one or more photons matches that of a resonant state. The ionization method of choice is generally dependent on the system under investigation, and needless to say, the apparatus at hand. Both REMPI and SPI have been employed in the work presented in this thesis, and these methods will be discussed in more detail in Sections 2.4.2 and 2.8, respectively. Of course, it should be noted that if the parent species is itself an ion then one of the nascent fragments will be born with a positive charge and can be detected directly.

The choice of pump-probe technique is most often determined by the particular aspects of the photodissociation we wish to investigate. As mentioned previously, when considering a photodissociation process, there are a number of questions that can be posed. By answering these questions we are able to reveal the various features of the photofragmentation process. Each of the questions which are most commonly raised when evaluating the outcome of a dissociation event will now be considered in turn.

1.2.2 What are the fragment identities?

The primary goal of any fragmentation study is to identify the product fragments. The illustrative potential energy diagrams, shown in Section 1.1.1, all depict cuts through the potential energy surfaces. Such diagrams only show the dissociation pathways available for fragmentation of a single bond. If the molecule has more than two atoms, as is the case for all the molecular systems presented in this work, the potential energy surfaces will be multidimensional. This means that there are a number of bonds which could potentially dissociate. As a result, it is often not clear from the outset which product fragments will be formed.

The most common way of identifying the products of a dissociation event is by analysing the masses of the fragments formed. Time-of-flight mass spectrometry (TOF-MS) [11] has the ability to ascertain the masses of the fragments. The Wiley-McLaren TOF spectrometer design [15], which is optimised to achieve high mass resolution, has become the standard in such apparati. Ions are accelerated towards a detector, which records their arrival times. These are dependent on the fragment masses, with lighter masses arriving before heavier ones.

1.2.3 How is the energy partitioned?

As discussed in Section 1.1.2, the energy available to the fragments is distributed between product internal energy and translational energy. The energy distributions which result from a photofragmentation process can give an indication of the type of mechanism involved in the dissociation process. For example, when we consider the photodissociation mechanisms presented in Section 1.1.1, the direct dissociation processes, shown in Figure 1.1 (a) and Figure 1.2 (a), would be the most likely to release a significant portion of the available energy into translation. In contrast, the molecules that dissociate via mechanisms occuring on a slower timescale, such as those illustrated in Figure 1.1 (b) and (c), and Figure 1.2 (b) and (c), will experience extensive energy redistribution, resulting in fairly statistical internal energy distributions. Since the most highly internally excited molecules will be those that are most likely to fragment, these types of mechanisms also yield fairly statistical translational energy distributions.

Techniques such as laser-induced fluorescence (LIF) and resonantly-enhanced multiphoton ionization (REMPI) have been employed to investigate the photofragment internal state distributions. LIF involves excitation of a fragmentation product to an emitting state. Analysis of the LIF spectra can reveal the identity of the fragment, as well as its internal energy distribution [9]. If a species is formed in an excited state, then its emission spectrum can sometimes be acquired directly without need for a LIF probe step.

REMPI, which will be discussed further in Section 2.8, also allows state-selective detection of a single fragmentation product (see [2] and references therein). Ionization of the fragment is achieved through single or multiple photon absorption to an intermediate electronic state, followed by additional photon absorption to an energy which exceeds the ionization potential. The ion signal intensity is measured as a function of probe wavelength, and from the REMPI peak intensities the internal state population distribution can be obtained.

Very high resolution spectra can be obtained from the LIF and REMPI techniques when suitably narrow bandwidth laser sources are employed. However, these techniques require a detailed prior understanding of the spectroscopy of the fragment of interest. In addition, both LIF and REMPI require that the fragment of interest has an electronic transition which is accessible (most commonly using light from a tuneable dye laser) through a one- or multi-photon transition [2].

Since the energy available to the fragments is distributed amongst the translational and internal degrees of freedom, as discussed in Section 1.1.2, and expressed as Equation (1.4),

if E_{av} is known then the internal energy of the fragments can be determined from the translational energy. E'_{int} is simply the difference between the available energy and the energy released into translation, E'_T. Therefore, it is common for the E'_{int} distribution to be calculated from the total translational energy distribution. A number of more general techniques have been developed to obtain the latter, including core-extraction time-of-flight measurements, photofragment translational spectroscopy (PTS), and velocity-map imaging (VMI). These methods are able to obtain the fragment velocities and, therefore, reveal the energy which is released into translation as a result of a fragmentation event [12, 13].

Photofragment translational spectroscopy (PTS) is an extension of TOF-MS. In a PTS experiment the photofragment arrival times are recorded [16]. The arrival time distributions for each photofragment can be fitted to obtain the translational energy distribution of the photofragments. Zare and co-workers implemented a slightly different enhancement of the TOF-MS technique. They combined TOF-MS with a photofragment detection method which they termed 'core extraction' [13]. Their original work focused on the use of this core sampling method in bimolecular reactions. However, the method has also been used successfully in photodissociation studies [17, 18]. The technique involves placing a pin hole in front of the TOF-MS detector so that ions recoiling laterally to the TOF axis do not reach the detector. Only fragments with a reduced velocity projection, i.e. those with a velocity parallel, or almost parallel, to the TOF axis, are detected; this produces a 1D sample through the core of the velocity sphere. Though this method leads to reduced detection sensitivity, the 1D projection of the velocity distribution which is obtained does give improved energy resolution compared to conventional PTS. Furthermore, recording data in several different experimental geometries, defined by the pump and probe laser propagation directions and polarisations, allows the full 3D velocity distribution to be reconstructed.

Doppler analysis of absorption (or emission) spectra also allows the determination of the velocity of the fragment. Doppler spectroscopy often employs the LIF technique, and, as such, is a less general technique than PTS or core-extraction. However, Doppler spectroscopy has been used to study a wide range of photoinitiated reactions ranging from photofragmentation to bimolecular reactions [19]. This technique uses the Doppler shift phenomenon to measure a 1D velocity distribution of a photofragment. In an absorption experiment, e.g. LIF, the frequency of light absorbed by the photofragment is dependent on the relative velocity between the laser beam used to probe the fragment, and the fragment itself. In order to Doppler resolve the spectra, the bandwidth of the probe laser must necessarily be very narrow, much narrower than the Doppler line width, so that features of the Doppler line shape may be resolved. Such experiments therefore require the use of an

etalon within the laser cavity [20]. One of the earliest Doppler spectroscopy-laser induced fluorescence studies, performed by Schmiedl et al., investigated the dissociation of hydrogen iodide at 266 nm [20]. Tuneable VUV radiation was used to scan across the transition of atomic hydrogen corresponding to the Lyman-α line. From the measured Doppler line shape the authors were able to obtain both the velocity and angular distribution of the H atom.

In recent years the techniques mentioned so far have been largely superseded by velocity-map imaging (VMI), which produces a two-dimensional projection of the three-dimensional velocity distribution of a photofragment. The general concepts behind the VMI technique, which has formed the foundation of the work presented in this thesis, will be discussed in Section 1.3. The experimental methods will be described in detail in Chapter 2.

The fragment speed distribution is readily extracted from the velocity-map ion image. The fragment translational energy, E_t' can be calculated from the measured fragment velocity, since the translational energy that a fragment possesses is dependent on its mass, m, and its velocity, v', according to the well known expression

$$E_t' = \frac{1}{2} m' v'^2 \tag{1.7}$$

Following a photodissociation event, the resultant total translational energy of the photofragments, E_T', can be expressed in terms of the reduced mass of the fragments, μ', and v_{rel}', their relative velocity.

$$E_T' = \frac{1}{2} \mu' v_{rel}'^2 \tag{1.8}$$

Since energy must be conserved, E_T' can also be expressed in terms of the translational energies of the individual fragments, E_t'. For the general photofragmentation event presented in Equation (1.1), in which the parent molecule AB yields fragments A and B, the resultant E_T' can be expressed as

$$E_T' = E_t'(\mathrm{A}) + E_t'(\mathrm{B}) = \frac{1}{2} m_A' v_A'^2 + \frac{1}{2} m_B' v_B'^2 \tag{1.9}$$

where m_A' and m_B' are the masses of fragments A and B, respectively, and v_A' and v_B' are the fragment velocities.

The conservation of momentum, as denoted by Equation (1.10), requires that on fragmentation the two products recoil in opposite directions. This gives us an expression by which to relate the product masses and velocities.

$$m_A v_A + m_B v_B = 0 \tag{1.10}$$

Equations (1.9) and (1.10) can be combined in order to yield expressions for the partitioning of translational energy between the two fragments, which gives fragment translational energies

$$E'_{\mathrm{t}}(\mathrm{A}) = \frac{m_{\mathrm{B}}}{m_{\mathrm{AB}}} E'_{\mathrm{T}} \qquad \text{and} \qquad E'_{\mathrm{t}}(\mathrm{B}) = \frac{m_{\mathrm{A}}}{m_{\mathrm{AB}}} E'_{\mathrm{T}} \tag{1.11}$$

Therefore, for the case when a fragmentation event yields two fragments, and the translational energy of fragment A (or B) can be obtained from the VMI experiment, then the total translational energy, E'_{T} , released in the fragmentation event can be calculated using Equation (1.11). For the case when both fragments (A and B) are detected then the two E'_{T} values calculated from their individual E'_{t} can be compared in order to confirm that the two fragments detected are indeed co-fragments, or, equivalently, their momenta may be compared.

1.2.4 Which electronic states are involved?

The anisotropy in the photofragment scattering distributions comes about due to the interaction between the electric vector, $\vec{\varepsilon}$, of the photolysis light and the transition dipole moment, $\vec{\mu}$, which is characteristic of the particular transition excited within the molecule. Therefore, the angular distributions of the photofragments reveal information about the electronic states involved in the dissociation event [21, 22].

With the use of linearly polarised light, techniques such as Doppler spectroscopy [21], core-extraction time-of-flight[13], and PTS [23], which are employed to obtain the photofragment translational energies, are also able to obtain the angular distributions of the fragments. However, velocity-map imaging, and extensions of this technique such as slice-imaging [24, 25], present the most straightforward method for obtaining the angular distributions [26]. Such techniques are able to measure the angular distribution directly, as, in the case of VMI, the 2D projection of the 3D Newton sphere is acquired, or, in the case of slice imaging, a cut through the middle of the Newton sphere is measured.

In an experiment, the molecules to be dissociated are usually randomly oriented in space (in a molecular beam, for example). When the pump light source is linearly polarised the polarisation vector $\vec{\varepsilon}_p$ selectively excites molecules with their transition dipole moments $\vec{\mu}$ parallel to $\vec{\varepsilon}_p$; the probability of absorbing a photon is given by

$$P = |\vec{\mu} \cdot \vec{\varepsilon}_p|^2 = \vec{\mu}^2 \vec{\varepsilon}_p^2 \cos^2\theta \tag{1.12}$$

where θ is the angle between $\vec{\mu}$ and $\vec{\varepsilon}_p$, as illustrated in Figure 1.4.

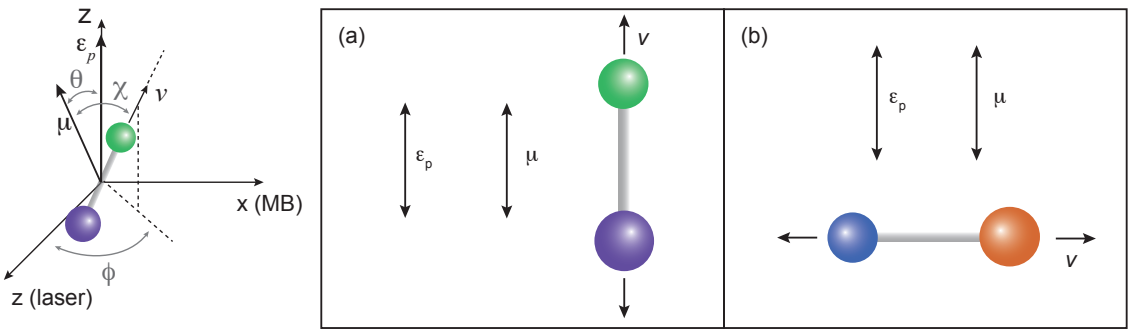

Figure 1.4: Vector correlations associated with (a) a parallel and (b) a perpendicular dissociation for a diatomic molecule.

It should be noted that using linearly polarised photolysis light ensures an axis of cylindrical symmetry within the 3D velocity distribution of the fragments. If we define a frame of reference such that the z axis lies parallel to $\vec{\varepsilon}_p$, then absorption of a photon, and therefore excitation of a molecule, depends on the orientation θ of the molecule with respect to the z axis, but not on the azimuthal angle ϕ (see Figure 1.4). This gives a C_∞ axis of rotational symmetry within the 3D distribution. This cylindrical symmetry axis turns out to be important particularly for the VMI technique, as it allows the reconstruction of the 3D velocity distribution from a 2D projection, as recorded in a standard 'crushed' VMI experiment. However, if the products are formed rotationally or orbitally aligned (see Section 1.2.5), the detection probability will depend on the laser polarisation, and therefore the cylindrical symmetry of the resulting image may be destroyed in such cases.

Since the probability of absorbing a photon, and therefore effecting a dissociation event, is dependent on the angle between $\vec{\mu}$ and $\vec{\varepsilon}_p$, by observing the angular distribution of the resulting fragments we can determine the orientation of $\vec{\mu}$ relative to the relative recoil velocity vector, $\vec{v}$, and therefore relative to the dissociating bond.

The intensity distribution of the velocity-map image as a function of the product speed, v, and the angle, θ, is given by

$$P(v,\theta) = P(v)[1+\beta_2(v)P_2(\cos\theta)] \tag{1.13}$$

where $P(v)$ is the speed distribution, and $\beta_2(v)$ is the (speed dependent) anisotropy parameter. $P_2(\cos\theta)$ is the second order Legendre polynomial of the $\cos\theta$ function, given in Equation (1.14).

$$P_2(\cos\theta) = \frac{1}{2}(3\cos^2\theta - 1) \tag{1.14}$$

It follows, therefore, that for each product speed, v, the angular distribution can be fit to the function

$$P(\theta) = [1 + \beta_2 P_2(\cos\theta)] \tag{1.15}$$

From this we can evaluate the anisotropy parameter, β_2, which characterises the angular distribution of the photofragments. β_2 takes values between -1 and +2, and is the expectation value of a function of the angle χ, which, as shown in Figure 1.4, is the angle between the the transition dipole moment and the recoil velocity.

$$\beta_2 = \langle P_2(\cos\chi)\rangle \tag{1.16}$$

Since the anisotropy parameter is a function of χ, by determining β_2 it is possible to gain an insight into the nature of the excited electronic state. Figure 1.4 illustrates the two limiting cases for single photon direct dissociation (as illustrated in Figure 1.1 (a), for example):

Case (a): $\vec{\mu}$, which is characteristic of the transition excited within the molecule, lies parallel to the dissociating bond ($\chi = 0°$) and therefore, parallel to the relative recoil velocity vector $\vec{v}$. It follows from Equation (1.12) that the maximum probability for absorbing a photon is when $\vec{\mu}$ is parallel to the polarization vector $\vec{\varepsilon}_p$ of the photolysis laser ($\theta = 0°$), and so in this case the products preferentially recoil along $\vec{\varepsilon}_p$. Therefore, when $\theta = 0°$ there will be a maximum in intensity in the angular distribution. In contrast, when $\theta = 90°$ the intensity will be at a minimum, since at this angle the probability of absorbing a photon, and therefore effecting a photodissociation event, is at its lowest. This variation in intensity, which is characteristic of a parallel transition, can be fit by β_2 = +2 and follows a $\cos^2\theta$ type function.

Case (b): In the molecular frame $\vec{\mu}$ lies perpendicular to the dissociating bond. In this case, the maximum probability of absorbing a photon is when the molecular bond axis is at right angles to $\vec{\varepsilon}_p$. On dissociation the fragments fly apart along the bond axis, which in this case lies preferentially perpendicular to $\vec{\varepsilon}_p$ (as shown). A perpendicular transition like this yields a variation in intensity which resembles a $\sin^2\theta$ function and is characterised by β_2 = -1.

Many molecules do not conform to either of these two extreme cases, and β_2 lies somewhere between -1 and +2. For example, if the timescale to dissociation following absorption of a photon is longer than the period of molecular rotation then the correlation will be lost, with a concomitant reduction in the magnitude of β_2. As a result, the anisotropy parameter, being sensitive to the lifetime of the parent molecule excited state, can give an idea

of the timescale of the dissociation [23]. Low values of β_2 can be indicative of dissociation mechanisms involving internal conversion, as illustrated in Figure 1.1 (b), or dissociation over a barrier, as depicted in Figure 1.1 (c). Furthermore, β_2 is influenced by the geometry of the parent molecule [27]. In the case of bent polyatomic molecules, $\vec{\mu}$ is unlikely to lie perfectly parallel or perpendicular to the dissociating bond axis, leading to intermediate values of β_2. It should also be noted that in the cases presented here the asymptotic recoil velocity is along the bond axis of the dissociating bond. In the general case, with an angle α between them, β_2 will be given by $\beta_2 = 2P_2(\cos\chi)P_2(\cos\alpha)$.

1.2.5 Does the fragmentation result in product alignment?

If polarised probe light is employed, the photofragment images can also reveal whether the product fragments are formed rotationally or electronically aligned. Such alignment is a result of the products being formed with a polarised distribution of rotational or electronic angular momentum vectors. The detection efficiency using a polarised probe laser (in a VMI experiment, for example) will be dependent on the angle between the polarisation vector $\vec{\varepsilon}_p$ of the probe laser and the transition dipole moment $\vec{\mu}$ for the detection transition, which correlates with the product angular momentum vector, $\vec{J}$. The probe laser selectively detects molecules with their transition dipole moments $\vec{\mu}$ parallel to $\vec{\varepsilon}_p$. Therefore, if the fragments are aligned, the detection efficiencies, and therefore the measured images, obtained when employing a probe laser polarised parallel to the plane for the detector will be different from those obtained when the polarisation vector is perpendicular to the plane of the detector. No alignment effects have been observed in the studies which will be presented in this thesis.

1.2.6 Are there multiple dissociation pathways involved?

Until now we have considered the energy partitioning and electronic states involved in a particular fragmentation pathway. However, particularly in the case of the fragmentation processes of polyatomic molecules, such as those presented in this thesis, multiple dissociation pathways are often active. Furthermore, it is worth noting at this stage that following an initial (primary) fragmentation, the fragments themselves may undergo additional (secondary) dissociation processes.

Different fragmentation pathways may yield either different co-fragments, or the same co-fragments in different electronic, vibrational, or rotational states. If there are multiple

active dissociation pathways, to gain a complete picture of the fragmentation process it is important to understand not only the dynamics of each pathway, but also, the relative importance of each of these pathways, which can be quantified in terms of a branching ratio or quantum yield.

Different dissociation pathways can reveal themselves in a number of ways. For example, if different pairs of co-fragments are formed, and the fragments are universally detected (see Section 2.4.2), then multiple mass fragments would be observed in a time-of-flight mass spectrum (TOF-MS). In contrast, if competing dissociation pathways yield the same mass fragments, but in different electronic states, then this would not be clear from a TOF-MS. In order to determine the production of the fragments in different electronic states an analysis of the internal state population distribution is required. Furthermore, the angular distributions of the fragments may be influenced if the fragments result from initial excitation to different excited states.

1.3 Velocity-map Imaging

The original ion imaging experiment was carried out by Chandler and Houston in 1987 [28]. Using what was essentially a standard Wiley-McLaren TOF setup [15] equipped with a position sensitive detector, the authors were able to obtain the 3D spatial distribution of state-selectively detected photofragments projected onto a 2D surface. As a result, the velocity distribution of the $CH_3(v = 0)$ fragments resulting from 266 nm photodissociation of methyl iodide, CH_3I, could be measured, and, therefore both the speed and angular information could be obtained directly.

A decade later Eppink and Parker significantly advanced the imaging technique by making improvements to the ion lens set up [29]. They removed the grids that were present in the Wiley-McLaren lens, therefore removing a major source of image distortion, and, furthermore, they introduced a third plate to the ion lens assembly. In the original ion imaging experiments a major issue which led to blurring and poor image resolution, and, therefore, velocity resolution, is the fact that since the ionization laser has a finite width, ions are formed within a finite interaction region. Eppink and Parker achieved much improved velocity resolution through velocity focusing, and so coined the term 'velocity-map imaging'. As illustrated in Figure 1.5, velocity focusing maps ions of the same velocity component in the image plane to the same point on the detector, regardless of their initial positions. In addition, VMI also introduces a magnification factor, M. Using the

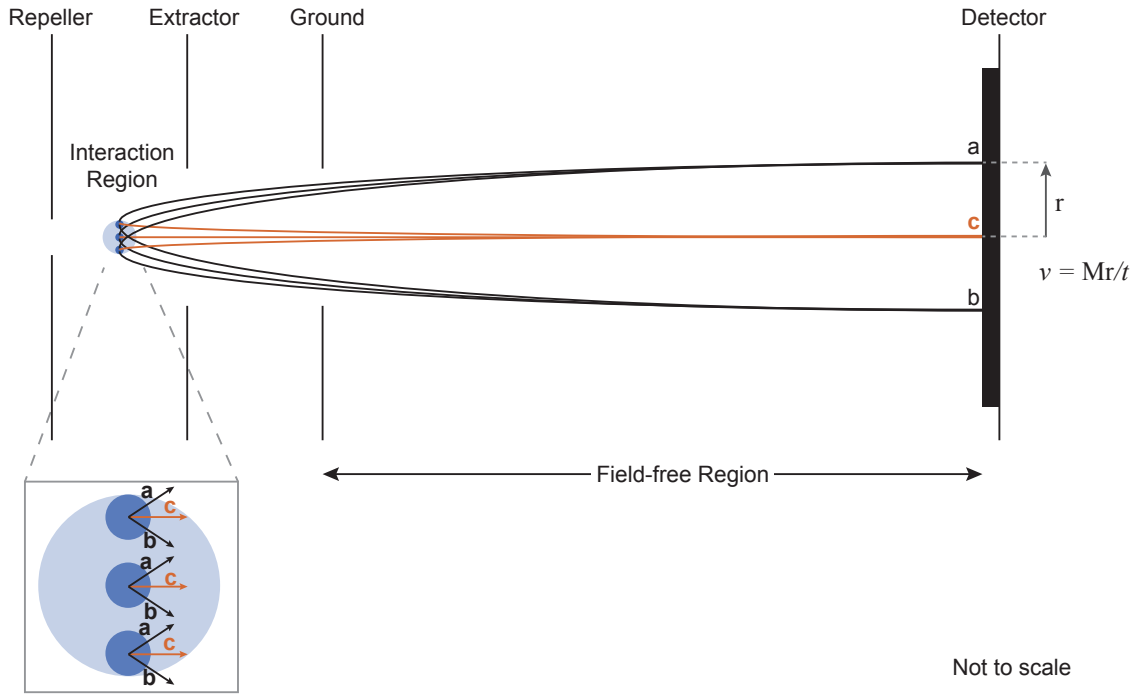

Figure 1.5: Illustration of velocity focusing. A cut through the VMI optics, which consist of three gridless plates: Repeller; Extractor; and Ground. The inset magnifies the interaction region (light blue), within which the velocities of nine different particles are shown. These particles originate from three different parts of the interaction region (each shown as a dark blue circle). Within each part there is a particle with transverse velocity **a**, another that has a velocity **b**, which is equal in magnitude but opposite in transversal direction to **a**, and a third particle which has zero transverse velocity, **c**. As shown, the particles which have the same initial velocity are mapped on the the same point on the detector (a, b or c), regardless of where they are produced within the interaction region. The radius from the center of the image, r, is proportional to the velocity and the flight time.

three plate assembly, consisting of a repeller, R, extractor, E and ground plate, G, Eppink and Parker serendipitously observed that a specific ratio of potentials on the repeller and extractor plates (V_E/V_R) would produce the velocity-map imaging conditions. The ratio V_E/V_R required for velocity focusing is dependent on the geometry of the imaging apparatus. The ion optics configuration, the position of the interaction region and the length of the field-free region will all vary the V_E/V_R ratio required.

As in the case of the traditional TOF experiments, the velocity-map-imaged fragment ions arrive at the detector in mass order. Although the three-electrode ion lens assembly does not achieve a mass resolution as high as the Wiley-McLaren setup, the velocity-map imaging lens set up does still have the effect of 'pancaking' the Newton spheres, i.e. for ions of a

given mass, the spread of their velocities is reduced along the TOF axis. Therefore, TOF spectra, with generally acceptable mass resolution, can be acquired from the velocity-map imaging apparatus. As a result, the masses, and, therefore the identities, of the fragment species can be obtained directly.

Since its conception, the VMI technique has become widely used not only in photodissociation studies, but it has also been employed in photoelectron imaging studies [30–32], and imaging photoelectron-photoion coincidence (iPEPICO) experiments with single [33], or two detector [34–36] setups. Femtosecond lasers have been employed with VMI apparati in order to carry out femtosecond time-resolved photoelectron spectroscopy [37, 38] and photodissociation studies [39]. Furthermore, VMI has found applications in the investigation of bimolecular reactions [40]. Due to its widespread use, ion imaging has been the focus of a number of texts; *Imaging in Molecular Dynamics*, edited by Whitaker [4], is quite comprehensive, and an interested reader may find the review articles by Heck and Chandler [41], Vallance [42], Ashfold et al. [26] and Chichinin et al. [14] insightful.

1.4 Imaging techniques for the study of larger molecular systems

Imaging techniques allow the complete velocity (i.e. speed and angular) distribution of the photofragments to be measured. Such information provides a great deal of insight into the forces and energetics driving the fragmentation process, in particular the potential energy surfaces involved. The 2009 review by Chichinin et al. [14] comprehensively summarised the systems that had been investigated in photofragment imaging studies, providing an insight into the extent to which imaging techniques have been employed to investigate photodissociation processes. Historically, photofragment imaging has been used to primarily investigate relatively small molecular systems, often only consisting of two or three atoms. For example, the photodissociation processes of molecules such as O_2 [43] and NO_2 (see [44, 45] and references therein) have been thoroughly investigated. However, there is a growing interest in the photofragmentation dynamics of larger systems. For example the photodissociation of acetaldehyde [46] and a number of acetaldehyde halide derivatives [47, 48] have been investigated using imaging techniques, as have a number of benzene derivatives (see [49–52] and [53] and references therein). Generally, in most of the imaging studies to date, regardless of the size of the parent molecule, one (or both) of the photofragmentation products resulting from a particular photofragmentation pathway has been detected state-selectively. Such studies produce highly detailed dynamical

information relating to a single fragmentation pathway. However, as the size of the parent molecule increases, the number of available photofragmentation pathways is also likely to increase, and so the fragmentation dynamics become significantly more complex. It is our aim to obtain a more comprehensive understanding of the dissociation dynamics of larger molecular systems by velocity-map imaging all of the photofragments. To achieve this, multi-mass imaging techniques are being developed [54–58], which will enable all of the fragmentation products to be imaged in one time-of-flight cycle in a velocity-map imaging mass spectrometry experiment [58, 59]. This thesis serves as one of the foundation stones of a wider imaging mass spectrometry project. The studies which have been included in this thesis, and the motivation behind them, will be discussed briefly in Section 1.5, which lays out the work on a chapter-by-chapter basis.

1.5 Chapter Summary

The overarching theme of this thesis is the study of photofragmentation processes using the velocity-map imaging technique. This introductory chapter has covered the general principles of photofragmentation and introduced the investigative techniques that have been employed. In Chapter 2 the physical aspects and practical use of the velocity-map imaging apparatus will be described. In the same chapter the individual studies that can be performed on the VMI apparatus, and the methods for undertaking such studies, will be discussed.

The studies included in this thesis form some of the initial stepping stones on the road to imaging mass spectrometry by means of velocity-map imaging (VMImMS). In order to achieve imaging mass spectrometry a number of prerequisites must be fulfilled. Primarily, all of the fragments formed in a dissociation event must be detected, i.e. ‘universal detection’ should be achieved. In Chapter 3, the UV photodissociation of alkyl iodides will be presented as an example of the use of VUV photoionization as a method of ‘universal detection’ for our velocity-map photofragment imaging experiments.

The purpose of multi-mass imaging, one of the aims of the VMImMS project, is to facilitate the study of large polyatomic systems. Photofragmentation of such species necessarily proceeds via several competing fragmentation pathways. In Chapter 4, the successful investigation of multiple photofragmentation channels will be demonstrated through a study of the various fragment ions resulting from UV photolysis of ethyl halide cation species.

One of the future goals of the multi-mass imaging project is to investigate the ultra-violet photodissociation (UVPD) of polypeptide compounds. UVPD is often a very rapid process in peptides, occurring on a much faster timescale than intramolecular vibrational redistribution, and leading to non-statistical fragmentation. Such dissociation processes are ideal for investigation with imaging techniques, from which it is possible to gain an understanding of the nature of the participating electronic states, together with the fragmentation mechanisms and dynamics of the dissociation process. As the first step towards such an investigation, N,N-dimethylformamide (DMF) has been chosen as a small-molecule model for the peptide bond. A study of DMF photofragmentation following laser photolysis at 193 nm will be presented in Chapter 5.

The study presented in Chapter 6 has investigated the photofragmentation of the DMF^+ *cation*. Mass spectrometry (MS), which is commonly employed as an analytical technique for the identification of large biomolecules, including polypeptides and proteins, involves fragmentation of the parent *ion*. Although MS reveals the masses of the fragments, it yields little information about the structures of the fragments resulting from a dissociation event. In Chapter 6, the identities of the fragments resulting from photofragmentation of our model peptide bond compound will be presented, and the mechanistic details of the primary fragmentation pathways of DMF^+ will be discussed.

A number of exploratory studies will be presented in Chapters 7 and 8. These have been performed in order to establish potential systems for future investigation using the multi-mass VMImMS technique. The studies demonstrate the use of the current velocity-map imaging apparatus for the investigation of gas-phase photochemical processes of organic compounds. Chapter 7 focuses on the rearrangement reactions of two groups of organic cations, the aliphatic aldehydes, and cyclic alkenes. In Chapter 8 a study of the retro-Diels-Alder reaction of gas-phase neutral cyclic alkenes will be presented.

The final chapter of this thesis, Chapter 9, summarises the work carried out so far, and discusses future work relating to the multi-mass velocity-map imaging mass spectrometry project.

References

[1] Simons, JP. *Photodissociation: a critical survey*. The Journal of Physical Chemistry **88**:7 1287–1293 (1984) (cited p. 2).

[2] Butler, LJ and Neumark, DM. *Photodissociation Dynamics*. Journal of Physical Chemistry **100**: 12801–12816 (1996) (cited p. 2, 12).

[3] Sato, H. *Photodissociation of Simple Molecules in the Gas Phase*. Chemical Reviews **101**:9 2687–2726 (2001) (cited p. 2).

[4] Parker, DH and Eppink, ATJB. *Imaging In Molecular Dynamics: Technology And Applications (A User's Guide)*. Ed. by Whitaker, B. Cambridge, 2003 (cited p. 8, 21).

[5] Norrish, RGW and Porter, G. *The application of flash techniques to the study of fast reactions*. Discussions of the Faraday Society **17**: 40–46 (1954) (cited p. 10).

[6] Das, RS and Agrawal, YK. *Raman spectroscopy: Recent advancements, techniques and applications*. Vibrational Spectroscopy **57**:2 163–176 (2011) (cited p. 10).

[7] Baer, T. *Vacuum UV Photophysics and Photoionization Spectroscopy*. Annual review of physical chemistry **40**:1 637–669 (1989) (cited p. 10).

[8] Popmintchev, T, Chen, MC, Arpin, P, Murnane, MM, and Kapteyn, HC. *The attosecond nonlinear optics of bright coherent X-ray generation*. Nature Photonics **4**:12 822–832 (2010) (cited p. 10).

[9] Clyne, MAA and McDermid, IS. *Laser-Induced Fluorescence: Electronically Excited States of Small Molecules*. Ed. by Lawley, KP. Vol. 50. Advances in Chemical Physics: Dynamics of the Excited State. 1982 (cited p. 10, 12).

[10] Kinsey, JL. *Fourier transform Doppler spectroscopy: A new means of obtaining velocity-angle distributions in scattering experiments*. The Journal of Chemical Physics **66**:6 2560–2565 (1977) (cited p. 10).

[11] Weickhardt, C, Moritz, F, and Grotemeyer, J. *Time-of-flight mass spectrometry: State-of the-art in chemical analysis and molecular science*. Mass Spectrometry Reviews **15**: 139–162 (1996) (cited p. 10, 11).

[12] Ashfold, MNR, Lambert, IR, Mordaunt, DH, Morley, GP, and Western, CM. *Photofragment translational spectroscopy*. The Journal of Physical Chemistry **96**: 2938–2949 (1992) (cited p. 10, 13).

[13] Simpson, WR, Orr-Ewing, AJ, Rakitzis, TP, Kandel, SA, and Zare, RN. *Core extraction for measuring state-to-state differential cross sections of bimolecular reactions*. The Journal of Chemical Physics **103**:17 7299–7312 (1995) (cited p. 10, 13, 15).

[14] Chichinin, AI, Gericke, KH, Kauczok, S, and Maul, C. *Imaging chemical reactions – 3D velocity mapping*. International Reviews in Physical Chemistry **28**:4 607–680 (2009) (cited p. 10, 21).

[15] Wiley, WC and McLaren, IH. *Time-of-Flight Mass Spectrometer with Improved Resolution*. The Review of Scientific Instruments **26**:12 1150–1157 (1955) (cited p. 11, 19).

[16] Busch, GE and Wilson, KR. *Triatomic Photofragment Spectra. I. Energy Partitioning in NO_2 Photodissociation*. The Journal of Chemical Physics **56**: 3626–3638 (1972) (cited p. 13).

[17] Barr, J, Torres, I, Bañares, L, Verdasco, JE, and Aoiz, FJ. *Near UV photodissociation of CD3SCD3: CD3 fragment vector correlations*. Chemical Physics Letters **373**:5-6 550–557 (2003) (cited p. 13).

[18] Nakanishi, R, Saitou, N, Ohno, T, Kowashi, S, Yabushita, S, and Nagata, T. *Photodissociation of gas-phase I_3^-: Comprehensive understanding of nonadiabatic dissociation dynamics*. The Journal of Chemical Physics **126**:20 204311 (2007) (cited p. 13).

[19] Gordon, RJ and Hall, GE. *Applications of Doppler Spectroscopy to Photofragmentation*. Advances in Chemical Physics **96**: (1996) (cited p. 13).

[20] Schmiedl, R, Dugan, H, Meier, W, and Welge, KH. *Laser Doppler spectroscopy of Atomic Hydrogen in the Photodissociation of HI*. Zeitschrift für Physik A Atoms and Nuclei **304**: 137–142 (1982) (cited p. 14).

[21] Zare, RN and Herschbach, DR. *Doppler Line Shape of Atomic Fluorescence Excited by Molecular Photodissociation*. Proceedings of The IEEE **51**:1 173–182 (1963) (cited p. 15).

[22] Solomon, J. *Photodissociation as Studied by Photolysis Mapping*. The Journal of Chemical Physics **47**:3 889–895 (1967) (cited p. 15).

[23] Busch, GE and Wilson, KR. *Triatomic Photofragment Spectra. II. Angular Distributions from NO_2 Photodissociation*. The Journal of Chemical Physics **56**: 3638–3654 (1972) (cited p. 15, 18).

[24] Gebhardt, CR, Rakitzis, TP, Samartzis, PC, Ladopoulos, V, and Kitsopoulos, TN. *Slice imaging: A new approach to ion imaging and velocity mapping*. Review of Scientific Instruments **72**:10 3848–3853 (2001) (cited p. 15).

[25] Townsend, D, Minitti, MP, and Suits, AG. *Direct current slice imaging*. The Review of Scientific Instruments **74**:4 2530–2539 (2003) (cited p. 15).

[26] Ashfold, MNR, Nahler, NH, Orr-Ewing, AJ, Vieuxmaire, OPJ, Toomes, RL, Kitsopoulos, TN, Garcia, IA, Chestakov, DA, Wu, SM, and Parker, DH. *Imaging the dynamics of gas phase reactions*. Physical Chemistry Chemical Physics **8**: 26–53 (2006) (cited p. 15, 21).

[27] Wilson, RJ, Mueller, JA, and Houston, PL. *Speed-Dependent Anisotropy Parameters in the UV Photodissociation of Ozone*. Journal of Physical Chemistry A **101**:41 7593–7599 (1997) (cited p. 18).

[28] Chandler, DW and Houston, PL. *Two-dimensional imaging of state-selected photodissociation products detected by multiphoton ionization*. The Journal of Chemical Physics **87**:2 1445–1447 (1987) (cited p. 19).

[29] Eppink, ATJB and Parker, DH. *Velocity map imaging of ions and electrons using electrostatic lenses: Application in photoelectron and photofragment ion imaging of molecular oxygen*. The Review of Scientific Instruments **68**:9 3477–3484 (1997) (cited p. 19).

[30] Mabbs, R, Grumbling, ER, Pichugin, K, and Sanov, A. *Photoelectron imaging: an experimental window into electronic structure*. Chemical Society Reviews **38**: 2169–2177 (2009) (cited p. 21).

[31] Grumbling, ER, Pichugin, K, Mabbs, R, and Sanov, A. *Photoelectron Imaging as a Quantum Chemistry Visualization Tool*. Journal of Chemical Education **88**:11 1515–1520 (2011) (cited p. 21).

[32] O'Keeffe, P, Bolognesi, P, Coreno, M, Moise, A, Richter, R, Cautero, G, Stebel, L, Sergo, R, Pravica, L, Ovcharenko, Y, and Avaldi, L. *A photoelectron velocity map imaging spectrometer for experiments combining synchrotron and laser radiations*. The Review of Scientific Instruments **82**:3 033109 (2011) (cited p. 21).

[33] Lehmann, CS, Ram, NB, and Janssen, MHM. *Velocity map photoelectron-photoion coincidence imaging on a single detector.* The Review of Scientific Instruments **83**:9 093103 (2012) (cited p. 21).

[34] Vredenborg, A, Roeterdink, WG, and Janssen, MHM. *A photoelectron-photoion coincidence imaging apparatus for femtosecond time-resolved molecular dynamics*. The Review of Scientific Instruments **79**:6 pages (2008) (cited p. 21).

[35] Bodi, A, Hemberger, P, Gerber, T, and Sztáray, B. *A new double imaging velocity focusing coincidence experiment: i2PEPICO*. The Review of Scientific Instruments **83**:8 083105 (2012) (cited p. 21).

[36] Garcia, GA, Cunha de Miranda, BK, Tia, M, Daly, S, and Nahon, L. *DELICIOUS III: A multipurpose double imaging particle coincidence spectrometer for gas phase vacuum ultraviolet photodynamics studies*. The Review of Scientific Instruments **84**:5 053112 (2013) (cited p. 21).

[37] Suzuki, T. *Femtosecond Time-Resolved Photoelectron Imaging*. Annual review of physical chemistry **57**:1 555–592 (2006) (cited p. 21).

[38] Stolow, A, Bragg, AE, and Neumark, DM. *Femtosecond Time-Resolved Photoelectron Spectroscopy*. Chemical Reviews **104**: 1719–1757 (2004) (cited p. 21).

[39] Blanchet, V. "Femtosecond resolved dynamics in small polyatomic molecules by velocity map imaging". *AIP Conference Proceedings*. 28TH INTERNATIONAL SYMPOSIUM ON RAREFIED GAS DYNAMICS. AIP, 2012, 1355–1364 (cited p. 21).

[40] Greaves, SJ, Rose, RA, and Orr-Ewing, AJ. *Velocity map imaging of the dynamics of bimolecular chemical reactions*. Physical Chemistry Chemical Physics **12**: 9129 (2010) (cited p. 21).

[41] Heck, AJR and Chandler, DW. *Imaging Techniques for the Study of Chemical Reaction Dynamics*. Annual review of physical chemistry **46**:1 335–372 (1995) (cited p. 21).

[42] Vallance, C. *'Molecular photography': velocity-map imaging of chemical events*. Philosophical Transactions of the Royal Society A: Mathematical, Physical and Engineering Sciences **362**: 2591–2609 (2004) (cited p. 21).

[43] Parker, DH. *Laser Photochemistry of Molecular Oxygen*. Accounts of Chemical Research **33**:8 563–571 (2000) (cited p. 21).

[44] Brouard, M, Cireasa, R, Clark, AP, Preston, TJ, and Vallance, C. *The photodissociation dynamics of NO_2 at 308 nm and of NO_2 and N_2O_4 at 226 nm*. Journal of Chemical Physics **124**:6 64309 (2006) (cited p. 21).

[45] Wilkinson, I and Whitaker, BJ. *Photodissociation of NO_2 in the $(2)^2B_2$ state: A slice imaging study and reinterpretation of previous results*. The Journal of Chemical Physics **129**:15 154312 (2008) (cited p. 21).

[46] Cruse, HA and Softley, TP. *Velocity-map imaging study of the photodissociation of acetaldehyde.* Journal of Chemical Physics **122**:12 124303 (2005) (cited p. 21).

[47] Deshmukh, S, Myers, JD, Xantheas, SS, and Hess, WP. *Investigation of Acetyl Chloride Photodissociation by Photofragment Imaging*. Journal of Physical Chemistry **98**: 12535–12544 (1994) (cited p. 21).

[48] Lee, KW, Jee, YJ, and Jung, KH. *Photodissociation dynamics of acetyl bromide at 234 nm*. The Journal of Chemical Physics **116**:11 4490–4496 (2002) (cited p. 21).

[49] Hadden, DJ, Williams, CA, Roberts, GM, and Stavros, VG. *Time-resolved velocity map imaging of methyl elimination from photoexcited anisole*. Physical Chemistry Chemical Physics **13**: 4494–4499 (2011) (cited p. 21).

[50] Hadden, DJ, Roberts, GM, Karsili, TNV, Ashfold, MNR, and Stavros, VG. *Competing $1\pi\sigma^*$ mediated dynamics in mequinol: O-H versus O-CH_3 photodissociation pathways.* Physical Chemistry Chemical Physics **14**: 13415–13428 (2012) (cited p. 21).

[51] Murdock, D, Crow, MB, Ritchie, GAD, and Ashfold, MNR. *UV photodissociation dynamics of iodobenzene: effects of fluorination.* The Journal of Chemical Physics **136**:12 124313 (2012) (cited p. 21).

[52] Unny, S, Du, Y, Zhu, L, Truhins, K, Gordon, RJ, Sugita, A, Kawasaki, M, Matsumi, Y, Delmdahl, R, Parker, DH, and Berces, A. *Above-Threshold Effects in the Photodissociation and Photoionization of Iodobenzene*. The Journal of Physical Chemistry A **105**:11 2270–2280 (2001) (cited p. 21).

[53] Han, K and He, G. *Photochemistry of aryl halides: Photodissociation dynamics*. Journal of Photochemistry and Photobiology C: Photochemistry Reviews **8**: 55–66 (2007) (cited p. 21).

[54] Nomerotski, A, Brouard, M, Campbell, E, Clark, A, Crooks, J, Fopma, J, John, JJ, Johnsen, AJ, Slater, C, Turchetta, R, Vallance, C, Wilman, E, and Yuen, WH. *Pixel Imaging Mass Spectrometry with fast and intelligent Pixel detectors*. Journal of Instrumentation **5**:7 C07007 (2010) (cited p. 22).

[55] Nomerotski, A, Adigun-Boaye, S, Brouard, M, Campbell, E, Clark, A, Crooks, J, John, JJ, Johnsen, AJ, Slater, C, Turchetta, R, Vallance, C, Wilman, E, and Yuen, WH. *Pixel imaging mass spectrometry with fast silicon detectors*. Nuclear Instruments and Methods in Physics Research Section A: Accelerators, Spectrometers, Detectors and Associated Equipment **633**: S243–S246 (2011) (cited p. 22).

[56] John, JJ, Brouard, M, Clark, A, Crooks, J, Halford, E, Hill, L, Lee, JWL, Nomerotski, A, Pisarczyk, R, Sedgwick, I, Slater, CS, Turchetta, R, Vallance, C, Wilman, E, Winter, B, and Yuen, WH. *PImMS, a fast event-triggered monolithic pixel detector with storage of multiple timestamps*. Journal of Instrumentation **7**:8 C08001 (2012) (cited p. 22).

[57] Wilman, ES, Gardiner, SH, Nomerotski, A, Turchetta, R, Brouard, M, and Vallance, C. *A new detector for mass spectrometry: Direct detection of low energy ions using a multi-pixel photon counter.* The Review of Scientific Instruments **83**:1 013304 (2012) (cited p. 22).

[58] Clark, AT, Crooks, JP, Sedgwick, I, Turchetta, R, Lee, JWL, John, JJ, Wilman, ES, Hill, L, Halford, E, Slater, CS, Winter, B, Yuen, WH, Gardiner, SH, Lipciuc, ML, Brouard, M, Nomerotski, A, and Vallance, C. *Multimass Velocity-Map Imaging with the Pixel Imaging Mass Spectrometry (PImMS) sensor: An Ultra-Fast Event-Triggered Camera for Particle Imaging*. The Journal of Physical Chemistry A **116**: 10897–10903 (2012) (cited p. 22).

[59] Brouard, M, Campbell, EK, Johnsen, AJ, Vallance, C, Yuen, WH, and Nomerotski, A. *Velocity map imaging in time of flight mass spectrometry*. The Review of Scientific Instruments **79**:12 123115 (2008) (cited p. 22).

2

Velocity-map imaging experiment

Contents

2.1 Vacuum system

The velocity-map imaging (VMI) studies presented in this thesis were performed on a custom built experimental apparatus. The instrument is shown in overview in Figure 2.1. The set-up consists of two differentially pumped chambers, referred to in the following as the source and imaging/detection chambers. Figure 2.2 shows a schematic representation of the internal components of the velocity-map imaging apparatus. The molecular beam source is contained within the source chamber, which is pumped by a turbomolecular pump (Pfeiffer

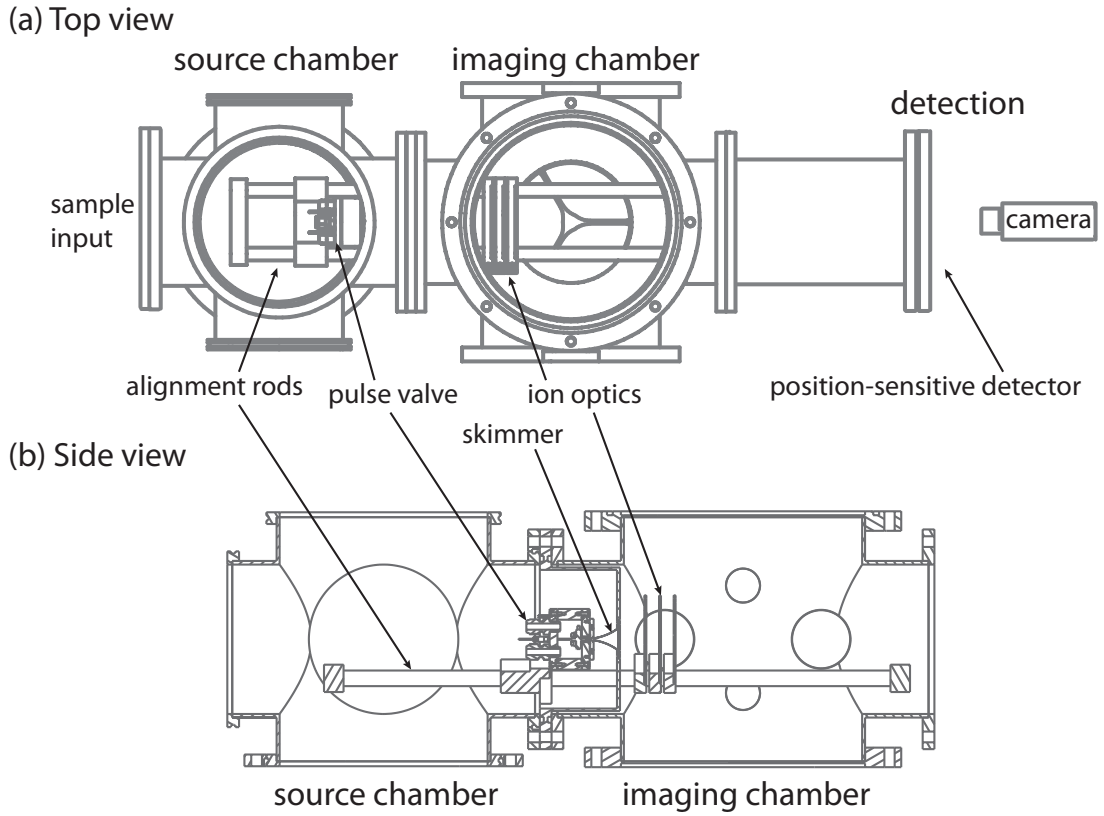

Figure 2.1: (a) Top view and (b) side view engineering diagrams of the velocity-map imaging apparatus, showing the pulse valve and ion optics along with the alignment rods on which these are mounted. [provided by Andrew Green, PTCL mechanical workshop]

Vacuum HiPace 1800) backed by a rotary vane pump (Edwards 18 m^3/hr). Under normal running conditions, with the molecular beam turned on, the pressure within this chamber is $\sim 1 \times 10^{-6}$ mbar. The source chamber connects through to the imaging chamber via a skimmer with a 1 mm diameter orifice. The imaging chamber is pumped by a turbomolecular pump (Pfeiffer Vacuum HiPace 700) backed by a rotary vane pump (Alcatel 21 m^3/hr). Under normal experimental conditions the pressure in this chamber is one order of magnitude lower than in the source chamber, $\sim 3 \times 10^{-7}$ mbar. The velocity-mapping ion optics are contained within the imaging chamber. The imaging chamber is attached directly to the field-free region, at the end of which the position-sensitive imaging detector is mounted. The experimental apparatus, from the molecular beam generation through to the detector, will now be discussed in detail in Sections 2.2 to 2.5.

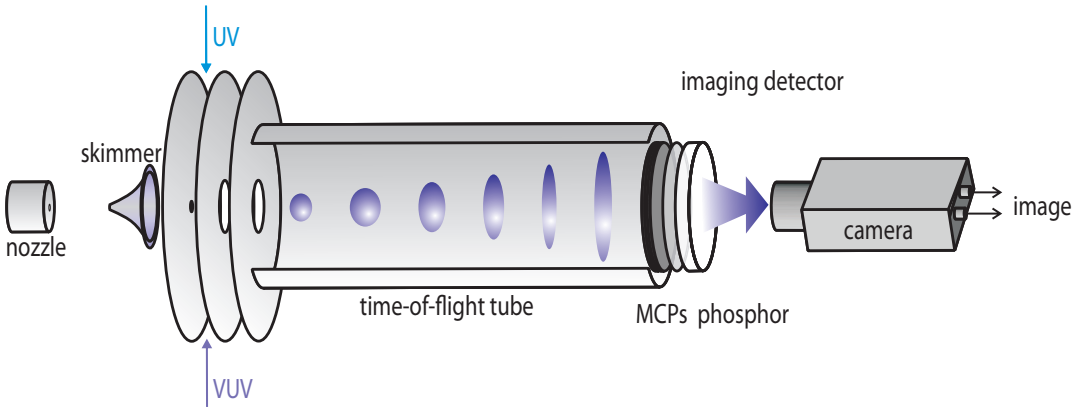

Figure 2.2: A schematic diagram of the internal components of the velocity-map imaging apparatus (not to scale).

2.2 Sample preparation and molecular beam source

As mentioned in Chapter 1, velocity-map imaging studies on a number of polyatomic molecules will be presented in this thesis. Samples of each molecule, which are all liquid at room temperature, were sourced from Sigma-Aldrich. All of the molecules investigated have a vapour pressure of at least 4 mbar at room temperature. Table 2.1 lists the systems investigated along with their chemical formulae, molecular masses and vapour pressures.

The sample is seeded within an inert gas, either helium or argon, and stored within a reservoir. To achieve this, a cold finger containing the sample is submerged in a dry ice/acetone cooling bath ($-78\,^{\circ}$C) in order to freeze the liquid. Any vapours remaining above the frozen sample are pumped out. Then the sample is allowed to thaw. A few of these freeze-thaw cycles are performed to ensure a pure sample vapour. The gas reservoir, which is initially evacuated, is partially filled using the vapour pressure of the sample liquid. Finally the reservoir is filled with an inert gas (He or Ar, $> 99.9\%$, BOC) to a total pressure of 2 bar. Seeding ratios varied depending on the molecule. These are specified in the relevant chapters.

In order to produce a molecular beam, a supersonic expansion is brought about by passing the gas mixture (at a backing pressure of $\sim$2 bar) through a small orifice (500μm) into the high vacuum within the source chamber. This is achieved using a pulsed solenoid valve (Parker Hannifin, series 9) operated at 10 Hz. On the condition that the nozzle orifice is larger than the mean free path of the molecules within the valve reservoir, multiple collisions occur as the gas passes through the orifice. These collisions have the effect

Table 2.1: Chemical formulae, molecular masses, and vapour pressures of the molecules studied in this thesis.

Chemical Name	Chemical Formula	Molecular Mass / u	Vapour Pressure / mbar (20 °C)
methyl iodide	CH_3I	142	533
ethyl iodide	C_2H_5I	156	170
ethyl bromide	C_2H_5Br	109	500
N,N-dimethylfomamide (DMF)	$HCON(CH_3)_2$	73	4.0
deuterated DMF	$DCON(CD_3)_2$	80	4.5
cyclohexene	C_6H_{10}	82	89
1-methylcyclohexene	C_7H_{12}	96	40
4-methylcyclohexene	C_7H_{12}	96	48
limonene	$C_{10}H_{16}$	136	2
butanal	$HC(O)C_3H_7$	72	128
hexanal	$HC(O)C_5H_{11}$	100	15
heptanal	$HC(O)C_6H_{13}$	114	5

of transferring momentum to the axial direction, as well as converting internal energy to translational motion, and so yield a molecular beam with a low beam temperature [1]. The molecules within the beam are successfully rotationally cooled, as well as translationally cooled in the transverse direction. However, it should be noted that this method is much less effective at vibrational cooling [2, 3].

The resultant beam velocity depends on the average mass and heat capacity of the gases in the gas mixture [1]. Therefore, the seeding gas itself, and the chosen seeding ratio, can influence the velocity of the molecular beam.

A skimmer, positioned 35 mm downstream of the nozzle orifice, separates the source and imaging chambers, and selects out the central part of the supersonic expansion (the ‘zone of silence’) to give a collimated molecular beam, which then enters the differentially pumped imaging chamber, which contains the ion optics assembly.

2.3 Ion optics

The ion optics, as shown schematically in Figure 2.3, consist of repeller (R), extractor (E), and ground (G) electrodes, each of which are 90 mm in diameter, 2 mm thick, and are

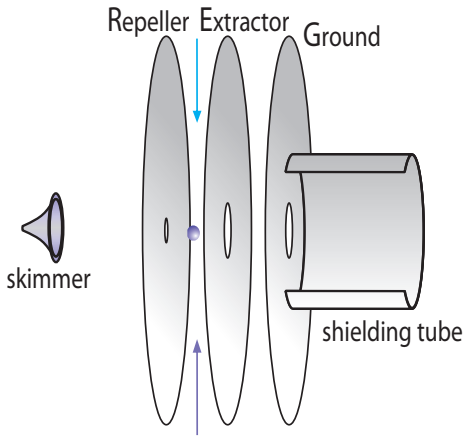

Figure 2.3: The ion optics assembly. Also shown are the skimmer and the paths of the lasers.

spaced apart by 15 mm. The repeller electrode has a central, conically shaped, 1 mm diameter aperture to admit the molecular beam, and the extractor and ground electrodes have 20 mm apertures to allow ion extraction. The ground electrode is fitted with a grounded shielding tube (50 mm long, 50 mm internal diameter, 2 mm thick) at the output to limit electric field penetration into the field-free drift region. To achieve velocity mapping conditions, the ratio of potentials applied to the extractor and repeller electrodes (V_E/V_R) is maintained at $\sim$0.71. The potential applied to the repeller electrode, V_R, was typically either 2 kV or 4 kV, with the lower potential yielding a greater degree of magnification in the images. The interaction region, the point at which the molecular beam is intersected orthogonally by the pulsed laser beams, lies midway between the repeller and extractor electrodes.

2.4 Laser system

The photolysis radiation required for the photodissociation experiments is provided by either a dye laser or an excimer laser. Photoionization of the parent molecules and/or the nascent fragments is achieved by single photon ionization at 118.2 nm.[1] In some cases, as discussed in Section 2.8, ionization is achieved by resonance-enhanced multiphoton ionization (REMPI) for which the dye laser is employed. Figure 2.4 shows a schematic diagram of the laser paths relative to the VMI apparatus, viewed from the top.

[1]Vacuum ultraviolet (VUV) light includes all wavelengths less than 200 nm, which are not transmitted through air. Therefore, technically the 193 nm light produced by the excimer is within the VUV range. However, since the excimer and dye laser wavelengths are used interchangeably for photolysis purposes the author chooses to refer to them under a collective term. For the purposes of this thesis 'UV' may be used to refer to wavelengths in the range 193 nm to $\sim$355 nm. 'VUV' will only be used to refer to the 118.2 nm light.

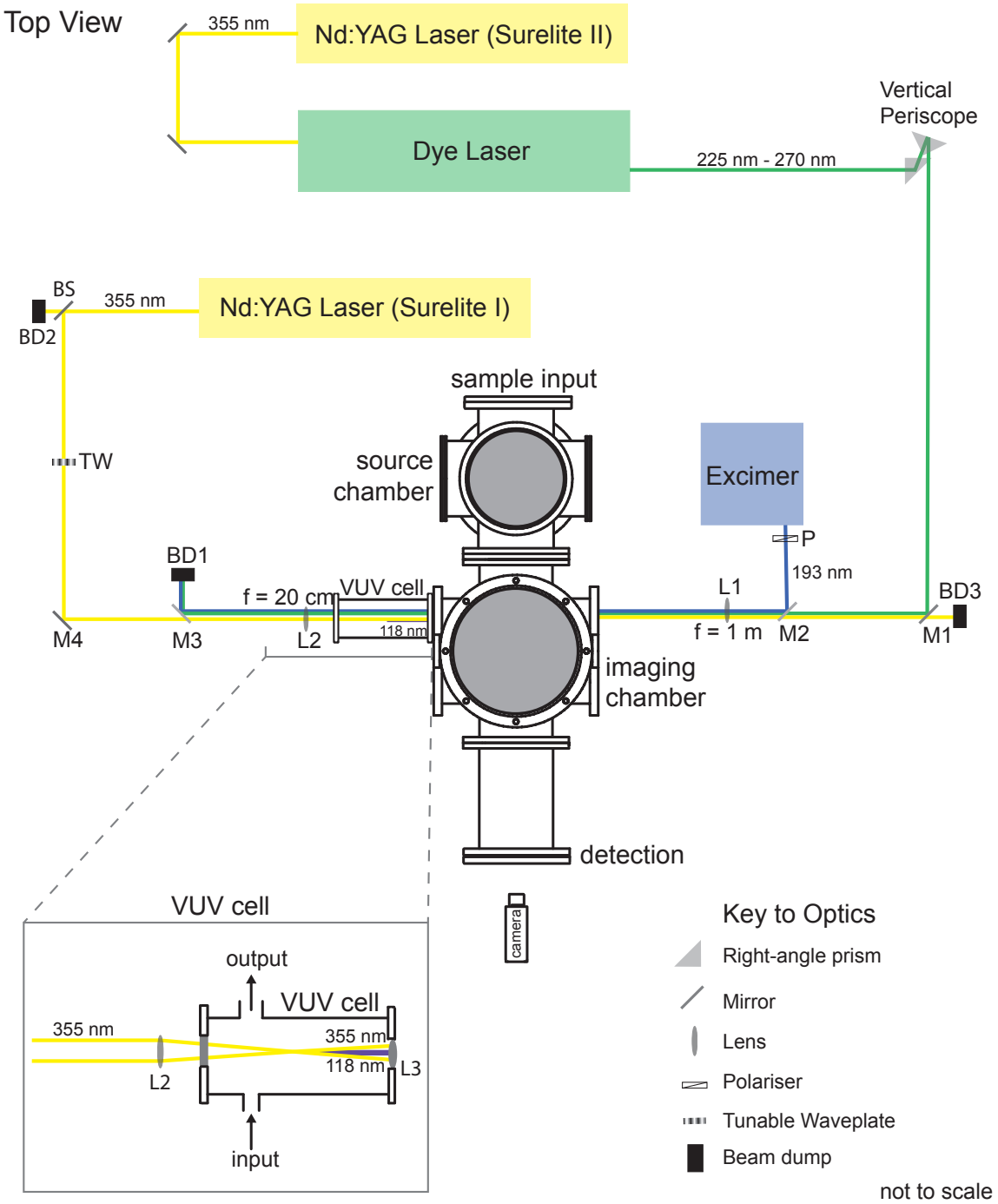

Figure 2.4: A schematic diagram of the laser system relative to the velocity-map imaging apparatus. The inset (bottom left) shows the VUV cell in more detail.

2.4.1 Dye and excimer lasers

A tuneable linearly polarized, frequency-doubled pulsed dye laser (Sirah Cobra Stretch, 7 ns pulse, laser energy ∼0.4 - 2 mJ/pulse in a 1x1 mm^2 spot size in interaction region, $\Delta\tilde{\nu} \simeq 0.3$ cm^{-1}) is pumped by the third harmonic of a Nd:YAG laser (Continuum Surelite II, 200 mJ per 7 ns pulse). Coumarin 450 and Coumarin 503 laser dyes were used to generate the fundamental wavelengths (450 nm - 540 nm) required for the work presented in this thesis. A BBO crystal is employed to frequency double the fundamental radiation generated by the dye laser. In this way the desired wavelength, in the range from around 225 nm to 270 nm, could be achieved. The frequency doubled laser light is then directed through a vertical periscope set-up consisting of two right-angle prisms. A dichroic mirror, M1, (High Reflectivity (HR) at 248 nm, High Transmittance (HT) $\geq$ 300 nm) is used to direct the laser beam toward the experimental apparatus. When the laser beam initially exits the frequency doubling unit the laser polarisation is horizontal, i.e. perpendicular to the plane of the imaging detector. However, when the beam enters the chamber, as a result of passing through the vertical periscope, the laser polarisation is parallel to the plane of the detector.

The 193 nm light is generated by a Neweks Excimer laser (PSX-100). This wavelength is produced from ArF excimer fluorescence. The ArF excimer is generated in an electric discharge from a premix of 0.2% F_2; 3.75% Ar; 96.05% He at a total pressure of 8 bar. On exiting the laser cavity the initially unpolarised 193 nm light is linearly polarised by a Glan-Taylor polariser. The 193 nm laser polarisation is set parallel to the plane of the imaging detector. A dichroic mirror, M2, (HR $>$ 95% at 193 nm, HT $>$ 90% at 355 nm), which is removed when the dye laser is in use, directs the laser beam toward the experimental apparatus. At the interaction region, the 193 nm laser energy per 5 ns pulse was in the range of $\sim$ 0.15 - 0.5 mJ in a 1x1 mm^2 spot.

Before entering the imaging chamber, the dye or excimer laser beam travels through a fused silica lens, L1, with a focal length, f, of either f = 1000 mm or f = 300 mm. The 1000 mm focal-length lens, which is positioned ∼600 mm before the interaction region, has the effect of collimating the beam as it passes through the interaction region, and is used in the instances when single photon conditions are desirable for the photolysis laser. Depending on the laser wavelength, the 300 mm focal length lens tightly focuses the laser at a point approximately 20 mm after the interaction region. These focusing conditions ensure that the beam is coming to a focus as it passes through the interaction region and avoids refocusing on other optics within the laser system. The 300 mm focal length lens

is employed in the case when higher photon densities are required than those that can be attained with the f = 1000 mm lens. On exiting the imaging chamber, the dye or excimer laser beam is reflected into a beam dump, BD1, using a dichroic mirror, M3, (HR $>$ 95% at 193 nm, HT $>$ 90% at 355 nm).

2.4.2 Photoionization laser

The technique of third-harmonic generation is employed in order to produce VUV light of wavelength 118.2 nm. By frequency tripling 354.7 nm radiation in a mixture of inert gases, photons with an energy of $\sim$10.49 eV are generated. This photon energy is above the ionization energy of many species, both parent molecules and fragments. The generated beam is therefore ideal for use as a photoionization laser since single photon ionization can be achieved. Since the process of frequency tripling in gases is fundamental to the generation of the 118 nm radiation, the underlying principles of this phenomenon will be now be laid out. After this, the testing of the setup for production of VUV light and its use as the photoionization laser will be discussed.

2.4.2.1 Frequency tripling in gases: general principles

The way in which matter interacts with light can be described by the polarisation, P, which under low light intensities is directly proportional to the electric field, E. Under these conditions, it is possible to express this relationship by a linear equation,

$$P = \chi^{(1)} E \tag{2.1}$$

where $\chi^{(1)}$ is the linear susceptibility. However, in the case of high photon densities, e.g. within a tight focus of a laser beam, nonlinear effects come into play, and P is expressed as

$$P = \chi^{(1)} E + \chi^{(2)} E^2 + \chi^{(3)} E^3 + ... \tag{2.2}$$

In this case, $\chi^{(2)}$ and $\chi^{(3)}$ are the second and third order nonlinear susceptibilities, respectively, which affect the magnitude of the nonlinear response of the material.

Here, we consider third harmonic generation (THG) (also referred to as 'frequency tripling'), which is a third-order effect.[2] THG involves the absorption of three photons of frequency

[2]Within an isotropic medium, as is the case considered here, for symmetry reasons, which will not be discussed here, all $\chi^{(2)}$ effects are reduced to zero.

ω_1, from a driving beam, followed by the emission of one photon of frequency ω_3, so that a second beam is generated (see Figure 2.5 (a)).

The energy of a photon is the product of its frequency, ω and the reduced Planck constant, $\hbar$. That is

$$E = \hbar\omega \tag{2.3}$$

In the case of THG, three photons, each of energy $(\hbar\omega_1)$, are destroyed and a single photon with an energy of $\hbar(3\omega_1)$ is generated. Since energy is conserved, the frequency of the emitted photon must be three times that of the absorbed light, $\omega_3 = 3\omega_1$.

For the method described here, xenon is employed in order to produced 118.2 nm light from a driving beam of wavelength 354.7 nm. Xenon is ideal for this process as it has a high third order nonlinear susceptibility, $\chi^{(3)}$. Following absorption of three photons from the driving beam, a xenon atom is excited to a virtual state, see Figure 2.5 (b). In this case, the virtual state lies very close in energy to the $5p^5 7s\ ^2P_{3/2}$ electronic excited state of xenon [4]. The closer, in energy, that a virtual state lies to a real state the more favourable the excitation process [5]. Furthermore, it is preferable to generate harmonics via a non-resonant process, as is the case here, rather than via a resonant process. Photons produced via a resonant process will have an energy equivalent to that of a resonance within the non-linear medium, and therefore, they would be readily reabsorbed by the medium. So, although excitation to a resonant state would increase the efficiency of the process, the reabsorption of the emitted photons would work to decrease the overall efficiency of the process.

Another factor that affects the overall efficiency of the tripling process relates to conservation of momentum. The momentum of a photon is given by

$$\mathbf{p} = \hbar\mathbf{k} \tag{2.4}$$

where $\mathbf{k}$ is the wave vector, which points along the direction of propagation of the light. The magnitude of $\mathbf{k}$ is dependent on the frequency of the light, ω, the refractive index, n, of the medium through which the light passes, and the speed of light, c, in a relationship given by

$$\mathbf{k} = n\omega/c \tag{2.5}$$

In order to optimise the efficiency of harmonic generation the wave vector mismatch, $\Delta\mathbf{k}$, between the generated light and driving laser beam must be minimised. In the case of third harmonic generation, the wave vector mismatch is given by $\Delta\mathbf{k} = \mathbf{k}_{\omega_3} - 3\mathbf{k}_{\omega_1}$. When $\Delta\mathbf{k} = 0$ the driving and generated beams are phase matched. Since the magnitude of $\mathbf{k}$ is dependent

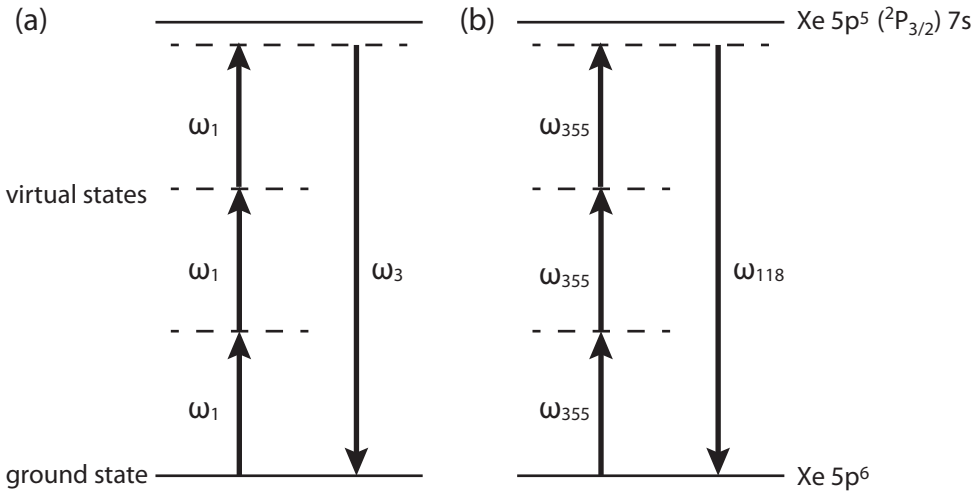

Figure 2.5: Schematic energy level diagrams displaying the absorption and emission of photons for (a) the general case of non-resonant third-harmonic generation and (b) 118 nm generation in xenon.

on the refractive index, $\Delta\mathbf{k}$ can be influenced by varying the refractive index n of the tripling medium. The refractive index is dependent on the frequency of the light that passes through the medium. The dispersion of a medium indicates the way in which n varies with ω. For a positively dispersive medium, n increases with increasing ω. Whereas, for a negatively dispersive medium, n decreases with increasing ω. Therefore, if two media of opposite dispersion are mixed together it is possible to manipulate the parameters that influence phase matching. By varying the mixing ratio of the two media, the overall refractive index can be influenced.

For the work described here, three photons of 355 nm light generate an outgoing photon of 118 nm light. Therefore,

$$\Delta\mathbf{k} = \mathbf{k}_{118} - 3\mathbf{k}_{355} \tag{2.6}$$

where $\mathbf{k}_{118}$ and $\mathbf{k}_{355}$ are the wave vectors for the 118 nm and 355 nm light, respectively. Xenon, which is used to generate the 118 nm light, is negatively dispersive. By mixing Xe with argon, which is positively dispersive, we can obtain an optimum 'phase matching ratio', which ensures that the efficiency of the tripling process is maximised.

The details of the laser setup employed for generation of the VUV light will be laid out in Section 2.4.2.2. A description of the initial experiments, which were undertaken in order to obtain the necessary mixing ratio of xenon and argon, will follow in Section 2.4.2.3.

2.4.2.2 118 nm radiation: for use as the photoionization laser

VUV light, of wavelength 118.2 nm, is produced by tripling the 354.7 nm third harmonic of a Continuum Surelite I Nd:YAG laser in a rare gas mixture of xenon and argon [5–8]. Typically, this process was achieved using pulse energies of 10 - 20 mJ per 7 ns pulse at 355 nm. The Continuum Surelite I Nd:YAG laser gives $\sim$ 70 mJ per pulse at 355 nm. A beamsplitter, labelled BS in Figure 2.4, is employed in order to select the desired 15 - 20% of the beam and to reflect it towards the experimental apparatus. The remainder of the beam passes through the beamsplitter and is blocked by a beam dump, BD2. The 355 nm laser beam then travels through a zero-order tuneable waveplate, TW, which rotates the direction of the polarisation of the beam by 90°. After this step, the 355 nm laser is polarised parallel to the plane of the detector. The laser beam is then steered through a lens, L2, (f = 200 mm) and travels through the entry window of a tripling gas cell, before coming to a tight focus in the center of this cell. By tightly focusing the 355 nm laser beam into the gas cell (see the inset at the bottom left of Figure 2.4) the high photon densities that are required for the non-resonant non-linear THG process are achieved. By using an inert gas mixture of Xe (BOC, $>$ 99.9%) and Ar (BOC, $>$ 99.9%), in a ratio of 1:11 (see Section 2.4.2.3), at a total pressure of 325 mbar, relatively efficient frequency tripling is achieved.

The gas cell, which contained the tripling medium, was mounted directly onto the experimental apparatus (see the inset in Figure 2.4). At the exit of the gas cell, the 355 nm and 118 nm light travel through a lithium fluoride lens, L3. The two laser beams are not separated before passing through the interaction region. The 355 nm beam, which is diverging as it passes through L3, is refocused at a distance of 10 cm after the interaction region. The 118 nm beam comes to a focus 50 mm after the interaction region. In this way, within the interaction region, the 355 nm beam is relatively broad and diffuse compared to the 118 nm beam. Since the two beams travel along the same trajectory it is not straightforward to measure the 118 nm energy separately from that of the 355 nm beam. Kung *et al.* achieved a conversion efficiency of $\sim$ 0.1% for this tripling process using xenon and argon [6, 7]. From this, we estimate an upper limit of $\sim$ 10 - 20 μJ per pulse for the energy of the generated 118 nm pulse. On exiting the experimental apparatus the 118 nm beam travels less than 20 cm through air (although O_2 has a dip in its absorption spectrum around 118 nm, this wavelength is still readily absorbed), and, in addition, would not pass through any optical elements that are not composed of MgF_2 or LiF. The 355 nm beam is dumped at the earliest possible stage, depending on which UV wavelength is being employed at the time, e.g. in the case where the dye laser is employed, the 355 nm laser passes through the dichroic mirror (HR at 248 nm, HT $\geq$ 300 nm) and enters a beam dump, BD3.

2.4.2.3 Generation of VUV light: testing and setup

As discussed in Section 2.4.2.1, the particular focusing conditions of the driving beam affects the phase matching conditions necessary for frequency tripling and, therefore, influences the ratio of xenon to argon required to achieve phase matching. As a result of this, the phase matching ratio is unique for a particular experimental setup. Therefore, before the VUV beam could be used for experimental purposes, it was necessary to establish the optimal phase matching ratio of xenon to argon. In order to determine this, nitric oxide (NO) was used as a test molecule in the molecular beam. NO has an ionization potential of 9.26 eV [9], which is below the 10.49 eV available from one photon of 118.2 nm light. Therefore, NO is a good system with which to test the current VUV setup, since absorption of a single photon of wavelength 118 nm will lead to ionization of the parent molecule, which can be detected with the current experimental apparatus.

In order to undertake the necessary calibration experiments, a pulsed molecular beam consisting of $\sim 5\%$ NO seeded in Ar, with a backing pressure of 2 bar, was generated. Initially, the tripling gas cell was evacuated using a turbomolecular pump (Pfeiffer Vacuum HiPace 10) backed by a diaphragm pump (Pfeiffer Vacuum MVP015-2), in order to ensure that there were no contaminating species (e.g. H_2O) present within the cell. The 355 nm beam was then tightly focused into the center of the gas cell. As the gas cell was initially empty, no 118 nm radiation was generated and therefore, no NO^+ signal was observed. In addition, since no ion signal was observed, it was clear that the 355 nm beam was not intense enough to achieve multiphoton ionization, eliminating a potential complicating factor. The cell was slowly filled with xenon, and some production of 118 nm radiation was achieved. The 118 nm light passed through to the interaction region where single photon absorption resulted in ionization of NO to form NO^+, which was detected by the experimental apparatus. The cell was continually filled with xenon until a maximum signal intensity was observed, at which point argon was slowly added to the gas cell. The phase matching ratio of the two gases was found when the NO^+ signal was at a maximum. The ideal phase matching ratio of xenon to argon was found to be 1:11 for the experimental setup described here. This compares well with the phase matching ratio of 1:10.5 published by Kung *et al.*, who have previously investigated the details of the process of frequency tripling 355 nm to yield 118 nm [7].

2.5 Detection

A 2D position sensitive detector is employed to detect the photoionized parent and product molecules. Following photoionization, the velocity-mapping field accelerates the parent molecule and nascent fragments through the apertures in the extractor and ground electrodes and into the field free flight tube. After a total flight distance of 482 mm from the laser interaction region the ions impinge upon the 2D position sensitive detector. The detector assembly (Photek VID240) consists of 40 mm diameter Chevron multichannel plates (MCPs) coupled to a P47 phosphor screen. The ions arrive at the detector in order of their mass-to-charge ratio, with the lightest ions arriving at earlier times, and heavier masses at later times (see Section 2.6). The ion lens system velocity-maps the ions such that all ions that have the same velocity component in the image plane arrive at the same point on the detector, regardless of their initial positions. The ion lens also has the effect of 'pancaking' the Newton spheres (see Section 1.1.3), minimising the arrival time spread Δt for each mass and hence optimising the resolution of the arrival time of the ions at the detector. By integrating the total signal recorded by the detector as a function of time, laser power or laser wavelength a number of different types of information can be obtained, namely time-of-flight mass spectra, laser power dependence and REMPI spectra. These will be discussed in Sections 2.6 to 2.8. When the signal across the detector is position-resolved, the velocity-map images are obtained. The details of image acquisition and processing will be discussed in Section 2.9.

2.6 Time-of-flight mass spectra

By recording the signal, integrated across the 2D imaging detector, as a function of time, the imaging apparatus can be used to carry out conventional time-of-flight mass spectrometry (TOF-MS) studies. These studies yield the identities and relative intensities of the fragmentation products that are detected. The TOF spectra can be obtained in two ways. In the first instance, a liquid light guide is used to direct light from the phosphor screen to a photomultiplier tube (PMT). The PMT signal is visualised on an oscilloscope (Tektonix TDS 2024B, four channel digital oscilloscope) and the TOF spectra may be read from the oscilloscope to a computer using Tektronix waveform data capture software. The mass resolution of the spectra acquired via this method is dependent on the decay time of the phosphor screen, and is therefore relatively low. With the current phosphor it is not possible to distinguish clearly between fragment peaks separated by 1 amu. When a higher mass

resolution is required, which is generally the case, then an alternative method is employed. This method involves time-gating the MCP, using a pulsed high voltage switch (Photek GM-MCP-2), and recording the total number of ions that arrive at the detector within the gated time period. The process is controlled by a custom built LabVIEW program. A pulse/delay generator (BNC Model 575) applies a gate of 20 ns to the MCP, and the gate is then stepped through the range of flight times of interest. At each step, the total number of ions detected by the camera at the flight time of interest is recorded over a user-specified number of TOF cycles, typically ten.

The recorded flight times of the ions correlate with the mass-to-charge ratios (*m/z*). Each ion of mass m and charge ze is accelerated through a potential V to a final velocity v, where

$$v = \sqrt{2zeV/m} \tag{2.7}$$

Therefore, the time required to traverse a flight distance of length d is,

$$t = d/v = d\sqrt{m/2zeV} \tag{2.8}$$

The mass-to-charge ratio can therefore be determined from

$$m/z = 2eVt^2/d^2 \tag{2.9}$$

This can be simplified to

$$m/z = at^2 \tag{2.10}$$

where a is a constant of proportionality given by

$$a = 2V/d^2 \tag{2.11}$$

From Equation (2.11) it is clear that this constant is dependent on two things. The first is the potential V through which the ions are accelerated, and therefore the potentials applied to the repeller and extractor plates, V_R and V_E, respectively. The second is the distance d that the ions travel before reaching the detector. This distance is dependent on the location of the interaction region, which is influenced by the physical alignment of the ionization laser relative to the detector. Therefore, ideally, the constant should be obtained for each TOF spectrum (or set of TOF spectra) acquired. For the studies discussed here, the parent ion was easily identified from the velocity-map images.[3] Using the measured t and known

[3]Since the ionization of molecules in the molecular beam has an almost negligible effect on their velocities, the velocity-map image reflects the distribution of velocities within the translationally cold molecular beam, i.e. approximately a Maxwell-Boltzmann distribution at a temperature of ~10 K. Therefore the parent ion appears as a small dot in the center of the image.

m/z values for the parent ion, the mass calibration factor for each TOF spectrum was calculated and the TOF spectra were converted to mass spectra. The calibration factors found for each repeller potential applied were found to be reproducible over the course of the studies presented in this thesis. Therefore, d remained constant over this period, which implies that the laser alignment relative to the repeller and extractor plates did not vary significantly.

A background spectrum, recorded with the molecular beam off, was taken in succession of each TOF spectrum, and subtracted from the 'beam on' data. This ensured that the data to be analysed only contained TOF peaks originating from the molecular beam and not from background gas in the vacuum chamber. For the two-colour studies, the TOF spectra from the individual laser contributions, acquired using only the pump or only the probe laser, were subtracted from the two-laser signal, which results when both lasers pass through to interaction region, to obtain the two-colour TOF-MS. The two-colour mass spectra show only those mass peaks that have a two-colour contribution, i.e. production of the ions in the spectrum requires the involvement of both UV and VUV lasers.

2.7 Laser power dependence studies

By measuring the photofragment signal intensities as a function of laser energy it is possible to determine the number of photons involved in the production of each of the observed fragmentation products. For a one-photon process the ion signal I is directly proportional to the laser pulse energy E. For a two-photon process the signal is proportional to the square of the laser pulse energy. In general for an n-photon process,

$$I = bE^n \tag{2.12}$$

Where b is a constant of proportionality. Taking logs gives,

$$\log(I) = n\log(E) + \log b \tag{2.13}$$

Log-log plots of signal intensity I versus laser energy E will therefore have slopes n which provide information on the number of photons involved in the fragmentation and ionization processes leading to formation of each ion. In order to obtain the signal intensities of the individual fragmentation products as a function of laser energy, TOF-MS are acquired (as detailed in Section 2.6) at a number of different laser energies. To quantify the total signal intensity at each mass, the TOF peaks are fitted using Gaussians. Linear fits to the plots of

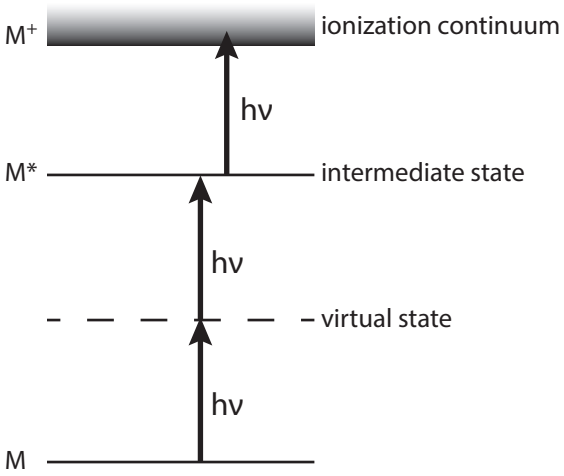

Figure 2.6: A schematic diagram of a (2+1) REMPI process.

log$I$ vs log$E$ are performed, these yield the number of photons n involved in formation of the observed ions. The laser-power-dependence studies that have been undertaken for the work included in this thesis have investigated the effect of the 355 nm and 118 nm laser energies on photofragment production. There are a number of ways in which the 355 nm laser energy can be varied. These include irising of the laser beam at a distance from the experimental apparatus, passing the beam through attenuation optics, and variation of the delay between the flashlamp and Q-switch trigger within the Nd:YAG laser. The tripling efficiency for production of 118 nm laser light can be controlled through variation of the xenon:argon mixing ratio. The details for individual studies will be discussed within the relevant chapters.

2.8 Resonance-enhanced multiphoton ionization

In addition to VUV photoionization, neutral photofragments were also detected using resonance-enhanced multiphoton ionization (REMPI). In contrast to VUV photoionization, which allows detection of all nascent photofragments with an ionization energy lower than the VUV photon energy, REMPI enables the state-specific detection of a single fragmentation product. The REMPI process involves single or multiple photon absorption to an intermediate electronic state, followed by additional photon absorption to an energy which surpasses the ionization potential. Figure 2.6 illustrates a (2+1) REMPI scheme, which involves an initial two-photon absorption to the electronically excited state M*, from which absorption of an additional photon leads to ionization. Since the REMPI process involves multiphoton absorption, a greater photon density is required within the interaction region than in the

case of a single photon process. To achieve this, the laser beam is tightly focused at a point approximately 20 mm after the interaction region. For a particular atom or molecule, there may be a number of intermediate states that will facilitate resonant detection. To determine the energies of these states, a tuneable, linearly polarized, frequency-doubled pulsed dye laser (see Section 2.4.1) can be scanned over a wavelength region. This is carried out via a custom built LabVIEW interface which steps the laser through the wavelength range of interest and acquires the time-of-flight signal from the oscilloscope at each step. In order to obtain the REMPI spectrum for a neutral species of interest, the total signal intensity of an individual mass peak, which results from REMPI detection of the neutral, is integrated as a function of wavelength. The peaks in the REMPI spectra indicate the wavelengths at which resonance-enhanced multiphoton ionization can be achieved.

2.9 Image acquisition, processing and analysis

In order to acquire an image of a specific ion of interest, the detector is gated at the arrival time of that ion by pulsing the rear MCP from +1000 V to +1500 V. The forward-backward spread of arrival times for each photofragment ion cloud was about 40 - 50 ns. The light from the phosphor screen is imaged by an intensified charge-coupled device (CCD) camera (Photonic Science Mini IDI), controlled via a LabVIEW interface. The data acquisition software captures a 691 x 691 pixel subarray of the CCD array on each TOF cycle. Images are acquired over thousands of laser shots, with more or less shots included depending on the signal-to-noise ratio. Background images, recorded with the molecular beam turned off, are subtracted from the 'beam on' images in order to remove any unwanted contributions from background gas in the imaging chamber. Background-subtracted images for the relevant two-laser and individual laser contributions are obtained. For the cases in which the two-colour signal is of interest, the individual one-colour images are subtracted from the overall (two-laser) image. The velocity-map images are subsequently processed using LabVIEW software employing the Polar Onion Peeling (POP) algorithm [10]. From the images of each photofragment the POP algorithm returns the radial distribution of the central slice through the 3D velocity distribution, integrated over angle, as well as the anisotropy parameter, β_2, which characterises the angular distribution of the photofragments (see Section 1.2.4. For the studies included in this thesis the β_2 values that are presented are a weighted average obtained over a translational energy range of interest.

Calibration is necessary in order to convert from pixel coordinates to photofragment velocities and therefore translational energies. In principle, we can obtain the transverse velocity

v of the fragment directly from the radial coordinate r of the image, using our knowledge of the time-of-flight t of the fragment.

$$v \simeq r/t \tag{2.14}$$

However, as discussed in Section 1.3, the velocity-mapping optics introduce a magnification factor, M, which must be taken into account.

$$v = Mr/t \tag{2.15}$$

Suitable calibration factors, which account for this magnification have been determined using the O^+ image from UV photodissociation of the O_2 molecule.

When the momentum-matched co-fragment is known, the measured translational energy, E_t, distribution of a particular photofragment is converted into the total translational energy distribution, E_T, using linear momentum conservation, as discussed in Section 1.2.3.

2.10 VMI calibration

2.10.1 Obtaining a calibration factor

Calibration of the radial or velocity coordinate of the velocity-map images is achieved by imaging the products of a molecular fragmentation process with a known translational energy release. As discussed in Section 1.2.3, following fragmentation of a bond within a molecule A-B, momentum is conserved, and therefore $m_A v_A = -m_B v_B$, where m and v are the mass and velocity of the fragments, respectively. From this an expression for the total translational energy release E_T can be derived.

$$E_T = E_t(A)\left(\frac{m_{AB}}{m_B}\right) = \frac{1}{2} m_A v_A^2 \left(\frac{m_{AB}}{m_B}\right) \tag{2.16}$$

where $E_t(A)$ is the translational energy of fragment A.

The radial coordinate r (measured in pixels) is proportional to the velocity of the fragment v_A (see Equation (2.15)). It follows therefore, since $E_T \propto v_A^2$ (Equation (2.16)), that

$$E_T = Cr^2 \tag{2.17}$$

where C is a mass-dependent conversion factor, which has a dependence on the time-of-flight of fragment A, t_A, and on the VMI magnification factor, M, in a relationship given by

$$C = \frac{1}{2} m_A \frac{M^2}{t_A^2}\left(\frac{m_{AB}}{m_B}\right) \tag{2.18}$$

As was discussed in Section 2.6 (and shown in Equation (2.8)), the time-of-flight t_{A} is dependent on the mass of the fragment m_A, the acceleration potential V, and the length of the flight tube d. Therefore, as C has a dependence on t it is also affected by these factors.

The calibration factor, as discussed here, is one in which the mass dependency is removed. An individual factor is obtained for each pair of repeller and extractor electrode potentials, as each of these results in a different effective potential V through which the ions are accelerated. No physical changes have been made to the length of the flight tube over the course of the experimental work carried out for this thesis, and in addition to this the results from the TOF-MS calibration show that the alignment of the lasers was unchanged. Therefore d is a constant that has been incorporated into the calibration factors that have been determined here.

Following a straightforward line of thought, it is possible to see how the mass dependency can be accounted for and a calibration factor obtained. By substituting in the expression for t_{A} from Equation (2.8) into Equation (2.18) we obtain

$$C = \frac{1}{2} m_{\mathrm{A}} \frac{M^2}{d^2 m_{\mathrm{A}}/2zeV} \left(\frac{m_{\mathrm{AB}}}{m_{\mathrm{B}}} \right) \tag{2.19}$$

Which simplifies to

$$\left(\frac{m_{\mathrm{B}}}{m_{\mathrm{AB}}} \right) C = \frac{M^2 zeV}{d^2} = C_u \tag{2.20}$$

where C_u is the calibration factor. In terms of C_u, E_{T} may be expressed as

$$E_{\mathrm{T}} = C_u \left(\frac{m_{AB}}{m_{\mathrm{B}}} \right) r^2 \tag{2.21}$$

Therefore, from Equation (2.16), which relates E_{T} to $E_{\mathrm{t}}(\mathrm{A})$, we obtain

$$E_{\mathrm{T}} = E_{\mathrm{t}}(\mathrm{A}) \left(\frac{m_{\mathrm{AB}}}{m_{\mathrm{B}}} \right) = C_u \left(\frac{m_{\mathrm{AB}}}{m_{\mathrm{B}}} \right) r^2 \tag{2.22}$$

And so it is clear that

$$E_{\mathrm{t}}(\mathrm{A}) = C_u r^2 \tag{2.23}$$

This result can be applied to any mass (A or B etc), and therefore Equation (2.23) is a general expression for converting the velocity axis in pixels to translational energy release.[4] It is clear from Equation (2.20) that in addition to incorporating the effect of the potential, V, and flight tube length, d, the calibration factor obtained accounts for the magnification

[4]The conversion from velocity in pixels to an energy scale involves a quadratic transformation. A Jacobian correction factor is used to account for the resultant mapping of the intensities of the distribution.

M which is a result of the velocity-map imaging conditions. As shown in Equation (2.16), the E_t of the detected fragment can be converted to E_T and photofragment velocity using mass-dependent conversion factors.

2.10.2 UV photodissociation of a diatomic molecule

As discussed in Section 1.1.2, following a dissociation event the energy available to the fragments, E_{av}, is released into translation, E_T, and internal excitation, E_{int}, of the fragments. In the case of photofragmentation of a diatomic molecule, the nascent atoms have no rotational or vibrational degrees of freedom. Therefore, E_{av} is distributed between product translational energy and any electronic excitation, $E_{electronic}$, of the atoms.

$$E_{av} = E_T + E_{electronic} \tag{2.24}$$

If the electronic energy is known then the product translational energy can be predicted very accurately. Therefore, a diatomic molecule is the ideal species with which to perform the photofragmentation experiments necessary to calibrate a velocity-map imaging apparatus.

In this case, molecular oxygen, O_2, is the diatomic molecule of choice. Absorption of a single ~225 nm UV photon excites O_2 from its electronic ground state $X^3\Sigma_g^-$ into the Herzberg continuum [11]. This continuum consists of three states: A $^3\Sigma_u^+$, c $^1\Sigma_u^-$, and A$'$ $^3\Delta_u$. At the dissociation limit these states correlate adiabatically with two ground-state oxygen atoms, with one atom having $j = 2$ and the other having $j = 0, 1$ or 2.

$$O_2 + h\nu \longrightarrow O(^3P_2) + O(^3P_{j=0,1,2}) \qquad (E_T = 0.38 \text{ eV}) \tag{2.25}$$

Absorption of two photons excites the O_2 molecule above the Schumann-Runge continuum to low lying Rydberg-valence complexes [12–14]. At this excitation energy, in addition to various bound states, there are a number of dissociative states present within the Frank-Condon region. The $B^3\Sigma_u^-$ and $II^3\Pi_g^-$ states are both dissociative and lead to formation of $O(^3P_2)$ with a $O(^1D_2)$ co-fragment, whereas the $I^1\Pi_g^-$ and $I^3\Pi_g^-$ states dissociate to form two ground-state oxygen atoms.[5]

$$O_2 + 2h\nu \longrightarrow O(^3P_2) + O(^1D_2) \qquad (E_T = 3.91 \text{ eV}) \tag{2.26}$$

[5]The energy of two photons of ~225 nm radiation is in excess of 11 eV. This energy is well above the dissociation thresholds to produce both $O(^3P) + O(^1D)$ and $O(^1D) + O(^1D)$ photofragment pairs. Since, for the calibration work discussed here, the $O(^3P_2)$ species is detected using (2+1) REMPI, only the dissociative states leading to production of the former of these photofragmentation products are detailed here.

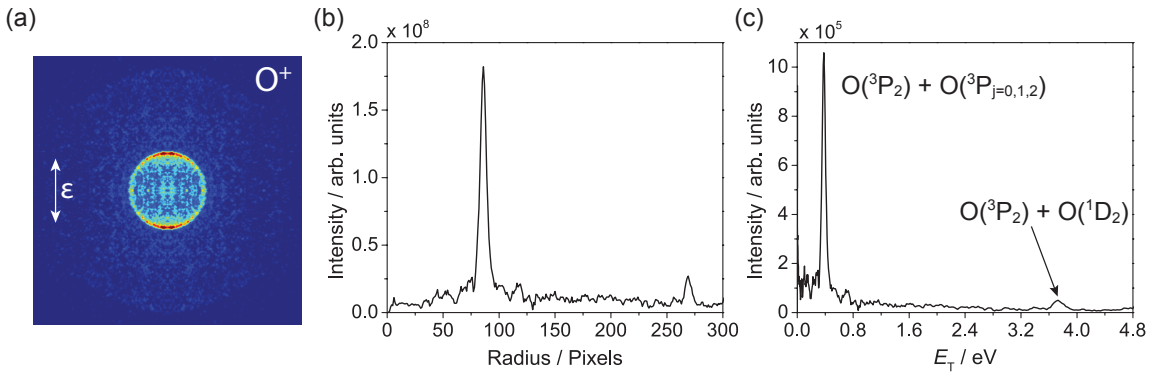

Figure 2.7: (a) A velocity-map image of the $O(^3P_2)$ atoms detected using (2+1) REMPI, the laser polarisation direction, indicated, was parallel to the plane of the detector. (b) the radial velocity distribution as a function of pixels from the image in (a), and (c) the total translational energy distribution which is obtained from the velocity distribution in (b) using a calibtration factor.

or

$$O_2 + 2h\nu \longrightarrow O(^3P_2) + O(^3P_j) \qquad (E_T = 5.87 \text{ eV}) \tag{2.27}$$

For the channels producing only ground state oxygen atoms, $O(^3P_2)$, (Equations (2.25) and (2.27)) following the dissociation event all of the energy available to the fragments E_{av} is released into translation E_T. In the case of $O(^3P) + O(^1D)$ production, part of E_{av} is consumed as electronic energy of the $O(^1D)$ fragment. The energy available for translation following ~225 nm photodissociation of O_2 is shown in parenthesis for each of the individual channels in Equations (2.25) to (2.27).

As has been observed in previous studies on molecular oxygen dissociation at ~225 nm [11], (2+1) REMPI detection (see Section 2.8) of $O(^3P_2)$ generally yields a velocity-map image with three distinct rings. These result from the well-defined product translational energies in each of the three dissociation channels. Since E_T for each of these features is well known, the measured radial distribution of the image can be used to obtain the pixel-to-velocity calibration factor.

Calibration factors have been obtained for the experimental apparatus discussed here at a number of different repeller potentials V_R. An image of the O^+ ions resulting from UV photodissociation of O_2 followed by (2+1) REMPI of the nascent oxygen atoms, acquired with V_R = 4 kV, is shown in Figure 2.7 (a). The velocity distribution extracted from this image is plotted in Figure 2.7 (b) as a function of pixel number. The total translational energy (E_T) distribution, which is obtained following conversion of the velocity axis to energy, is shown in Figure 2.7 (c). With the repeller potential that was employed in this

case, we have 'zoomed in' to the lower translational energy region. Two components are observed in the E_T distribution. The first, at 0.38 eV, corresponds to $O(^3P_2)$ formed with a ground state oxygen co-fragment having $j = 0, 1 \text{ or } 2$. The peak at higher E_T results from the $O(^3P_2)$ ground state atoms which are produced with an $O(^1D_2)$ co-fragment following two-photon absorption at 225 nm. The translational energy of the fragments produced by the third photodissociation channel, which has been discussed above, and is represented by Equation (2.27), falls outside of the translational energy region that has been recorded in this case.

It should be noted that, as in the case of Figure 2.7 (a), for all of the ion images that will be presented in this thesis the raw data will be displayed, i.e. the velocity-map image which is the 2D projection of the 3D Newton sphere of ions. The images have been symmetrized for display purposes only, and are shown on an arbitrary colour scale from red (high intensity) to blue (low intensity). The intensity in the E_T distribution shown in fig. 2.7 (c) is displayed in arbitrary units. In the chapters that follow, the E_T distributions will either be displayed normalized on the maximum, or with the area under the distribution normalized to unity, as is most appropriate.

References

[1] Vallance, C. *Generation, characterisation, and applications of atomic and molecular alignment and orientation*. Physical Chemistry Chemical Physics **13**: 14427–14441 (2011) (cited p. 32).

[2] Casavecchia, P. *Chemical reaction dynamics with molecular beams*. Reports on Progress in Physics **63**: 355–414 (2000) (cited p. 32).

[3] Ashfold, MNR, Nahler, NH, Orr-Ewing, AJ, Vieuxmaire, OPJ, Toomes, RL, Kitsopoulos, TN, Garcia, IA, Chestakov, DA, Wu, SM, and Parker, DH. *Imaging the dynamics of gas phase reactions*. Physical Chemistry Chemical Physics **8**: 26–53 (2006) (cited p. 32).

[4] Humphreys, CJ and Paul Jr, E. *Interferometric Wavelength Determinations in the First Spectrum of ^{136}Xe*. Journal of the Optical Society of America **60**:10 1302–1310 (1970) (cited p. 37).

[5] Bjorklund, G. *Effects of focusing on Third-Order Nonlinear Processes in Isotropic Media*. IEEE Journal of Quantum Electronics **11**:6 287–296 (1975) (cited p. 37, 39).

[6] Kung, AH, Young, JF, and Harris, SE. *Generation of 1182 Å radiation in phase-matched mixture of inert gases*. Applied Physics Letters **22**:6 301–302 (1973) (cited p. 39).

[7] Kung, AH, F, YJ, and Harris, SE. *Erratum: Generation of 1182 Å radiation in phase-matched mixtures of inert gases*. Applied Physics Letters **28**:5 294 (1976) (cited p. 39, 40).

[8] Mahon, R, McIlrath, TJ, Myerscough, VP, and Koopman, DW. *Third-Harmonic Generation in Argon, Kryption and Xenon: Bandwidth Limitations in the Vicinity of Lyman-α*. IEEE Journal of Quantum Electronics **15**:6 444–451 (1979) (cited p. 39).

[9] Lias, SG. *"Ionization Energy Evaluation" in NIST Chemistry WebBook, NIST Standard Reference Database Number 69, (retrieved June 19, 2013)*. Ed. by Linstrom, PJ and Mallard, WG. National Institute of Standards and Technology, Gaithersburg MD, 20899 (cited p. 40).

[10] Roberts, GM, Nixon, JL, Lecointre, J, Wrede, E, and Verlet, JRR. *Toward real-time charged-particle image reconstruction using polar onion-peeling.* The Review of Scientific Instruments **80**: 053104 (2009) (cited p. 45).

[11] Buijsse, B, Zande, WJ van der, Eppink, ATJB, Parker, DH, Lewis, BR, and Gibson, ST. *Angular distributions for photodissociation of O_2 in the Herzberg continuum*. The Journal of Chemical Physics **108**:17 7229–7243 (1998) (cited p. 48, 49).

[12] Wu, SM, Chestakov, D, Groenenboom, GC, Zande, WJ van der, Parker, DH, Wu, G, Yang, X, and Vallance, C. *Angular momentum polarisation in the O(^{1}D) products*

of O_2 photolysis via the $B\,^3\Sigma_u^-$ state. Molecular Physics **108**:7-9 1145–1157 (2010) (cited p. 48).

[13] Parker, DH. *Laser Photochemistry of Molecular Oxygen*. Accounts of Chemical Research **33**:8 563–571 (2000) (cited p. 48).

[14] Morrill, JS, Ginter, ML, Lewis, BR, and Gibson, ST. *The ($X\,^2\Pi_g$) $ns\sigma_g\,^{1,3}\Pi_g$ Rydberg states of O_2: Spectra, structures, and interactions*. The Journal of Chemical Physics **111**:1 173–185 (1999) (cited p. 48).

3

UV Photodissociation of Alkyl Iodides

Contents

3.1 Introduction

The work described in this chapter demonstrates the use of universal ionization in combination with the velocity-map imaging technique. The photodissociation of methyl iodide and ethyl iodide has been investigated. Chandler and Houston originally employed the ion imaging technique to investigate the dissociation of methyl iodide (CH_3I) at 266 nm [1, 2]. The state-selectively ionized CH_3 photofragments were projected onto a two-dimensional detector. The beauty of ion imaging is that the speed and angular distributions of the photofragments could be determined directly from the spatial distribution recorded.

Since then, methyl iodide has become the benchmark molecule for ion imaging studies of photodissociation processes.

However, well before the ground-breaking ion imaging studies of Chandler and Houston, and the prominence of CH_3I studies among the ion imaging community, this molecule was already of interest to the wider scientific community. In 1935, Mulliken presented his findings on the absorption spectra of CH_3I [3]. He suggested that the A-band spectrum consisted of two or three components which could correlate to two pairs of fragmentation products. Iodine could be formed in either its ground ($^2P_{3/2}$) or spin-orbit excited state ($^2P_{1/2}$), with the co-fragment, CH_3, in its electronic ground state. Later, Porret and Goodeve studied the UV absorption of CH_3I, and discussed their results in terms of two dissociation channels, $I(^2P_{3/2}) + CH_3$ (commonly denoted as the I channel), and $I(^2P_{1/2}) + CH_3$ (commonly denoted as the I^* channel), resulting from fragmentation of the C-I bond [4], as had been suggested by Mulliken. Hunter and Kristjansson used photoacoustic spectroscopy to obtain the I^* quantum yield at a number of wavelengths across the A-band, providing information on the competition between the I and I^* dissociation channels as a function of energy [5]. Their results indicated that the variation of the I^* quantum yield as a function of wavelength was a unimodal function, with the quantum yield peaking at around $\Phi(I^*) = 0.75$ in the wavelength region around 260 to 270 nm. At this time it was speculated that an initial excitation followed by curve-crossing to a different state could influence the I^* quantum yield. Photofragment translational spectroscopy (PTS) studies carried out by Sparks *et al.* and Barry *et al.* were able to resolve the translational energy distributions for the I and I^* dissociation channels [6, 7]. In addition, the vibrational population distribution in the υ_2 umbrella bending mode of the methyl radical was also determined [6, 7].

It was not until the availability of ion imaging techniques, in particular velocity-map imaging, that the anisotropy parameters, along with the I^* quantum yields, were determined as a function of photolysis wavelength. Following their improvements on the ion imaging technique (see Section 1.3) [8], Eppink and Parker undertook a comprehensive velocity-map imaging (VMI) study of the photodissociation of CH_3I across the A-band [9, 10]. In agreement with the photoacoustic studies of Hunter and Kristjansson [5] and the PTS studies of Y.T. Lee and co-workers [6] and Barry and Gorry [7], the iodine photofragment was observed primarily in the spin-orbit excited state within the photolysis wavelength range 240 to 300 nm. At longer wavelengths, iodine was observed mainly in the ground state. The angular distributions for the I^* dissociation channel showed mainly parallel character throughout the A-band, quantified by a large positive value of the anisotropy parameter,

β. This results from direct dissociation following an initial excitation via a parallel transition. The data for the I channel also exhibited parallel character at shorter photolysis wavelengths, which is consistent with an initial excitation via a parallel transition, followed by curve-crossing before full dissociation. At longer wavelengths the anisotropy parameter for the I channel was significantly reduced. The details of these dissociation dynamics and the curve-crossing behaviour of the alkyl halides will be discussed in detail in Section 3.2.

The work summarised above by no means provides a comprehensive account of the photodissociation studies of CH_3I. Following decades of detailed research there exists a myriad of literature discussing the photofragmentation of this molecule. The studies discussed here merely illustrate some of the earlier work performed on the A-band dissociation. As spectroscopic techniques have continued to develop, CH_3I has continued to be widely studied. Recently, CH_3I photodissociation dynamics have been investigated using cutting-edge techniques such as time-resolved imaging, and slice imaging [11–13].

At this point it should be noted that CH_3I is only one of the many alkyl iodides which have been studied spectroscopically. The spectroscopic techniques mentioned above have been applied to many other molecules in this series. For example, the UV photodissociation of ethyl iodide (C_2H_5I) has been investigated extensively, with a number of further studies involving a range of alkyl iodides [14–23]. C_2H_5I dissociation also leads to production of iodine, in either the ground or spin-orbit excited state, partnered by an alkyl co-fragment, C_2H_5, in its ground electronic state. Laser induced fluorescence (LIF), PTS and imaging studies have been undertaken to investigate the dissociative states involved in the two dissociation channels [15–18]. PTS and imaging studies have determined the angular and speed distributions of the C_2H_5I fragmentation products [20, 22, 23]. By far the most comprehensive study on C_2H_5I photodissociation was undertaken by Tang *et al.* [20], who investigated the dissociation dynamics across the A-band, in the wavelength range from 245 to 283 nm, using the VMI technique. At photolysis wavelengths within the central region of the A-band, the I^* dissociation channel dominates. The variation in the anisotropy parameter across the A-band for the I channel indicates curve-crossing (see Section 3.2).

The numerous studies into the photodissociation of C_2H_5I and CH_3I, grant us a wealth of information that forms the basis for interpretation of the current work.

3.2 Background: CH_3I and C_2H_5I A-band dissociation

3.2.1 A-band photodissociation of methyl iodide

The A-band of methyl iodide results from a $\sigma^* \leftarrow$ n transition from the lone pair on iodine to the lowest anti-bonding molecular orbital. The band is comprised of five electronically excited states, which arise from spin-orbit interactions induced by the unpaired electron remaining on the iodine atom. Figure 3.1 (a) (adapted from reference [17]) depicts the electronic states in relation to those of the C_{3v} point group in the absence of spin-orbit interactions. From this it can be seen that four of the states within the A-band originate from the splitting of the ^3E state that results from spin-orbit interactions.

Figure 3.1 (b) (adapted from reference [9]) shows the absorption spectrum of CH_3I in the region of the A-band. There are three significant contributions to the total absorption. As denoted by Mulliken [24], in descending energetic order, these are $^1Q_1$, $^3Q_0$ and $^3Q_1$. The strongest absorption is that of $^3Q_0$, with $^1Q_1$ and $^3Q_1$ (shown here 50 times magnified) playing minor roles. The equivalent excitations are illustrated in Figure 3.1 (a). The $^1E \leftarrow A_1$ ($^1Q_1$) transition is fully allowed. As a result of spin-orbit interactions, the $\Delta S = 0$ selection rule is relaxed, and therefore excitations involving changes in spin multiplicity are observed, as seen for the $^3Q_0$ and $^3Q_1$ transitions. The two low lying E symmetry states, in the strong-field limit, are thought to be essentially degenerate. The $A_2 \leftarrow A_1$ transition is symmetry forbidden and therefore does not contribute to the absorption spectrum.

The excited states are dissociative along the C-I bond axis, leading to formation of methyl (CH_3) in its electronic ground state, and iodine in either its ground ($^2P_{3/2}$) or spin-orbit excited ($^2P_{1/2}$) state.

$$CH_3I + h\nu \longrightarrow CH_3I^* \longrightarrow CH_3(v) + I(^2P_{3/2}) \tag{3.1}$$

$$CH_3I + h\nu \longrightarrow CH_3I^* \longrightarrow CH_3(v) + I(^2P_{1/2}) \tag{3.2}$$

As shown in the correlation diagram in Figure 3.1 (a), the $^1Q_1$ and $^3Q_1$ states, accessed via perpendicular transitions from ground state CH_3I, dissociate to form iodine in its spin-orbit ground state and methyl in its ground electronic state (see Equation (3.1)). Dissociation of the $^3Q_0$ state, accessed via a parallel transition, leads to production of spin-orbit excited iodine, with a methyl co-fragment in its ground electronic state (see Equation (3.2)). In the discussion that follows, and throughout this chapter, the name 'iodine' will be used when discussing the iodine atom in either the ground or spin-orbit excited state. I and I^* will be used to refer to ground and spin orbit excited state iodine atoms, respectively.

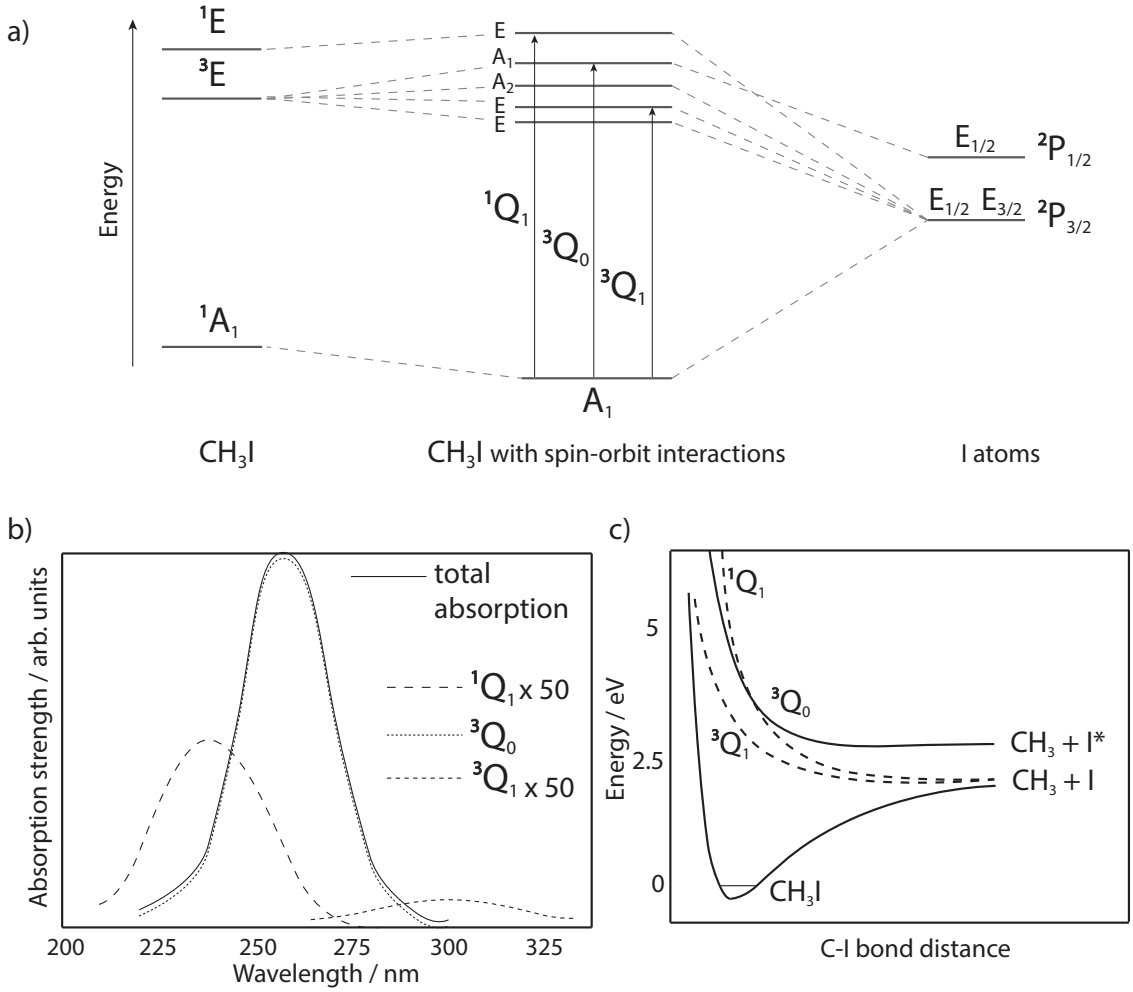

Figure 3.1: (a) correlation diagram, (b) the absorption cross-section, and (c) schematic potential energy curves for the states involved in the A-band dissociation of CH_3I. These figures have been adapted from references that are identified in the text.

Figure 3.1 (c) shows a schematic two-dimensional cut through the CH_3I potential energy surfaces, along the C-I coordinate (adapted from reference [9]). Only the $^1Q_1$, $^3Q_0$ and $^3Q_1$ excited states are depicted. Excitation to the lowest lying state, $^3Q_1$, results in the production of CH_3 and I ($^2P_{3/2}$), with the angular distributions of the photofragments reflecting the perpendicular transition, quantified by $\beta = -1$. However, the picture becomes more complex when considering the higher lying states. A curve-crossing is present between the $^1Q_1$ and $^3Q_0$ states. This crossing plays a key role in the dissociation dynamics following excitation within the A-band, influencing the experimentally observed photofragment angular distributions and the branching into the I and I^* dissociation channels. Following excitation in the middle of the A-band, both I and I^* fragments are observed. For the I^*

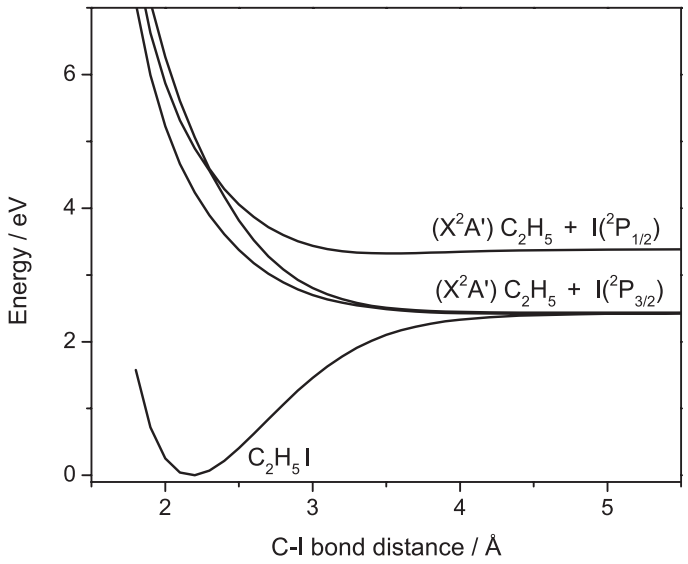

Figure 3.2: Potential energy curves for the states involved in the A-band exciation of C_2H_5I, from [25].

dissociation channel $\beta = 2$, as expected following a parallel transition to the $^3Q_0$ state and direct dissociation on this surface. The anisotropy parameter for the I channel also has a large positive value. This behaviour may seem unexpected as this channel directly correlates with states accessed via perpendicular transitions from the ground state CH_3I. The initial excitation to the $^3Q_0$ state dominates in the central region of the A-band, and within the Frank-Condon region the $^1Q_1$ state lies at higher energy. Initial excitation occurs to the $^3Q_0$ state via a parallel transition. Curve-crossing to the $^1Q_1$ state leads to the population in the I channel. The fragmentation products maintain their original angular distribution determined by the initial parallel excitation, yielding a large positive value for β. At higher excitation energies, the $^1Q_1$ state is accessed. This results in a decrease in the anisotropy parameter, due to the perpendicular character of this transition.

3.2.2 Potential energy surfaces for ethyl iodide

As in the case of methyl iodide, a $\sigma^* \leftarrow$ n transition from the lone pair on iodine to the lowest anti-bonding molecular orbital results in the A-band of ethyl iodide [26]. This consist of numerous excited states, all of which are either A$'$ or A$''$ symmetry and, therefore, electronically accessible. This comes about as a result of the reduction in symmetry of C_2H_5I, which is of the C_S point group, as compared to CH_3I, which belongs to the C_{3V} point group. Figure 3.2 shows potential energy curves for states involved in the A-band ex-

Table 3.1: Ionization energies of methyl iodide, ethyl iodide and their photofragments.

Name	Chemical Formula	Ionization Energy / eV	Reference
methyl iodide	CH_3I	9.54 ± 0.02	[27]
ethyl iodide	C_2H_5I	9.349 ± 0.001	[27]
iodine (I)	$I(^2P_{3/2})$	10.45126	[27]
iodine (I*)	$I(^2P_{1/2})$	9.509	Calculated [27–29]
methyl	CH_3	9.84 ± 0.01	[27]
ethyl	C_2H_5	8.117 ± 0.008	[30]

citation of C_2H_5I. For clarity, only three of the excited states are shown here. As is the case of CH_3I, the excited states are dissociative along the C-I bond coordinate, and photofragmentation results in production of the ethyl fragment in its ground electronic state, with iodine in its spin-orbit ground or excited state.

$$C_2H_5I + h\nu \longrightarrow C_2H_5I^* \longrightarrow C_2H_5(v) + I(^2P_{3/2}) \tag{3.3}$$

$$C_2H_5I + h\nu \longrightarrow C_2H_5I^* \longrightarrow C_2H_5(v) + I(^2P_{1/2}) \tag{3.4}$$

In the case of C_2H_5I, a curve-crossing is also present along the dissociation coordinate.

3.3 Experiment

The custom-built VMI spectrometer has been described in detail in Chapter 2. The molecular beam was formed by supersonic expansion of a gas mixture comprising $\sim 0.1\%$ ethyl iodide (iodoethane, Sigma Aldrich, 99%), or methyl iodide (iodomethane, Sigma Aldrich, 99%) seeded in 2 bar He (BOC, $> 99.9\%$). Under these seeding conditions no cluster formation was observed. Within the ion optics assembly, the molecular beam was intersected orthogonally by the UV photolysis and VUV probe laser beams. UV light, in the wavelength range $\sim$ 230 - 270 nm, photolysed the neutral alkyl iodide. Following a delay of $\sim$20 ns, the VUV light ionized the nascent fragments. The I and I^* fragments were additionally detected at resonance (see Section 3.4.4). In all cases, the laser beams were linearly polarised parallel to the plane of the imaging detector. The ionization energies (IE) of CH_3I, C_2H_5I and their photofragments are shown in Table 3.1. As discussed in Chapter 2, the VUV light produced is of wavelength 118.22 nm, which has a photon energy of 10.49 eV.

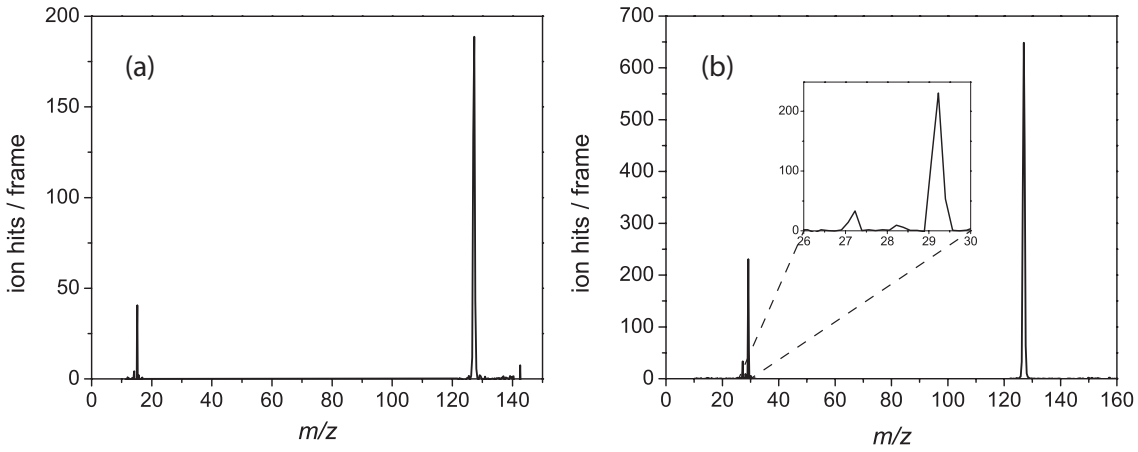

Figure 3.3: Two-colour time-of-flight mass spectra for (a) methyl iodide photolysis at 240 nm and (b) ethyl iodide photolysis at 257.6 nm.

The alkyl iodides studied, and their photofragments have IEs below the available 10.49 eV. Therefore, single photon ionization was achieved in all cases. The ionized parent molecules and nascent fragments were then velocity-mapped on to the 2D imaging detector.

Time-of flight mass spectra (TOF-MS) are presented here, along with the data obtained from the velocity-map images of the fragments. Spectra and images were recorded for single-laser signals as well as two-laser signal. As discussed in Chapter 2, the single-laser signals have been subtracted from the overall signal in order to obtain the two-colour pump-probe signal.

3.4 Results & Discussion

3.4.1 Time-of-flight mass spectra

Figure 3.3 shows representative two-colour time-of-flight mass spectra (TOF-MS) for (a) methyl iodide and (b) ethyl iodide. Time-of-flight spectra reveal the masses of the fragments produced following a photodissociation event (see Section 2.6), and so it is possible to identify the photofragments. Figure 3.3 (a) shows the fragments resulting from photolysis of methyl iodide at 240 nm followed by single-photon ionization at 118.22 nm. The intense peak at m/z = 127 is iodine, and the one at m/z = 15 is methyl (CH_3). The TOF-MS data demonstrates that both of the primary fragmentation products are detected in one time-of-flight cycle.

The TOF-MS in Figure 3.3 (b) shows the fragments produced on photolysis of ethyl iodide with 257.6 nm light. Again, both primary dissociation products are observed, with the iodine fragment at *m/z* = 127, and the ethyl fragment (C_2H_5) at *m/z* = 29. The inset magnifies the *m/z* = 26 - 30 region. Signal is observed at *m/z* = 27 and 28. *m/z* = 28 could result from H-loss from ethyl to produce C_2H_4, but more likely it is a result of under-subtraction of the individual laser contributions. *m/z* = 27 ($C_2H_3^+$) results from H_2-loss from the ethyl cation.

$C_2H_3^+$ production

The C-I bond dissociation energy in C_2H_5I is 2.353 eV [16]. Using a photolysis energy of $\sim$ 5 eV, the dissociation leaves the iodine and C_2H_5 photofragments with more than 2 eV of excess energy. Part of this excess energy will go into internal excitation of the ethyl fragment. The ionization energy of the C_2H_5 fragment is 8.117 eV [30]. Therefore, when ionizing the nascent ethyl fragment with 10.49 eV, the $C_2H_5^+$ ion is produced with a significant amount of internal energy. Only 2.109 eV is required for H_2 loss from the ethyl cation [31]. Therefore, a fraction of the $C_2H_5^+$ will undergo secondary fragmentations to produce $C_2H_3^+$.

3.4.2 CH_3I and C_2H_5I photofragment translational energy distributions

As discussed in Section 3.2, the UV photolysis of both CH_3I and C_2H_5I lead to production of iodine in its ground or spin-orbit excited state, and the alkyl fragment in its ground electronic state. By employing VUV ionization it has been possible to simultaneously detect both I and I^* fragments. Non-resonant single-photon ionization ensured that all vibrationally excited states of the alkyl fragments were detected in a single velocity-map image. Analysis of the translational energy distributions extracted from the velocity-map images of the photofragments yields information about the energy partitioning between internal modes and product translation.

The UV photodissociation of CH_3I was investigated with 240 nm and 266 nm light, using the VMI technique combined with VUV laser ionization. The translational energy distributions of the individual fragments have been extracted from the VMI images, as described in Chapter 2. The total translation energy (E_T) distributions of the nascent fragments are shown in Figure 3.4 for photolysis with (a) 240 nm and (b) 266 nm light. The green traces

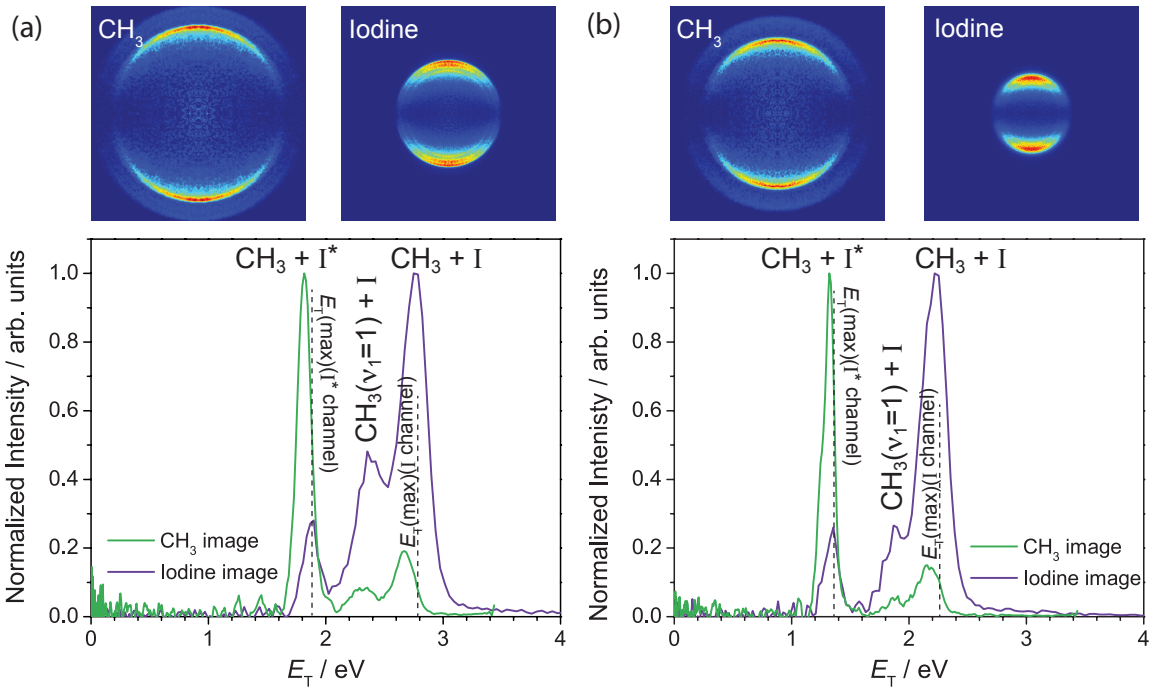

Figure 3.4: The E_T distributions following methyl iodide photolysis with (a) 240 nm and (b) 266 nm light. Those obtained from the CH_3 images are shown in green, and those from the iodine images in purple. The vertical dashed lines indicate the maximum translational energy for the non-rotating ground vibrational state $CH_3(v = 0)$ fragment released in the I and I^* channels.

were obtained from the CH_3 images, and those in purple are from the iodine images. The E_T distributions show three distinct peaks. The peaks appear at the same translational energy regardless of whether they were obtained from images of the iodine or methyl fragments. However, there is an apparent difference in the peak intensities of the E_T distributions extracted from the iodine images, compared to those from the CH_3 images. This has also been observed in the iodine images from C_2H_5I dissociation. It is due to the iodine ionization process with a 118 nm photon, and will be discussed in detail in Section 3.4.3. Only the distributions obtained from the alkyl images have been taken into account when calculating the I^* quantum yield.

On photolysis with 240 nm light the peak in the E_T distribution at 1.8 eV corresponds to the I^* dissociation channel, Equation (3.2). The peak at 2.7 eV corresponds to the I dissociation channel, Equation (3.1). The peak at 2.29 eV was assigned to methyl with one quantum excited in the symmetric C-H stretch released in the I dissociation channel. The energy difference between this peak and the vibrationless $CH_3(v = 0)$ released in the I dissociation channel, 0.38 eV, agrees with the $CH_3(v_1 = 1)$ rotationless energy level, which is

at 0.3725 eV [32]. At 266 nm photolysis, the same three peaks, as previously assigned, are observed, though these are now shifted to lower translational energy. The additional energy on photolysis with 240 nm light, relative to photolysis with 266 nm light, is channelled into photofragment translation. The vertical dashed lines in Figure 3.4 indicate the maximum translational energy release, E_T(max), which would be obtained for the case when all of the energy available to the fragments in the I and I* dissociation channels is released into translation. In calculating E_T(max), the energy from the photon, hν_{UV}, and the energy required to break the bond, D_0(C-I) = 2.39 eV [18], have been taken into account. However, the internal energy of the parent molecule has not be considered. For this reason the tails of the peaks exceed E_T(max). In forming the molecular beam, the supersonic expansion does not achieve perfect cooling, and therefore a fraction of the parent molecules in the molecular beam will have some vibrational excitation. Despite this, it is clear that the majority of the available energy is partitioned into translation of the recoiling fragments. The breadth in the peaks of the E_T distributions corresponding to the I and I* dissociation channels is due to population of up to two quanta in the ν_2 vibration, the umbrella bending mode of the methyl fragment. The energy difference between these peaks is $\sim$0.9 eV, i.e. only slightly less than the iodine spin-orbit splitting of 0.942 eV [33]. The methyl fragment from the I dissociation channel is formed with slightly more internal energy than in the I* channel; this comes about due to the sudden change of the reaction coordinate from $^3Q_0$ to $^1Q_1$ at the conical intersection, as discussed by Amamatsu *et al.* [34], which channels more of the excess energy into the internal energy of the methyl photofragment in the I dissociation channel.

The A-band photodissociation of CH_3I has been studied in detail by Eppink and Parker [9, 10]. The single-photon ionization data, presented here, agree with their observations. In their studies they employed REMPI detection to state-selectively ionize the CH_3 and iodine photofragments. They also observed that the product vibrational energy is mainly partitioned into ν_2. In addition, at higher photolysis energies, such as those employed for this work, they observed that a fraction of molecules is excited with one quantum of ν_1, the symmetric C-H stretch [9, 10].

Velocity-map images were acquired for the C_2H_5 and iodine photofragments following C_2H_5I photolysis at a number of wavelengths across the A-band. Figure 3.5 shows the E_T distributions obtained from the images of C_2H_5 and iodine fragments detected using single-photon ionization at 118 nm, following photolysis of C_2H_5I with (a) 248 nm, and (b) 266 nm light. Two peaks of varying relative intensity are observed in these E_T distributions. The peak at lower E_T is assigned to C_2H_5 released in the I* channel, Equation (3.4). The

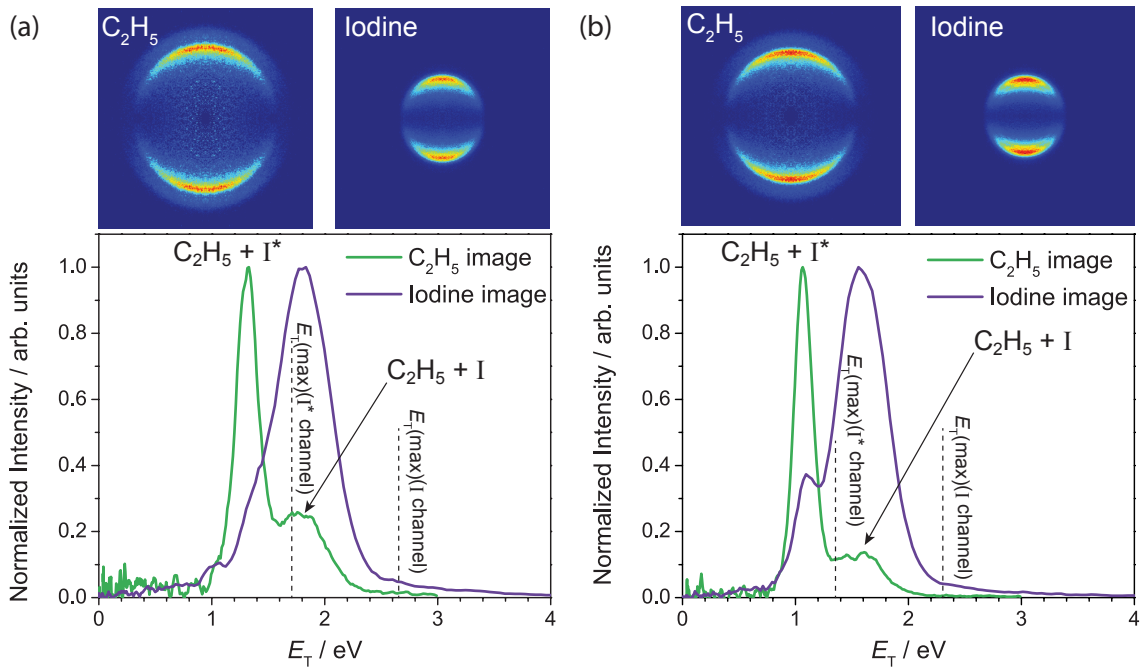

Figure 3.5: The E_T distributions following ethyl iodide photolysis with (a) 248 nm and (b) 266 nm light. The distributions obtained from C_2H_5 images are shown in green, and those from the iodine images in purple. The vertical dashed lines indicate the maximum translational energy for the non-rotating ground vibrational state $C_2H_5(v = 0)$ fragment released in the I and I^* channels.

peak at higher E_T is assigned to C_2H_5 released in the I channel, Equation (3.3). Table 3.2 shows the energies of the peaks in the E_T distributions, which correspond to the I and I^* dissociation channels, for four photolysis wavelengths: 236 nm, 248 nm, 257 nm, and 266 nm. It appears that as the photon energy increases (from 4.66 eV with 266 nm light to 5.25 eV with 236 nm light), the fraction of available energy released into translation remains essentially unchanged. Regardless of the photolysis wavelength, the I dissociation channel results in a fraction of around 0.68 of the available energy being released into translation. In the case of the I^* dissociation channel, this fraction is significantly higher, 0.78. This indicates that the C_2H_5 fragment has very different internal energy distributions in the two dissociation channels. This is reflected in the translational energy difference between the I and I^* photofragments, which for each photolysis wavelength is only $\sim$0.45 eV, significantly less than the iodine spin-orbit splitting of 0.942 eV [33]. As a result of the change in reaction coordinate during curve-crossing, the nascent ethyl fragments from the I dissociation channel are formed with significantly more internal energy than those from the I^* dissociation channel.

The work of Tang *et al.* [20] employed the REMPI technique in combination with VMI

Table 3.2: The photolysis wavelengths, corresponding photon energies, and the most probable total translational energies for the I and I* dissociation channels.

Photolysis Wavelength / nm	Photon Energy / eV	I channel / eV	I* channel / eV
236	5.25	1.96	1.51
248	5.00	1.80	1.34
257	4.81	1.74	1.20
266	4.66	1.51	1.07

to state-selectively detect and image the I, I*, and C_2H_5 fragments resulting from A-band photodissociation of C_2H_5I. In their work, for each dissociation channel, the fraction of the available energy released into translation was also observed to be constant across the wavelength range investigated, with a larger fraction of the available energy being released as internal energy in the I dissociation channel. In the previous work, at photolysis wavelengths shorter than ∼260 nm, it was observed that, as a result of the multiphoton conditions required for REMPI detection, a competing multiphoton dissociative ionization channel came into play. This process yielded $C_2H_5{}^+$, via an initial two photon ionization to form $C_2H_5I^+$. The peak that resulted essentially obscured the low energy region of the E_T distributions obtained from the images of $C_2H_5{}^+$. In the previous work, it was only with the E_T distributions obtained from images of I and I* that it was possible to confirm that the low energy region was of no particular interest. In the current study, the use of single-photon photolysis conditions along with VUV photoionization ensure that such multiphoton processes do not occur. The E_T distributions shown here, obtained from the images of VUV photoionized C_2H_5, are able to reveal directly that, even at higher photolysis energies, there is no significant population of the photofragments released with very low translational energies.

3.4.3 Ionization of the iodine fragment

As noted in the previous section, the relative intensities of the peaks corresponding to the I and I* channels in the E_T distributions determined from the iodine images differ considerably from those obtained from the alkyl fragment images (see Figure 3.4 in the case of CH_3I, and Figure 3.5 for C_2H_5I). Analysis of the TOF-MS spectra shown in Figure 3.3 reveals that in both spectra the iodine peak (m/z = 127) is significantly more intense than the signal from the alkyl fragment. These observations are unexpected, as each fragmentation event results in production of an iodine atom and an alkyl fragment in a one-to-one ratio. Therefore, either the alkyl fragment is detected less efficiently than the iodine one

or the iodine fragment is detected preferentially to the alkyl fragment. The relative peak intensities of the two peaks in the E_T distributions are also observed to vary depending on which fragment is detected. In the following a number of aspects that could be the cause of these discrepancies will be considered. It should be noted that the relative peak intensities obtained from the alkyl images agree well with the literature [10, 20].

Space-charge effects result from a high density of charged particles being produced within a small ionization volume. For a molecular beam experiment this occurs when a large number of ions are created within the interaction region. The ions then repel one another. For VMI data this has the effect of blurring the image, decreasing the energy resolution and broadening the E_T peaks. This broadening of the peaks may reduce the apparent intensities. However, this would affect all ions formed within the interaction region more or less equally and cannot explain the differences in the relative intensities of the two peaks in the E_T distributions obtained from the alkyl fragment images as compared to those obtained from the iodine images.

If the probe laser is polarised, alignment effects could influence the efficiency with which the fragments are detected. The pump-probe experiments described here were performed with both pump and probe laser polarised in the plane of the detector. To check for possible alignment of the alkyl or iodine fragments, the polarisation of the probe laser was switched from parallel to perpendicular to the plane of the detector. Images were acquired for both the alkyl and iodine fragments. No significant differences were observed in the E_T distributions, nor in the angular intensity distributions of the recoiling iodine or alkyl fragments. Therefore, there was no evidence of rotational or orbital alignment of the products.

Photodissociation studies of alkyl halides have been reported in the literature [35, 36]. In addition to the fragments from single molecule dissociation, cluster dissociation can lead to production of other species. For example, dissociation of the van der Waals dimer $(CH_3I)_2$ has been shown to produce I_2^+ [36]. This behaviour is not observed for CH_3I dissociation. In the case of $(CH_3I)_2$, I_2^+ is produced via dissociation of the ionized dimer. I_2^+ then goes on to dissociate to form I^+. Therefore, with regards to the current work, it was necessary to rule out any possible contribution from clusters. As described in Section 3.3, these experiments were performed with both CH_3I and C_2H_5I seeded with less than 0.1% in He buffer gas. The photolysis laser beam intersected with the rising edge of the molecular beam pulse. This is the region of the molecular pulse where clusters are unlikely to be formed. Under these conditions no clusters were observed in the time-of-flight spectrum. However, it is possible that clusters could have been formed but were fully dissociated before they could be detected. Therefore, to ensure that this was not the case, clusters

needed to be observed in the TOF. In an attempt to form and observe clusters of the C_2H_5I molecule, a gas mixture was made with argon as the carrier gas. When the source backing pressure is maintained, cluster formation is promoted by use of a heavier carrier gas [37], in this case Ar instead of He. In addition to this, the plateau of the molecular pulse, the region where clusters are most likely to form, was probed. Under these conditions the C_2H_5I dimer and trimer clusters (and the C_2H_5I-Ar complex) were observed in the TOF. A very small signal at the arrival time for I_2^+ was also observed. These clusters were not present in the TOF when probing the early part of the molecular pulse. This gives evidence that, although under certain conditions clusters could be formed, they were not present in the experiments presented in this work.

It has been suggested that the photoionization cross-sections of the alkyl fragments could have an internal energy dependence. This would mean that internally hot fragments were ionized more or less preferentially than internally cold fragments. However, this would only explain the results for C_2H_5I dissociation, where the internal excitation of the C_2H_5 fragment varies by $\sim$0.4 eV between the I and I^* dissociation channels. In the case of CH_3I dissociation, the internal energy of the CH_3 fragment is very similar for both channels and a variation in the photoionization cross-section as a function of internal energy could not account for the observed discrepancy. In addition, experiments performed by Fan and Pratt, in which C_2H_5 fragments with internal energies ranging from 0.2 to 1.1 eV were produced and detected, showed no evidence for an internal energy dependence on the photoionization cross-section of the ethyl fragment [38].

After considering all of these scenarios, and taking into account that the E_T distributions obtained from the alkyl images agree well with the ones seen in the literature [10, 20], we conclude that the discrepancy must be related to the iodine atom. It is observed that the I fragment is detected 'preferentially' to the I^* fragment. The lowest ionization threshold of the I atom is 10.45 eV, producing $I^+(^3P_2)$ [27]. Photoelectron spectroscopy experiments revealed a broad, intense line at $\sim$10.5 eV which is attributed to formation of this ion [28]. VUV photoionization of iodine at 118.22 nm leads to population of this ionic state. In addition, Berkowitz *et al.*, in their study of the partial photoionization cross-sections of atomic iodine, observed a Rydberg feature at 118.276 nm (10.4827 eV). They assigned it to the n^*=4 member of the ns series converging to the $^3P_1$ state of I^+ [39]. VUV probe excitation of I ($^2P_{3/2}$) could also populate this state. Fano discussed the effect of autoionization as resulting from the interaction of a discrete state with a continuous spectrum [40]. Since the populated Rydberg state lies within the ionization continuum, configuration interaction between the discrete and continuous spectrum could result in autoionization. It is likely

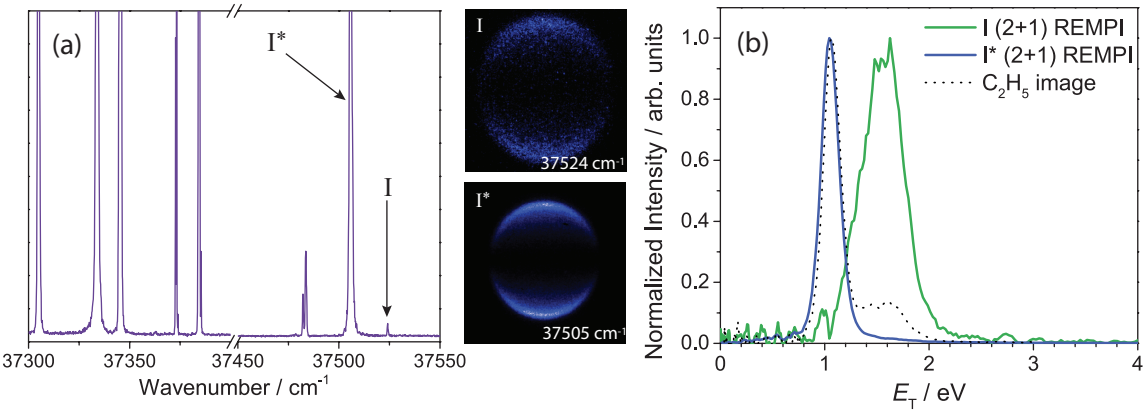

Figure 3.6: (a) REMPI spectrum for iodine around 266 nm. I and I* resonances are indicated. The images shown are those obtained for I (top) and I* (bottom) photofragments produced on dissociation of ethyl iodide and detected using REMPI. The polarization of the laser was vertical in-the-plane of the image. (b) The total translational energy distributions of I (green) and I* (purple) obtained from the corresponding images (left). The E_T distribution obtained from the image of C_2H_5, detected by means of single-photon non-resonant ionization, is shown as the black dashed line.

that a superposition of direct ionization and excitation followed by autoionization enhance the I channel signal in the iodine velocity-map images.

3.4.4 REMPI detection of iodine photofragments

The velocity-map images presented so far have been obtained using universal (non-resonant) ionization. In order to complement the universal ionization data, in this work the iodine fragments have also been state-selectively detected. Figure 3.6 (a) shows a REMPI spectrum[1] for iodine, in the wavelength region from 268 nm to 266 nm. The iodine atoms resulted from the dissociation of C_2H_5I. The iodine fragments detected using REMPI were imaged at several wavelengths within the A-band of the C_2H_5I molecule. Typical images of the I and I* photofragments are shown in Figure 3.6. By assessing the velocity distributions of the fragments, shown in Figure 3.6 (c), the I and I* identities were confirmed. The E_T distribution of the C_2H_5 + I* photofragments (blue trace), obtained from the image of REMPI detected I*, peaks at 1.06 eV. It can be observed that the C_2H_5 + I photofragments are born with more translational energy than those resulting from the I* dissociation; the E_T distribution for the I dissociation channel (green trace), obtained from the image of REMPI detected I, peaks at 1.54 eV. The form of these two distributions agree with those in the

[1] See Section 2.8 for details on REMPI spectra data acquisition.

literature [18, 20]. The wavelengths chosen for resonant detection of the I and I* states of iodine are labelled in Figure 3.6 (a).

In Figure 3.6 (c) the E_T distribution obtained from the image of C_2H_5, detected by means of single-photon non-resonant ionization, is plotted (as the black dashed line) alongside those obtained from the images of REMPI detected I and I*. The I* image sampled the whole internal energy distribution for the C_2H_5 + I* channel. The width of the E_T distribution obtained from I* detected via (2+1) REMPI is identical in width to the peak which corresponds to the C_2H_5 + I* channel in the E_T distribution obtained from the C_2H_5 image. This implies that single-photon ionization also samples the entire internal energy distribution for this channel. The same follows for the I dissociation channel. The E_T distribution obtained from the C_2H_5 image effectively corresponds to a weighted sum of the individual E_T distributions for the C_2H_5 + I* and C_2H_5 + I channels obtained from images of the REMPI detected I* and I atoms, respectively. This is also the case for the E_T distribution obtained from the iodine image detected via single-photon ionization, not shown here. However, in the latter case, due to the enhanced detection of I, as a result of the 118 nm photoionization step, this does not reflect the branching into the I and I* dissociation channels, which will be discussed in Section 3.4.6.

3.4.5 Anisotropy parameters

As discussed in Section 1.2.4, the anisotropy parameter β characterises the angular distribution of the photofragments, which reflects the direction of the transition dipole moment for the initial excitation relative to the fragmenting bond. This parameter is an important indicator of the states involved in the initial excitation step. The angular distributions of the alkyl and iodine photofragments resulting from initial alkyl iodide excitation to the A-band, and the effects of curve-crossings between different electronic states, were discussed generally in Section 3.2.

Figure 3.7 shows the recoil anisotropy parameter (β) values for (a) the I* dissociation channel, and (b) the I dissociation channel, obtained from both methyl and iodine detection, following CH_3I photolysis with 240 nm and 266 nm light. The anisotropy parameter values obtained from the angular distributions of CH_3 and iodine photofragments detected via single photon ionization are shown in black, and the ones from the angular distributions of iodine photofragments detected via (2+1) REMPI at ~266 nm are shown in green. As shown in Figure 3.7 (a), following photolysis of CH_3I with 240 nm or 266 nm light

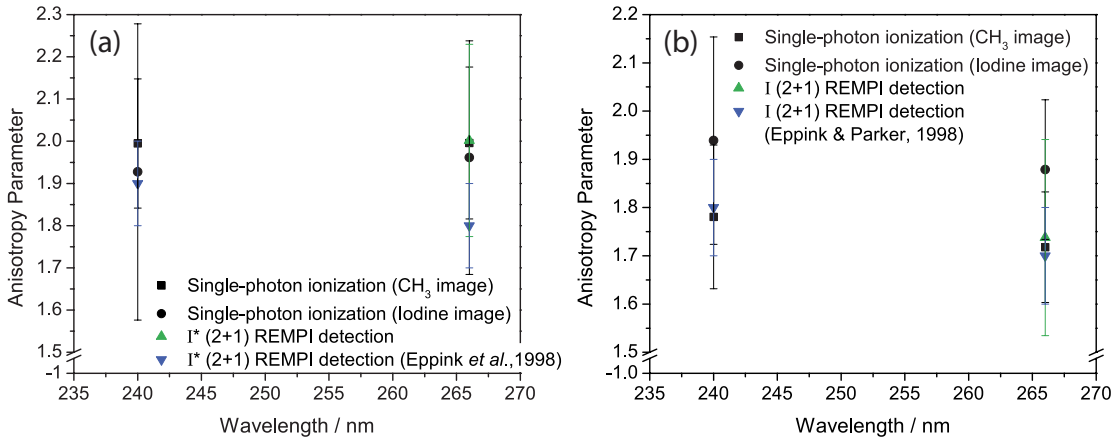

Figure 3.7: Anisotropy parameters for (a) CH_3 + I^*, and (b) CH_3 + I dissociation channels following methyl iodide photolysis with 240 nm and 266 nm light.

yields the CH_3 + I^* photofragments with $\beta = 1.99$. These values, obtained from the images of CH_3 detected using single-photon ionization, are slightly higher than those obtained from the images of iodine detected via single-photon ionization, which give $\beta = 1.92$ and $\beta = 1.96$ for the CH_3 + I^* photofragments resulting from 240 nm and 266 nm photolysis of CH_3I, respectively, however, these values agree well within experimental error. The $^3Q_0$ state dominates the region of the absorption band which both of these photolysis wavelengths access. The initially excited $^3Q_0$ state correlates diabatically with the CH_3 + I^*. Therefore, the anisotropy parameters of these photofragments reflect the initial excitation via a parallel transition. The observed anisotropy parameters of the CH_3 + I photofragments, shown in Figure 3.7 (b), also have large positive anisotropy parameter values. The images of CH_3 detected via single-photon ionization give $\beta = 1.78$ and $\beta = 1.72$ for the CH_3 + I photofragments resulting from CH_3I photolysis with 240 nm and 266 nm light, respectively. The I dissociation channel in this region of the A-band also results from an initial excitation to the $^3Q_0$ state, via a parallel transition. The non-limiting value of β results since the initial excitation is followed by a non-adiabatic curve crossing to the $^1Q_1$ state, which dissociates to form the CH_3 + I photofragments. We have compared our measured anisotropy parameters for the I and I^* dissociation channels with the ones obtained Eppink and Parker at the same wavelengths (blue data points) [9], and found them to agree within experimental error.

Figure 3.8 shows the anisotropy parameters for (a) the I^* dissociation channel, and (b) the I channel dissociation channels resulting from C_2H_5I photolysis at a number of wavelengths across the A-band. The anisotropy parameter values extracted from the ion images of C_2H_5 and iodine fragments detected via single-photon ionization are shown in black. The green

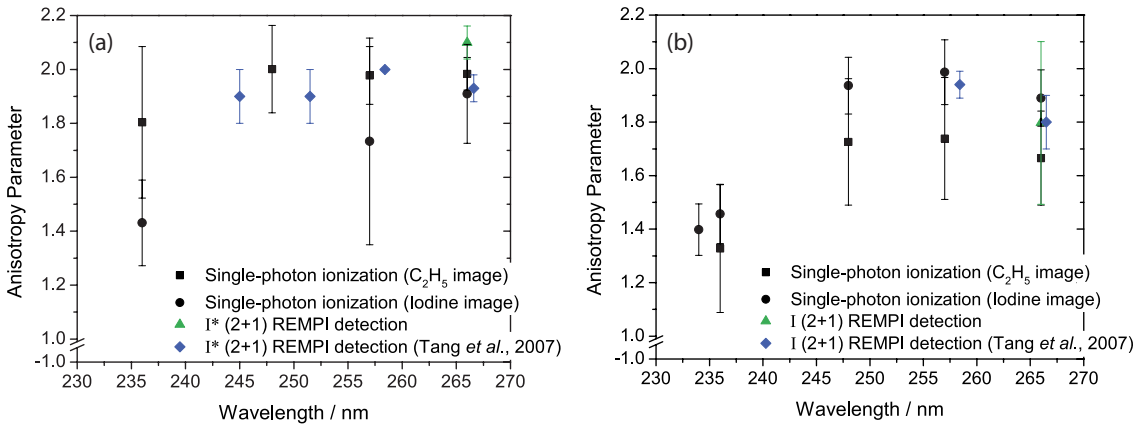

Figure 3.8: The anisotropy parameters for (a) C_2H_5 + I^*, and (b) C_2H_5 + I dissociation channels following ethyl iodide dissociation within the A-band.

triangles represent β values extracted from the I and I^* images recorded using REMPI detection. The β values obtained from the photofragment images of this work have been compared to those from the work of Tang *et al.* (blue diamonds) [20]. For the C_2H_5 + I^* channel, shown in Figure 3.8 (a), $\beta \sim 2$ within the 240 nm to 270 nm region investigated; for photolysis with 266 nm light, $\beta = 1.98$ for the I^* dissociation channel obtained from images of the C_2H_5 detected via single-photon ionization; with 257 nm light, $\beta = 1.98$; and with 248 nm light, $\beta = 2.00$. Although $\beta = 2$ for the I^* channel at 248 nm is slightly higher than previously observed, the anisotropy parameter values for the I^* channel obtained from the C_2H_5 images agree well within experimental uncertainty with those of the previous study. The images of iodine detected via single-photon ionization, particularly at the shortest photolysis wavelength, appear to give lower values for the anisotropy parameter than those obtained from the C_2H_5 images. This is most likely an adverse effect of the preferential ionization of the I fragments with this detection method, which results in the I^* dissociation channel being partially obscured.

As shown in Figure 3.8 (b), the anisotropy parameter values for the C_2H_5 + I channel resulting from C_2H_5I photolysis within the wavelength range 240 nm to 270 nm are slightly reduced from those of the I^* dissociation channel, but they are still large and positive. Again, the values compare with those from the work of Tang *et al.* (blue diamonds) [20]. The anisotropy parameters for the I dissociation channel obtained from the images of C_2H_5 detected via single-photon ionization are $\beta = 1.67$, following photolysis with 266 nm; $\beta = 1.74$, with 257 nm light; and $\beta = 1.73$ with 248 nm light. The values obtained from the images of iodine detected via single-photon ionization appear to exceed these values by $\sim$0.2 in each case. It is unclear as to whether this is due to the enhanced signal in the I

dissociation channel as a result of 118 nm photoionization.

Within the 240 nm to 270 nm wavelength range, initial excitation via a parallel transition dominates. This is reflected in the anisotropy parameter values for the products from both the I and I* dissociation channels. As was observed for CH_3I photofragmentation, I* and its alkyl co-fragment are formed via direct dissociation from the initial state, whereas the I channel results from a curve-crossing prior to dissociation. At the shortest photolysis wavelength, 236 nm, $\beta = 1.80$ for the I* channel, and for the I channel $\beta = 1.32$, are obtained from the images of C_2H_5 detected via single-photon ionization. At this wavelength, in addition to the state accessed via a parallel transition, a higher lying electronic state, which correlates directly with the C_2H_5 + I photofragmentation products, becomes excited, via a perpendicular transition. Curve-crossing from this higher-lying state can also lead to production of C_2H_5 + I*. The combination of parallel and perpendicular transitions results in the observed reduced values of β for both the I and I* dissociation channels.

3.4.6 I* quantum yield

In the study of the UV photodissociation of the alkyl iodides, the I* quantum yield, Φ(I*), provides experimental insight into the dissociation dynamics of these molecules. Φ(I*) gives a representation of the competition between the I and I* dissociation channels. Therefore, Φ(I*) can be used, together with the E_T distributions and angular distributions of the recoiling photofragments, in order to gain information on the initially accessed state(s), and on curve crossings that may have occurred during the dissociation process.

In this section, Φ(I*) for CH_3I and C_2H_5I photolysis at a number of different wavelengths will be presented, and the method by which these were obtained will now be described. The I* quantum yield is calculated as:

$$\Phi(\mathrm{I}^*) = \frac{\mathrm{N}^*}{\mathrm{N}+\mathrm{N}^*} \tag{3.5}$$

where N and N* are the number of iodine fragments formed in the ground, I, and spin-orbit excited state, I*, respectively, following the dissociation of the alkyl iodide. Only the images obtained for the alkyl fragments have been used to calculate the I* quantum yield. In the E_T spectra, the peaks corresponding to the I and I* dissociation channels were identified, and fitted with Gaussians. From the fit, the area under the curve was obtained for each peak. Since single-photon ionization of CH_3 samples the whole E_T distribution, these areas are directly proportional to N and N*, and can be used to calculate Φ(I*) according

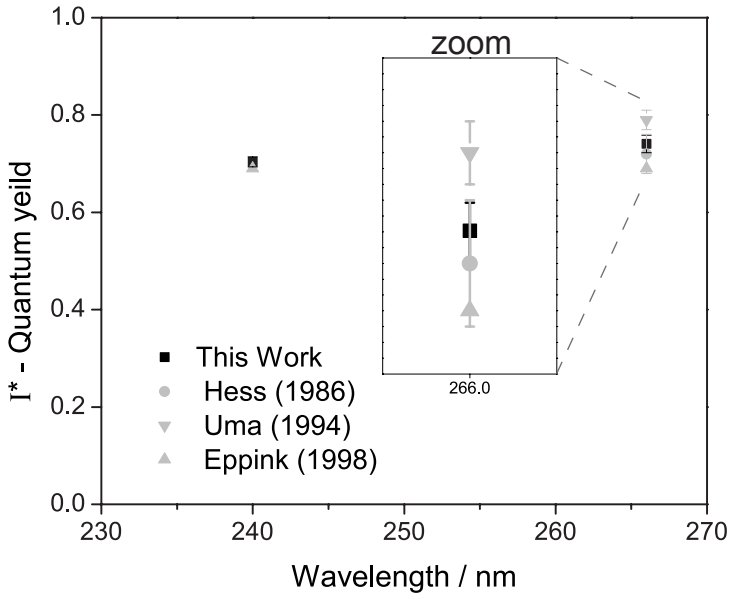

Figure 3.9: I^* quantum yield for methyl iodide within the A-band. The values from this work are shown in black. Those from previous studies are shown in grey (see key for details).

to Equation (3.5). The errors displayed in Figure 3.9 and Figure 3.10 are those which propagate through from the standard deviation errors of the Gaussian fits.

The $\Phi(I^*)$ obtained in this work, following CH_3I photolysis with 240 nm and 266 nm light, are shown in black in Figure 3.9. For photolysis of CH_3I with 266 nm light, $\Phi(I^*)$ = 0.74, which falls within the range of previously published $\Phi(I^*)$ values (plotted in grey) for CH_3I photolysis at this wavelength [9, 19, 41]. For photolysis at 240 nm, $\Phi(I^*)$ = 0.7, which agrees with that obtained by Eppink and Parker (plotted as a grey triangle) [9]. These $\Phi(I^*)$ values indicate that at both photolysis wavelengths the I^* dissociation channel is the major dissociation pathway. Initial excitation in this region of the A-band is to the $^3Q_0$ state, which directly correlates this the CH_3 + I^* products. The observed reduction in $\Phi(I^*)$, when photolysing with 240 nm light, as compared to 266 nm light, comes about since the increase in excitation energy now means that a larger fraction of excitations result in curve-crossing to the $^1Q_1$ state, and dissociate to form CH_3 + I.

$\Phi(I^*)$ for C_2H_5I photolysis at a number of wavelengths across the A-band are shown as black squares in Figure 3.10. The value of $\Phi(I^*)$ is observed to reduce with higher excitation energy (shorter wavelength), from $\Phi(I^*)$ = 0.74 at 266 nm, to $\Phi(I^*)$ $\sim$0.65 at 257 nm and 248 nm, and to $\Phi(I^*)$ = 0.57 at 236 nm. This general trend comes about due to the increase in probability of curve-crossing with an increase in excitation energy. This

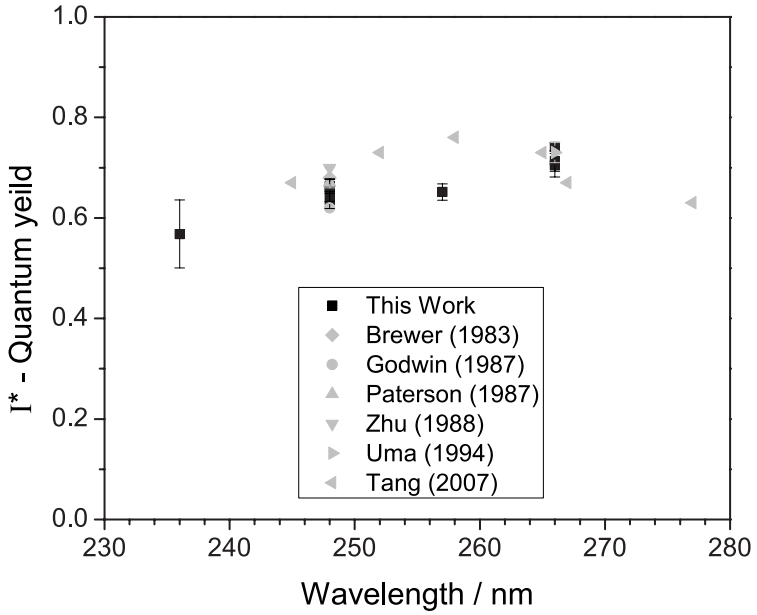

Figure 3.10: I^* quantum yield obtained from the ethyl images following A-band photodissociation of C_2H_5I. The values from this work are shown in black. Those from previous studies are shown in grey (see key for details).

curve-crossing occurs from the initially excited state, analogous to the $^3Q_0$ state of CH_3I, which dissociates to form C_2H_5 + I^*, to the state which yields C_2H_5 + I photofragments. At the shortest photolysis wavelength, 236 nm, the highest lying state (analogous to the $^1Q_1$ state of CH_3I) is also initially accessed, which dissociates to form C_2H_5 + I. Therefore, at this photolysis wavelength, a combination of parallel and perpendicular transitions occur. In the previous section this was observed to reduce the anisotropy parameter value. In the case of the I^* quantum yield, since direct dissociation can occur to form the C_2H_5 + I photofragmentation products, the I dissociation channel becomes more significant, and the value of $\Phi(I^*)$ is reduced compared to that from photolysis of C_2H_5I at longer wavelengths. As well as reflecting the dissociation dynamics across the A-band, the values of $\Phi(I^*)$ obtained for the wavelength range investigated also agree with the results of previous studies. In Figure 3.10 the values of $\Phi(I^*)$ obtained in this work (black squares) have been compared with those from the literature (plotted in grey) [15–20]. Generally, our work appears to give slightly lower values for $\Phi(I^*)$ than those obtained by Tang *et al.* at a number of wavelengths across the A-band [20]. However, no experimental uncertainties were published for their quantum yield values. Several other studies have employed photolysis wavelengths of 248 nm and 266 nm, and the $\Phi(I^*)$ values from the present study are consistent with these within experimental uncertainty.

3.5 Conclusion

A comprehensive VMI study has been undertaken, which has investigated the photodissociation of CH_3I and C_2H_5I across their A-bands. Single-photon ionization allows non-resonant detection of all the photofragments resulting from dissociation of a molecule (provided their ionization energies are lower than 10.5 eV). Individual photofragments can then be velocity-map imaged, which allows measurement of the velocity and angular distributions of the recoiling photofragments, and additionally, provides information about the branching between different dissociation channels. It has been observed that ionization effects result in an enhancement of the I signal compared to the I^* signal. Therefore, in this case, the iodine images could not be used to obtain the I^* quantum yield. However, $\Phi(I^*)$ could readily be obtained from the corresponding alkyl fragment image. The anisotropy parameters obtained from the iodine and alkyl images were found to be self-consistent (within experimental uncertainty) for the products of the I and I^* dissociation channels. The internal energy distribution of the $C_nH_{(2n+1)}$ photofragments released in the I dissociation channel is 'hotter' than for those released in the I^* channel. Following photolysis at wavelengths within the central region of the A-band, the C_nH_{2n+1} + I^* channel is found to be the major photofragmentation pathway for both CH_3I and C_2H_5I. An initial excitation via a parallel transition leads to direct dissociation to form $C_nH_{(2n+1)}$ + I^*. Curve-crossing leads to population of the $C_nH_{(2n+1)}$ + I photofragmentation channel. The anisotropy parameter values for both $C_nH_{(2n+1)}$ + I^* and $C_nH_{(2n+1)}$ + I photofragment pairs reflect the initial excitation of the alkyl iodide via a parallel transition. The results obtained from this VMI study are consistent with the work previously reported in the literature on CH_3I and C_2H_5I A-band dissociation, and this work demonstrates the effective use of single photon ionization as a viable photofragment detection method.

References

[1] Chandler, DW and Houston, PL. *Two-dimensional imaging of state-selected photodissociation products detected by multiphoton ionization*. The Journal of Chemical Physics **87**:2 1445–1447 (1987) (cited p. 53).

[2] Chandler, DW, W Thoman Jr., J, Janssen, MHM, and Parker, DH. *Photofragment imaging: the 266 nm photodissociation of CH_3I*. Chemical Physics Letters **156**:2-3 151–158 (1989) (cited p. 53).

[3] Mulliken, R. *Structure, Ionization and Ultraviolet Spectra of Methyl Iodide and Other Molecules*. Physical Review **47**:5 413–415 (1935) (cited p. 54).

[4] Porret, D and Goodeve, CF. *The continuous absorption spectrum of methyl iodide*. Transactions of the Faraday Society **33**: 690–693 (1937) (cited p. 54).

[5] Hunter, TF and Kristjansson, KS. *Photoacoustic measurements of photofragmentation in CH3I*. Chemical Physics Letters **58**:2 291–294 (1978) (cited p. 54).

[6] Sparks, RK, Shobatake, K, Carlson, LR, and Lee, YT. *Photofragmentation of CH_3I: Vibrational distribution of the CH_3 fragment*. The Journal of Chemical Physics **75**:8 3838–3846 (1981) (cited p. 54).

[7] Barry, MD and Gorry, PA. *Photofragmentation dynamics of CH_3I at 248 nm*. Molecular Physics **52**:2 461–473 (1984) (cited p. 54).

[8] Eppink, ATJB and Parker, DH. *Velocity map imaging of ions and electrons using electrostatic lenses: Application in photoelectron and photofragment ion imaging of molecular oxygen*. The Review of Scientific Instruments **68**:9 3477–3484 (1997) (cited p. 54).

[9] Eppink, ATJB and Parker, DH. *Methyl iodide A-band decomposition study by photofragment velocity imaging*. The Journal of Chemical Physics **109**:12 4758 (1998) (cited p. 54, 56, 57, 63, 70, 73).

[10] Eppink, ATJB and Parker, DH. *Energy partitioning following photodissociation of methyl iodide in the A band: A velocity mapping study*. The Journal of Chemical Physics **110**:2 832–844 (1999) (cited p. 54, 63, 66, 67).

[11] González, MG, Rodriguez, JD, Rubio-Lago, L, Garcia, Ga, and Bañares, L. *Slice imaging and wave packet study of the photodissociation of CH3I in the blue edge of the A-band: evidence of reverse $^3Q_0 \leftarrow^1 Q_1$ non-adiabatic dynamics*. Physical Chemistry Chemical Physics **13**:36 16404 (2011) (cited p. 55).

[12] Nalda, R de, Izquierdo, JG, Durá, J, and Bañares, L. *Femtosecond multichannel photodissociation dynamics of CH_3I from the A band by velocity map imaging*. The Journal of Chemical Physics **126**:2 021101 (2007) (cited p. 55).

[13] Nalda, R de, Durá, J, Garcia, Ga, Izquierdo, JG, González-Vázquez, J, and Bañares, L. *A detailed experimental and theoretical study of the femtosecond A-band photodissociation of CH_3I*. The Journal of Chemical Physics **128**:24 244309 (2008) (cited p. 55).

[14] Riley, SJ and Wilson, KR. *Excited fragments from excited molecules: energy partitioning in the photodissociation of alkyl iodides*. Faraday Discussions **53**: 132–146 (1972) (cited p. 55).

[15] Brewer, P, Das, P, Ondrey, GS, and Bersohn, R. *Measurement of the relative populations of $I(^2P^0{}_{1/2})$ and $I(^2P^0{}_{3/2})$ by laser induced vacuum ultraviolet fluorescence*. The Journal of Chemical Physics **79**:2 720–723 (1983) (cited p. 55, 74).

[16] Paterson, C, Godwin, FG, and Gorry, PA. *Photofragmentation dynamics of C_2H_5I and CF_3CH_2I at 248 nm*. Molecular Physics **60**:4 729–747 (1987) (cited p. 55, 61, 74).

[17] Godwin, FG, Gorry, PA, Hughes, PM, Raybone, D, Watkinson, TM, and Whitehead, JC. *Two-photon VUV laser-induced fluorescence detection of $I(^2P_{1/2})$ and $I(^2P_{3/2})$ from alkyl iodide photodissociation at 248 nm*. Chemical Physics Letters **135**:1-2 163–169 (1987) (cited p. 55, 56, 74).

[18] Zhu, Q, Cao, JR, Wen, Y, Zhang, J, Zhong, X, Huang, Y, Fang, W, and Wu, X. *Photodissociation channels and energy partitioning in the photofragmentation of alkyl iodides*. Chemical Physics Letters **144**:5-6 486–492 (1988) (cited p. 55, 63, 69, 74).

[19] Uma, S and Das, PK. *Dynamics of $I(^2P_{1/2})$ production in the ultraviolet photodissociation of alkyl iodides*. Canadian Journal of Chemistry **72**:3 865–869 (1994) (cited p. 55, 73, 74).

[20] Tang, Y, Lee, Wb, Hu, Z, Zhang, B, and Lin, Kc. *Productions of I , I *, and C_2H_5 in the A-band photodissociation of ethyl iodide in the wavelength range from 245 to 283nm by using ion-imaging detection Productions of I, I*, and C_2H_5 in the A-band photodissociation of ethyl iodide in the wavelength*. The Journal of Chemical Physics **126**:6 064302 (2007) (cited p. 55, 64, 66, 67, 69, 71, 74).

[21] Uma, S and Das, PK. *Production of $I(^2P_{1/2})$ in the ultraviolet photodissociation of α-branched alkyl iodides*. The Journal of Chemical Physics **104**:12 4470 (1996) (cited p. 55).

[22] Bi, W, Xu, X, Huang, J, Xiao, D, and Zhu, Q. *High-resolution photofragment translational spectroscopy for the UV photodissociation of C2H5I*. Science in China Series B: Chemistry **50**:4 476–482 (2007) (cited p. 55).

[23] Zhang, XP, Lee, Wb, and Lin, Kc. *Nonadiabatic Transition in the A-Band Photodissociation of Ethyl Iodide from 294 to 308 nm by Using Velocity Imaging Detection*. The Journal of Physical Chemistry A **113**:1 35–39 (2009) (cited p. 55).

[24] Mulliken, RS. *Intensities in Molecular Electronic Spectra X. Calculations on Mixed-Halogen, Hydrogen Halide, Alkyl Halide, and Hydroxyl Spectra*. The Journal of Chemical Physics **8**:5 382 (1940) (cited p. 56).

[25] Karsili, TNV. *PES of ethyl iodide*. Laser Chemistry, Spectroscopy and Dynamics Group, Bristol University (cited p. 58).

[26] Boschi, RA and Salahub, DR. *The far ultra-violet spectra of some 1-iodoalkanes*. Molecular Physics **24**:2 289–299 (1972) (cited p. 58).

[27] Lias, SG. *"Ionization Energy Evaluation" in NIST Chemistry WebBook, NIST Standard Reference Database Number 69, (retrieved June 19, 2013)*. Ed. by Linstrom, PJ and Mallard, WG. National Institute of Standards and Technology, Gaithersburg MD, 20899 (cited p. 59, 67).

[28] Tremblay, J, Larzilliere, M, Combet Farnoux, F, and Morin, P. *Photoelectron spectroscopy of atomic iodine produced by laser photodissociation*. Physical Review A **38**:7 3804–3807 (1988) (cited p. 59, 67).

[29] Luc-Koenig, E, Morillon, C, and Vergès, J. *Etude Expérimentale et Théorique de l'Iode Atomique. Observation du Spectre d'Arc Infrarouge, Classification et Structure Hyperfine*. Physica Scripta **12**:4 199–219 (2007) (cited p. 59).

[30] Lias, SG and Liebman, JF. *"Ion Energetics Data" in NIST Chemistry WebBook, NIST Standard Reference Database Number 69, National Institute of Standards and Technology, Gaithersburg MD, 20899, http://webbook.nist.gov, (retrieved March 29, 2013).* Ed. by Linstrom, PJ and Mallard, WG (cited p. 59, 61).

[31] Chase Jr, MW, Davies, CA, Downey Jr, JR, Frurip, DJ, McDonald, RA, and Syverud, AN. *JANAF Thermochemical Tables 3rd Edition*. 1985 (cited p. 61).

[32] Hädrich, S, Hefter, S, Pfelzer, B, Doerk, T, and Jauernik, P. *Determination of the absolute Raman cross section of methyl*. Chemical Physics **256**: 83–86 (1996) (cited p. 63).

[33] Kramida, A, Ralchenko, Y, Reader, J, and NIST, AT. NIST Atomic Spectra Database *(ver. 5.0), [Online]. Available: http://physics.nist.gov/asd [August 23]*. National Institute of Standards and Technology, Gaithersburg, MD, 2013 (cited p. 63, 64).

[34] Amatatsu, Y, Yabushita, S, and Morokuma, K. *Full nine-dimensional ab initio potential energy surfaces and trajectory studies of A-band photodissociation dynamics: $CH_3I^* \rightarrow CH_3+I$, CH_3+I^*, and $CD_3I^* \rightarrow CD_3+I$, CD_3+I^**. The Journal of Chemical Physics **104**:24 9783–9794 (1996) (cited p. 63).

[35] Fan, YB, Randall, KL, and Donaldson, DJ. *Photochemistry of alkyl halide dimers*. The Journal of Chemical Physics **98**:6 4700 (1993) (cited p. 66).

[36] Vidma, KV, Baklanov, AV, Khvorostov, EB, Ishchenko, VN, Kochubei, Sa, Eppink, AeTJB, Chestakov, DA, and Parker, DH. *UV photodissociation of the van der*

Waals dimer (CH3I)2 revisited: pathways giving rise to ionic features. The Journal of Chemical Physics **122**:20 204301 (2005) (cited p. 66).

[37] Hagena, OF and Obert, W. *Cluster Formation in Expanding Supersonic Jets: Effect of Pressure, Temperature, Nozzle Size, and Test Gas*. The Journal of Chemical Physics **56**:5 1793–1802 (1972) (cited p. 67).

[38] Fan, H and Pratt, ST. *Photoionization of hot radicals: C_2H_5, n-C_3H_7, and i-C_3H_7*. The Journal of Chemical Physics **123**:20 204301 (2005) (cited p. 67).

[39] Berkowitz, J, Batson, C, and Goodman, G. *Photoionization of atomic iodine and atomic tellurium*. Physical Review A **24**:1 149–160 (1981) (cited p. 67).

[40] Fano, U. *Effects of Configuration Interaction on Intensities and Phase Shifts*. Physical Review **124**:6 1866–1878 (1961) (cited p. 67).

[41] Hess, WP, Kohler, SJ, Haugen, HK, and Leone, SR. *Application of an InGaAsP diode laser to probe photodissociation dynamics: I quantum yields from n- and i-C_3F_7I and CH_3I by laser gain vs absorption spectroscopy*. The Journal of Chemical Physics **84**:4 2143–2149 (1986) (cited p. 73).

4

Fragmentation dynamics of the ethyl bromide and ethyl iodide cations

Contents

4.1 Introduction

The study presented in this chapter focuses on the UV photodissociation of the ethyl bromide ($C_2H_5Br^+$) and ethyl iodide ($C_2H_5I^+$) cations, generated through VUV photoionization with 118.2 nm light. This work demonstrates a VMI study in which multiple fragmentation pathways have been investigated.

As discussed in Chapter 3, starting with the first demonstration of ion imaging by Chandler and Houston in 1987 [1], methyl iodide has proven to be a popular molecule for demonstrating new experimental imaging methods in chemical dynamics, and has been widely studied by velocity-map imaging (VMI) and related techniques [2–5]. Unsurprisingly, interest has extended to the photodynamics of other methyl halides (CH_3X), and there have

been several studies on CH_3Cl, CH_3Br, and CH_3I in both their neutral (see [6] and references therein) and cationic forms [7–13]; these earlier studies provide a valuable point of reference for the present investigations into the photofragmentation of two ethyl halide cations, $CH_3CH_2Br^+$ and $CH_3CH_2I^+$. In the case of neutral CH_3X, the primary dissociation channel following excitation at UV wavelengths is C−X bond fission to form a methyl radical with a ground or spin-orbit excited neutral halogen atom (henceforth represented as X and X*), CH_3 + X/X* (see [2, 3, 14–16] and references therein). C−X bond fission is also the dominant dissociation pathway following photoexcitation of CH_3X^+ cations at low photon energies ($\leq$ 4 eV), leading to production of a methyl cation with a halide co-fragment, CH_3^+ + X/X* [9, 17]. The alternative C−X bond fission channel, yielding CH_3 + X^+ fragments, opens at higher excitation energies [8]. The observed fragmentation behaviours of both neutral and cationic methyl halide species can be rationalised in terms of the excited electronic states accessible upon photoexcitation, and the way in which their respective potential energy surfaces (PESs) correlate with the available dissociation limits. The ground ($^2E_{3/2}$) and first excited ($^2E_{1/2}$) states of CH_3X^+ correlate with CH_3^+ + X products. In the case of CH_3Br^+, the next lowest lying dissociation limit involves CH_3^+ + Br* products, whereas for CH_3I^+, the CH_3 + I^+ limit lies below that for forming CH_3^+ + I* products [9–11], reflecting the larger spin-orbit splitting of the I atom.

Previous photoexcitation studies involving ethyl halide cations, $C_2H_5X^+$, have identified the analogous C−X bond fission channels and several additional pathways, each of which results in one singly charged species and one or more neutral fragments. In the cases of $C_2H_5Br^+$ and $C_2H_5I^+$, photoelectron-photoion coincidence (PEPICO) methods have been used to study fragmentation processes yielding $C_2H_5^+$ ions following excitation at energies $\leq$3 eV above the respective C−X bond dissociation limits [18, 19]. More recently, these same $C_2H_5X^+$ cations have been employed in determinations of the heat of formation of $C_2H_5^+$ [20, 21]. Tang et al. [22] have reported images of I^+ fragments formed following one-colour multiphoton excitation of C_2H_5I at wavelengths $\lambda \leq 266$ nm. These products were plausibly attributed to one-photon dissociation of $C_2H_5I^+$ cations that were themselves formed by two-photon excitation (via the A band) of C_2H_5I. Apart from this study, we are not aware of any other photofragment imaging studies of the ethyl iodide cation. Xu et al. [23] have reported a detailed photolysis study of $C_2H_5Br^+$ cations at one wavelength (355 nm), including data from time-of-flight (TOF) mass spectrometry and velocity-map imaging of the observed fragment ions. These authors also refute an earlier suggestion that $C_2H_5^+$ formation occurs via an ion-pair mechanism, following 118 nm excitation of C_2H_5Br [24].

In order to form a more complete picture of the dissociation dynamics of $C_2H_5X^+$, the photofragmentation processes of $C_2H_5Br^+$ and $C_2H_5I^+$ have been investigated as a function of UV excitation wavelength (in the range 236 nm - 355 nm) by means of velocity-map imaging. This study presents (i) a much more detailed analysis of the photofragmentation of $C_2H_5Br^+$ cations than reported hitherto, based on measurements with sufficient mass resolution to allow distinction between channels yielding, for example, $C_2H_5{}^+$, $C_2H_4{}^+$ and $C_2H_3{}^+$ fragment ions, and (ii) the first detailed investigation into the multiple photodissociation pathways available to $C_2H_5I^+$ cations.

4.2 Methods

4.2.1 Experimental

The velocity-map imaging experimental setup that was employed for the study presented in this chapter has been described in detail in Chapter 2. The molecular beam was generated by supersonic expansion of a gas mixture comprising $\sim$1% ethyl bromide (bromoethane, Sigma Aldrich, $>$ 99%) or ethyl iodide (iodoethane, Sigma Aldrich, $>$ 99%) seeded in 2 bar He (BOC, $>$ 99.9%). Within the ion optics assembly, the pulsed molecular beam was intersected orthogonally by the co-propagating 355 nm and 118 nm beams, the 355 nm laser having been used to generate the 118 nm light. The latter was employed to ionize the parent molecule, and in some of the experiments (termed 'one-laser') the 355 nm light was used to effect photolysis of the ethyl halide cation of interest. In all other 'two-laser' experiments, the dye laser was employed to produce UV photolysis light in the wavelength range 236 - 266 nm. In these experiments, a short time delay of $\sim$20 ns was employed between the ionization and photolysis pulses, whereas in the 355 nm photolysis studies, the two pulses were coincident in time. All laser beams were linearly polarised, with their respective electric field vectors, ε, aligned parallel to the plane of the imaging detector.

$C_2H_5Br^+$ and $C_2H_5I^+$ photolysis was investigated at 355 nm and 266 nm, with additional studies at 248 nm and 236 nm for $C_2H_5I^+$. Given the temporal coincidence of the 355 nm and 118 nm pulses, we recognise that the 'one-laser' images could, in principle, contain contributions from 355 nm photolysis of the neutral ethyl halide, followed by 118 nm ionization of the resulting fragments. However, no electronic states of either of the neutral parent molecules are accessed by one-photon absorption at 355 nm, and the absorption cross-sections at 355 nm are therefore negligible compared to those at 118 nm. Given this, and the evident similarities between the one and two-laser images, we concur with the conclusions

reached by Xu et al. [23] that the one-laser experiments do indeed probe 355 nm photolysis of $C_2H_5X^+$ cations formed by 118 nm photoionization, and include the results of such studies here along with those from the two-laser experiments. As noted earlier, $C_2H_5X^+$ photolysis yields one ionic and at least one neutral fragment. Neutral halogen atoms can be detected via resonance-enhanced multiphoton ionization (REMPI) [25–28] (see Section 2.8 for details). This method is employed here for detecting Br and Br* fragments, using wavelengths of 266.64 nm and 266.70 nm, resonant with the $4p^45p(^4P^o_{3/2})\leftarrow 4p^5(^2P^o_{3/2})$ and $4p^45p(^4S^o_{3/2})\leftarrow 4p^5(^2P^o_{1/2})$ two-photon transitions, respectively [28, 29].

The ions were velocity-map imaged onto the position-sensitive ion detector. To identify the ions formed in a given experiment, time-of-flight mass spectra (TOF-MS) were recorded. These revealed the arrival times for the fragment and parent ions, and showed no evidence of cluster formation. Images were then acquired for the arrival times corresponding to ions of interest. Images from photolysis at wavelengths other than 355 nm were obtained by successively recording the necessary 'two-laser' and 'one-laser' images, and subtracting accordingly. Total translation energies, E_T, are obtained by scaling the experimentally derived translational energy, E_t, of the monitored fragment ion ($Frag^+$) by the mass factor $m_{C_2H_5X}/(m_{C_2H_5X}\text{-}m_{Frag})$, where $m_{C_2H_5X}$ is the mass of the ethyl halide of interest, and m_{Frag} is the mass of the fragment ion.

4.2.2 Computational Methodology

The computational calculations presented in this chapter were carried out by Tolga Karsili of the Bristol Laser group. Here we give an account of the computational methods employed.

The Molpro 2010.1 [30] computational package was used to optimise the geometry of ground state $C_2H_5I^+$ and $C_2H_5Br^+$ cations using Møller-Plesset second order perturbation theory (MP2) with a cc-pVTZ Dunning's contracted correlation consistent basis set of triple-ζ quality, assigned to all atoms [31]. A 46 electron relativistic effective core potential [32] along with the larger cc-pVTZ-pp basis of Peterson et al. [33] was used to treat the I atom.

Rigid-body potential energy curves (PECs) along the RC−I and RC−Br coordinates were calculated for both cations with the rest of the nuclear framework fixed at the ground state MP2 equilibrium geometry. C_S symmetry (of the heavy atom chain) was maintained throughout these rigid-body scans. Spin-orbit (SO) free PECs were calculated using a state-averaged (SA) CASSCF reference wavefunction involving the first three $^2A'$ and $^2A''$ states,

and the first $^4A'$ and $^4A''$ states. The energies of all states were calculated using a complete active space with second order perturbation theory (CASPT2) and the SA-CASSCF reference wavefunction. An imaginary level shift of 0.5 a.u. was used in all CASPT2 calculations to encourage convergence and to eliminate intruder state effects. The same cc-pVTZ basis set as used for the geometry optimisations was used for both the SA-CASSCF and CASPT2 calculations, along with an active space consisting of 8 electrons in 6 orbitals (the two halogen centred p_x out-of-plane and p_y in-plane orbitals, the C−X bond centred σ and σ^* orbitals, an extra I-centred core orbital of a$'$ symmetry and an additional virtual a$'$ orbital).

Deriving the corresponding spin-orbit-coupled PECs proved challenging. Calculations using the above reference wavefunction and active space failed to converge at large RC−X, but satisfactory convergence at long range could be achieved with a reduced state averaging (just the three $^2A'$ and $^2A''$ states) and the same active space as above. Spin-orbit-coupled states were then calculated by evaluating $\hat{H}_{SO}$ in a basis of ψ_{elec}; these states are henceforth labelled using the extended irreducible representation including both spin-orbit-free and spin parts. CASPT2 (rather than CASSCF) energies of the spin-orbit-free states were used in the diagonalization of the SO coupling matrix in order to allow for some treatment of dynamic correlation. As shown below, such rigid body scans are useful in understanding the various parent cation to photoproduct correlations, but are of limited energetic value. In particular, the geometry of the ground state $C_2H_5^+$ cation is very different from that of the ethyl radical or of the ethyl group in the parent cation [34, 35], so the CASPT2 calculations substantially overestimate the C−X bond strength in the parent cation.

Possible transition states for HBr elimination from $C_2H_5Br^+$ were investigated using density functional theory (DFT) with the Becke 3-parameter exchange Lee Yang Parr (B3LYP) functional and the 6-311+(2*df,p*) Pople basis set within the Gaussian 09 computational package [36], and optimised using the QST2 algorithm.

4.3 Results & Discussion

The spin-orbit-free PECs for $C_2H_5I^+$ from the CASPT2 rigid-body scans are shown in Figure 4.1 (a). These provide a convenient starting point for understanding the various excited states of the ethyl halide cations, and their likely primary fragmentation mechanisms. In C_S symmetry, the 'ground state' is a $1^2A'/1^2A''$ pair (the analogue of the ^2E ground state of CH_3I^+), that asymptotically correlates with the $C_2H_5^+ + I$ fragmentation products. The

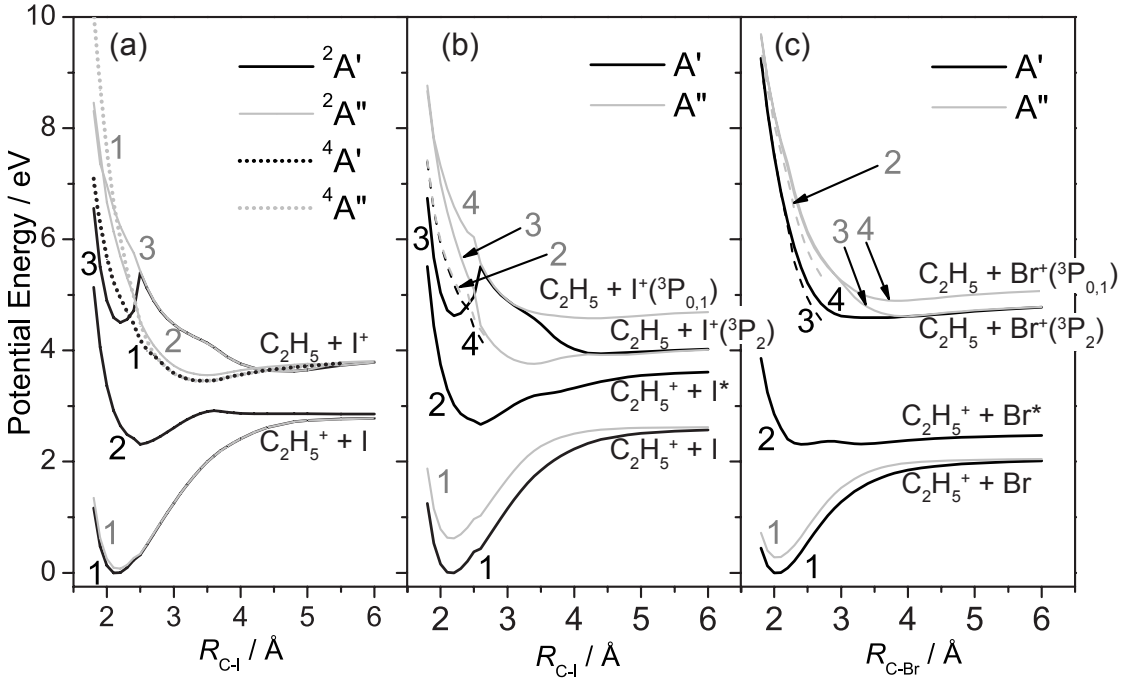

Figure 4.1: Calculated potential energy curves plotted as a function of C-X bond length for (a) $C_2H_5I^+$ (spin-orbit free), (b) $C_2H_5I^+$ (spin-orbit coupled), and (c) $C_2H_5Br^+$ (spin-orbit coupled). The energies shown are relative to that of the molecule in its ion ground state. Energies have been calculated every 0.1 Å along the C−X bond coordinate.

first excited ($2^2A'$) PEC that correlates to the same limit is attributable to a $p_{x/y} \leftarrow \sigma$ promotion in the vertical Franck-Condon (vFC) region. All of the various doublet and quartet spin-orbit-free PECs correlating to the $C_2H_5 + I^+$ limit appear to be (at best) very weakly bound. These states involve substantial contribution from $\sigma^* \leftarrow p_{x/y}$ promotion, and in the case of the long range part of the $3^2A'$ PEC, $\sigma^* \leftarrow \sigma$ promotion. The short range minimum in this $3^2A'$ PEC can be traced to electron excitation from the HOMO-2 orbital, (a non-bonding core orbital centred on the iodine atom that lies below the bonding σ orbital in energy) to the non-bonding $p_{x/y}$ orbitals. The analogous excitation is responsible for the reported well in the B^2E potential of CH_3I^+ [17].

The corresponding spin-orbit-coupled PECs for $C_2H_5I^+$ are shown in Figure 4.1 (b), while the analogous spin-orbit-coupled PECs for $C_2H_5Br^+$ are shown in Figure 4.1 (c). It should be noted that both of these figures are hybrids. Spin-orbit-coupled PECs derived using the smaller SA-CASSCF wavefunction are shown as solid lines. Calculations at short R_C − X ($\leq$2.7 Å) using the same state averaged wavefunction as for the spin-orbit-free PECs (i.e. including the two quartet spin-orbit-free states) reproduce the energies of these states to

within 0.1 eV and, in addition, place one extra A′ and A″ PEC within the energy range of interest. These additional spin-orbit-coupled PECs are shown as dashed lines in Figure 4.1 (b) and Figure 4.1 (c).

The spin-orbit-coupled PECs present a number of notable features. For example, the 'ground state' is split into 1A′ and 1A″ PECs, which, by analogy with CH_3X^+, have sometimes been termed $X_1{}^2E$ and $X_2{}^2E$ (see reference [37] and references therein), both of which asymptotically correlate with the ground state $C_2H_5{}^+ + X$ products; the 2A′ PECs correlate to $C_2H_5{}^+ + X^*$ products; and the degeneracy of the $C_2H_5 + X^+$ asymptote in Figure 4.1 (a) is lifted by the ^3P_J splitting of the X^+ ion. These various PECs will be considered as and when required in the subsequent discussion.

4.3.1 Ethyl halide cation formation

Figure 4.2 shows composite energy diagrams for (a) $C_2H_5Br^+$ and (b) $C_2H_5I^+$ up to a total energy of ∼16 eV above the zero-point level of the ground state neutral molecule. The displayed energies of the ground state cations are from mass-analysed threshold ionization spectroscopy: C_2H_5I: IE(X_1A') = 75406±5 cm^{-1}; IE(X_2A'') = 80110±5 $cm^{-}1$ [37] ; C_2H_5Br: IE(X_1A') = 83099±5 cm^{-1}; IE(X_2A'') = 85454±5 cm^{-1} [38] (these values have been converted to eV in Table 4.1). The right hand side of each diagram shows the energies of the various dissociation products, all of which can be estimated from available thermochemical data, i.e. ionization energies (IE), appearance energies (AE), dissociation energies (D) and enthalpies of formation ($\Delta_f H$) using appropriate Hess's Law cycles. The energies of the product channels, and the data used to determine these energies, are summarised in Table 4.1. Notwithstanding the rigidity constraints, we note that the present spin-orbit-coupled calculations succeed in reproducing the relative strengths of the $C-X^+$ bonds in $C_2H_5I^+$ and $C_2H_5Br^+$.

In the present work, the $C_2H_5X^+$ cations are formed by single -photon ionization of the corresponding neutral molecule. As shown by the horizontal dashed black line in each panel of Figure 4.2, one photon of 118 nm light provides an energy of 10.487 eV (84582 cm^{-1}), which comfortably exceeds the first ionization energy of both ethyl halides. Given the non-bonding nature of the $p_{x/y}$ highest occupied molecular orbital in C_2H_5X, Franck-Condon arguments would suggest that 118 nm photoionization of the jet-cooled parent molecule will favour formation of $C_2H_5X^+$ ions in the ground (v = 0) vibrational level of the X_1A' (and X_2A'') states. This is as suggested by Xu et al. [23], and is also consistent with the reported He I photoelectron spectrum [47, 48]. In the case of direct ionization all of the

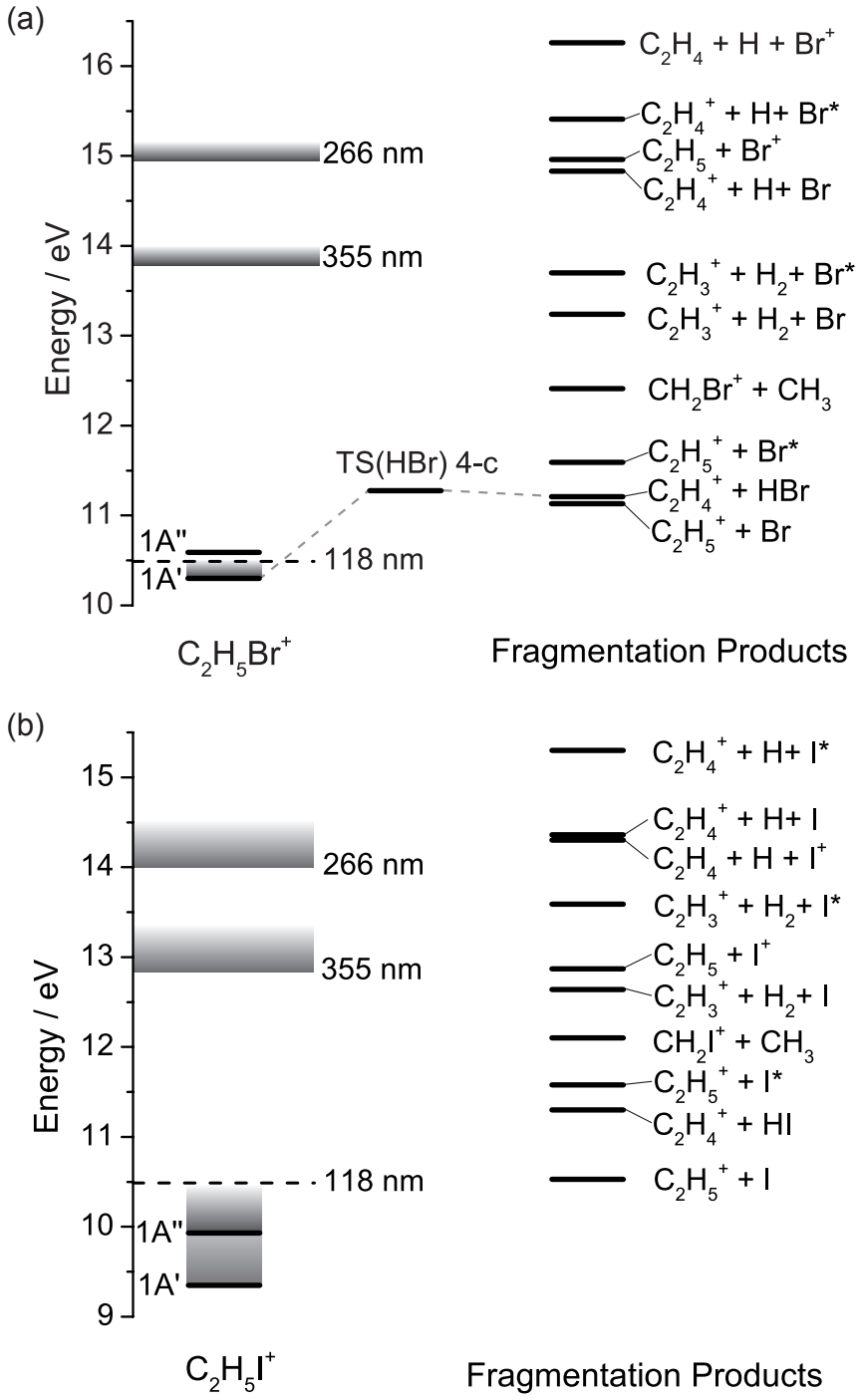

Figure 4.2: Energy level diagrams incorporating the lower lying dissociation pathways of (a) $C_2H_5Br^+$ and (b) $C_2H_5I^+$. The black horizontal levels indicate the electronic states of the $C_2H_5X^+$ parent ions. The black horizontal dashed lines indicate the energy of the 118 nm photon. The grey shaded regions, marked 355 nm and 266 nm, indicate approximately the region of the potential energy landscape to which the ions are excited on absorption of a UV photon of the wavelength indicated.

Table 4.1: Energies of the ground state $C_2H_5Br^+$ and $C_2H_5I^+$ parent cations and of the lower lying dissociation limits, referenced to the respective ground state neutral molecule in its zero-point vibrational level.

	ΔE / eV	Source
$C_2H_5Br \rightarrow$		
$C_2H_5Br^+$ $X_1A'(X_2A'')$	10.30 (10.59)	IE(C_2H_5Br) [38, 39]
$C_2H_5^+ + Br(Br^*)$	11.13 (11.59)	$AE_{0K}(C_2H_5^+)$ [21], S-O splitting [39]
$C_2H_3^+ + H_2 + Br(Br^*)$	13.24 (13.70)	$AE_{0K}(C_2H_5^+)$ [21], $D_0(C_2H_3^+-H_2)$ [40], S-O splitting [39]
$C_2H_4^+ + H + Br(Br^*)$	14.96 (15.41)	$AE_{0K}(C_2H_5^+)$ [21], IE(C_2H_5) [34], $D_0(C_2H_4-H)$ [40], IE(C_2H_4) [41], S-O splitting [39]
$C_2H_4^+ + HBr$	11.21	$AE_{0K}(C_2H_5^+)$ [21], IE(C_2H_5) [34], $D_0(C_2H_4-H)$ [40], IE(C_2H_4) [41], $D_0(H-Br)$ [42]
$Br^+ + C_2H_5$	14.83	$AE_{0K}(C_2H_5^+)$ [21], IE(C_2H_5) [34], IE(Br) [39]
$Br^+ + C_2H_4 + H$	16.26	$AE_{0K}(C_2H_5^+)$ [21], IE(C_2H_5) [34], IE(Br) [39], $D_0(C_2H_4-H)$ [40]
$CH_2Br^+ + CH_3$	12.41	$\Delta_f H_{0K}(CH_2Br^+)$ [43] $\Delta_f H_{0K}(CH_3)$ [44], $\Delta_f H_{0K}(C_2H_5Br)$[21]
$C_2H_5I \rightarrow$		
$C_2H_5I^+$ $X_1A'(X_2A'')$	9.35 (9.93)	IE(C_2H_5I)[37, 39]
$C_2H_5^+ + I(I^*)$	10.53 (11.48)	$AE_{0K}(C_2H_5^+)$ [21], S-O splitting [39]
$C_2H_3^+ + H_2 + I(I^*)$	12.64 (13.59)	$AE_{0K}(C_2H_5^+)$ [21], $D_0(C_2H_3^+-H_2)$ [40], S-O splitting [39]
$C_2H_4^+ + H + I(I^*)$	14.36 (15.30)	$AE_{0K}(C_2H_5^+)$ [21], IE(C_2H_5) [34], $D_0(C_2H_4-H)$ [40], IE(C_2H_4) [41], S-O splitting [39]
$C_2H_4^+ + HI$	11.30	$AE_{0K}(C_2H_5^+)$ [21], IE(C_2H_5) [34], $D_0(C_2H_4-H)$ [40], IE(C_2H_4) [41], $D_0(H-I)$ [45]
$C_2H_4 + HI^+$	11.18	$AE_{0K}(C_2H_5^+)$ [21], IE(C_2H_5) [34], $D_0(C_2H_4-H)$ [40], IE(HI) [46],
$I^+ + C_2H_5$	12.87	$AE_{0K}(C_2H_5^+)$ [21], IE(C_2H_5) [34], IE(I) [39]
$I^+ + C_2H_4 + H$	14.30	$AE_{0K}(C_2H_5^+)$ [21], IE(C_2H_5) [34], IE(I) [39], $D_0(C_2H_4-H)$ [40]
$CH_2I^+ + CH_3$	12.10	$\Delta_f H_{0K}(CH_2I^+)$ [43] $\Delta_f H_{0K}(CH_3)$ [44], $\Delta_f H_{0K}(C_2H_5I)$[21]

excess energy is released as electron kinetic energy, whereas, an autoionization pathway would result in all of the excess energy being retained as internal excitation of the $C_2H_5X^+$ cation. The shaded regions under the horizontal dashed black lines in Figure 4.2 indicate the possible spread of internal energies in the parent cations following VUV photoionization. The panels in Figure 4.2 also show two further sets of shaded horizontal regions that indicate the spread of energies of the $C_2H_5X^+$ cations that could be reached by UV excitation with either 355 nm or 266 nm light.

4.3.2 Photofragmentation pathways of the ethyl halide cations

4.3.2.1 Fragment ion identification

As noted in Section 2, $C_2H_5Br^+$ fragmentation has been investigated following photolysis at 355 nm and 266 nm, while $C_2H_5I^+$ fragmentation has been studied at 355 nm, 266 nm, 248 nm and 236 nm. As illustrated in Figure 4.3, the time-of-flight mass spectra (TOF-MS) obtained following UV photoexcitation of the ethyl halide cations reveal the formation of several different cation fragments, which can be identified by their mass-to-charge (*m/z*) ratios.

As shown in Figure 4.3 (a), UV photolysis of $C_2H_5Br^+$ mainly yields fragments in the mass range *m/z* 27 - 29. The ethyl ($C_2H_5^+$, *m/z* 29) and vinyl ($C_2H_3^+$, *m/z* 27) cation signals are slightly more intense than that of the ethene cation ($C_2H_4^+$, *m/z* 28) when exciting at 355 nm, at which wavelength we also detect a weak signal at *m/z* 93/95 attributable to the $CH_2{}^{79}Br^+$ / $CH_2{}^{81}Br^+$ cation (not shown here). These same fragment ions are detected when photolysing with 266 nm light, but with differing peak intensities. The vinyl cation is a major fragmentation product at this shorter wavelength, and the ethyl ion appears to be a minor product. Additional fragment masses are also observed at this wavelength, including the acetylene (or vinylidene) cation ($C_2H_2^+$, *m/z* 26) and CH_2^+ (*m/z* 14).

In the TOF-MS obtained following 355 nm photolysis of $C_2H_5I^+$, Figure 4.3 (b), the ethyl cation (*m/z* 29) dominates. Smaller signals are also observed at *m/z* 26 ($C_2H_2^+$), 27 ($C_2H_3^+$), 28 ($C_2H_4^+$), 127 (I^+) and 141 (CH_2I^+, not shown here). $C_2H_3^+$ and I^+ signals dominate the TOF mass spectra measured at shorter photolysis wavelengths (e.g. 266 nm), with the ethyl cation ($C_2H_5^+$) contributing little to the spectrum. The shoulder on the high mass side of the I^+ peak most likely corresponds to HI^+ (*m/z* 128).

To summarise, the TOF-MS presented here indicate formation of $C_2H_3^+$, $C_2H_4^+$, $C_2H_5^+$ and CH_2X^+ products following UV photolysis of both $C_2H_5Br^+$ and $C_2H_5I^+$ cations, and,

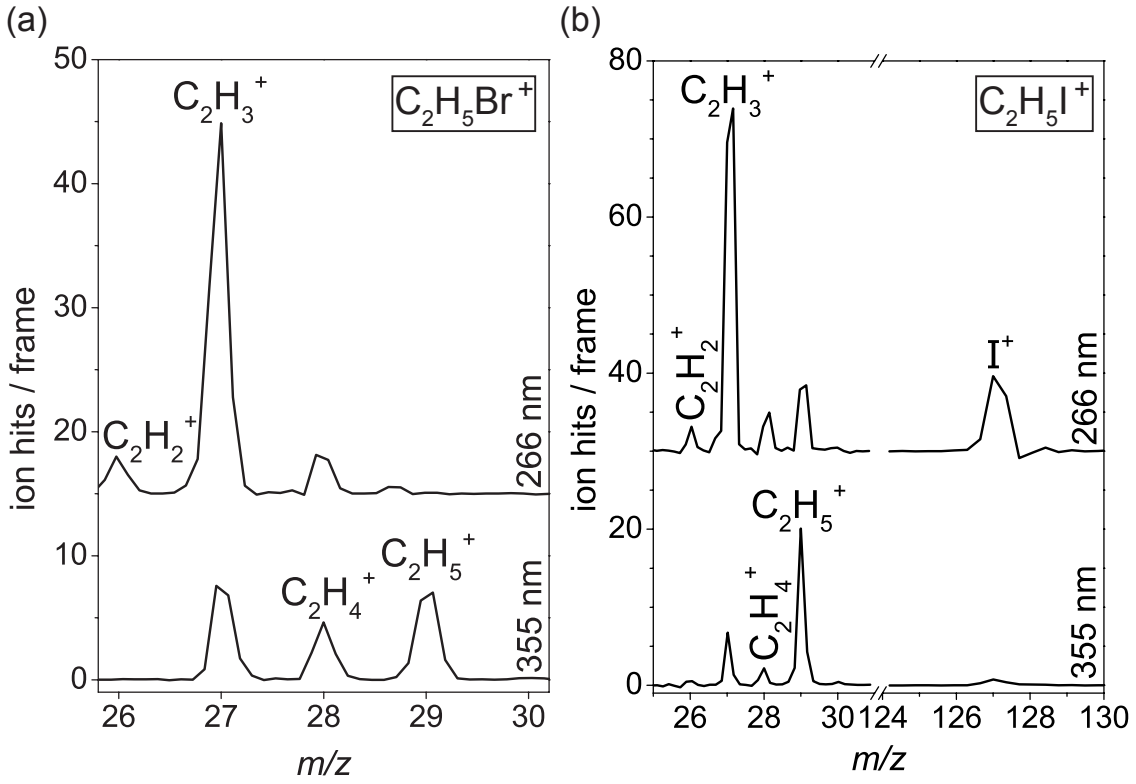

Figure 4.3: Time-of-flight mass spectra for the 355 nm and 266 nm photolysis of (a) $C_2H_5Br^+$, and (b) $C_2H_5I^+$. The 266 nm traces for $C_2H_5Br^+$ and $C_2H_5I^+$ have been shifted vertically by 15 and 30 ion hits, respectively.

in the latter case, I^+ is also observed. Energetic considerations indicate that the weak $C_2H_2{}^+$ and $CH_2{}^+$ fragment ion signals must arise from multiphoton excitations involving at least one further UV photon. In this study, we focus on the one-(UV)-photon pathways and, while the possible influence of multiphoton fragmentations on the measured primary ion signals must be considered, we will not attempt to unravel mechanistic details of the $C_2H_2{}^+$ and $CH_2{}^+$ formation processes. One-photon fragmentation channels consistent with the observed fragment ions and energetic considerations will now be considered.

4.3.2.2 Energetically accessible photofragmentation pathways

The following primary fragmentation channels are accessible to both $C_2H_5Br^+$ and $C_2H_5I^+$ cations within the range of photolysis wavelengths investigated.

1. carbon-halogen (C−X) bond cleavage

$$C_2H_5X^+ + h\nu \rightarrow C_2H_5^+ + X \quad (\text{or } X^*)$$

2. ethene cation production

   (a) $$C_2H_5X^+ + h\nu \rightarrow C_2H_4{}^+ + HX$$

   (b) $$C_2H_5X^+ + h\nu \rightarrow C_2H_4{}^+ + H + X$$

3. vinyl cation formation

$$C_2H_5X^+ + h\nu \rightarrow C_2H_3^+ + H_2 + X \quad (\text{or } X^*)$$

4. carbon-carbon (C−C) bond cleavage

$$C_2H_5X^+ + h\nu \rightarrow CH_2X^+ + CH_3$$

As shown in Figure 4.2, a fifth dissociation channel, yielding I^+ products, is accessible in the case of $C_2H_5I^+$:

5. C−X bond cleavage to produce the X^+ cation

$$C_2H_5I^+ + h\nu \rightarrow C_2H_5 + I^+$$

Channel 1, which is observed for both $C_2H_5Br^+$ and $C_2H_5I^+$, involves C−X bond cleavage to yield an ethyl cation along with a neutral halogen atom, in either its ground (X) or spin-orbit excited (X^*) state. The spin-orbit excited states lie at energies of 0.457 eV (Br^*) and 0.943 eV (I^*) above the respective ground states [39]. Channel 5 also involves C−X bond cleavage, but yields an X^+ cation along with a neutral ethyl radical. The threshold energy for this process in the case of $C_2H_5Br^+$ (∼4.5 eV above the ground state cation) is too high for this channel to be observed in the current study. The corresponding C−I bond fission in $C_2H_5I^+$ has a lower threshold energy (∼3.6 eV/∼2.9 eV above the X_1A'/X_2A'' states of the $C_2H_5I^+$ parent ion). As shown in Figure 4.1, several dissociative states of $C_2H_5I^+$ correlate with different spin-orbit components of the $C_2H_5 + I^+(^3P_J)$ limit, however in the present study it is not possible to distinguish between these limits.

There are two possible channels leading to $C_2H_4{}^+$ product formation. The first, Channel 2(a), involves concerted elimination of a neutral HX molecule. This is the lowest thermochemical threshold for forming $C_2H_4{}^+$, lying between the $C_2H_5{}^+$ + X/X^* thresholds for both $C_2H_5Br^+$ and $C_2H_5I^+$ (Figure 4.2, and Table 4.1). This product channel is accessible for both $C_2H_5X^+$ cations at the energies investigated. Such a process might feasibly occur from an excited state or, after internal conversion, on the ground state potential energy surface (PES). An alternative sequential loss of X and H atoms, Channel 2(b), can also be

envisaged, e.g. primary C−X bond fission, followed by subsequent H atom loss from a highly internally excited $C_2H_5^+$ co-fragment. However, reference to Figure 4.2 suggests that such a one-photon induced process might only contribute at the very shortest excitation wavelengths. We note that, in addition to the $C_2H_4^+$ + HX channel, C_2H_4 + HX^+ products (with the charge residing on the HX rather than the C_2H_4 fragment) might also arise; indeed, Irsa [49] identified an appearance threshold of 11.7 eV for HI^+ products in an electron impact excitation study of C_2H_5I. As noted previously, the weak shoulder on the high *m/z* side of the I^+ peak in the TOF mass spectrum measured following UV photolysis of $C_2H_5I^+$ may indicate some contribution from this process, but this channel is not considered further in this study.

Vinyl cation production, Channel 3, could either arise via a stepwise process or a concerted three-body fragmentation mechanism. The former of these, which seems more likely, would involve loss of H_2 from highly internally excited $C_2H_5^+$ cations produced via Channel 1.

C−C bond cleavage, Channel 4, was not considered in the earlier VMI study of $C_2H_5Br^+$ photolysis [23], however the present study shows evidence of CH_2X^+ ion formation following UV photolysis of both $C_2H_5Br^+$ and $C_2H_5I^+$. Such a finding is fully consistent with the threshold energies of ∼2.1 eV and ∼2.8 eV (defined relative to the ground state parent cation) for C−C bond fission in $C_2H_5Br^+$ and $C_2H_5I^+$, respectively.

The various fragment ion yields, which provide a measure of the branching ratios into each of the channels listed above, are seen to depend both on the choice of parent ion and on the photolysis wavelength. In principle, relative branching ratios can be obtained directly from the TOF-MS, but such analyses are complicated by possible unimolecular decay of internally excited primary fragments (e.g. $C_2H_5^+$) and/or unintended multiphoton absorptions. Such complications will arguably be least problematic when using longer-wavelength (355 nm) photolysis photons, and it is instructive to compare the present findings for $C_2H_5Br^+$ with those from the earlier VMI study [23]. The present study finds the following relative ion yields for C_2H_5Br of $C_2H_5^+$: $C_2H_3^+$: $C_2H_4^+$: CH_2Br^+ = 0.41 : 0.38 : 0.20 : 0.01, i.e. the major fragmentation pathways yield $C_2H_5^+$ and $C_2H_3^+$ cations (each accounting for ∼40% of the total fragment ion signal), with $C_2H_4^+$ production accounting for most of the remainder. These observations agree with those of Xu *et al.* [23]. $CH_2Br^+ + CH_3$ products clearly constitute a minor channel, missed in the earlier study [23], but observed here most probably as a result of the enhanced detection sensitivity available in the present experiment.

The relative fragment ion yields arising in the 355 nm photolysis of $C_2H_5I^+$ cations formed by 118 nm photoionization of C_2H_5I are noticeably different from those for C_2H_5Br, i.e. $C_2H_5^+ : C_2H_3^+ : C_2H_4^+ : CH_2I^+ : I^+ = 0.62 : 0.19 : 0.06 : 0.02 : 0.12$. The $C_2H_5^+ +$ I channel makes a far greater contribution to the total fragment ion yield, and the relative yield of $C_2H_3^+$ ions is much reduced in comparison with $C_2H_5Br^+$. C−C bond fission (yielding $CH_2I^+ + CH_3$ fragments) is again a minor process, as is $C_2H_4^+$ ion formation. In contrast to $C_2H_5Br^+$, the $C_2H_5 + I^+$ Channel 5 is accessible upon 355 nm photolysis of $C_2H_5I^+$, and is seen to contribute >10% of the total fragment ion signal.

Velocity-map images were recorded for all of the more abundant fragment ions formed following photolysis of both parent ions at the various UV wavelengths studied. Illustrative data sets are displayed in Figure 4.4 and Figure 4.5 for $C_2H_5Br^+$ and $C_2H_5I^+$, respectively. Analysis of the images allows determination of the velocity distribution of each fragment ion, and thus the distribution of total translational energies, P(E_T), associated with a given fragmentation channel. These E_T distributions resulting from photolysis of $C_2H_5Br^+$ and $C_2H_5I^+$ are shown in Figure 4.4 and Figure 4.5, respectively. The associated (velocity-dependent) spatial anisotropy parameters, β, which characterise the angular scattering distribution, can also be determined from the ion images. The data acquired from velocity-map imaging the nascent fragments is discussed in light of the available electronic structure calculations.

4.3.2.3 Photodissociation dynamics of $C_2H_5Br^+$

The P(E_T) distributions derived from analysis of the $C_2H_5^+$ images from photolysis of $C_2H_5Br^+$ with 266 nm and 355 nm light are displayed as blue and green traces, respectively, in Figure 4.4 (a). For each of the photolysis wavelengths studied, Table 4.2 lists:

1. The maximum total translational energy of the fragmentation products, E_T(max). This is calculated as the residual energy from the UV photon not consumed in bond breaking or formation of electronically excited fragments. Two values are quoted in the table: E_T(max), calculated on the basis that the UV photon excites parent cations from their $X_1A'(v=0)$ electronic and vibrational ground state; and E_T(MAX), where we assume UV excitation of parent cations formed with the maximum possible internal energy allowed in a 118 nm photoionization process.

2. The mean fraction $\langle f_T \rangle$ of the available energy, E_T(max) (or E_T(MAX)), released into translation of the fragmentation products. These values have been quoted to two decimal places (2 d.p.) in order to reflect the confidence in $\langle f_T \rangle$.

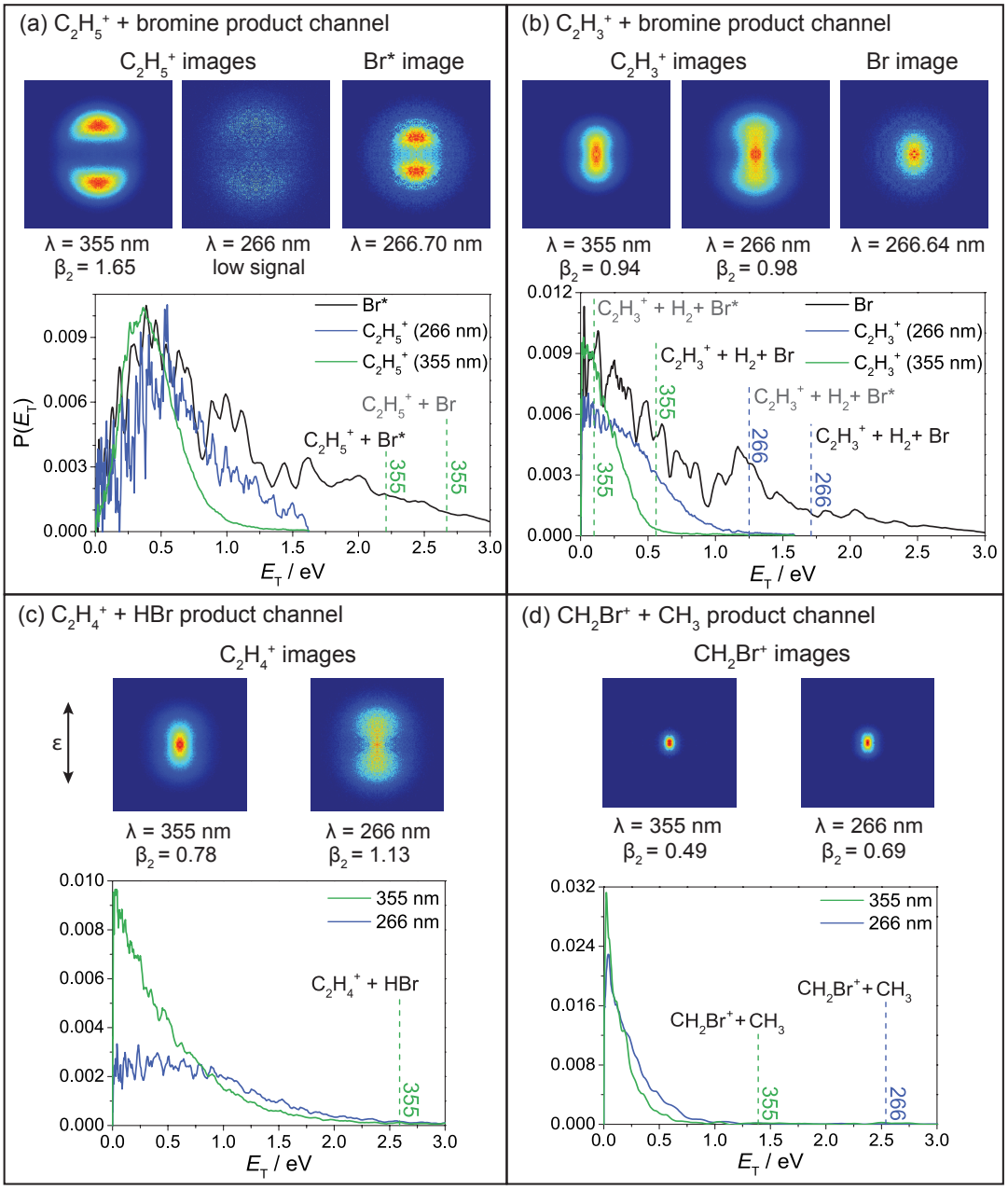

Figure 4.4: Total translational energy (E_T) distributions for the accessible product channels of $C_2H_5Br^+$ photolysis: (a) $C_2H_5^+$ + Br/Br*, (b) $C_2H_3^+$ + H_2 + Br, (c) $C_2H_4^+$ + HBr; and (d) CH_2Br^+ + CH_3. The P(E_T) distributions derived from the velocity-map images of the ions produced following photolysis of $C_2H_5Br^+$ at 355 nm and 266 nm are displayed in green and blue, respectively. The vertical dashed lines indicate the maximum translational energy E_T(max) of the photofragments following photolysis at 355 nm (green) and 266 nm (blue), assuming that the UV photon excites parent cations from their $X_1A'(v=0)$ electronic and vibrational ground state. The E_T distributions for Br* and Br, detected using (2+1) REMPI, are plotted in black alongside the $C_2H_5^+$ and $C_2H_3^+$ data, in (a) and (b), respectively. The velocity-map images shown have been symmetrized for presentation purposes only.

Table 4.2: Energetic parameters for the photofragmentation pathways of $C_2H_5Br^+$: the maximum total translational energy, E_T(max); and the average fraction $\langle f_T \rangle$ of E_T(max) that goes into product translational energy (to 2 d.p.).

Fragmentation products	λ / nm	E_T(max) (E_T(MAX)) / eV	$\langle f_T \rangle$
$C_2H_5^+ + Br$	355	2.67 (2.85)	0.14 (0.13)
	266	3.36 (3.55)	0.14 (0.13)
$C_2H_5^+ + Br^*$	355	2.21 (2.40)	0.17 (0.16)
	266	3.82 (4.01)	0.16 (0.15)
$C_2H_3^+ + H_2 + Br$	355	0.56 (0.74)	0.22 (0.17)
	266	1.71 (1.90)	0.14 (0.12)
$C_2H_3^+ + H_2 + Br^*$	355	0.10 (0.29)	- (0.43)
	266	1.25 (1.44)	0.19 (0.16)
$C_2H_4^+ + H + Br$	355	- (-)	-
	266	- (0.18)	-
$C_2H_4^+ + HBr$	355	2.59 (2.77)	0.12 (0.11)
	266	3.74 (3.93)	0.07 (0.07)
$Br^+ + C_2H_5$	355	- (-)	not observed
	266	0.12 (0.31)	
$CH_2Br^+ + CH_3$	355	1.39 (1.57)	0.10 (0.09)
	266	2.54 (2.73)	0.07 (0.06)

The values in Table 4.2 can be interpreted by considering the various available pathways to forming the observed dissociation products. 355 nm and 266 nm photoexcitation are likely to populate the $2A'$ excited state (see Figure 4.1 (c)). The available data implies that this state can decay in (at least) two different ways.

The potential energy curves shown in Figure 4.1 (c) suggest that the $2A'$ excited state is dissociative along the C−Br stretch coordinate, and correlates to $C_2H_5^+ + Br^*$ products. This prediction is supported by the measured $C_2H_5^+$ images, shown in Figure 4.4 (a), which reveal an anisotropic E_T distribution peaking at $E_T > 0$, consistent with direct dissociation from an excited state. The near-limiting parallel recoil anisotropy ($\beta \sim 1.7$), which is consistent with that measured by Xu *et al.* [23], implies that the $C_2H_5^+$ products recoil along an axis parallel to the ε vector of the UV radiation. Given axial recoil, this implies that the transition dipole moment is directed along the breaking bond. This suggests that, as in the corresponding neutral C_2H_5Br dissociation, the parent excitation gains transition probability by mixing with the higher energy ($3A'$) state, which has substantial $\sigma^* \leftarrow \sigma$

character [50].

As shown in Table 4.2, when photolysing with 355 nm or 266 nm light, whether we assume that $C_2H_5^+$ is produced with a Br or Br* co-fragment, the mean translational energy, $\langle E_T \rangle$, is only ∼15 % of E_T(max). This implies that the cation fragments must be formed with substantial internal excitation, as noted also by Xu et al. [23]. The internal excitation reflects the very different equilibrium geometry of the 2A′ and the X_1A'/X_2A'' states in coordinates other than the C−Br stretch coordinate plotted in Figure 4.1. This can be expected to facilitate efficient internal conversion through conical intersections to these latter states. Such processes are likely to occur on a timescale comparable to that for excited state C−Br bond fission. Such pathways are expected to yield highly vibrationally excited $C_2H_5Br^+$ ions, at least some of which (see Figure 4.1) will evolve towards ground state $C_2H_5^+$ + Br products.

Additional imaging studies of the Br/Br* atoms formed following photoexcitation of $C_2H_5Br^+$ at wavelengths ∼266.6 nm (chosen to enable (2+1) REMPI detection of these atoms) were performed in an effort to determine the spin-orbit state of the bromine atoms accompanying the $C_2H_5^+$ products. It should be noted that these experiments are complicated due to the fact that 118 nm, 355 nm and 266.6 nm photons all pass through the interaction region, and that both of the latter wavelengths can photolyse $C_2H_5Br^+$ cations and thus contribute to the measured signal. The measured images are shown in Figure 4.4. The intense inner lobes of the Br* image, attributable to 355 nm photolysis of $C_2H_5Br^+$, display similar recoil anisotropy to that of the $C_2H_5^+$ fragments. The associated P(E_T) distribution, derived assuming $C_2H_5^+$ co-fragments, is shown as the black line in Figure 4.4 (a). It is dominated by a broad peak centred at E_T ∼0.5 eV, and matches well with the P(E_T) distributions obtained from the $C_2H_5^+$ images measured at both 355 nm and at 266 nm. We take this to indicate that the $C_2H_5^+$ fragments are formed with Br* co-products via direct dissociation from the 2A' state of $C_2H_5Br^+$.[1]

The P(E_T) distribution obtained from the ground state Br image, shown in black in Figure 4.4 (b), peaks at $E_T < 0.1$ eV and does not compare well with the P(E_T) distribution of the $C_2H_5^+$ fragments. Thus, though we cannot totally exclude $C_2H_5^+$ + Br production, comparison of the P(E_T) distributions extracted from the $C_2H_5^+$ images recorded at

[1]The feature centred at E_T ∼1 eV in Figure 4.4 (a) arises from Br* products formed via photolysis of neutral (rather than cationic) ethyl bromide, and is not removed completely when subtracting the '266 nm only' signal. This has been verified through VMI studies of the neutral dissociation products in separate experiments - as reported also by Tang et al. [26]. This feature is henceforth ignored when discussing the cation fragmentation.

355 nm and at 266 nm and from the Br/Br* images measured at the latter wavelength implies that the majority of the detected $C_2H_5^+$ ions are formed in conjunction with a Br* co-fragment.[2]

The relevant images in Figure 4.4 (b) suggest that the $C_2H_3^+$ products are more likely to be formed in association with Br than with Br* co-fragments. This view is reinforced by the evident similarity of the P(E_T) distributions derived from the $C_2H_3^+$ and Br images, also shown in Figure 4.4 (b). Given the lightness of the H_2 fragment, this similarity is expected if the former arise from secondary decay of highly vibrationally excited primary $C_2H_5^+$ fragments. This would be consistent with a dynamical mechanism involving rapid radiationless transfer to the ground state PES (from the initially excited state) and dissociation along the C−X bond to yield $C_2H_5^+$ + Br, the former of which undergoes H_2 loss. Further support for this interpretation comes from examining the calculated maximum translational energies for the $C_2H_3^+$ + H_2 + Br and $C_2H_3^+$ + H_2 + Br* products (assuming dissociation following excitation from the zero-point level of both spin-orbit states of the parent cation) illustrated in Figure 4.4 (b) by two pairs of dashed vertical lines. The P(E_T) distribution derived from the $C_2H_3^+$ image clearly extends beyond the maximum translational energy predicted for the $C_2H_3^+ + H_2 + Br^*$ channel following 355 nm photolysis, but tails off before the $C_2H_3^+ + H_2 + Br$ product limit. Therfore, though we cannot completely exclude dissociation to $C_2H_3^+ + H_2 + Br^*$ products, we conclude that most of the $C_2H_3^+$ products are formed via a sequential three-body dissociation yielding H_2 and ground state Br atom co-fragments.

Figure 4.4 (c) shows the images of the $C_2H_4^+$ fragment ions formed following photolysis with 355 nm and 266 nm light. These products could also arise via a two or three body dissociation process (i.e. HBr elimination or loss of H and Br atoms). P(E_T) distributions derived from the images are also shown in Figure 4.4 (c), and the experimentally derived $\langle f_T \rangle$ values are shown in Table 4.2 along with the E_T(max) values calculated for the two possible $C_2H_4^+$ product forming channels. As Figure 4.2 (a) shows, a 355 nm photon provides insufficient energy for the three-body dissociation (yielding H and Br co-fragments). Though energetically possible when exciting at 266 nm, the P(E_T) distribution derived from the $C_2H_4^+$ images measured at this wavelength extends well beyond the maximum translation energy for the three body dissociation process. Thus the presence of $C_2H_4^+$ ions indicates formation of HBr co-fragments, though these have not been directly detected. The P(E_T) distributions derived in the present work both peak at or near zero, implying

[2]Again the distribution of interest is contaminated by a '266 nm only' feature at E_T ∼1.25 eV, which we have ignored in our analysis.

high levels of internal excitation in the products, ∼90 % of E_T(max), and consistent with unimolecular decay on the ground state PES. The $C_2H_4^+$ images are anisotropic, with β ∼0.8 for dissociation at 355 nm. This suggests that, as with $C_2H_3^+$ formation, the process of radiationless transfer to the ground state PES and subsequent HBr elimination occurs much faster than would be predicted by any purely statistical description of the dissociation process. While HBr elimination on the ground state PES could potentially occur via either a three-centre or a four-centre transition state, our DFT calculations have succeeded in locating a four-centre transition state lying ∼1.05 eV above the potential minimum of the ground state cation. Previous studies of this fragmentation process in the case of selectively deuterated ethyl bromide cations concluded that the process can occur via a three-centre and a four-centre species, with the four-centre transition state yielding a faster rate than the three-centre species as a result of a lower barrier to formation of the former [23].

The final fragmentation channel observed here, Channel 4, involves C−C bond fission and formation of CH_2Br^+ + CH_3 products. The CH_2Br^+ images measured following photolysis with 355 nm and 266 nm light, shown in Figure 4.4 (d), are small and mildly anisotropic (β ∼0.5). The P(E_T) distributions derived from these images peak at zero, implying that the CH_2Br^+ + CH_3 products are also formed with high levels of internal excitation. Once again, this behaviour is understandable, qualitatively at least, in terms of non-statistical dissociation of internally 'hot' ground state molecules formed following radiationless transfer from the initially excited state after some pre-extension of the C−Br bond.

4.3.2.4 Photodissociation dynamics of $C_2H_5I^+$

The images of the various fragment ions resulting from $C_2H_5I^+$ photolysis (Figure 4.5) imply similarities, but also some differences between the fragmentation dynamics of $C_2H_5I^+$ and $C_2H_5Br^+$ following photoexcitation at the wavelengths studied. The spin-orbit-coupled potential energy curves shown in Figure 4.1 (b), and the energy level diagram shown in Figure 4.2 (b), suggest that excited states correlating not just to $C_2H_5^+$ but also I^+ products should be energetically accessible at all of the UV wavelengths of present interest. This is confirmed by the fragment ion TOF-MS shown in Figure 4.3 (b), and by the images shown in Figure 4.5 (a) and (b). As in the case of $C_2H_5Br^+$, we consider the various fragmentation channels in turn. E_T(max) (E_T(MAX)) and $\langle f_T \rangle$ values for the various photofragmentation channels are listed in Table 4.3.

The $C_2H_5^+$ image obtained when exciting C_2H_5I with the 118/355 nm photon combination is obviously very different from that obtained following excitation of C_2H_5Br in the same

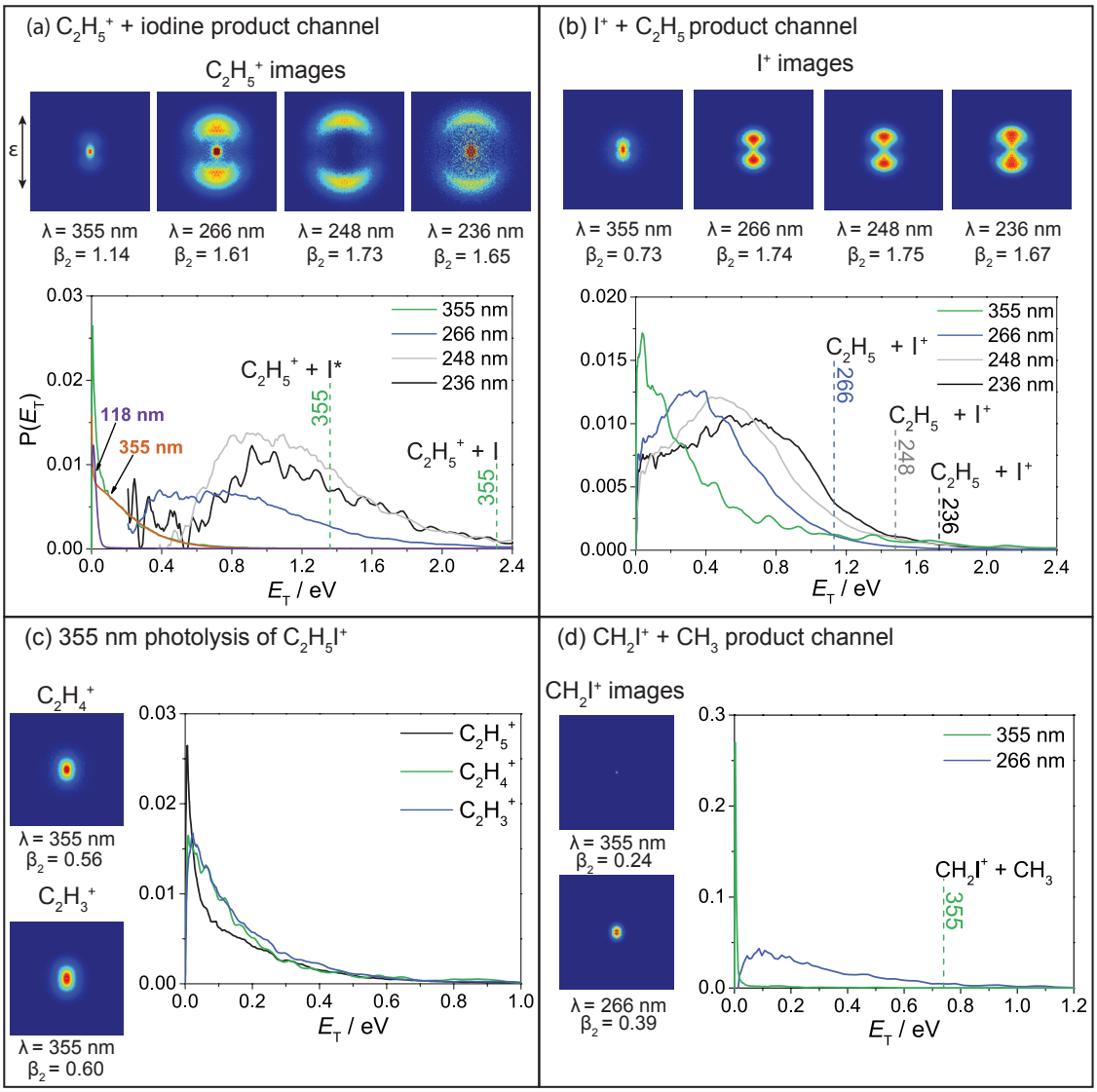

Figure 4.5: Total translational energy P(E_T) distributions for the accessible product channels of $C_2H_5I^+$ photolysis: (a) $C_2H_5^+$ + I/I* at all four photolysis wavelengths; (b) C_2H_5 + I^+ at all four photolysis wavelengths; (c) $C_2H_5^+$ + I/I* (black), $C_2H_4^+$ + HI (green) and $C_2H_3^+$ + H_2 + I (blue) at 355 nm; and (d) CH_2I^+ + CH_3 at 355nm and 266 nm. The maximum translational energy E_T(max) (assuming that the UV photon excites parent cations from their $X_1A'(v{=}0)$ electronic and vibrational ground state) are indicated by vertical dashed lines in the cases where they fall within the ET scale shown. The velocity-map images shown have been symmetrized for presentation purposes only.

Table 4.3: Energetic parameters for the photofragmentation pathways of $C_2H_5I^+$: the maximum total translational energy, E_T(max); and the average fraction $\langle f_T \rangle$ of E_T(max) that goes into product translational energy (to 2 d.p.).

Fragmentation products	λ / nm	E_T(max) (E_T(MAX)) / eV	$\langle f_T \rangle$
$C_2H_5^+ + I$	355	2.31 (3.45)	0.09 (0.06)
	266	3.47 (4.61)	0.29 (0.21)
	248	3.82 (4.96)	0.30 (0.23)
	236	4.07 (5.21)	0.30 (0.23)
$C_2H_5^+ + I^*$	355	1.36 (2.50)	0.15 (0.08)
	266	2.52 (3.66)	0.39 (0.27)
	248	2.87 (4.01)	0.39 (0.28)
	236	3.12 (4.26)	0.39 (0.29)
$C_2H_3^+ + H_2 + I$	355	0.20 (1.34)	0.62 (0.09)
	266	1.36 (2.50)	0.13 (0.07)
	248	1.71 (2.85)	0.12 (0.07)
	236	1.96 (3.10)	0.11 (0.07)
$C_2H_3^+ + H_2 + I^*$	355	- (0.39)	- (0.32)
	266	0.41 (1.55)	0.44 (0.12)
	248	0.76 (1.90)	0.26 (0.11)
	236	1.01 (2.15)	0.21 (0.10)
$C_2H_4^+ + H + I$	355	- (-)	-
	266	- (0.78)	- (0.26)
	248	- (1.13)	-(0.23)
	236	0.24 (1.38)	- (0.20)
$C_2H_4^+ + HI$	355	1.54 (2.68)	0.09 (0.05)
	266	2.70 (3.84)	0.08 (0.05
	248	3.05 (4.19	0.09 (0.06)
	236	3.30 (4.44)	0.08 (0.06)
$I^+ + C_2H_5$	355	- (1.11)	1 (0.23)
	266	1.13 (2.27)	0.30 (0.15)
	248	1.48 (2.62)	0.34 (0.19)
	236	1.73 (2.87)	0.35 (0.21)
$CH_2I^+ + CH_3$	355	0.74 (1.88)	0.07 (0.03)
	266	1.90 (3.04)	0.23 (0.14)
	248	2.25 (3.39)	not observed
	236	2.50 (3.64)	

way. The radius of the image from C_2H_5I is small, and the associated P(E_T) distribution, shown in Figure 4.5 (a), peaks at zero and extends to E_T ~0.8 eV. In the case of C_2H_5I, a 118 nm photon alone provides just sufficient energy to cause dissociative ionization to $C_2H_5^+$ + I products. This process is assumed to be the source of the central spot in the $C_2H_5^+$ image and the associated spike at $E_T = 0$ in the P(E_T) distribution. 118 nm excitation also leads to parent ion formation, however, and the tail of the P(E_T) distribution extending to E_T ~0.8 eV is attributed to 355 nm photolysis of these $C_2H_5I^+$ ions. An attempt has been made to separate these two contributions by fitting the radial distribution to a sum of two Gaussians, and the resulting fitted contributions from 118 nm dissociative ionization and 355 nm photolysis are shown in purple and orange, respectively, in Figure 4.5 (a). A translational energy of E_T ~0.8 eV is far below the maximum value permitted by energy conservation, even in the case that all of the $C_2H_5I^+$ parent ions are formed in the zero-point level of the ground ($1A'$) state and the atomic co-fragments are formed in the I^* state. In practice, 118 nm ionization can be expected to form parent ions in the $1A''$ excited state also, and there is no a priori reason to exclude formation of ground state I atoms, so it is clear that these $C_2H_5^+$ ions are formed with high levels of internal excitation, reflected in the low $\langle f_T \rangle$ values listed for the $C_2H_5^+$ formation channels in Table 4.3. Extracting a reliable β-parameter is hampered by the small size of the image, but our best analysis suggests $\beta \sim 1.2$.

This data should be contrasted with the $C_2H_5^+$ images recorded at 266, 248 and 236 nm, also shown in Figure 4.5 (a), all of which show an anisotropic ring of fast products (characterised by $\beta \sim 1.6$-1.7) and P(E_T) distributions that peak progressively further from $E_T = 0$.[3] Recalling Figure 4.1, the most plausible explanation for the anisotropic $C_2H_5^+$ product yield is initial excitation to the $3A'$ and/or $4A'$ ($\sigma\sigma^*$) states, followed either by prompt adiabatic dissociation to C_2H_5 + I^+ products, or diabatic dissociation via radiationless transfer through a conical intersection to $C_2H_5^+$ + I^* products. The images unfortunately do not allow us to identify the spin-orbit state of the iodine co-fragment, and attempts to use (2+1) REMPI to detect I/I^* products from 266 nm photolysis of $C_2H_5I^+$ were thwarted by the large 266 nm laser induced I^+ yield.

Two other features of these two-laser images merit note. As in the case of $C_2H_5Br^+$, the P(E_T) distributions peak well below the maximum E_T value allowed by energy conservation, implying substantial internal excitation of the fragment cation. This is consistent with the large change in equilibrium geometry of the C_2H_5 moiety on dissociation. Secondly,

[3]The central spot in some of these images is due to imperfect subtraction of the dissociative ionization signal from the 118/355 nm laser and is not considered further.

the P(E_T) distribution determined at 266 nm, shown in blue in Figure 4.5 (a), appears bimodal. The TOF-MS recorded when exciting at this wavelength (Figure 4.3 (b)) shows a substantial I^+ yield, implying a major role for the $C_2H_5 + I^+$ fragmentation channel. Tang et al. [22] have demonstrated efficient (1+1)REMPI of neutral C_2H_5 fragments (via the 3s Rydberg state [51]) in this wavelength region, which gives an additional contribution to the $C_2H_5{}^+$ image. Comparison of the P(E_T) distributions derived from the $C_2H_5{}^+$ and I^+ images suggests that the shoulder at $E_T \sim$0.4 eV is attributable to 266 nm two-photon ionization of neutral ethyl radicals from the $C_2H_5 + I^+$ pathway, while the peak at $E_T \sim$0.8 eV is associated with $C_2H_5{}^+ + I$ product formation.

The I^+ images obtained at all four photolysis wavelengths, shown in Figure 4.5 (b), are markedly different from those of the $C_2H_5{}^+$ fragments shown in Figure 4.5 (a). Therefore, we can confirm that the observed I^+ does not originate from the neutral iodine formed as the co-fragment to $C_2H_5{}^+$. The images measured at the three shorter wavelengths are clearly anisotropic ($\beta \sim 1.7$) and the derived P(E_T) distributions (Figure 4.5 (b)) all peak at $E_T > 0$ and extend to the maximum E_T values expected on the basis of energy conservation, i.e. estimated on the basis of simple C$-$I bond fission following excitation of spin-orbit excited $C_2H_5I^+$ cations, undergoes fragmentation to yield ground state $I^+(^3P_2)$ ions. The observed energy disposal is very reminiscent of that observed for the $C_2H_5{}^+$ product ions at these wavelengths, and can be explained in the same way, i.e. photoexcitation to the $3A'$ and/or $4A'$ ($\sigma\sigma^*$) states followed by prompt dissociation to (in this case) the adiabatic products $C_2H_5 + I^+$. The 'one laser' (355 nm photolysis) I^+ data is also reminiscent of that seen when monitoring $C_2H_5{}^+$ fragment ions. The recoil velocity distribution is more isotropic ($\beta \sim 0.7$), and the P(E_T) distribution peaks near $E_T = 0$ (but shows no additional 'spike' as a 118 nm photon provides insufficient energy to access the $C_2H_5 + I^+$ dissociative ionization channel). Such behaviour, together with that for the $C_2H_5{}^+$ products observed at the same wavelength, may be explained by near-threshold excitation to the lowest adiabatic potential correlating to I^+ products, $3A'$, which possesses a shallow minimum in the vertical Franck-Condon region (see Figure 4.1). Excitation is followed by slower dissociation both to $C_2H_5 + I^+$ and - following non-adiabatic population transfer - to $C_2H_5{}^+ + I$ products.

We now consider possible mechanisms for formation of $C_2H_3{}^+$ and $C_2H_4{}^+$ fragment ions, both of which are observed at all four photolysis wavelengths investigated. 'One laser' images, corresponding to 355 nm photolysis, are shown in Figure 4.5 (c), along with a comparison of the P(E_T) distributions derived for the $C_2H_5{}^+$, $C_2H_4{}^+$ and $C_2H_3{}^+$ ions. In the case of $C_2H_5Br^+$, (2+1) REMPI studies of the neutral Br and Br^* fragments led us to conclude that most of the detected $C_2H_5{}^+$ ions are partnered by Br^* atoms, and that

H_2 elimination from highly internally excited $C_2H_5^+$ ions formed together with Br co-fragments is the main source of the observed $C_2H_3^+$ ions. Unfortunately, no such insights are forthcoming in the case of $C_2H_5I^+$, as we were unable to employ REMPI detection for the I and I* products. Thus our discussion of possible $C_2H_3^+$ (and $C_2H_4^+$) formation routes is guided by energetic considerations. As noted above, the energy of a 118 nm photon exceeds the dissociative ionization threshold for forming $C_2H_5^+$ fragments, which must be formed with little internal or translational energy. Even a 355 nm photon provides more than enough energy to excite these fragments well above the threshold for H_2 elimination and $C_2H_3^+$ fragment formation (see Figure 4.2 (b)). Photoionization at 118nm also yields parent cations, which we assume are formed in both the X_1A' and X_2A'' states. The threshold energy for three-body dissociation to $C_2H_3^+ + H_2 + I$ products lies ~3.3 eV(~2.7 eV) above the $X_1A'(X_2A'')$ states of the parent cation and is thus accessible even when exciting at 355 nm (i.e. with a photon of energy 3.49 eV). Notwithstanding the multiplicity of possible routes to forming $C_2H_3^+$ products, the balance of evidence suggests that, as in the case of $C_2H_5Br^+$, H_2 elimination from highly internally excited $C_2H_5^+$ fragments formed by UV photolysis is the major route to the observed $C_2H_3^+$ products.

The C−H bond strength in $C_2H_5^+$ is ~3.82 eV (Figure 4.2 (b)), so photolysis of $C_2H_5^+$ fragments arising from dissociative photoionization could also contribute to the observed $C_2H_4^+$ ion yield at 266, 248 and 236 nm. Again, we focus on the data from 355 nm photolysis. The threshold energy for three-body dissociation to $C_2H_4^+ + H + I$ products (4.94 eV or 4.36 eV when defined relative to the X_1A' and X_2A'' states of the cation, respectively) is too high for parent ion photolysis to be a feasible route to $C_2H_4^+$ fragments at 355 nm, but the alternative HI elimination channel, the analogue of that proposed to account for HBr formation in the case of $C_2H_5Br^+$ photolysis, appears eminently plausible. As was the case for $C_2H_5Br^+$, the average translational energies, $\langle E_T \rangle$, derived from the $C_2H_4^+$ fragment ion images increase as the excitation wavelength is reduced, and the bulk of the available energy, ~90 % of E_T(max), is partitioned into product internal excitation. Both of these features are consistent with unimolecular decay of internally 'hot' parent molecules following radiationless transfer to the ground state PES.

Figure 4.5 (d) shows images of the CH_2I^+ products formed via the C−C bond fission channel following excitation of $C_2H_5I^+$ at 355 and 266 nm. The P(E_T) distribution in the former case is very narrow (more so than in the case of $C_2H_5Br^+$) and peaks at $E_T = 0$. Moving to shorter excitation wavelength (266 nm) results in a CH_2I^+ image with a larger radius and a P(E_T) distribution which peaks a little above zero and extends to higher E_T, but still stops well short of the E_T(max) value for $CH_2I^+ + CH_3$ products. As in the case of the

$C_2H_4^+$ products, such energy disposal is most readily understood in terms of unimolecular decay of internally excited ground state $C_2H_5I^+$ cations.

4.4 Conclusion

We have presented an in-depth velocity-map imaging study of the different photofragmentation pathways that arise following UV photoexcitation of two ethyl halide cations, $C_2H_5I^+$ and $C_2H_5Br^+$. The branching between the fragmentation channels that yield the various observed ions has been obtained for both ethyl halide cations following photolysis with 355 nm light. For both species C−X bond cleavage to yield $C_2H_5^+$ is the major fragmentation pathway. For $C_2H_5Br^+$ photolysis the ratio for $C_2H_5^+$: $C_2H_4^+$: $C_2H_3^+$: CH_2Br^+ is 0.41 : 0.38 : 0.20 : 0.01. In the case of $C_2H_5I^+$ photolysis, the ratio for $C_2H_5^+$: $C_2H_4^+$: $C_2H_3^+$: CH_2I^+ : I^+ is 0.62 : 0.19 : 0.06 : 0.02 : 0.12. The images obtained for these fragment ions resulting from UV photolysis of $C_2H_5Br^+$ and $C_2H_5I^+$ suggest many similarities in the fragmentation dynamics of these ethyl halide cations. The VMI data has been interpreted alongside potential energy curves for the ground and low-lying excited states of both cations. Based on the information to hand, five likely fragmentation pathways have been proposed:

1. Prompt carbon-halogen (C−X) bond cleavage to yield $C_2H_5^+ + X^*$.
2. The ethene cations ($C_2H_4^+$) most plausibly arise from unimolecular decay (loss of HX) from highly vibrationally excited electronic ground state parent cations.
3. The vinyl cation ($C_2H_3^+$) fragment ions arise from unimolecular decay (H_2 elimination) of highly internally excited $C_2H_5^+$ cations, which in the case of $C_2H_5Br^+$ are most likely partnered with Br co-fragments.
4. Carbon-carbon (C−C) bond cleavage resulting in formation of $CH_2X^+ + CH_3$ presents as a minor competing pathway.
5. Prompt C−I bond cleavage to produce $C_2H_5 + I^+$ has been observed in the case of $C_2H_5I^+$.

Channel 1 and Channel 5 both involve direct C−X bond fission following initial photoexcitation. In contrast, the other three channels are thought to occur following radiationless transfer from the initial photoexcited state. Data from detailed high-dimensionality *ab inito* calculations would be required in order to gain a more detailed mechanistic understanding of the various fragmentation pathways.

References

[1] Chandler, DW and Houston, PL. *Two-dimensional imaging of state-selected photodissociation products detected by multiphoton ionization*. The Journal of Chemical Physics **87**:2 1445–1447 (1987) (cited p. 81).

[2] Nalda, R de, Durá, J, Garcia, Ga, Izquierdo, JG, González-Vázquez, J, and Bañares, L. *A detailed experimental and theoretical study of the femtosecond A-band photodissociation of CH_3I*. The Journal of Chemical Physics **128**:24 244309 (2008) (cited p. 81, 82).

[3] Eppink, ATJB and Parker, DH. *Methyl iodide A-band decomposition study by photofragment velocity imaging*. The Journal of Chemical Physics **109**:12 4758 (1998) (cited p. 81, 82).

[4] Chandler, DW, W Thoman Jr., J, Janssen, MHM, and Parker, DH. *Photofragment imaging: the 266 nm photodissociation of CH_3I*. Chemical Physics Letters **156**:2-3 151–158 (1989) (cited p. 81).

[5] Eppink, ATJB and Parker, DH. *Energy partitioning following photodissociation of methyl iodide in the A band: A velocity mapping study*. The Journal of Chemical Physics **110**:2 832–844 (1999) (cited p. 81).

[6] Chichinin, AI, Gericke, KH, Kauczok, S, and Maul, C. *Imaging chemical reactions – 3D velocity mapping*. International Reviews in Physical Chemistry **28**:4 607–680 (2009) (cited p. 82).

[7] Tsai, BP, Baer, T, Werner, AS, and Lin, SF. *Photoelectron-photoion coincidence study of the ionization and fragment appearance potentials of bromo- and iodomethanes*. The Journal of Physical Chemistry **79**:6 570–574 (1975) (cited p. 82).

[8] Mintz, DM. *Kinetic energy release distributions for the dissociation of internal energy selected CH_3I^+ and CD_3I^+ ions*. The Journal of Chemical Physics **65**:6 2407–2415 (1976) (cited p. 82).

[9] Eland, JHD, Frey, R, Kuestler, A, Schulte, H, and Brehm, B. *Unimolecular dissociations and internal conversions of methyl halide ions*. International Journal of Mass Spectrometry and Ion Physics **22**:1-2 155–170 (1976) (cited p. 82).

[10] Blanchet, V, Samartzis, PC, and Wodtke, AM. *UV photodissociation of methyl bromide and methyl bromide cation studied by velocity map imaging.* The Journal of Chemical Physics **130**:3 034304 (2009) (cited p. 82).

[11] Kawasaki, M, Sato, H, Kikuchi, T, Kobayashi, R, and Arikawa, T. *Angular-Distributions of CH_3^+ Photofragments From CH_3I^+ Prepared by Multiphoton Ionization*. The Journal of Chemical Physics **87**: 5739–5745 (1987) (cited p. 82).

[12] Bae, YJ and Kim, MS. *Photodissociation Spectroscopy of CD_3I^+ Generated by Mass-Analyzed Threshold Ionization for Structure Determination*. ChemPhysChem **9**:12 1709–1714 (2008) (cited p. 82).

[13] Bodi, A, Shuman, NS, and Baer, T. *On the ionization and dissociative photoionization of iodomethane: a definitive experimental enthalpy of formation of CH_3I.* Physical Chemistry Chemical Physics **11**:46 11013–11021 (2009) (cited p. 82).

[14] Godwin, FG, Gorry, PA, Hughes, PM, Raybone, D, Watkinson, TM, and Whitehead, JC. *Two-photon VUV laser-induced fluorescence detection of $I(^2P_{1/2})$ and $I(^2P_{3/2})$ from alkyl iodide photodissociation at 248 nm*. Chemical Physics Letters **135**:1-2 163–169 (1987) (cited p. 82).

[15] Gougousi, T, Samartzis, PC, and Kitsopoulos, TN. *Photodissociation study of CH_3Br in the first continuum*. The Journal of Chemical Physics **108**:14 5742–5746 (1998) (cited p. 82).

[16] Townsend, D, Lee, SK, and Suits, AG. *DC Slice Imaging of CH_3Cl Photolysis at 193.3 nm*. The Journal of Physical Chemistry A 8106–8114 (2004) (cited p. 82).

[17] Locht, R, Dehareng, D, Hottmann, K, Jochims, HW, Baumgärtel, H, and Leyh, B. *The photoionization dynamics of methyl iodide (CH_3I): a joint photoelectron and mass spectrometric investigation*. Journal of Physics B: Atomic, Molecular and Optical Physics **43**:10 105101 (2010) (cited p. 82, 86).

[18] Baer, T, Buchler, U, and Klots, CE. *Kinetic Energy Release Distributions For The Dissociation Of Internal Energy Selected $C_2H_5I^+$ Ions*. Journal de Chimie Physique **77**:7/8 739–743 (1980) (cited p. 82).

[19] Miller, BE and Baer, T. *Kinetic Energy Release Distribution in the Fragmentation of Energy-Selected Vinyl and Ethyl Bromide Ions*. Chemical Physics **85**: 39–45 (1984) (cited p. 82).

[20] Baer, T, Song, Y, Liu, J, Chen, W, and Ng, CY. *Pulsed field ionization-photoelectron photoion coincidence spectroscopy with synchrotron radiation: The heat of formation of the $C_2H_5^+$ ion*. Faraday Discussions **115**: 137–145 (2000) (cited p. 82).

[21] Borkar, S and Sztáray, B. *Self-consistent heats of formation for the ethyl cation, ethyl bromide, and ethyl iodide from threshold photoelectron photoion coincidence spectroscopy.* The Journal of Physical Chemistry A **114**:20 6117–6123 (2010) (cited p. 82, 89).

[22] Tang, Y, Lee, Wb, Hu, Z, Zhang, B, and Lin, Kc. *Productions of I , I *, and C_2H_5 in the A-band photodissociation of ethyl iodide in the wavelength range from 245 to 283nm by using ion-imaging detection Productions of I, I*, and C_2H_5 in the A-band photodissociation of ethyl iodide in the wavelength*. The Journal of Chemical Physics **126**:6 064302 (2007) (cited p. 82, 103).

[23] Xu, D, Price, RJ, Huang, J, and Jackson, WM. *Photodissociation of the Ethyl Bromide Cation at 355 nm by Means of TOF-MS and Ion Velocity Imaging Techniques*. Zeitschrift für Physikalische Chemie **215**:2/2001 253–271 (2001) (cited p. 82, 84, 87, 93, 96, 97, 99).

[24] Suto, K, Sato, Y, Reed, CL, Skorokhodov, V, Matsumi, Y, and Kawasaki, M. *Ion Fragment Imaging of the Ion-Pair Photodissociation of CH_3Cl, CH_3Br, C_2H_5Cl, and C_2H_5Br at 118 nm*. The Journal of Physical Chemistry A **101**:7 1222–1226 (1997) (cited p. 82).

[25] Tang, B, Zhu, R, Tang, Y, Ji, L, and Zhang, B. *Photodissociation dynamics of C_2H_5Br and n-C_3H_7Br in UV region*. Chemical Physics **303**:1-2 37–42 (2004) (cited p. 84).

[26] Tang, Y, Ji, L, Zhu, R, Wei, Z, and Zhang, B. *Photodissociation Study of Ethyl Bromide in the Ultraviolet Range by the Ion-Velocity Imaging Technique*. ChemPhysChem **6**:10 2137–2144 (2005) (cited p. 84, 97).

[27] Chichinin, AI. *Chemical Properties of Electronically Excited Halogen Atoms $X(^2P_{1/2})$ (X=F, Cl, Br, I)*. Journal of Physical Chemistry Reference Data **352**: 869–928 (2006) (cited p. 84).

[28] Zhu, R, Tang, B, Ji, L, Tang, Y, Zhang, S, and Zhang, B. *Photodissociation dynamics of n-alkyl bromide at 234 and 267 nm*. Optics Communications **235**:4-6 325–331 (2004) (cited p. 84).

[29] Tang, Y, Ji, L, Tang, B, Zhu, R, Zhang, S, and Zhang, B. *Studies on photodissociation of alkyl bromides at 234 and 267 nm*. Chemical Physics Letters **392**:4-6 493–497 (2004) (cited p. 84).

[30] Werner, HJ, Knowles, PJ, Knizia, G, Manby, FR, Schütz, M, Celani, P, Korona, T, Lindh, R, Mitrushenkov, A, Rauhut, G, Shamasundar, KR, Adler, TB, Amos, RD, Bernhardsson, A, Berning, A, Cooper, DL, Deegan, MJO, Dobbyn, AJ, Eckert, F, Goll, E, Hampel, C, Hesselmann, A, Hetzer, G, Hrenar, T, Jansen, G, Köppl, C, Liu, Y, Lloyd, AW, Mata, RA, May, AJ, McNicholas, SJ, Meyer, W, Mura, ME, Nicklass, A, O'Neill, DP, Palmieri, P, Pflüger, K, Pitzer, R, Reiher, M, Shiozaki, T, Stoll, H, Stone, AJ, Tarroni, R, Thorsteinsson, T, Wang, M, and Wolf, A. *MOLPRO, version 2010.1, a package of ab initio programs*. Tech. rep. 2010 (cited p. 84).

[31] Dunning, TH. *Gaussian basis sets for use in correlated molecular calculations. I. The atoms boron through neon and hydrogen*. The Journal of Chemical Physics **90**:2 1007 (1989) (cited p. 84).

[32] Dolg, M. *Habilitationsschrift*. Universität Stuttgart, 1997 (cited p. 84).

[33] Peterson, KA, Shepler, BC, Figgen, D, and Stoll, H. *On the Spectroscopic and Thermochemical Properties of ClO, BrO, IO, and Their Anions*. The Journal of Physical Chemistry A **110**:51 13877–13883 (2006) (cited p. 84).

[34] Ruscic, B, Berkowitz, J, Curtiss, La, and Pople, Ja. *The ethyl radical: Photoionization and theoretical studies*. The Journal of Chemical Physics **91**:1 114 (1989) (cited p. 85, 89).

[35] Andrei, HS, Solcà, N, and Dopfer, O. *IR spectrum of the ethyl cation: evidence for the nonclassical structure.* Angewandte Chemie International Edition **47**:2 395–397 (2008) (cited p. 85).

[36] Frisch, MJ, Trucks, GW, Schlegel, HB, Scuseria, GE, Robb, MA, Cheeseman, JR, Scalmani, G, Barone, V, Mennucci, B, Petersson, GA, Nakatsuji, H, Caricato, M, Li, X, Hratchian, HP, Izmaylov, AF, Bloino, J, Zheng, G, Sonnenberg, JL, Hada, M, Ehara, M, Toyota, K, Fukuda, R, Hasegawa, J, Ishida, M, Nakajima, T, Honda, Y, Kitao, O, Nakai, H, Vreven, T, Montgomery, JA, Peralta, JE, Ogliaro, F, Bearpark, M, Heyd, JJ, Brothers, E, Kudin, KN, Staroverov, VN, Kobayashi, R, Normand, J, Raghavachari, K, Rendell, A, Burant, JC, Iyengar, SS, Tomasi, J, Cossi, M, Rega, N, Millam, JM, Klene, M, Knox, JE, Cross, JB, Bakken, V, Adamo, C, Jaramillo, J, Gomperts, R, Stratmann, RE, Yazyev, O, Austin, AJ, Cammi, R, Pomelli, C, Ochterski, JW, Martin, RL, Morokuma, K, Zakrzewski, VG, Voth, GA, Salvador, P, Dannenberg, JJ, Dapprich, S, Daniels, AD, Farkas, Foresman, JB, Ortiz, JV, Cioslowski, J, and Fox, DJ. *Gaussian 09, Revision B.01*. Tech. rep. 2009 (cited p. 85).

[37] Knoblauch, N, Strobel, A, Fischer, I, and Bondybey, VE. *Two-photon ionization and dissociation of ethyl iodide*. The Journal of Chemical Physics **103**:October 5417–5427 (1995) (cited p. 87, 89).

[38] Tang, B, Zhang, S, Wang, Y, Tang, Y, and Zhang, B. *One-color two-photon mass-analyzed threshold ionization spectroscopy of ethyl bromide through a dissociative intermediate state.* The Journal of Chemical Physics **123**:16 164305 (2005) (cited p. 87, 89).

[39] Kramida, A, Ralchenko, Y, Reader, J, and NIST, AT. NIST Atomic Spectra Database *(ver. 5.0), [Online]. Available: http://physics.nist.gov/asd [August 23]*. National Institute of Standards and Technology, Gaithersburg, MD, 2013 (cited p. 89, 92).

[40] Fan, H and Pratt, ST. *Photoionization of hot radicals: C_2H_5, n-C_3H_7, and i-C_3H_7*. The Journal of Chemical Physics **123**:20 204301 (2005) (cited p. 89).

[41] Willitsch, S, Hollenstein, U, and Merkt, F. *Ionization from a double bond: rovibronic photoionization dynamics of ethylene, large amplitude torsional motion and vibronic coupling in the ground state of $C_2H_4^+$*. Journal of Chemical Physics **120**:4 1761–1774 (2004) (cited p. 89).

[42] Regan, PM, Langford, SR, Orr-Ewing, AJ, and Ashfold, MNR. *The ultraviolet photodissociation dynamics of hydrogen bromide*. The Journal of Chemical Physics **110**:1 281–288 (1999) (cited p. 89).

[43] Lago, AF, Kercher, JP, Bodi, A, Sztáray, B, Miller, B, Wurzelmann, D, and Baer, T. *Dissociative photoionization and thermochemistry of dihalomethane compounds*

studied by threshold photoelectron photoion coincidence spectroscopy. Journal of Physical Chemistry A **109**:9 1802–1809 (2005) (cited p. 89).

[44] Ruscic, B, Boggs, JE, Burcat, A, and Császár, AG. *IUPAC critical evaluation of thermochemical properties of selected radicals. Part I.* Journal of Physical Chemistry Reference Data **34**:2 573–656 (2005) (cited p. 89).

[45] Langford, SR, Regan, PM, Orr-Ewing, AJ, and Ashfold, MNR. *On the UV photodissociation dynamics of hydrogen iodide*. Chemical Physics **231**:2-3 245–260 (1998) (cited p. 89).

[46] Lias, SG. *"Ionization Energy Evaluation" in NIST Chemistry WebBook, NIST Standard Reference Database Number 69, (retrieved June 19, 2013)*. Ed. by Linstrom, PJ and Mallard, WG. National Institute of Standards and Technology, Gaithersburg MD, 20899 (cited p. 89).

[47] Giuliani, A, Motte-Tollet, F, Delwiche, J, Mason, NJ, Jones, NC, Gingell, JM, Walker, IC, and Hubin-Franskin, MJ. *Electronic excitation and oscillator strength of ethyl bromide by vacuum ultraviolet photoabsorption and electron energy loss spectroscopy*. The Journal of Chemical Physics **112**:14 6285–6292 (2000) (cited p. 87).

[48] Giuliani, A, Motte-Tollet, F, Delwiche, J, Heinesch, J, Mason, NJ, Gingell, JM, Walker, IC, Jones, NC, and Hubin-Franskin, MJ. *Electronic excitation and oscillator strength of ethyl iodide by VUV photoabsorption and electron energy loss spectroscopy*. The Journal of Chemical Physics **110**:21 10307–10315 (1999) (cited p. 87).

[49] Irsa, AP. *Electron Impact Studies on C_2H_5Cl, C_2H_5Br, and C_2H_5I*. The Journal of Chemical Physics **26**:1 18–22 (1957) (cited p. 93).

[50] Alekseyev, AB, Liebermann, HP, Buenker, RJ, and Yurchenko, SN. *An ab initio study of the CH_3I photodissociation. I. Potential energy surfaces*. The Journal of Chemical Physics **126**:23 234102 (2007) (cited p. 97).

[51] Wendt, HR and Hunziker, HE. *The UV spectra of primary, secondary, and tertiary alkyl radicals*. The Journal of Chemical Physics **81**:2 717–723 (1984) (cited p. 103).

5

193 nm Photodissociation of N,N-dimethylformamide

Contents

5.1 Introduction

There is significant interest in the fragmentation dynamics of amide systems, primarily due to their relevance to peptide bonds within proteins. As well as allowing photodamage mechanisms to be studied in such systems, photodissociation is increasingly being employed as an analytical tool to investigate the structures of biological molecules such as small polypeptides and proteins [1]. Generally, the latter type of investigations have been carried out on the *cationic* species. However, as will be seen in Chapter 6, cationic species are highly fluxional, and undergo many rearrangement reactions; H-transfer reactions are common, and simple bond cleavages are not often observed. Studies on *neutral* species allow us to observe direct bond cleavage processes, without rearrangement of the parent

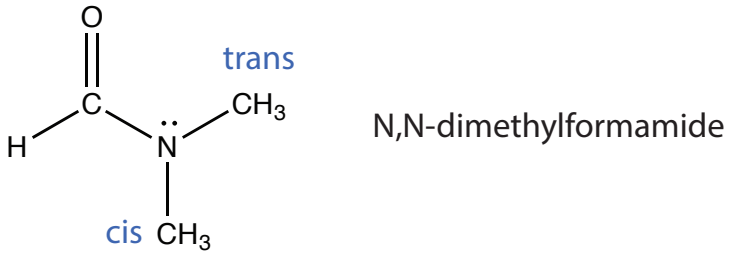

Figure 5.1: The structure of N,N-dimethylformamide. The methyl substituent groups (cis and trans) are labelled according to conventional protein nomenclature.

species. Therefore, such studies perhaps give a more representative idea of the dynamics that occur in processes such as UV photodegradation of polypeptides and other polymers that contain amide functional groups as building blocks.

N,N-dimethylformamide (DMF), shown in Figure 5.1, is the amide system chosen for this work, with the N−CO bond linkage providing a model for a peptide bond. DMF, as is the general case for amides, has a planar structure. This is due to donation of the lone pair on nitrogen into the C=O π bonding system, which gives partial double bond character to the N−CO 'peptide' bond. This planarity is key to protein structure and polymer formation. The partial double bond character of the N−CO bond means that there is restricted rotation about this bond, and the methyl groups are not equivalent. As shown in Figure 5.1, these groups can be labelled cis and trans to the C=O group. The protein convention for nomenclature, which is the inverse of the standard convention [2], is taken here.

Here we present an experimental study into the 193 nm photolysis of DMF, which has primarily employed the velocity-map imaging (VMI) technique. Excitation of DMF with 193 nm (6.41 eV) light results in either promotion of a electron from a oxygen lone pair to the π^* antibonding orbital localized in the C=O moiety, referred to as the n$\rightarrow \pi^*$ excitation, or promotion of a lone-pair 2pπ electron on the nitrogen to the antibonding π^* C=O orbital, referred to as the $\pi \rightarrow \pi^*$ transition [3–6]. The n$\rightarrow \pi^*$ and $\pi \rightarrow \pi^*$ transitions correspond to population of the S_1 and S_2 electronic states, respectively.

Forde *et al.* have previously investigated the photofragmentation of DMF at 193 nm using photofragment translational spectroscopy (PTS) [7, 8]. Since then, Liu *et al.* [6] and Eckert-Maksić and Antol [9] have undertaken theoretical studies of DMF photodissociation. The photodissociation of DMF can be viewed as occurring by one of three initial bond cleavages, illustrated in Figure 5.2, which give the three radical product channels:

1. N−CO 'peptide' bond fission: $\quad HCON(CH_3)_2 \rightarrow HCO + NC_2H_6$

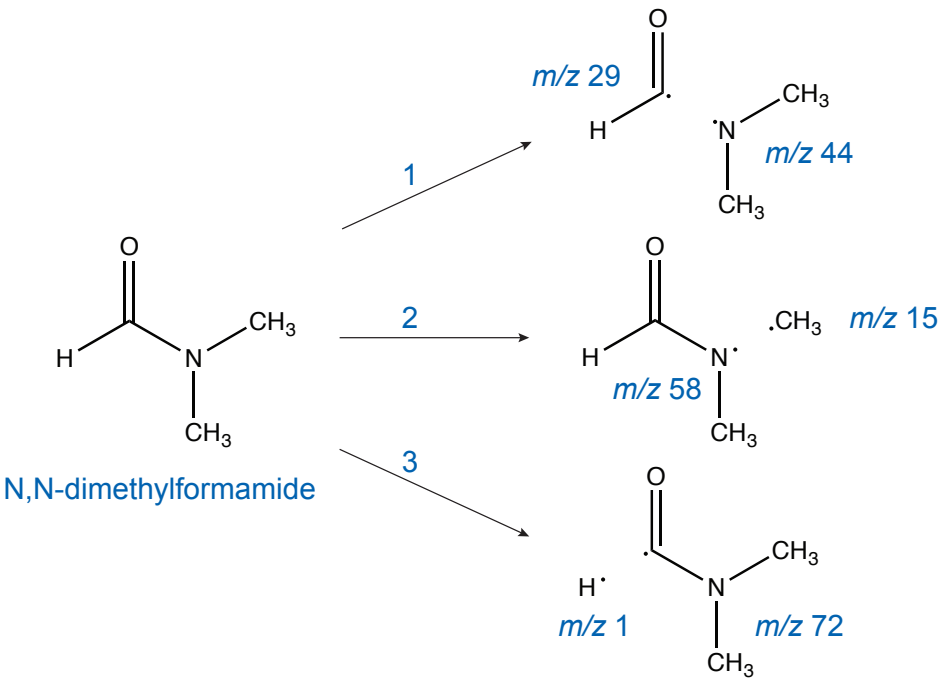

Figure 5.2: Three fragmentation pathways of DMF, each leading to formation of radical products. Pathway 1 involves N−CO 'peptide' bond fission, Pathway 2 results from N−CH_3 bond fragmentation, and Pathway 3 results in H loss.

2. N−CH_3 bond fragmentation: $HCON(CH_3)_2 \rightarrow HCONCH_3 + CH_3$

3. H loss: $HCON(CH_3)_2 \rightarrow H + CON(CH_3)_2$

As will be discussed in Section 5.3, the photofragments that result from these bond cleavage channels can be formed in a number of different electronic states.

The experimental study of Forde *et al.* found that, following 193 nm photolysis of DMF, fission of the N−CO bond was found to be the dominant product channel [8]. The same authors found fission of the N−CH_3 bond as a competing dissociation channel. H loss from DMF has not previously been experimentally observed.

In the current work, the time-of-flight mass spectra allow identification and quantification of the fragmentation products, the ion images provide information about the translational energy and angular distributions of the recoiling photofragments, and H Rydberg atom photofragment translational spectroscopy has been employed specifically to investigate H loss from DMF. The information from each of these experimental methods, together with recent ab initio calculations (detailed in Section 5.2.2), allows further understanding of the

dissociation dynamics of the DMF molecule. It should be noted that the work presented in this chapter is a subset of data from a multi-wavelength dynamical study of DMF, the full analysis of which will present a fuller picture.

5.2 Methods

5.2.1 Experiment

The velocity-map imaging experimental setup has been described in detail in Chapter 2. The following is a brief description of the experimental conditions. A mixture of $\sim 0.2\%$ N,N-dimethylformamide (Sigma-Aldrich, $>$99.8%) seeded in 2 bar of He (BOC, $> 99.9\%$) undergoes a supersonic expansion into vacuum to generate the molecular beam. Within the interaction region, the molecular beam is intersected, at right angles, by two counter-propagating linearly polarized laser beams of wavelengths 193 nm and 118.2 nm, separated in time by about 20 ns. The DMF molecules are photolysed by a 193 nm photon, and the resulting neutral dissociation products are ionized by a VUV photon of wavelength 118.2 nm (referred to as 118 nm or VUV from now onwards). The nascent ions are velocity-mapped onto a position sensitive detector. Time-of-flight mass spectra (TOF-MS) and velocity-map images are recorded as described in Sections 2.6 and 2.9, respectively. We record TOF-MS spectra (or velocity-map images) with (i) only the VUV laser present in the interaction region, (ii) both the 193 nm and VUV laser beams present, and (iii) only the 193 nm laser present, each with both the molecular beam on and off. The TOF-MS spectra (or velocity-map images) obtained with only the VUV laser and with only the 193 nm light are subtracted from the TOF-MS spectrum (or velocity-map image) obtained with both 193 nm and VUV light to give the final 'two-colour signal' TOF-MS spectrum (or velocity-map image). We do not spatially separate the 355 nm and 118 nm lasers before they enter the interaction region. In order to check if the 355 nm light makes any contribution to the N,N-dimethylformamide dissociation, we recorded TOF-MS spectra with only the 355 nm laser present in the interaction region, and with 193 nm and 355 nm lasers, with both molecular beam on and off. There was no contribution on the molecular beam signal from the 355 nm light in either of the spectra.

In order to investigate the hydrogen loss from DMF, H-atom Rydberg Tagging measurements have been performed in collaboration with the Bristol Laser group. The H Rydberg atom photofragment translational spectroscopy (PTS) experiment has been described previously [10]. In brief, the apparatus consists of two differentially pumped volumes (a source

chamber, with base pressure $p \leq 2\times10^{-6}$ mbar, and an interaction/detection chamber with $p \leq 6\times10^{-8}$ mbar) separated by a skimmer. A pulsed molecular beam comprising DMF (Sigma Aldrich, >99%, room temperature vapour pressure) in ~1 bar of Ar was expanded through a pulsed valve and skimmed prior to photolysis. H atoms formed in this interaction region were probed by two-photon (121.6 nm + 366 nm) double resonant excitation *via* the *2p* state to a high *n* Rydberg state. Rydberg atoms that recoil along the axis orthogonal to the plane containing the molecular beam and the photolysis/probe laser reach a detector, which is located at a distance *d* from the interaction region, where their time-of-flight are recorded. An extraction field of 50 Vcm^{-1} applied across the interaction region ensures prompt removal of any H^+ ions created in the interaction region.

5.2.2 Computational methodology

The computation calculations were carried out by Tolga Karsili of the Bristol Laser group. Here we give an account of the computational methods employed. The results of the calculations will be presented in full in a future publication [11].

Using the Gaussian 09 [12] electronic structure package, the ground-state optimized geometry of neutral N,N-dimethylformamide was obtained using the Møller-Plesset second order perturbation theory (MP2), in conjunction with a Dunning's contracted and augmented correlation consistent basis set of triple ζ quality: aug-cc-pvtz, assigned to all atoms. The geometry was then reoptimized using density function theory (DFT) calculations, which employed the Becke-3rd parameter Lee, Yang, Parr (B3LYP) functional in conjugation with the 6-311+g(2df,p) basis set, to calculate the product energies for a number of DMF fragmentation pathways. The MOLPRO Version 2010.1 [13] computational package was employed for all other calculations. Vertical excitation energies and transition dipole moments (μ) of various neutral states of DMF were calculated using a state-averaged complete active space self-consistent field (SA-CASSCF) method, employing the same aug-cc-pVTZ basis set as implemented above. These calculations were based on the MP2 optimised geometry. The choice of active space was motivated by an attempt to describe all significant static correlation effects in the ground and excited electronic states in as even-handed a way as possible across the potential energy surface, whilst keeping the computational expense as minimal as possible. The active space comprised 14 electrons arranged in 10 orbitals (14/10). All valence electrons, except the oxygen 2s, are included within the active space, as well as the C=O centered π^* and two σ^* virtual orbitals. Individual potential energy curves (PECs) along the N−C 'peptide', carboxyl C−H, and dimethylamino N−C stretching coordinates

were calculated for the ground and various excited electronic states of the DMF neutral molecule. These calculations employed the complete active space with second order perturbation (CASPT2) theory that was based upon the fully SA-CASSCF reference wavefunction, with the remainder of the nuclear framework frozen at the ground-state optimised geometry. A small imaginary level shift of 0.5 a.u. was applied to encourage convergence and to circumvent the presence of intruder states for all CASPT2 calculations. Vertical excitation energies obtained from the CASPT2 calculations are in good agreement with the available experimental data [3, 4], while others at the EOM-CCSD/aug-cc-pVTZ level of theory are not. However, the latter calculations, which were carried out at the MP2/aug-cc-pVTZ optimised geometry, also provided information about the μ, and estimations of the oscillator strengths (f) accompanying various electronic transitions.

5.3 Results and Discussion

Following absorption of a single 193 nm photon, the N,N-dimethylformamide molecule, $HCON(CH_3)_2$, can be expected to fragment via one of three pathways (illustrated in Figure 5.2), each leading to formation of radical products:

1. N−CO 'peptide' bond fission: $HCON(CH_3)_2 \rightarrow HCO + N(CH_3)_2$

2. N−CH_3 bond fragmentation: $HCON(CH_3)_2 \rightarrow HCONCH_3 + CH_3$

3. H loss: $HCON(CH_3)_2 \rightarrow H + CON(CH_3)_2$

The CASPT2 rigid-body scans, described in the previous section, provide cuts through the low lying electronic states of the DMF molecule, and insight into the fragmentation dynamics. Figure 5.3 (a) shows a cut along the 'peptide' C−N bond coordinate, and panels (b) and (c) in Figure 5.3 show equivalent cuts along the dimethylamino N−C, and carboxyl C−H stretching coordinates, respectively. The asymptotes along the various bond stretching coordinates have been assigned for each of the electronic states.

Along the C−N bond coordinate:

- the S_0 state asymptotically correlates with the formyl radical in its first excited electronic state, HCO ($\tilde{A}^2A''$), and the dimethylamidogen radical in its ground state, $N(CH_3)_2$ ($\tilde{X}^2B_1$), labelled as HCO^* + $N(CH_3)_2$.

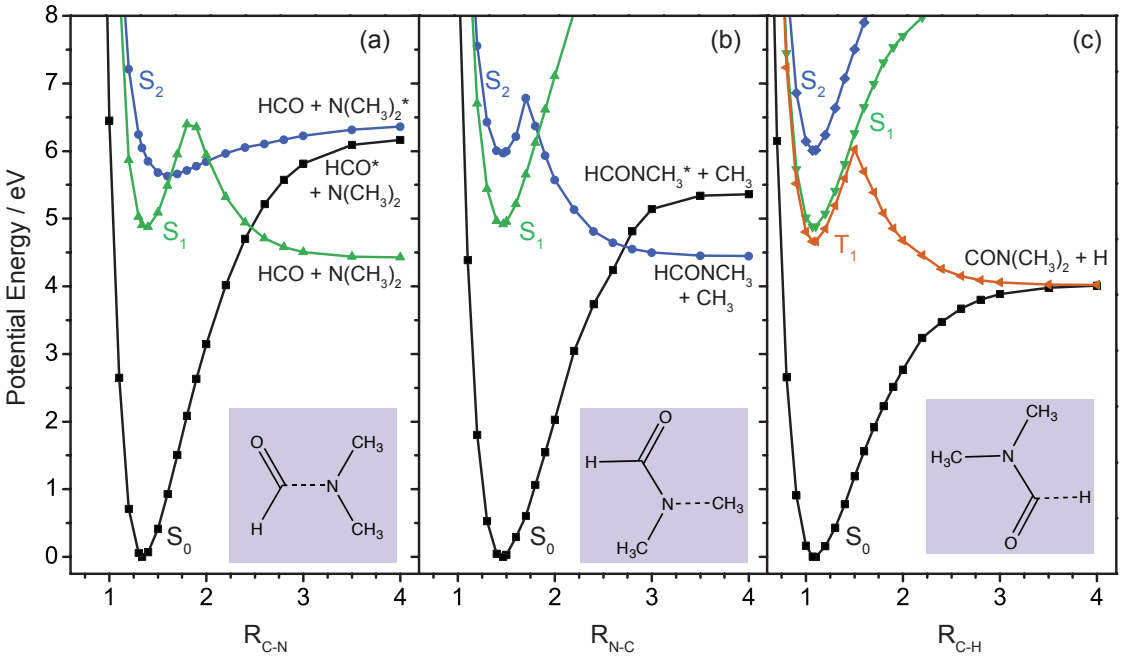

Figure 5.3: Cuts through the potential energy surfaces of the low lying electronic states of DMF, along (a) the 'peptide' C−N, (b) the dimethylamino N−C, and (c) the carboxyl C−H bond stretching coordinates. The electronic ground state (S_0) is shown in black. The first and second excited singlet states (S_1 and S_2) are shown in green and blue, respectively. The first excited triplet state (T_1, shown in orange) is also included in (c). The asymptotes have been assigned. Illustrations of DMF, with the stretching bond shown as a dashed line, are included in each panel.

- the S_1 excited state, which exhibits a significant energy barrier, asymptotically correlates with ground state products, labelled HCO + $N(CH_3)_2$.
- the S_2 excited state asymptotically correlates with the formyl radical in its electronic ground state, HCO ($\tilde{X}^2A'$), and dimethylamidogen in its first electronic excited state, $N(CH_3)_2$ ($\tilde{A}^2A_1$), labelled HCO + $N(CH_3)_2{}^*$.

Figure 5.4 shows the range of photofragments that are energetically accessible following photoexcitation of DMF with a single 193 nm photon. The product energies, shown relative to the electronic ground state of DMF, have been obtained from the DFT calculations described in Section 5.2.2. The products resulting from N−CO 'peptide' bond fragmentation are highlighted in blue. The first excited electronic states of HCO and $N(CH_3)_2$, which lie at energies of 1.15 eV [14] and 1.43 eV[1] above their respective electronic ground states, are

[1]This value is an experimental estimate obtained by subtracting from the available energy the maximum translational energy of the $N(CH_3)_2{}^*$ fragments (obtained from the E_T distribution from the ion image of *m/z* 43). This value compares with the one estimated by Forde *et al.* (1.56 eV) using a similar method [8].

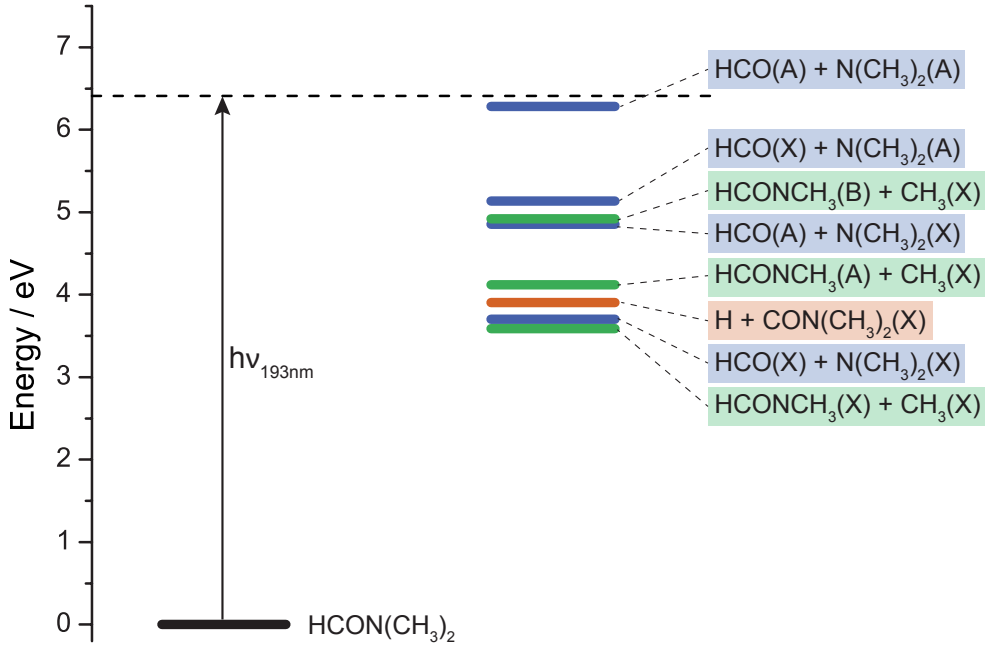

Figure 5.4: Product energies for the various DMF dissociation channels, shown relative to the electronic ground state of DMF. The horizontal dashed black line indicates the 193 nm photon energy. In this figure, X, A and B symbols have been employed to represent the ground, first, and second electronic excited states of the photofragments, respectively.

the highest electronic excited states of the photofragments formed here. As in Figure 5.3 (a), in the text that follows, the first electronic excited states of HCO and $N(CH_3)_2$ will be referred to as HCO^* and $N(CH_3)_2{}^*$, respectively.

Along the dimethylamino N−C bond stretching coordinate:

- the S_0 state asymptotically correlates with the methyl radical (CH_3) in its ground state, and its co-fragment ($HCONCH_3$) in its first electronic excited state, labelled $HCONCH_3{}^* + CH_3$
- the S_1 excited state is bound within the energy region investigated.
- the S_2 excited state asymptotically correlates over an energy barrier with the ground state products, labelled $HCONCH_3 + CH_3$.

Along the carboxyl C−H stretching coordinate:

- the S_0 state asymptotically correlates with the ground state products, labelled as $CON(CH_3)_2 + H$.

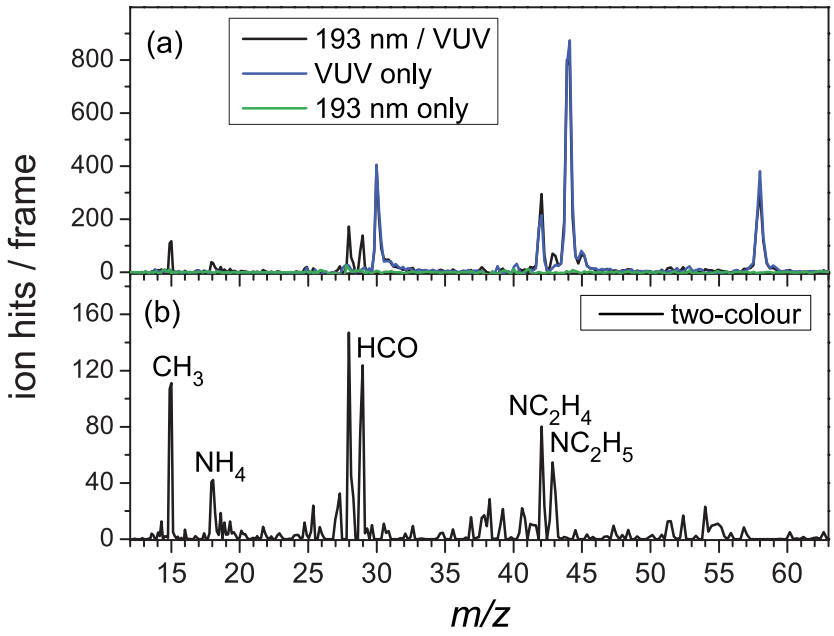

Figure 5.5: The time-of-flight mass spectra shown in panel (a) illustrate the different laser contributions to the ion signal observed. The trace in black shows the case when both lasers (193 nm and VUV) pass through the interaction region. The blue (VUV-only) and green (193 nm only) traces show the signal that arises when only the VUV laser or only the 193 nm laser pass through the interaction region. In panel (b) the two-colour TOF-MS shows the *m/z* peaks that result from 193 nm photolysis of DMF, followed by VUV photoionization of the nascent fragments.

- both the S_1 and S_2 excited states are bound within the investigated energy region.

A great deal of information about the various fragmentation pathways can be extracted from the time-of-flight mass spectra and velocity-map images, as discussed in the following sections.

5.3.1 Time-of-Flight Mass Spectra

Figure 5.5 shows the TOF-MS spectra following 193 nm photolysis of DMF, with single-photon VUV ionization of the resulting fragments. The TOF-MS when both 193 nm and 118 nm photons are present in the interaction region (black), when only the VUV laser is present (blue) and when only the 193 nm photon is present (green) are shown in Figure 5.5 (a). The two-colour (pump-probe) mass spectrum is presented in Figure 5.5 (b).[2]

[2]The IP of DMF is 9.13 eV [15]. The DMF^+ cation (*m/z* 73, not shown) is formed following VUV photoionization of neutral DMF. The peaks observed in the VUV-only mass spectrum (blue) are the result of dissociative ionization, which is the subject of the study presented in Chapter 6.

The peaks can be identified based on their mass-to-charge (*m/z*) ratios, and the assignment is shown in Figure 5.5 (b) with the exception of *m/z* 28 (see section 5.3.3.2). The photofragment identification presented here has taken into account the potential contributions to the same peak in the mass spectrum from ions with identical *m/z* ratios. For example, the HCO fragment (from N−CO bond fission) and a NCH_3^+ fragment (from possible secondary fragmentation processes) both appear at *m/z* 29. Furthermore, *m/z* 18, 28, 29, 42, and 43 could have potential contributions from NH_4^+/H_2O^+, CO^+/NCH_2^+, $CON/NC_2H_4^+$, and $CON/NC_2H_4^+$, respectively. In order to resolve these issues, TOF-MS spectra have been recorded for 193 nm dissociation of deuterated DMF ($DCON(CD_3)_2$, DMF-d_7) with detection of the nascent photofragments via single-photon VUV ionization. With the deuterated analogue, the DCO fragment appears at *m/z* 30, whereas, a NCD_3 fragment has *m/z* 32. In the two-colour mass spectrum of DMF-d_7 the peak at *m/z* 30 is present, but no signal is observed at *m/z* 32, confirming the assignment of HCO to the *m/z* 29 mass peak for the non-deuterated isotopologue. Further information has been obtained from the photofragment velocity-map images, through momentum matching of partner fragments, for example. We are therefore confident in our assignment of the identities of the various mass peaks observed in Figure 5.5 (b). As will be discussed at various points throughout this chapter, the origins of the fragment ions observed in Figure 5.5 (b) have been confirmed primarily through energetic considerations.

HCO and $N(CH_3)_2$ fragments

Breaking of the N−CO bond in DMF leads to the formation of HCO, *m/z* 29, and $N(CH_3)_2$, *m/z* 44, fragments. The HCO fragment is present in the two colour mass spectrum, Figure 5.5 (b), whereas *m/z* 44 is not observed.

Although the ionization potential (IP) of the $N(CH_3)_2$ fragment is still up for debate, ionization energies of 5.17 eV [16] and 9.1±0.2 eV [17] have been reported. We infer an experimental value maximum IP of 7.88 eV (see Section 5.3.2.1 for details). Both the reported values, and our experimentally inferred one, are below the VUV photoionization energy employed here. Therefore, this fragment should be detected. However, since the $N(CH_3)_2$ fragment is not observed in the two-colour mass spectrum, Figure 5.5 (b), it is likely that this fragment, either in its neutral or ionized form, undergoes secondary fragmentation.

The N−CO bond dissociation energy in DMF is 3.704 eV, therefore, absorption of a 193 nm photon (6.41 eV) leaves about 2.71 eV of available energy to be distributed amongst the

translational and internal (rotational, vibrational and electronic excitation) degrees of freedom of the HCO and $N(CH_3)_2$ photofragments. The bond dissociation energies, obtained from the DFT calculations, for $N(CH_3)_2$ neutral to form NC_2H_5 + H, and NC_2H_4 + H_2 are 1.51 eV and 1.21 eV, respectively. Although the ionization potentials for both the H-atom and H_2 molecule are above the VUV photon energy employed here, the ionization potential for the NC_2H_5 fragment, 9.14 eV [17], and for the NC_2H_4 fragment, 9.8 eV [17], are accessible with one 118 nm photon. These two secondary dissociation channels are possible; however, as will be discussed further in Section 5.3.2.2, the observed maximum translational energies of these fragments exceeds the maximum energy available to the fragments following neutral secondary dissociation.

Close inspection of the 193 nm only TOF-MS shown in Figure 5.5 (a) reveals that the *m/z* 44 ion is observed in a one-laser experiment. Following 193 nm photodissociation of the DMF molecule, the resultant $N(CH_3)_2$ fragment can be ionized on absorption of a second 193 nm photon, without significant dissociative ionization occurring. This allows us to detect at least some of the $N(CH_3)_2$ primary fragmentation products, and indicates that the secondary dissociation of this fragment occurs as a result of VUV photoionization.

The three secondary dissociation processes of the $N(CH_3)_2^+$ cation are of great importance in this study. This ion has been found to be highly unstable, with facile fragmentation to form $NC_2H_5^+$, *m/z* 43, and $NC_2H_4^+$, *m/z* 42, daughter ions by H-atom and H_2 molecule loss, respectively [8]. Both $NC_2H_5^+$ and $NC_2H_4^+$ fragments are observed in the two-colour mass spectrum, shown in Figure 5.5 (b). The $N(CH_3)_2^+$ cation also fragments to form the *m/z* 18 ion, which is assigned to NH_4^+.

CH_3 and $HCONCH_3$ fragments

Primary $N-CH_3$ bond fission in DMF yields CH_3 with an $HCONCH_3$ co-fragment. As will be discussed further in Section 5.3.3.1, the TOF-MS measurements, together with information from the imaging experiment, indicate that the *m/z* 15 ion is CH_3 from primary $N-CH_3$ bond fission. The $HCONCH_3$ co-fragment, *m/z* 58, it is not observed in the mass spectrum shown in Figure 5.5 (b). Either the ionization potential of this fragment is greater than the 10.49 eV available from a single VUV photon, or $HCONCH_3$ undergoes further fragmentation.

Branching into the N−CO 'peptide' and N−CH_3 fragmentation channels

In the two-colour TOF-MS spectrum, the peak at *m/z* 29 is assigned to HCO, which results from primary dissociation of N−CO bond. The peaks at *m/z* 18, 42 and 43 are assigned to NH_4^+, $NC_2H_4^+$, and $NC_2H_5^+$, respectively, which all derive from secondary dissociation processes of the $N(CH_3)_2$ co-fragment, following VUV photoionization. The peak at *m/z* 15 is assigned to CH_3, and is considered to be the only peak in the TOF-MS to result from primary dissociation of the N−CH_3 bond.

The relative branching into the two observed primary fragmentation channels, HCO + $N(CH_3)_2$ and $HCONCH_3$ + CH_3, has been estimated by integrating the areas under the peaks corresponding to NH_4^+, $NC_2H_4^+$ and $NC_2H_5^+$, and to CH_3^+, respectively. It has been assumed that the ion detection efficiencies due to the MCP detector are mass independent, and that the ionization cross sections are similar for the neutral fragments. The resulting branching ratio between the two primary fragmentation channels HCO + $N(CH_3)_2$: $HCONCH_3$ + CH_3 is 0.76 : 0.24. This ratio qualitatively reflects that obtained by Forde *et al.* of 0.64 : 0.36 for HCO + $N(CH_3)_2$: $HCONCH_3$ + CH_3 [8]. However, we note that the two studies are not directly comparable, primarily since in the latter the DMF sample was heated to 235°C, presumably yielding DMF parent molecules with a higher degree of internal excitation than in the present study. However, in both cases the N−CO bond cleavage is more prevalent than N−CH_3 bond fission.

Although the HCO fragment has been observed in the two-colour TOF-MS, it has not been taken into account in this branching calculation due to possible secondary dissociation. The HCO fragment consistently yields around 20 % less signal that that observed for the fragments resulting from $N(CH_3)_2$ dissociative ionization. Dissociative ionization of HCO following VUV photoionization has been ruled out. Although the IP of the HCO fragment (8.12 eV [15]) lies well below the VUV photon energy, the lowest dissociative ionization threshold of the HCO^+ cation, which yields H^+ + CO, lies 14.207 eV above the neutral ground state of HCO [18]. In contrast, the bond dissociation energy of neutral HCO to form H + CO is relatively low (0.609 eV [19]). If a sufficient amount of the available energy is released as internal energy of the HCO fragment, secondary dissociation of this fragment is possible. If this secondary dissociation does occur, then the VMI experiment is blind to it, since, the IPs of both H-atom (13.60 eV [15]) and CO (14.01 eV [15]) exceed the 10.49 eV available from a single VUV photon. Though there could be a number of explanations for the observed discrepancy in signal intensity, information from imaging, which will be

discussed in detail in Section 5.3.2, indicates that the principal reason is this secondary dissociation of neutral HCO.

To summarise, the TOF-MS acquired following 193 nm photodissociation of DMF, indicate that 76% of fragmentations result with N−CO 'peptide' bond fission, whereas only 24% involve N−CH_3 bond fragmentation.[3] Secondary fragmentation of the neutral HCO fragment is likely to occur, and VUV photoionization of $N(CH_3)_2$ results in dissociative ionization, with loss of H-atom, H_2 and C_2H_2 from the $N(CH_3)_2^+$ cation to form $NC_2H_5^+$, $NC_2H_4^+$, and NH_4^+ fragment ions, respectively. The information obtained from velocity-map imaging the ions that result from processes involving an initial N−CO 'peptide' bond fission will be discussed in Section 5.3.2. The processes that compete with primary N−CO bond fission will be considered further in Section 5.3.3.

5.3.2 'Peptide' bond dissociation

Absorption of a 193 nm photon followed by N−CO bond fission leaves about 2.71 eV available energy, which is distributed as internal and translational energy of the HCO and $N(CH_3)_2$ photofragments. As shown in Figure 5.3 (a), dissociation along the N−CO coordinate could take place on several low-lying singlet potential energy surfaces. The S_0 singlet ground state of DMF correlates asymptotically to the HCO* dissociation channel. The S_1 ($n\pi^*$) first singlet excited state correlates, over an energy barrier, to electronic ground state products, while the S_2 ($\pi\pi^*$) second singlet excited state correlates asymptotically to the $N(CH_3)_2{}^*$ channel. Forde *et al.* found that following absorption of a 193 nm photon, photofragmentation of DMF occurs through initial excitation of the S_2 state, and either proceeds via direct dissociation leading, to the $N(CH_3)_2{}^*$ dissociation channel, or via decay mechanisms leading to ground state photoproducts [8].

5.3.2.1 Primary Fragmentation

The velocity-map ion imaging technique enables measurement of the translational energy distribution of the dissociation products, from which the internal state distribution can be inferred. Figure 5.6 shows the ion images of the HCO and $N(CH_3)_2$ photofragments that result from DMF photolysis with 193 nm light. Since HCO (*m/z* 29) and the $N(CH_3)_2$ (*m/z* 44) are co-fragments, it it possible to obtain the total translation energy (E_T) from the measured translational energy (E_t) of either fragment, due to momentum matching of these

[3] It has not been possible to consider the H-loss processes here.

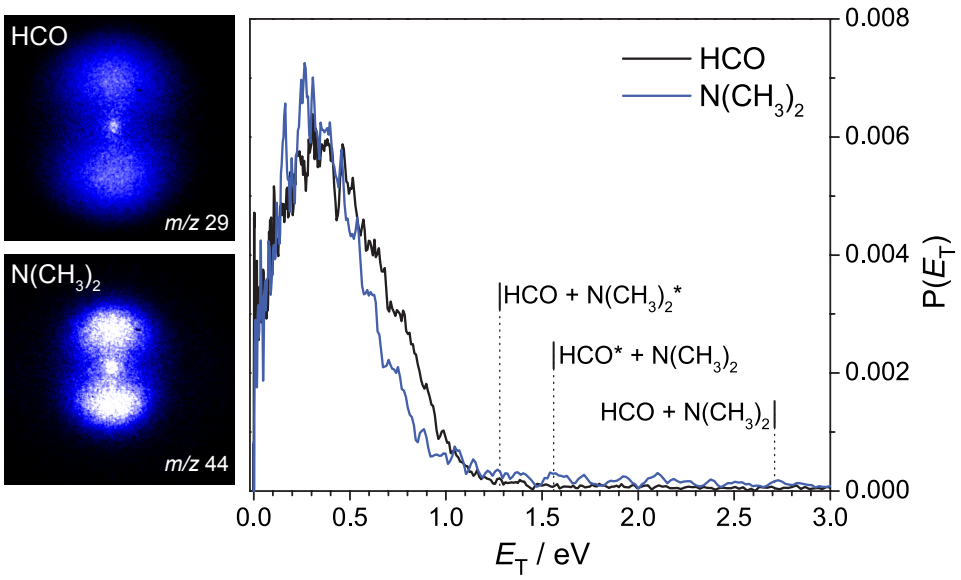

Figure 5.6: Total translational energy distributions obtained from ion images of HCO (*m/z* 29, black trace) and $N(CH_3)_2$ (*m/z* 44, blue trace) following 193 nm photolysis of DMF. The HCO fragment was ionized with a 118 nm photon, while the $N(CH_3)_2$ fragment was ionized with another 193 nm photon. The area under each $P(E_T)$ distribution is normalized to unity. The vertical dotted black lines indicate the maximum translational energies for the three energetically accessible dissociation channels that result from N−CO 'peptide' bond fission.

fragments (as discussed in Section 1.2.3).[4] The E_T distributions determined from images of both fragments are shown in the figure. The HCO fragment was ionized with a 118 nm photon, while the $N(CH_3)_2$ fragment was ionized with another 193 nm photon. The vertical dotted lines in the figure indicate the maximum accessible translational energies, i.e. the expected translational energy when all of the available energy is released into translation, for the three energetically accessible N−CO dissociation channels.

The single-photon ionization method in this work means that the HCO and $N(CH_3)_2$ photofragments are not selectively detected in a specific quantum state. The measured translational energy distributions for the two fragments therefore reflect the electronic, vibrational and rotational state distributions of the nascent fragments. After fragmentation of the 'peptide' bond, the total translational energy distributions determined from the HCO and $N(CH_3)_2$ ion images should be identical. However, the translational energy distribution obtained from the $N(CH_3)_2$ ion image is narrower than the one obtained from the HCO ion image.

[4]The E_T distribution labelled HCO was obtained from the measured E_t distribution of the HCO fragment multiplied by the mass factor (73/44). The same procedure was carried out to obtain the total translational distribution from the $N(CH_3)_2$ measured E_t distribution, except that in this case the mass factor is (73/29).

In this particular situation, as will now be discussed, the difference is mainly due to the different detection schemes employed in the two cases.

The *m/z* 44 ion image shown in Figure 5.6 was obtained in a one-laser experiment, in which the DMF molecule absorbs one 193 nm photon leading to C−N bond cleavage, and the $N(CH_3)_2$ fragment is then ionized by a second 193 nm photon. Under these conditions, only a single mass appears in the mass spectrum, at *m/z* 44, corresponding to the $N(CH_3)_2^+$ ion, with no evidence of any secondary fragmentation processes. The translational energy distribution obtained from the ion image of $N(CH_3)_2$ is depleted in the 0.5-1 eV translational energy region, relative to that obtained from the HCO ion image. The most likely explanation for this is that $N(CH_3)_2$ products formed with significant internal excitation are more likely to be ionized by the second 193 nm photon, leading to a fall off in detection efficiency with increasing translational energy (i.e. decreasing internal energy).

Primarily owing to the fact that the $N(CH_3)_2^+$ cation is highly unstable, the IP for the $N(CH_3)_2$ fragment is still open to debate. From the total translational energy distribution obtained from the $N(CH_3)_2$ ion image, we attempt to derive the value of its IP. The measured cut off for the $N(CH_3)_2$ E_T distribution is 1.24 eV, therefore, the maximum internal energy of the highest E_T fragments is 1.47 eV. Internal excitation of the $N(CH_3)_2$ fragment would have the effect of lowering the photon energy required to exceed the IP threshold. If the extreme case is considered, in which all the available internal energy is distributed as internal energy of the $N(CH_3)_2$ fragment, i.e. the HCO fragment is produced with no rotational, vibration, or electronic excitation, then the observed E_T 'cut off' for the $N(CH_3)_2$ fragments suggests a maximum IP for this fragment of 7.88 eV.

Having addressed the discrepancy at high translational energies, the features that are apparent in the E_T distribution can be considered. These distributions are fairly broad indicating that many internal states of the co-fragments are produced. There are a number of regular steps that appear in the 0.5 to 1 eV energy range in the E_T distribution obtained from the HCO ion image, which are also observed in the E_T distribution obtained from the $N(CH_3)_2$ ion image. The separation between these steps is about 0.1 eV. The likely superposition of multiple different vibrational excitations, combined with the achievable velocity resolution of the experiment, means that it is not possible to assign these features definitively. However, these steps could indicate excitation of one quantum in the ν_2 bending mode of the HCO fragment, the vibrational energy of which is 0.13 eV or 0.10 eV for ground and excited states of HCO, respectively. Excitation of such a mode would be consistent with impulsive dissociation of the N−CO bond. However, there are also a number of $N(CH_3)_2$ vibrational modes that could be excited, including the ν_9 mode (0.11 eV) that corresponds

to antisymmetric N−C stretch. The images shown in Figure 5.6 are highly anisotropic, indicating that dissociation occurs on a timescale much faster than molecular rotation. This is consistent with an impulsive dissociation that would lead to bending excitations in the two fragments. The anisotropy paramaters obtained from these images will be discussed in detail in Section 5.3.2.4.

5.3.2.2 Secondary fragmentation processes

We have seen that intact $N(CH_3)_2$ ions can be detected via 193 nm photoionization. However, VUV photoionization yields unstable $N(CH_3)_2{}^+$ ions, which rapidly undergo secondary dissociation to yield $NC_2H_5^+$, $NC_2H_4^+$, and $NH_4{}^+$. As will be discussed, the translational and angular distributions of these secondary fragment ions reflect that of the primary $N(CH_3)_2$ fragment, and therefore we can gain further insight into the primary N−CO bond fission process by analysing the velocity-map images of these secondary fragmentation products.

First we shall consider the $NC_2H_5^+$ and $NC_2H_4^+$ fragment ions, which result from H-atom and H_2 losses, respectively. These H and H_2 co-fragments are so light relative to the observed fragment ions that conservation of momentum means they will carry off essentially all of the translational energy released in the secondary fragmentation step. Therefore, the translational energy release distributions of the fragment ions may be assumed to reflect those of the primary $N(CH_3)_2$ product. The ion images of $NC_2H_5^+$ and $NC_2H_4^+$ are shown in Figure 5.7, along with the E_T distributions obtained from these images.[5] As will be discussed further in Section 5.3.2.4, the anisotropy in the images presented in this section is strong evidence that these fragments do indeed result from secondary dissociation of $N(CH_3)_2$. The observation of the intact $N(CH_3)_2{}^+$ ion following 193 nm ionization, but not following 118 nm ionization, implies that $N(CH_3)_2$ undergoes dissociative ionization on absorption of a high energy VUV photon, rather than neutral dissociation. The E_T distributions, shown in Figure 5.7, of the $NC_2H_5{}^+$ and $NC_2H_4{}^+$ fragment ions allow us to confirm that the neutral dissociation of $N(CH_3)_2$ to form NC_2H_5 and NC_2H_4 does not play a significant role in the dissociation dynamics considered here. The 'cut off' for the E_T distribution obtained from the image of $NC_2H_5{}^+$, indicates that around 1.25 eV of the 2.71 eV available energy is released into translation. If we consider the extreme case in which all of

[5] In order to obtain the total translational energy distributions from the individual E_t distributions, the two-step, three-body process which yields these fragment ions has been treated as a one-step, two-body dissociation. The E_T distributions shown in Figure 5.7, derived from the $NC_2H_5{}^+$ and $NC_2H_4{}^+$ ion images, are obtained by multiplying the individual E_t distributions with the (73/29) mass factor.

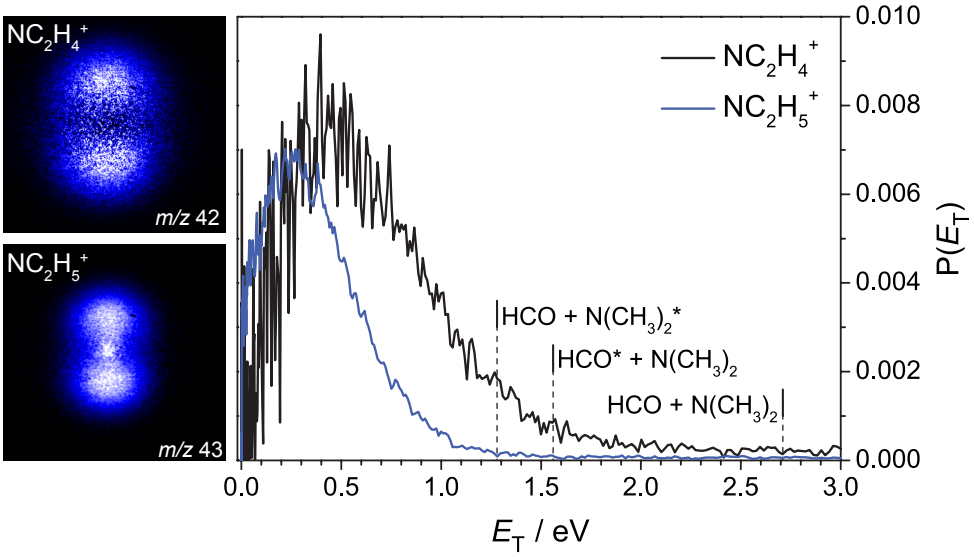

Figure 5.7: Total translational energy distributions obtained from velocity-map images of $NC_2H_4^+$ (*m/z* 42, black trace) and $NC_2H_5^+$ (*m/z* 43, blue trace), which both result from secondary dissociation of the $N(CH_3)_2$ photofragment. The area under each $P(E_T)$ distribution is normalized to unity, and the maximum translational energies for the lowest lying fragmentation products that result from N−CO 'peptide' bond fission are indicated by the vertical dashed black lines.

the remaining available energy goes into vibrational excitation of the $N(CH_3)_2$ fragment, which could therefore be channeled into bond breaking, the $N(CH_3)_2$ fragments produced with high translational energy would only have about 1.46 eV of internal energy. Therefore, even in the extreme case proposed here, these fragments would not have enough internal energy to undergo neutral secondary dissociation to yield NC_2H_5 + H, for which the bond dissociation energy is 1.51 eV. The case is the same for $NC_2H_4^+$ production. Although the neutral bond dissociation energy of $N(CH_3)_2$ to form NC_2H_4 + H_2 is lower, 1.21 eV, the E_T distributions obtained from the image of $NC_2H_4^+$ extends out to higher translational energy than in the case of $NC_2H_5^+$.

The E_T distribution obtained from the $NC_2H_4^+$ ion image is substantially broader than the one obtained from the $NC_2H_5^+$ ion image. This comes about since the former contains a contribution from the ground electronic state of $N(CH_3)_2$, as proposed by Forde *et al.* [8] through means of a complimentary experiment with trimethylamine. Dissociative ionization of the excited electronic state of $N(CH_3)_2^*$ yields both $NC_2H_4^+$ and $NC_2H_5^+$. We regard the E_T distribution obtained from the $NC_2H_5^+$ ion image as corresponding to the E_T distribution of the HCO + $N(CH_3)_2^*$ dissociation channel. The slow component in the E_T distribution obtained from the $NC_2H_4^+$ ion image also corresponds to the $N(CH_3)_2^*$

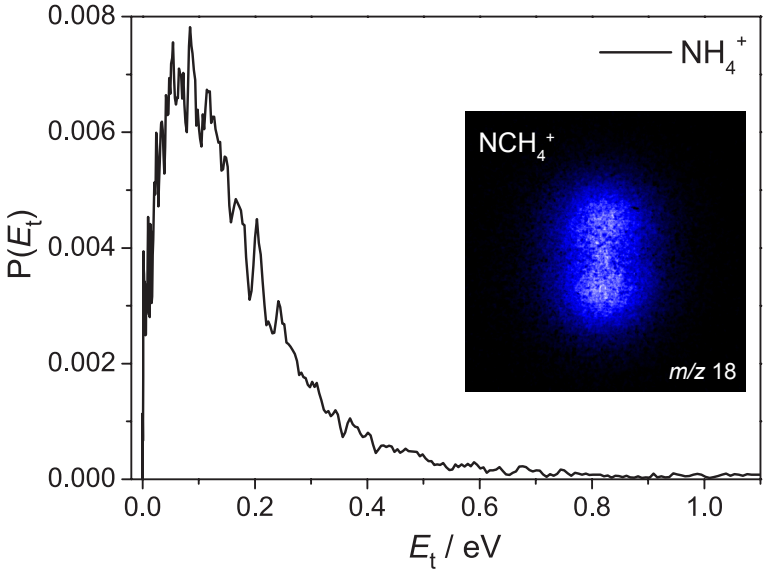

Figure 5.8: Translational energy distribution obtained from the velocity-map image of NH_4^+ (*m/z* 18), which results from secondary dissociation of the $N(CH_3)_2$ photofragment following VUV photoionization.

dissociation channel, whereas, the fast component, not observed in the E_T distribution obtained from the $NC_2H_5^+$ ion image, is assigned to the HCO^* + $N(CH_3)_2$ dissociation channel.

As discussed in Section 5.3.1, the NH_4^+ fragment ion also originates from a secondary fragmentation of $N(CH_3)_2$ following VUV photoionization. The velocity-map image of NH_4^+, and the translation energy distribution obtained from this image are shown in Figure 5.8. Note that the energy scale has not yet been converted to total translational energy. It may at first be thought that the secondary fragmentation event that yields NH_4^+ will have a more significant recoil kick than in the case of $NC_2H_4^+$ or $NC_2H_5^+$, which would result in substantial broadening of the E_t of the NH_4^+ ion relative to that of the primary $N(CH_3)_2$ fragment. However, the excess energy gained in the ionization step is consumed in rearrangement and fragmentation of the $NC_2H_6^+$ fragment ion, and, therefore, the velocity kick that occurs when $NC_2H_6^+$ loses C_2H_2 to form NH_4^+ is negligible.

The *m/z* 18 fragment ion could at a first glance of the TOF-MS, shown in Figure 5.5 (b), be assumed to be a water (H_2O) impurity in the molecular beam. However, analysis of the DMF-d_7 TOF-MS, and further information obtained from imaging, allows us to be confident with the assignment of NH_4^+ for this mass peak. In the deuterated analog of the TOF-MS, the peak corresponding to ND_4^+ (*m/z* 22) is observed, whereas the D_2O peak (*m/z* 20) is not present. In addition, the E_T distribution obtained from the *m/z* 18 ion image

has a broad translational energy distribution, and therefore must result from a fragmentation event. If a water impurity in the molecular beam were ionized,[6] the resulting ion would not have any significant transverse velocity, and would be observed as a central dot when velocity-map imaged.

5.3.2.3 Branching within the 'peptide' bond fragmentation channel

From the TOF-MS data we have estimated the branching ratio between the N−CO 'peptide' bond fission and N−CH_3 fragmentation channels. Within the 'peptide' bond fragmentation channel, we can analyse features of the measured translational energy release distributions to quantify the contributions to the signal from different electronic states of the nascent fragments. As discussed, and illustrated in Figure 5.3 (a), following 193 nm photoexcitation of DMF, N−CO bond fission can result in formation of (i) the ground state products, HCO + $N(CH_3)_2$, (ii) the formyl radical in its first excited electronic state with a ground state dimethylamidogen co-fragment, HCO* + $N(CH_3)_2$, and (iii) a ground state formyl radical with the dimethylamidogen radical in its first excited electronic state, HCO + $N(CH_3)_2{}^*$.

Reconstruction of the E_T distribution resulting from N−CO bond fission

As discussed, though 193 nm light does achieve ionization of some of the primary $N(CH_3)_2$ fragments, this method does not detect all of the nascent $N(CH_3)_2$ fragments. Therefore, in the following we consider the $NH_4{}^+$, $NC_2H_4{}^+$, or $NC_2H_5{}^+$ fragment ions which result from dissociative ionization of $N(CH_3)_2$ following VUV photoionization. The sum of the scaled individual total translational energy distributions obtained from the velocity-map images of each of these secondary fragment ions gives the total translational energy distribution for the 'peptide' bond fragmentation channel. The individual contributions to the overall E_T distribution can be determined from the two-colour TOF-MS spectrum, shown in Figure 5.5 (a). Integrating the areas under the three peaks corresponding to $NH_4{}^+$, $NC_2H_4{}^+$, and $NC_2H_5{}^+$ in the TOF-MS spectrum gives the following experimental weighting coefficients: 0.17, 0.49, and 0.34 for *m/z* 18, 42, and 43, respectively. By multiplying each total translational energy distribution by its corresponding weighting coefficient, and then summing the individual contributions, it has been possible to obtain the 'reconstructed' E_T distribution shown in blue in Figure 5.9. This reconstructed distribution represents the distribution that would be obtained if it were possible to directly detect all of the primary

[6] It is noted that the ionization of water would have to occur in a multiphoton process since its IP, 12.62 eV [15], exceeds the energy available from one VUV photon.

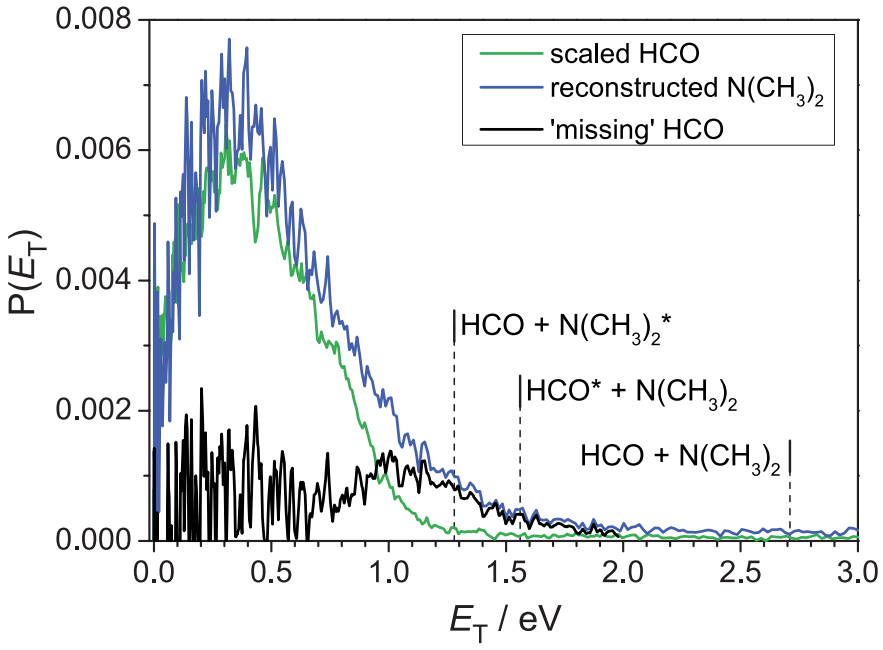

Figure 5.9: A scaled P(E_T) distribution obtained from the image of HCO (green) is compared to the reconstructed $N(CH_3)_2$ P(E_T) distribution (blue), which takes into account contributions from all the fragments that result from secondary dissociation of this species (see text for details). The 'missing' HCO trace (black) has been obtained by subtracting the former from the latter. The vertical dashed black lines indicate the maximum translational energies for the lowest lying fragmentation products that result from N−CO 'peptide' bond fission.

$N(CH_3)_2$ photofragments. The low energy region of this reconstructed E_T distribution (up to around 1 eV) has contributions from all three secondary fragmentation products, which result from secondary dissociation of the $N(CH_3)_2^*$ fragment. The main contribution to the high energy region, which extends to around 1.8 eV, comes from $NC_2H_4^+$ resulting from ground state $N(CH_3)_2$ secondary dissociation.

Neutral dissociation of the HCO fragment

The reconstructed E_T distribution has been compared with that obtained from the image of the HCO co-fragment, shown in Figure 5.9 in green. This latter P(E_T) distribution has been scaled to account for the discrepancy between the number of observed HCO fragments and the total number of fragments resulting from secondary dissociation of $N(CH_3)_2$, as mentioned in the discussion of branching ratios in Section 5.3.1. The third distribution (shown in black in Figure 5.9) has been obtained by subtracting this HCO P(E_T) distribution from the reconstructed P(E_T) distribution. Such a distribution gives an idea of which (and what fraction) of the HCO fragments undergo neutral dissociation, and are therefore

not detected (hence, the label of 'missing' HCO). As discussed, the low energy region of the reconstructed E_T distribution has been assigned to $N(CH_3)_2^*$ production. Since the channel resulting in formation of both photofragments in their first excited electronically excited states is not accessed here, the low energy region must correspond to production of $N(CH_3)_2^*$ + HCO. We consider that the low energy region of the 'missing' HCO E_T distribution corresponds to production of ground state HCO that has sufficient internal energy to go above the H + CO dissociation threshold. The higher energy region of this E_T distribution, in the range from around 0.6 eV to 1.8 eV, is considered to correspond to formation of electronically excited HCO^* (formed with ground state $N(CH_3)_2$) that undergoes predissociation to yield H + CO.

Branching between the HCO^*, $N(CH_3)_2^*$ and CH_3 dissociation channels

In summary, analysis of the E_T distributions obtained from the ion images of all of the fragments resulting from N−CO 'peptide' bond fission reveals that the high E_T fragments result from the HCO^* + $N(CH_3)_2$ dissociation channel, whereas those at lower E_T result from the HCO + $N(CH_3)_2^*$ dissociation channel. The dissociation channel that produces ground state products, which is symmetry forbidden within the planar framework of DMF, is not thought to be active. The channel that yields both fragments in the first electronic excited state, HCO^* + $N(CH_3)_2^*$, is only just accessible with the photon energy available from 193 nm light. However, this channel is also symmetry forbidden, and is not thought to play a significant role in the dissociation dynamics resulting from 193 nm photolysis of DMF.[7] Therefore, only the HCO^* and $N(CH_3)_2^*$ channels from N−CO 'peptide' bond dissociation will be considered in the following relative branching. By taking into account the CH_3 elimination channel, which will be discussed in the next section, it is possible to evaluate the relative branching between the three DMF dissociation channels: the HCO* channel, the $N(CH_3)_2^*$ channel, and methyl elimination channel. HCO^* + $N(CH_3)_2$: HCO + $N(CH_3)_2^*$: $HCONCH_3$ + CH_3 = 0.06 : 0.74 : 0.24.[8]

As discussed, there can only be a limited comparison between the work presented here and the study by Forde *et al.* [8]. In the previous work, many of the mass peaks observed were assigned contributions from several different fragments, which resulted from primary and secondary dissociation. In the current work, from the TOF-MS following 193 nm photolysis of DMF-d_7, in combination with information obtained from imaging, it has been

[7] Excitation and dissociation of vibrationally excited parent molecules (resulting from inefficient cooling in the supersonic expansion) to yield these products may account for the intensity occasionally observed in the central region of the velocity-map images.

[8] This ratio has been obtained from the relative ratio of the photofragments observed in the TOF-MS, and the branching into HCO^* and $N(CH_3)_2^*$ channels from the E_T distribution of *m/z* 42.

possible to clarify the identities of these fragments shown in Figure 5.5 (b). In addition, from the E_T distributions of the fragments resulting from primary N−CO bond fission, the contribution to the DMF dissociation from the HCO* dissociation channel has been observed for the first time. Forde *et al.* obtained a branching ratio of 0.15 : 0.49 : 0.36 for HCO + $N(CH_3)_2$: HCO + $N(CH_3)_2$* : $HCONCH_3$ + CH_3. As discussed the ground state product channel is not thought to be active here. The current work has also observed the dominant channel to be production of HCO + $N(CH_3)_2$*, which have been assigned to the asymptote of the S_2 state.

5.3.2.4 Photofragment angular distributions

As illustrated by the PECs shown in Figure 5.3 (a), initial excitation to the S_1 electronic excited state of DMF leads to ground state $N(CH_3)_2$ and HCO, whereas direct dissociation on S_2 along the N−CO bond coordinate leads to electronically excited $N(CH_3)_2$*, and ground state HCO. The former dissociation yields fragments with more translational energy than those that result from the latter dissociation channel.

The angles of the transition dipole moments (μ) relative to the dissociating N−CO bond have been calculated (as described in Section 5.2.2) for the S_0/S_1 and S_0/S_2 transitions as 9° and 14.5°, respectively. Both transitions are nearly 'parallel', for which the limiting anisotropy parameter is β=2. From the μ angles, anisotropy parameters have been calculated for each of the transitions. For $S_0 \leftarrow S_1$ we obtain β=1.92, and for $S_0 \leftarrow S_2$, β=1.81. However, such calculations assume a rapid dissociation. As shown in Figure 5.3 (a) the S_1 state exhibits an energy barrier to dissociation, and S_2 is partially bound.

The ion image of HCO, shown in Figure 5.6, yields an anisotropy parameter of 0.95 in the low E_T energy range from 0.2 eV to 0.6 eV, corresponding to the HCO + $N(CH_3)_2$* dissociation channel. The value of the anisotropy parameter is observed to increase to 1.6 in the high E_T energy range from 0.6 to 1.2 eV, corresponding to the HCO* + $N(CH_3)_2$ dissociation channel. The ion image of the $N(CH_3)_2$ fragment (detected via 193 nm photoionization) yields an E_T distribution that corresponds to HCO + $N(CH_3)_2$* production. The anisotropy parameter obtained from this image has a value of 1.15. These large positive anisotropy parameters obtained for both the HCO* and $N(CH_3)_2$* dissociation channels indicate an initial 'parallel' transition, which is consistent with initial population of both the S_1 and S_2 states.

The images of the NH_4^+, $NC_2H_4^+$, and $NC_2H_5^+$ fragment ions, shown in Figures 5.7 and 5.8, all display significant and quite similar anisotropy, which assists in confirming

that these fragment ions do indeed result from an initial N−CO 'peptide' bond dissociation. As will be seen in Section 5.3.3, such anisotropy is not observed for those fragments that result from competing dissociation channels. Anisotropy parameters from the $NC_2H_4^+$ image have been obtained for the low E_T region, which corresponds to production of HCO + $N(CH_3)_2^*$, and for the high E_T range, which corresponds to production of HCO^* + $N(CH_3)_2$. These are 1.07 and 1.24, respectively. An anisotropy parameter value of 1.28 and 0.9 has been obtained from the $NC_2H_5^+$ and NH_4^+ ion image. These fragments result from secondary dissociation of $N(CH_3)_2^*$. Though secondary dissociation may have the effect of reducing the observed anisotropy, the values obtained will at least qualitatively reflect the anisotropy resulting from primary fragmentation.

It appears that the images of the fragments resulting from the HCO + $N(CH_3)_2^*$ dissociation channel yield anisotropy parameter values of around $\beta = 1$. These fragments are assigned to the asymptotic limit of the S_2 state. The observed β are reduced as compared to the calculated value for an initial $S_0 \leftarrow S_2$ transition. This reduction in the angular distribution may come about as a result of the partially bound character of the S_2 state. HCO^* + $N(CH_3)$ photofragments appear to result with larger β. These fragments are assigned to the asymptotic limit of the S_0 state, therefore a fast crossing from the initially excited state to the S_0 state must occur as dissociation proceeds along the N−CO bond stretching coordinate.

5.3.3 Competing fragmentation channels

5.3.3.1 Methyl elimination channel

As shown by the PECs displayed in Figure 5.3 (b), dissociation along the $N-CH_3$ stretching coordinate on the S_2 state of DMF proceeds over a barrier to yield the electronic ground state $HCONCH_3$ + CH_3 products. The DFT calculations return a DMF $N-CH_3$ bond dissociation energy of 3.60 eV to yield these ground state products. The S_1 excited electronic state is bound within the energy region accessed here, whereas the S_0 state correlates with the first excited state of $HCONCH_3^*$ formed with a ground state CH_3 co-fragment. The energy of this $HCONCH_3^*$ fragment lies at an energy of 0.53 eV above its electronic ground state. The second excited state of $HCONCH_3$ is also energetically accessible following 193 nm photolysis of DMF, since it lies only 1.33 eV above its ground state. In contrast, the first excited state of the CH_3 radical is 5.73 eV above its ground state [20], and therefore will not be formed.

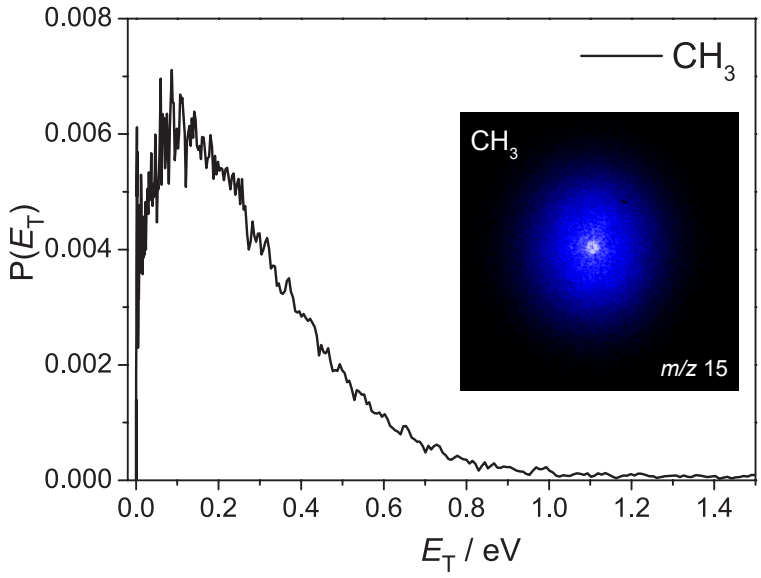

Figure 5.10: Total translational energy distribution obtained from the velocity-map image of CH_3 (*m/z* 15), which results from primary N−CH_3 bond fragmentation.

Of the two primary photofragments that result from N−CH_3 bond fragmentation, only CH_3, with *m/z* 15, is observed in the TOF-MS. This indicates one of two things: either the $HCONCH_3$ fragment, *m/z* 58, has an IP that exceeds the energy of the 118 nm photon employed for the photoionization step, or the fragment ion formed as a result of VUV photoionization is very unstable and undergoes secondary fragmentation.

The total translational energy distribution obtained from the CH_3 ion image, shown in Figure 5.10, exhibits a broad, structureless peak at lower E_T than was observed for the fragments resulting from primary 'peptide' bond fission. The energy released into translation in the N−CH_3 bond dissociation channel is significantly less than the available energy. The observed distribution is consistent with initial excitation to a bound region of the excited state (S_1 or S_2) and a dissociation mechanism that proceeds either over a barrier (such as that on the S_2 state), or via internal conversion (IC) followed by fragmentation of internally 'hot' parent molecules on the S_0 state. Such processes result in highly internally excited fragments, with only a small fraction of the available energy being released into translation. The CH_3 ion image displays an isotropic angular distribution. Such a distribution can be the result of a slow dissociation (either over a barrier or via IC).

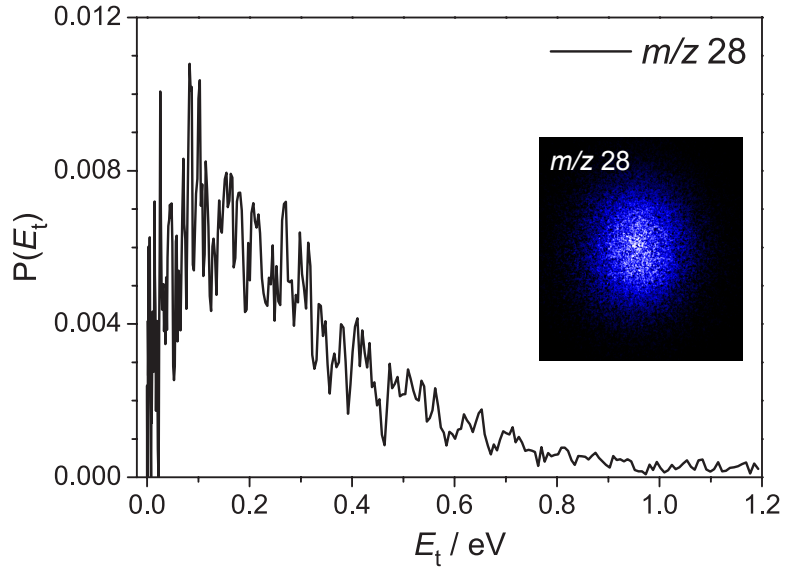

Figure 5.11: Translational energy distribution obtained from the velocity-map image of *m/z* 28, which potentially results from a molecular dissociation channel.

5.3.3.2 *m/z* 28 production

The fragment observed at *m/z* 28 in the TOF-MS presents another possible competing fragmentation channel. The ion image of *m/z* 28, shown in Figure 5.11 is fairly isotropic, and this fragment is not thought to originate from primary N−CO 'peptide' bond fission. *m/z* 28 could correspond to a number of different fragment ions, including CO^+ and $NCH_2{}^+$.

The production of *m/z* 28 does not correspond to formation of neutral CO. If the CO fragment was formed as a neutral it would not be possible to detect it, since the IP of this fragment, 14.01 eV [15], exceeds the photon energy of a single VUV photon. The CO^+ ion could potentially be formed from a dissociative ionization of $HCONCH_3$. However, *m/z* 28 is not observed in the two-colour TOF-MS of DMF-d_7, which could indicate that this fragment is not CO^+.

As will be discussed in Chapter 6, the $NCH_2{}^+$ ion has been observed in the dissociation of the DMF^+ ion, though its structure is unconfirmed. In the case of DMF^+ ion photolysis this fragment ion could result from secondary dissociation of either $NC_2H_6^+$ or $HCONHCH_2{}^+$. However, in the case of the neutral dissociation study, it is most likely that *m/z* 28 corresponds to $NCH_2{}^+$, which results with a neutral OCH_2 co-fragment from dissociative ionization of $HCONCH_3$. Considering that a significant fraction of the energy available to the fragments would be consumed in the rearrangement, and the secondary fragments

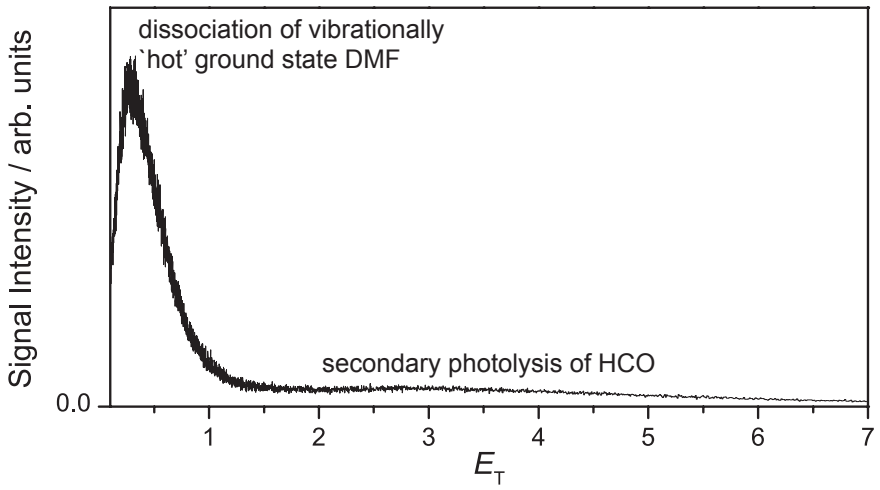

Figure 5.12: E_T spectrum derived from the H atom TOF spectra for DMF photolysis with 193 nm light.

would have little recoil kick, it can be expected that the translational and angular distributions of the secondary fragments would reflect those of the primary ones, as was observed for NH_4^+.

5.3.3.3 H elimination

In collaboration with the Bristol laser group, H Rydberg atom photofragment translational spectroscopy has been employed to investigate H loss from DMF. TOF spectra of H atoms from photolysis of DMF were acquired at an excitation wavelength of 193 nm. These were converted to total translational energy release, E_T, spectra of the H + $CON(CH_3)_2$ products, with respective masses m_H and m_R, where R is the radical co-fragment, using the relationship

$$E_T = \frac{1}{2} m_H \left(1 + \frac{m_H}{m_R}\right) \left(\frac{d}{t}\right)^2 \tag{5.1}$$

where d is the length of the flight tube (36.9 cm). A t^{-3} Jacobian has been applied to re-bin the intensities. The co-fragment resulting from primary C−H bond fission in DMF would have m_R = 72.09 u.

The E_T spectrum derived from the H atom TOF spectra from DMF photolysis with 193 nm light is displayed in Figure 5.12. The spectrum displays a peak at low E_T (<0.5 eV) that stretches to E_T ∼1.5 eV, and a low intensity feature extending to much higher translational energy. The profile of this signal at low E_T, and its relative insensitivity to changes in

excitation wavelength,[9] suggests that this component is most likely attributable to H atoms from the unimolecular decay of highly vibrationally excited ground state parent molecules formed following internal conversion from the excited electronic state(s) populated in the initial photon absorption [21]. The fast component extends to an E_T that is far greater than can be accommodated in terms of C–H bond fission within the methyl or aldehydic groups, but would be consistent with secondary photolysis of HCO radicals.[10]

5.4 Conclusions

We have presented our preliminary analysis of the 193 nm photolysis of N,N-dimethylformamide. This amide presents three fragmentation channels: (i) N−CO 'peptide' bond fission, which yields HCO + $N(CH_3)_2$, (ii) N−CH_3 bond fragmentation, which yields $HCONCH_3$ + CH_3, and (iii) H-atom loss. A branching ratio has been obtained for the N−CO and N−CH_3 fragmentation channels, HCO + $N(CH_3)_2$: $HCONCH_3$ + CH_3 = 0.76 : 0.24, which agrees qualitatively with the ratio obtained by Forde *et al.* [8]. Analysis of the E_T distributions obtained from images of the fragments resulting from primary N−CO 'peptide' bond fission reveals the production of the HCO* + $N(CH_3)_2$ and HCO + $N(CH_3)_2$* photofragments, with the latter being significantly more abundant. The non-statistical translational energy distributions and large positive anisotropy parameters obtained from the images of the fragments resulting from primary N−CO 'peptide' bond fission indicate that this is a relatively rapid process. The E_T distributions obtained from the HCO and $N(CH_3)_2$ primary photofragments show evidence for bending excitations in these products, which is consistent with an impulsive dissociation. The primary CH_3 photofragment, resulting from N−CH_3 bond fragmentation, has been observed, whereas its co-fragment, $HCONCH_3$, most likely undergoes secondary dissociation to form *m/z* 28. N−CH_3 dissociation yields highly internally excited fragmentation products, which display isotropic angular distributions, in contrast to those observed for the fragments that result from primary N−CO 'peptide' bond fission. An overall branching ratio for HCO* + $N(CH_3)_2$: HCO + $N(CH_3)_2$* : $HCONCH_3$ + CH_3 of 0.06 : 0.74 : 0.24 has been obtained. H loss from DMF has been investigated though H Rydberg atom photofragment translational spectroscopy. This has revealed that H loss most likely results from unimolecular decay of highly vibrationally excited ground

[9] H loss from DMF has been investigated at a number of different UV wavelengths using the H Rydberg atom PTS, the results of which will be presented in full in a future publication [11].

[10] The details of this will be discussed further, in light of the results of H atom production at a range of photolysis wavelengths, in the future publication [11].

state parent molecules, which are formed following internal conversion from the excited electronic state(s) that are populated in the initial photon absorption.

References

[1] Brodbelt, JS. *Shedding Light on the Frontier of Photodissociation*. Journal of the American Society for Mass Spectrometry **22**:2 197–206 (2011) (cited p. 111).

[2] Clayden, G, Warren, S, Greeves, N, and Wothers, P. *Organic Chemistry*. Oxford University Press (2000) (cited p. 112).

[3] Hunt, HD and Simpson, WT. *Spectra of Simple Amides in the Vacuum Ultraviolet*. Journal of the American Chemical Society **75**:18 4540–4543 (1953) (cited p. 112, 116).

[4] Kaya, K and Nagakura, S. *Vacuum Ultraviolet Absorption Spectra of Simple Amides*. Theoretica Chimica Acta **7**:2 117–123 (1967) (cited p. 112, 116).

[5] Serrano-Andrés, L and Fülscher, MP. *Theoretical Study of the Electronic Spectroscopy of Peptides. 1. The Peptidic Bond: Primary, Secondary, and Tertiary Amides*. Journal of the American Chemical Society **118**:48 12190–12199 (1996) (cited p. 112).

[6] Liu, D, Fang, W, Lin, Z, and Fu, X. *The photodissociation of N,N-dimethylformamide: A complete active space self-consistent field study*. The Journal of Chemical Physics **117**:20 9241 (2002) (cited p. 112).

[7] Forde, NR, Myers, TL, and Butler, LJ. *Chemical reaction dynamics when the Born-Oppenheimer approximation fails Understanding which changes in the electronic wavefunction might be restricted*. Faraday Discussions **108**: 221–242 (1997) (cited p. 112).

[8] Forde, NR, Butler, LJ, and Abrash, SA. *Electronic accessibility of dissociation channels in an amide: N,N-dimethylformamide photodissociation at 193 nm*. The Journal of Chemical Physics **110**:18 8954–8968 (1999) (cited p. 112, 113, 117, 121–123, 127, 131, 137).

[9] Eckert-Maksić, M and Antol, I. *Study of the Mechanism of the N-CO Photodissociation in N, N-Dimethylformamide by Direct Trajectory Surface Hopping Simulations*. The Journal of Physical Chemistry A **113**:45 12582–12590 (2009) (cited p. 112).

[10] Cronin, B, Nix, M, Qadiri, RH, and Ashfold, M. *High resolution photofragment translational spectroscopy studies of the near ultraviolet photolysis of pyrrole*. Physical Chemistry Chemical Physics **6**: 5301–5041 (2004) (cited p. 114).

[11] Lipciuc, ML, Gardiner, SH, Karsili, TNV, Ashfold, MNR, and Vallance, C. *193 nm photolysis of N,N-dimethylformamide: a velocity-map imaging study*. in preparation (2013) (cited p. 115, 137).

[12] Frisch, MJ, Trucks, GW, Schlegel, HB, Scuseria, GE, Robb, MA, Cheeseman, JR, Scalmani, G, Barone, V, Mennucci, B, Petersson, GA, Nakatsuji, H, Caricato, M, Li, X, Hratchian, HP, Izmaylov, AF, Bloino, J, Zheng, G, Sonnenberg, JL, Hada, M, Ehara, M, Toyota, K, Fukuda, R, Hasegawa, J, Ishida, M, Nakajima, T, Honda, Y,

Kitao, O, Nakai, H, Vreven, T, Montgomery, JA, Peralta, JE, Ogliaro, F, Bearpark, M, Heyd, JJ, Brothers, E, Kudin, KN, Staroverov, VN, Kobayashi, R, Normand, J, Raghavachari, K, Rendell, A, Burant, JC, Iyengar, SS, Tomasi, J, Cossi, M, Rega, N, Millam, JM, Klene, M, Knox, JE, Cross, JB, Bakken, V, Adamo, C, Jaramillo, J, Gomperts, R, Stratmann, RE, Yazyev, O, Austin, AJ, Cammi, R, Pomelli, C, Ochterski, JW, Martin, RL, Morokuma, K, Zakrzewski, VG, Voth, GA, Salvador, P, Dannenberg, JJ, Dapprich, S, Daniels, AD, Farkas, Foresman, JB, Ortiz, JV, Cioslowski, J, and Fox, DJ. *Gaussian 09, Revision B.01*. Tech. rep. 2009 (cited p. 115).

[13] Werner, HJ, Knowles, PJ, Knizia, G, Manby, FR, Schütz, M, Celani, P, Korona, T, Lindh, R, Mitrushenkov, A, Rauhut, G, Shamasundar, KR, Adler, TB, Amos, RD, Bernhardsson, A, Berning, A, Cooper, DL, Deegan, MJO, Dobbyn, AJ, Eckert, F, Goll, E, Hampel, C, Hesselmann, A, Hetzer, G, Hrenar, T, Jansen, G, Köppl, C, Liu, Y, Lloyd, AW, Mata, RA, May, AJ, McNicholas, SJ, Meyer, W, Mura, ME, Nicklass, A, O'Neill, DP, Palmieri, P, Pflüger, K, Pitzer, R, Reiher, M, Shiozaki, T, Stoll, H, Stone, AJ, Tarroni, R, Thorsteinsson, T, Wang, M, and Wolf, A. *MOLPRO, version 2010.1, a package of ab initio programs*. Tech. rep. 2010 (cited p. 115).

[14] Jacox, ME. *Vibrational and Electronic Energy Levels of Polyatomic Transient Molecules (retrieved October 30, 2013)*. Ed. by Linstrom, PJ and Mallard, WG. NIST Chemistry WebBook, NIST Standard Reference Database Number 69. National Institute of Standards and Technology, Gaithersburg MD, 20899 (cited p. 117).

[15] Lias, SG. *"Ionization Energy Evaluation" in NIST Chemistry WebBook, NIST Standard Reference Database Number 69, (retrieved June 19, 2013)*. Ed. by Linstrom, PJ and Mallard, WG. National Institute of Standards and Technology, Gaithersburg MD, 20899 (cited p. 119, 122, 129, 135).

[16] Lias, SG and Liebman, JF. *"Ion Energetics Data" in NIST Chemistry WebBook, NIST Standard Reference Database Number 69, National Institute of Standards and Technology, Gaithersburg MD, 20899, http://webbook.nist.gov, (retrieved March 29, 2013).* Ed. by Linstrom, PJ and Mallard, WG (cited p. 120).

[17] Forde, NR, Butler, LJ, Ruscic, B, Sorkhabi, O, Qi, F, and Suits, A. *Characterization of nitrogen-containing radical products from the photodissociation of trimethylamine using photoionization detection*. The Journal of Chemical Physics **113**:8 3088–3097 (2000) (cited p. 120, 121).

[18] Koch, A, Hemert, MC van, and Dishoeck, EF van. *Photodissociation of the HCO^+ ion. Two dimensional calculations through the $I^1\Pi$ state*. The Journal of Chemical Physics **103**:16 7006 (1995) (cited p. 122).

[19] Mourik, T van, Dunning, TH, and Peterson, KA. *Ab Initio Characterization of the $HCO^x(x = -1, 0, +1)$ Species: Structures, Vibrational Frequencies, CH Bond Dissociation Energies, and HCO Ionization Potential and Electron Affinity*. The Journal of Physical Chemistry A **104**:11 2287–2293 (2000) (cited p. 122).

[20] Settersten, TB, Farrow, RL, and Gray, JA. *Coherent infrared–ultraviolet double-resonance spectroscopy of CH_3*. Chemical Physics Letters **370**:1-2 204–210 (2003) (cited p. 133).

[21] Feltham, EJ, Qadiri, RH, Cottrill, E, Cook, PA, Cole, JP, Balint-Kurti, GG, and Ashfold, MNR. *Ketene photodissociation in the wavelength range 193 - 215 nm: The H atom production channel*. The Journal of Chemical Physics **119**:12 6017–6031 (2003) (cited p. 137).

6

Photofragmentation of the N,N-dimethylformamide cation

Contents

6.1 Introduction

Peptide bonds link amino acids within polypeptide chains, which form proteins. These large macromolecules are an essential part of life as we know it. An increasingly important method for determining the structures of such large biomolecules is through the analysis of the fragmentations which occur in mass spectrometry (MS) [1–5]. There are a range of methods used to achieve fragmentation within mass spectrometers. These include infrared multiphoton photodissociation (IRMPD), collision induced dissociation (CID), also known as collision-assisted dissociation (CAD), electron capture dissociation (ECD), and ultraviolet photodissociation (UVPD) (see [6] and references therein). Different activation methods achieve different fragmentation patterns. For example, IRMPD involves small incremental transfer of energy, and the excitation generally occurs on a timescale which

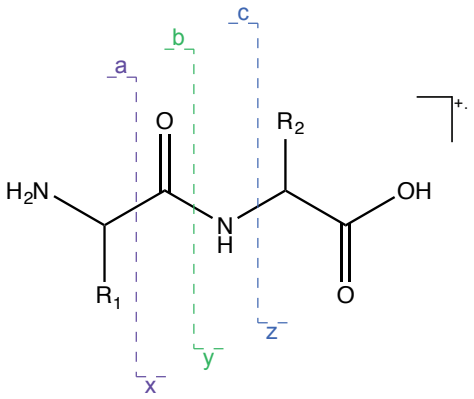

Figure 6.1: Structure of a generic dipeptide radical cation. Three bond fragmentations are illustrated, see text for details.

allows for intramolecular vibration redistribution. As a result of this, IRMPD generally results in statistical dissociation, with the weakest bond being most likely to fragment. In contrast, UVPD directly transfers a significant amount of energy to the species of interest. Such a process would be more likely to result in fast direct cleavage of a bond within the absorbing chromophore, without further vibrational redistribution.

In order to discuss in a clear and concise way the various possible fragment ions, the mass spectrometry community has developed a succinct nomenclature. The labelling of the fragment ions is illustrated for a generic dipeptide in Figure 6.1. If, following fragmentation, the amino-termius (left-hand side) retains the charge, the ion is labelled **a**, **b** or **c**. However, if the charge remains on the carboxy-terminus then the ion is labelled **x**, **y** or **z**. The allocated letter depends on which bond has been broken within the peptide chain. The primary fragmentation within polypeptides is of the C-N peptide amide bond [5], resulting in formation of either **b** or **y** ions.

At present, there is no fundamental theory to predict the fragmentation patterns of proteins in mass spectrometry studies. It is often the case that the true structure of the fragment ions is not known [5]. Though MS obtains the masses of the fragments, it alone is not able to reveal the connectivity within the parent molecule. Generally, MS studies are combined with techniques such as ion mobility spectrometry [7–10] and hydrogen/deuterium exchange [11–13] to determine the structure of proteins.

It is neither practical, nor currently possible, to undertake dynamical studies, such as those presented here, on such large species. However, fragment imaging studies on model peptide-bond-containing compounds can reveal how the larger biomolecules, which contain such structures, might be expected to dissociate. As discussed in Chapter 5, N,N-

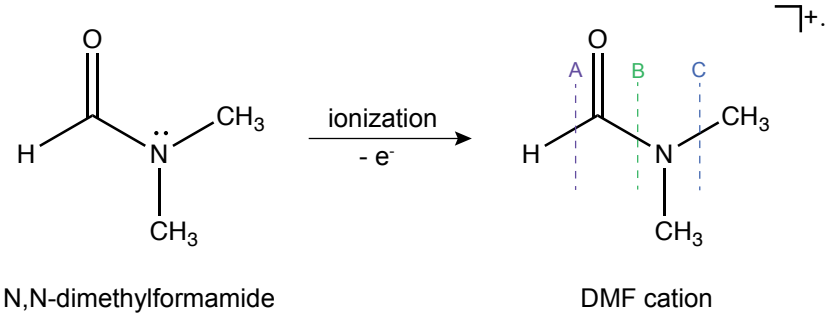

Figure 6.2: N,N-dimethylformamide cation. Labelling of the bond fragmentations is consistent with Figure 6.1, see text for details.

dimethylformamide (DMF), shown in Figure 6.2, with its carbonyl-nitrogen bond linkage, has been chosen as our model for a peptide bond.

MS studies involve fragmentation of the parent *ion*, generated by means of electrospray ionization (ESI), matrix-assisted laser desorption/ionization (MALDI), electron impact (EI) ionization or vacuum-ultra violet (VUV) photoionization [1–5, 14]. Therefore, the work presented here, which employs time-of-flight mass spectrometry and velocity-map imaging, has investigated the photofragmentation of the DMF *cation*, DMF^+, generated by means of VUV photoionization.

Arimura and Yoshikawa [15] have identified a number of key photofragment ions resulting from VUV photoionization of DMF in the energy range 9 - 13 eV. They were able to measure the appearance energies of these fragment ions and of the DMF parent cation (*m/z* 72). Three of the fragment ions observed, $CON(CH_3)_2{}^+$ (*m/z* 72), $NC_2H_6^+$ (*m/z* 44), and $HCONCH_3{}^+$ (*m/z* 58), were assigned to unimolecular decomposition processes of the parent ion:

(A) H loss (from the carbonyl carbon)

$$HCON(CH_3)_2^+ \rightarrow H + CON(CH_3)_2^+$$

(B) N−CO ‘peptide’ bond cleavage

$$HCON(CH_3)_2^+ \rightarrow HCO + NC_2H_6^+$$

(C) $N-CH_3$ bond fragmentation

$$HCON(CH_3)_2^+ \rightarrow HCONCH_3^+ + CH_3$$

The bond cleavages involved in these fragmentation processes are illustrated in Figure 6.2. Channel (B) involves fragmentation of the 'peptide' bond, which is of particular interest in the current work. The $NC_2H_6^+$ ion, which results from this apparently simple N−CO bond cleavage process, was observed to have an appearance energy (AE) of 10.59 eV [15]. However, a second rise in intensity of the *m/z* 44 ion, at around 12.2 eV, was also apparent. From these observations Arimura and Yoshikawa constructed a schematic plan of the potential energy surfaces of the DMF cation, along the lines of that shown in Figure 6.3 (b). The first appearance energy was assigned to formation of HCO + $NC_2H_6^+$ from a vibrationally excited ground state DMF^+ parent ion. Excitation to a bound excited state, at around 12 eV (above the neutral ground state of the DMF parent), followed by internal conversion to a dissociative state, results in the formation of the same HCO + $NC_2H_6^+$ products, but with significantly more of the available energy released into product translation.

The AEs of the ions resulting from Channel (A), $CON(CH_3)_2{}^+$, and Channel (C), $HCONCH_3{}^+$, were both determined to be 10.77 eV [15]. Since these AEs were so similar to the first AE of $NC_2H_6^+$, the formation of all three ions was tentatively attributed to fragmentation of the vibrationally excited parent ion in its electronic ground state. Such an internally excited parent molecule was considered to result from an ionization step involving the removal of an electron from the antisymmetric π molecular orbital (which if the conjugation between the carbonyl and nitrogen were removed would exist as a lone pair on N), which reduces the strength of the N−CO bond and causes significant structural changes within the parent molecule.

In quick succession to Arimura and Yoshikawa's study, though apparently without reference to this previous work, Riley and Baer [16] undertook a photoelectron-photoion coincidence (PEPICO) study of the unimolecular decay of low energy DMF cations, in the photon energy range 11.11 - 11.49 eV. Although the $CON(CH_3)_2{}^+$ ion, Channel (A), is energetically accessible in the energy region investigated [15], Riley and Baer concluded that the *m/z* 72 ion did not result from H loss from the parent cation, but was in fact formed from fragmentation of a DMF cluster [16]. Therefore, the authors focused their investigation on Channel (B) and Channel (C). Through RRKM modelling of the PEPICO data, barriers to dissociation were found at energies of 1.60 eV and 1.68 eV (above the ground state of the parent ion), for Channel (B) and Channel (C), respectively.

The consistency in the barrier heights for Channel (B) and Channel (C) determined by Riley and Baer [16] and the AEs of the corresponding ions determined by Arimura and Yoshikawa [15], serves to strengthen the argument that photoionization results in formation of internally excited parent ions that have enough energy to surpass the dissociation

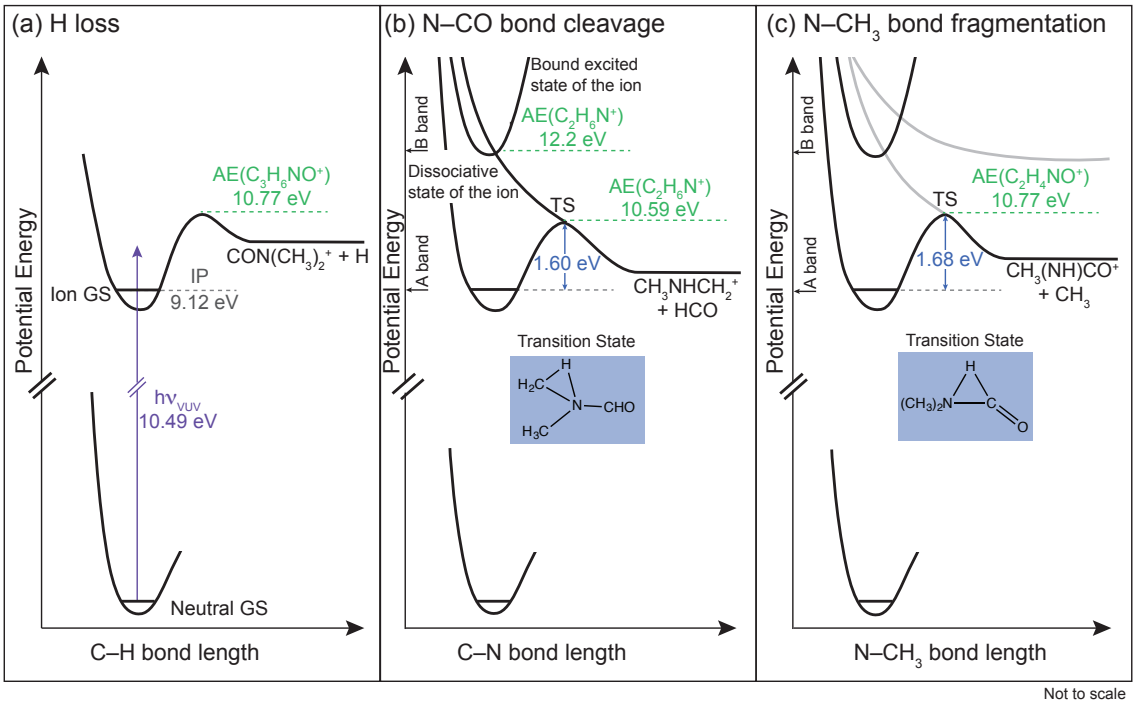

Figure 6.3: Schematic diagrams of the electronic states involved in three different photofragmentations of DMF^+. (a), (b) and (c) show cuts through different dimensions of the multidimensional potential energy surfaces of DMF^+, along (a) the C−H, (b) the C−N, and (c) the N−CH_3 bond stretching coordinates. The appearance energies obtained by Arimura and Yoshikawa [15] are shown in green. The barrier heights for the transition states (TS, illustrated), calculated by Riley and Baer [16], are shown in blue.

thresholds for these channels. This can be visualised with the aid of the schematic diagrams shown in Figure 6.3, which serve to illustrate the various electronic states involved in three different bond fragmentation channels that result on photolysis of DMF^+. The individual panels show cuts through different dimensions of the multidimensional potential energy surfaces of DMF^+, along (a) the C−H, (b) the C−N, and (c) the N−CH_3 bond stretching coordinates. These diagrams are based on the initial idea from Arimura and Yoshikawa [15], but also incorporate the tight transition states (TSs) associated with the barriers to dissociation, identified by Riley and Baer [16]. These tight TSs, which yield low energy fragmentation products, are characteristic of rearrangement processes, not simple bond cleavages, as might otherwise be expected when simply considering the molecular mass of the products of these fragmentation channels. The structures of the TSs have been found through ab initio calculations [16]. As illustrated in Figure 6.3 these transition states both involve 1,2 H-shifts. Channel (B) results in formation of $CH_2NHCH_3^+$, following loss of HCO. Channel (C) produces $CH_3(NH)CO^+$, with loss of CH_3.

In recent years, Baumgärtel and co-workers have shown an interest in the fragmentation processes of gas-phase prebiotic and biotic species (see for example [17–19]). Their VUV photoionization mass spectrometry study of DMF [17] brought renewed interest to the fragmentation of the DMF cation. In the study by Baumgärtel and co-workers, the ions resulting from dissociative photoionization of DMF at 20 eV were identified, and fragment ion assignments were made. As will become evident from the discussion in Section 6.3, it was apparent that in a number of cases there were several fragment ions which could potentially contribute to the signal observed at a particular *m/z*. Some of the fragment ions could be assigned unambiguously, and Baumgärtel and co-workers [17] generally agreed with the ion identities put forward by Arimura and Yoshikawa in their earlier study [15]. However, several ion identities remained ambiguous.

The current work extends the investigation into the photofragmentation processes of the DMF cation. This work has employed 10.49 eV photoionization with UV dissociation of the parent cation. The velocity-map imaging experiment used to detect the resulting ions ensures that not only are the fragment ions identified from time-of-flight mass spectra, but also, the velocity-map images of the ions yield information about the speed and angular distributions of the products. From the latter, the dissociation dynamics leading to production of the observed fragment ions can be revealed. In addition, in an attempt to confirm the identities of the fragment ions resulting from dissociative ionization of DMF, the current study has also investigated the fragmentation of the deuterated-DMF (DMF-d_7) cation.

6.2 Experiment

The photofragmentation of DMF and DMF-d_7 cations has been investigated using the custom-built VMI spectrometer described in Chapter 2. The DMF and DMF-d_7 samples, which have a purity of $>$99.8% and $>$99.5%, respectively, were sourced from Sigma Aldrich. For the experiments carried out here, the molecular beam was formed of a gas mixture comprising $\sim$0.2% DMF or DMF-d_7 in 2 bar He (BOC, $>$ 99.9%). Within the ion optics assembly, the molecular beam was intersected orthogonally by the co-propagating 118 nm and 355 nm beams, the 355 nm laser having been used to generate the 118 nm light. 118 nm light ionized the parent molecule and the 355 nm light photolysed the parent ion. In order to extend the energy range investigated, UV light in the wavelength range 225 nm - 258 nm was additionally employed to photolyse the parent ion. In this latter case the UV laser passed through the interaction region $\sim$20 ns after the 118 nm photoionization pulse.

All the laser beams were linearly polarised parallel to the plane of the imaging detector. The parent and nascent fragment ions were velocity-mapped onto the 2D imaging detector. Time-of-flight mass spectra and ion images were acquired and processed as described in Section 2.6 and Section 2.9, respectively.

6.3 Results & Discussion

6.3.1 DMF cation formation

The lowest vertical ionization threshold of DMF, 9.12 eV [20], involves removal of an electron from an antisymmetric π molecular orbital [21]. A second vertical ionization threshold, at around 9.4 eV, entails removal of an electron from the lone pair on oxygen [21]. These two ion states lie close in energy and yield a single feature, the A band, in the photoelectron spectrum [15, 21]. The photon energy of the 118 nm photoionization laser, which exceeds both of these low lying thresholds, lies within the Frank-Condon gap between the A and B bands of the DMF cation [21], as was the case in the experiments of Riley and Baer [16].[1] Despite this, a significant parent cation signal has been observed following photoionization of DMF with 118 nm light.[2] Since the photon energy (10.49 eV) exceeds the ionization thresholds within the A band of the DMF cation, the ejected electron may originate from a number of locations within the molecule. If the electron is removed from the lone pair on oxygen (second vertical ionization threshold), then it can be expected that this would have little influence on the structure of the DMF cation, since this electron is not involved in the bonding within the molecule. However, removal of an electron from the antisymmetric π molecular orbital, as discussed by Arimura and Yoshikawa [15], would have a significant effect on the DMF cation structure, and would potentially yield a highly internally excited parent molecule. Unfortunately, in the present work it is not possible to determine the internal energy of the parent ion formed following VUV photoionization. Therefore, in Section 6.3.4, when considering the energetics of the photofragmentation processes of DMF^+, we have considered two limiting cases: (1) the ejected electron departs with all of the excess energy, and the parent ion is formed in $v = 0$; and (2) the electron is emitted with 'zero' kinetic energy, *i.e.* all of the energy in excess of the first ionization threshold is available to the DMF cation.

[1] Approximate onsets for the A and B bands are illustrated in Figure 6.3.

[2] The magnitude of the DMF cation signal can be observed relative to the fragments and clusters in the TOF-MS (obtained under 'clustering' conditions) shown in Figure 6.4.

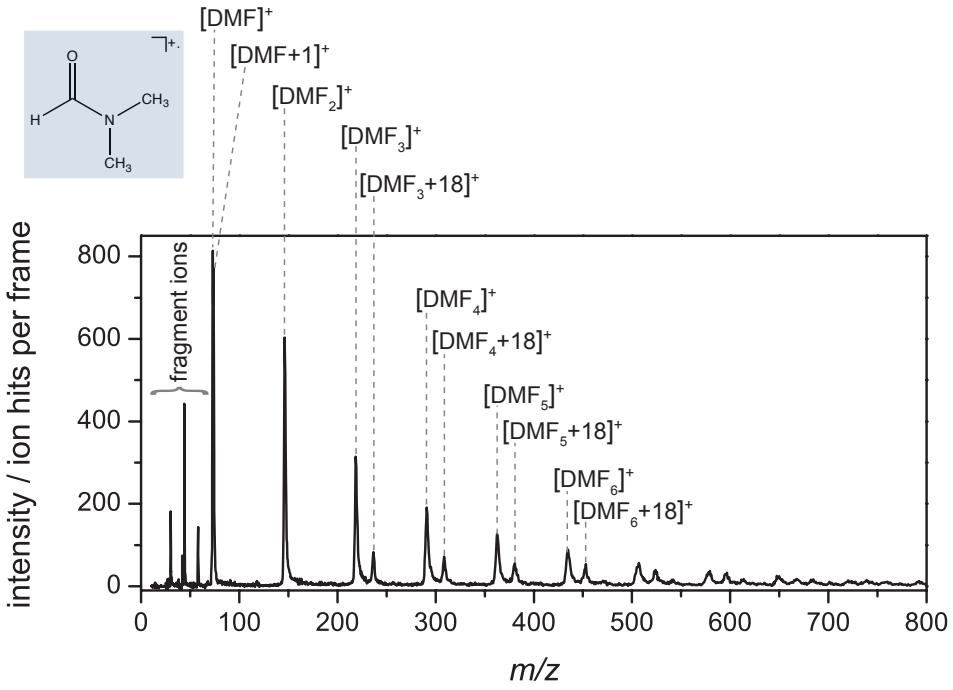

Figure 6.4: TOF-MS of DMF, under clustering conditions, following irradiation with 118 nm and 355 nm light.

6.3.2 DMF clusters

Several of the previous studies of DMF (neutral and cation) fragmentation have noted the formation of clusters within the molecular beam [16, 22]. In the present study it has been observed that *under certain contitions* DMF readily forms large clusters, see for example the time-of-flight mass spectrum (TOF-MS) in Figure 6.4. Such cluster formation is not unexpected, as DMF, with its carbonyl function group, can form hydrogen bonds. The formation of DMF dimers and larger clusters has also been discussed with regards to the liquid-phase behaviour of DMF [23]. Liquid-phase DMF clusters have been modelled with molecular dynamics simulations [24], though such clusters have not been observed in the liquid studies of DMF [23].

Hydrogen bonds are commonly found within protein structures. These bonds are extremely important in determining the secondary structure of proteins. Therefore, investigation of H-bonded cluster formation could prove interesting. However, the aim of this particular study is not to investigate clusters, but the photofragmentation of single DMF cation units. Therefore, these clustering effects have been minimised by reducing the flux of gas passing through the nozzle.

The *m/z* 74, $[DMF+1]^+$, signal is strongly dependent on the density of clusters in the beam. As shown in Figure 6.4, the signal from this ion is almost equivalent in intensity to the parent ion, $[DMF]^+$, signal. Under 'non-clustering' conditions, the dimer, $[DMF_2]^+$, and higher order clusters are absent in the TOF, and the *m/z* 74 signal is observed only (at most) as a very small shoulder on the strong parent ion peak at *m/z* 73.

Riley and Baer concluded that the *m/z* 72 ion also resulted from dissociation of DMF clusters (larger than the dimer) [16]. In this current work, under 'non-clustering' conditions, the *m/z* 72 ion signal has been observed as a low mass shoulder on the very intense parent ion peak, and therefore has not been considered further. However, we can confirm that under 'non-clustering' conditions the ratio of this *m/z* 72 ion to the *m/z* 73 parent ion is significantly reduced as compared to clustering conditions. Therefore, there is at least a contribution to *m/z* 72 from cluster fragmentation.

The time-of flight mass spectra (TOF-MS) obtained under 'non-clustering' conditions, along with the data from the velocity-map images of the fragment ions of interest, will now be presented.

6.3.3 Fragment ion identification from time-of-flight mass spectra

As noted in Section 6.2, photofragmentation of the DMF and DMF-d_7 cations, formed by VUV photoionization, has been investigated at a number of UV photon energies. The time-of-flight mass spectra which result from photolysis of DMF^+ using 355 nm, 258 nm, 235 nm, 230 nm and 225 nm light are shown in Figure 6.5. DMF-$d_7{}^+$ TOF-MS resulting from photolysis at the two shortest wavelengths, 355 nm and 258 nm, and one additional wavelength, 243 nm, are shown in Figure 6.6. The intensities in the TOF-MS have been normalised to the *m/z* 44 and *m/z* 50 base peaks in Figure 6.5 and Figure 6.6, respectively. The intensities of the significant *m/z* peaks in the DMF TOF-MS are shown in Table 6.1. The intensities of a select few peaks in the DMF-d_7 TOF-MS are shown in Table 6.2. The values shown in these tables are relative to the intensities of *m/z* 44 and *m/z* 50 base peaks for DMF and DMF-d_7, respectively. [3]

The fragment ions resulting from DMF^+ ($DMF\text{-}d_7^+$) fragmentation will now be discussed in turn, with reference to Figure 6.5 (Table 6.1) and Figure 6.6 (Table 6.2).

[3]The recorded DMF-d_7 TOF-MS will have contributions from peaks resulting from the dissociation of DMF, which cannot be fully eliminated from the DMF-d_7 sample. These have been highlighted in the TOF-MS.

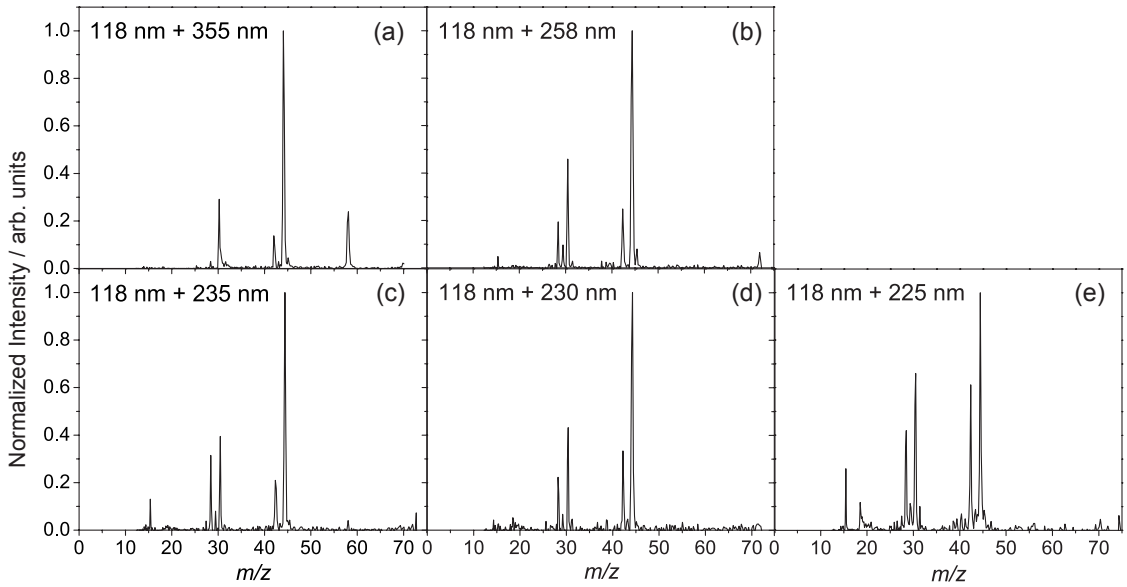

Figure 6.5: TOF-MS of DMF following photoionization with 118 nm light and photolysis of the cation with (a) 355 nm, (b) 258 nm, (c) 235 nm, (d) 230 nm, and (e) 225 nm light. The signal in each case has been normalized relative to the base peak (*m/z* 44).

Table 6.1: The relative intensities of the fragment ion mass peaks resulting from UV photolysis of DMF. ‡The ions which are most likely to correspond with the observed *m/z* have been included in this table.

m/z	Ion‡	UV wavelength / nm				
	118 nm +	355	258	235	230	225
15	CH_3^+	-	2.6	7.9	2.6	18.9
18	NH_4^+	0.7	0.7	4.9	6.5	18.2
28	CNH_2^+	2.4	6.0	23.5	17.4	53.4
29	HCO^+	-	6.5	4.0	2.5	18.1
30	CH_4N^+	39.1	36.1	37.9	35.0	78.3
42	$NC_2H_4^+$	11.7	20.9	25.7	21.4	57.1
43	$NC_2H_5^+$	1.6	1.4	3.2	4.5	8.4
44	$CH_3NHCH_2^+$	100	100	100	100	100
45	$NC_2H_7^+$	4.8	4.7	3.6	3.9	8.3
58	$HCONHCH_2^+$	28.1	-	-	-	-

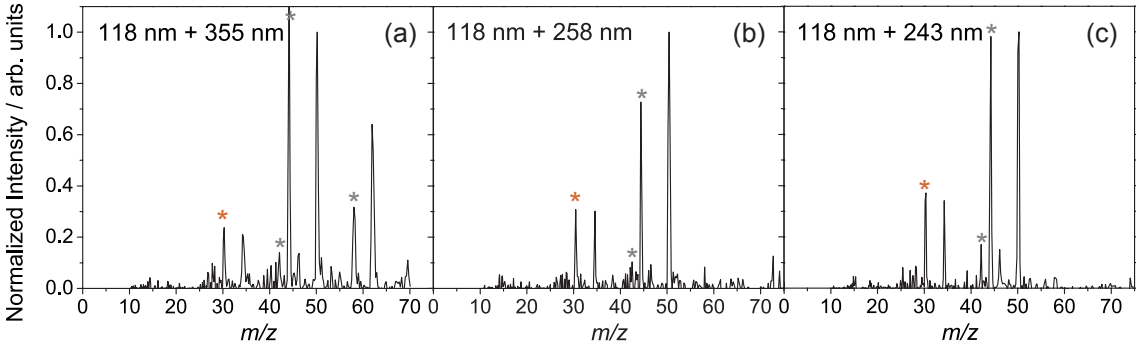

Figure 6.6: TOF-MS of DMF-d_7 following photoionization with 118 nm light and photolysis of the cation with (a) 355 nm, (b) 258 nm, and (c) 243 nm light. The signal in each case has been normalized relative to the *m/z* 50 peak. The significant peaks which result from non-deuterated DMF are marked with grey asterisks. Orange asterisks indicate peaks which potentially have contributions from DMF and DMF-d_7.

Table 6.2: The relative intensities of the fragment ion mass peaks resulting from UV photolysis of DMF-d_7. ‡The ions which are most likely to correspond with the observed *m/z* have been included in this table. Those ions that result from photolysis of non-deuterated DMF are shown in grey.

m/z	Ion‡	UV wavelength / nm		
	118 nm +	355	258	243
30	CH_4N^+ / DCO^+	22.1	26.8	36.3
34	CD_4N^+	25.8	19.7	24.5
42	$NC_2H_4^+$	13.7	7.6	9.8
44	$CH_3NHCH_2^+$	93.0	50.5	78.1
46	$NC_2D_4^+$	10.8	8.4	14.1
50	$CD_3NDCD_2^+$	100	100	100
58	$CH_3(NH)CO^+$	31.3	-	-
62	$CD_3(ND)CO^+$	56.8	-	-

***m/z* 58 (62)** Channel (C), as illustrated in Figure 6.3 (c), yields the **c** ion, $CH_3(NH)CO^+$ (*m/z* 58), with a CH_3 co-fragment. The ion structure, proposed by Riley and Baer, is considered to be formed following a 1,2 H-shift from the carbonyl carbon to the nitrogen within a tight transition state [16]. Baumgärtel and co-workers [17], without reference to the work of Riley and Baer [16], suggested an alternative rearrangement, with transfer of the hydrogen on the carbonyl carbon to the oxygen. However, there was no thermochemical evidence given for this process. The *m/z* 58 ion is only observed at the lowest photon energy ($\lambda = 355$ nm). As will be seen, it is highly likely that this ion undergoes secondary fragmentations when higher photolysis energies are employed.

***m/z* 45** This ion has only been reported once before, in the study by Baumgärtel and co-workers [17], though no detailed discussion of its origin was presented. The ratio of *m/z* 45 to *m/z* 44 is greater than would be expected if the *m/z* 45 ion results only from ^{13}C isotope contributions. *m/z* 45 corresponds to $NC_2H_7^+$, which would be formed with a CO co-fragment. One possible structure of this ion is $HN(CH_3)_2{}^+$, which would require a hydrogen transfer step from the carbonyl carbon to the nitrogen. A rearrangement of this sort, with elimination of a molecular co-fragment, would result in very energetically favourable products. However, such a rearrangement would have a significant energetic barrier, as observed for $CH_3(NH)CO^+$ production.

***m/z* 44 (50)** The lowest energy fragmentation of the N−CO 'peptide bond' yields the **y** ion, *m/z* 44, with a neutral HCO co-fragment. This ion, $NC_2H_6^+$, is the major ionic fragment across the range of photolysis energies investigated. The measured photon impact appearance energy for $NC_2H_6^+$ is 10.59 eV [15]. As revealed by Riley and Baer [16], and shown in Figure 6.3 (b), the *m/z* 44 ion is formed following significant (intra)molecular rearrangement. Riley and Baer located a barrier resulting from a 1,2 H-shift, which must be overcome to yield HCO + $CH_3NHCH_2{}^+$. Baumgärtel and co-workers [17] noted that there are a number of isomers of $NC_2H_6^+$ which have low enough enthalpies of formation to be possible candidates for *m/z* 44. However, they concur that from a structural point of view $CH_3NHCH_2{}^+$ is the most likely.

***m/z* 43** This ion, $NC_2H_5{}^+$, most probably results from a secondary dissociation process, which involves H loss from *m/z* 44. The estimated appearance energy for this ion through this channel is around 13.2 eV [17]. As shown in Table 6.1, as the photolysis energy increases so does the intensity of *m/z* 43 relative to *m/z* 44. This would correlate with a mechanism which is dependent on the internal energy of the nascent *m/z* 44 ion. Baumgärtel and co-workers [17] also put forward a dissociative ionization mechanism, with a minimum AE of around 9.4 eV, which involves H transfer from the methyl group to

the carbonyl carbon to yield $NC_2H_5^+$ with an H_2CO co-fragment. However, if this were the route to formation of the observed *m/z* 43 ion, since this appearance energy is lower than the AE for *m/z* 44, we would not expect the observed variation in peak intensity (relative to *m/z* 44) with increasing photon energy.

***m/z* 42 (46)** H_2 loss from $NC_2H_6^+$ (*m/z* 44) yields *m/z* 42, $NC_2H_4^+$. D_2 loss from DMF-d_7^+ fragmentation is observed to be a fairly minor, but still evident, signal in the TOF-MS. Such a secondary dissociation process will be dependent on the internal excitation of the initially formed $NC_2H_6^+$. As in the case for *m/z* 43, it can be observed that the intensity of this secondary fragmentation product relative to *m/z* 44 generally increases with increasing photolysis energy (see Table 6.1). From the relative intensities of the *m/z* 42 and *m/z* 43 signals it appears that the relatively low internal energies of the nascent $CH_3NHCH_2^+$ ions favour H_2 loss over H loss, which is consistent with the observations of Baumgärtel and co-workers [17].

***m/z* 30 (34)** This ion was observed in the work of Arimura and Yoshikawa [15] and Baumgärtel and co-workers [17]. The latter speculated (among other less probable assignments) that the *m/z* 30 ion has the structure CH_4N^+ and is formed as a primary fragmentation product with a CH_3CO co-fragment. Photofragmentation of DMF-d_7^+ yields *m/z* 34, CD_4N^+, which is consistent with such an assignment. However, Arimura and Yoshikawa [15] observed a rise in *m/z* 30 intensity, which coincided with a drop in *m/z* 58 intensity. Therefore, they assigned *m/z* 30 as the CH_4N^+ ion, which is formed with a CO co-fragment following secondary fragmentation of *m/z* 58, $CH_3(NH)CO^+$. Such a process would involve a rearrangement with a 1,2 H-shift from the methyl carbon to the nitrogen, with fragmentation of the N−CO bond, to yield $H_2N{=}CH_2^+$.

***m/z* 29 (30)** *m/z* 29 is only observed at the shorter photolysis wavelengths ($\leq$258 nm). The most obvious assignment for this mass is HCO, from 'peptide' bond rupture, as in Channel (B), but with the resultant charge residing on the HCO co-fragment. In MS terminology, this would be referred to as the **b** ion. Unfortunately it has not been possible to cleanly subtract out the non-deuterated DMF contribution from the TOF-MS of DMF-d_7^+ shown in Figure 6.6. Therefore, the DCO peak at *m/z* 30 has contamination from non-deuterated DMF. However, by comparing the relative ratio of the *m/z* 30 and *m/z* 34 signals in the TOF-MS of DMF-d_7^+ with those of *m/z* 44 and *m/z* 50, it is possible to gain at least a qualitative idea of whether there is a contribution to *m/z* 30 from DMF-d_7^+. On photolysis with 355 nm light these ratios are very similar (around 0.25:1), as would be expected for a specific ratio of DMF^+ to DMF-d_7^+, yielding the non-deuterated and deuterated forms of these ions, which have been discussed above. However, on photolysis at 258 nm and 243

nm the ratio of *m/z* 30 to *m/z* 34 (0.5:1) is greater than the *m/z* 44 to *m/z* 60 ratio (0.25:1). This implies that there is an additional contribution to *m/z* 30 from the DCO^+ ion. At the short photolysis wavelengths the DCO^+ ion is generated, which confirms that the *m/z* 29 signal that is observed to result on photolysis of DMF^+ with higher photolysis energies comes about due to HCO^+ production.

***m/z* 28** This ion has been observed at all photolysis wavelengths employed, though the signal is very low following ion photolysis with the longest wavelength, 355 nm. There is a general increase in intensity relative to *m/z* 44 with increasing photon energy. Baumgärtel and co-workers [17] put forward three potential identities for *m/z* 28: CO^+; $HCNH^+$; and $CNH_2{}^+$. In the TOF-MS of DMF-d_7^+ the *m/z* 28 signal is very low. In fact, the ratio of the *m/z* 28 signal to that at *m/z* 44 reflects that in the DMF TOF-MS. If CO^+ were generated from DMF-d_7^+ this ratio should increase. Therefore, the more probable assignment of *m/z* 28 is $HCNH^+$ or $CNH_2{}^+$, either of which could result from secondary dissociation of either $NC_2H_6^+$ (*m/z* 44) or $HCONHCH_2{}^+$ (*m/z* 58).

***m/z* 18** This is a very weak signal in the TOF-MS of DMF^+, which increases with increasing photolysis energy. TOF-MS of DMF-d_7^+ show weak signals at *m/z* 22, which aid in confirming that this ion is $NH_4{}^+$. This ion, which is formed with a C_2H_2 co-fragment, results from yet another secondary fragmentation of the *m/z* 44 ion.

***m/z* 15** $CH_3{}^+$ probably results from a fragmentation of the N-methyl bond, as in Channel (C), with the positive charge remaining on the methyl fragment. Baumgärtel and co-workers [17] claimed that the much more intense signal observed at *m/z* 15 as compared to *m/z* 58 was, in accordance with Stevenson's rule, evidence that the ionization energy of the neutral species corresponding to the *m/z* 58 fragment, $CH_3(NH)CO$, was much higher than that of the methyl radical (9.48 eV [25]). However, it is evident from the TOF-MS of DMF^+ that the *m/z* 58 ion is observed at the lowest photolysis energies, but not at the higher ones. Our justification for this is that the more internally excited *m/z* 58 products undergo secondary fragmentation processes. If we consider only the TOF-MS from 355 nm photolysis, the intensity of the *m/z* 58 ion is a third of the intensity of *m/z* 44, whereas *m/z* 15 is not observed. This would imply the converse of the claim of Baumgärtel and co-workers [17]; the IE of $CH_3(NH)CO$ is substantially less than that of the methyl radical. However, for Stevenson's rule to apply there should be no barrier to the formation of either of the product ions. Since this is known not to be the case for $CH_3(NH)CO^+$ production, and most likely is not the case for $CH_3{}^+$ formation, we can simply state that the barrier to formation of the $CH_3(NH)CO^+ + CH_3$ products is lower than that to forming the *m/z* 15 ion.

In summary, the use of 118 nm light enables us to generate a low energy DMF^+ parent ion, which when photolysed with UV light yields a wide range of fragmentation products. By employing UV light in the wavelength range from 355 nm to 225nm, it is possible to access an energy range from around 3.49 eV (min) to 6.88 eV (max) above the ground state of the DMF^+ ion. In contrast, the TOF spectra of Baumgärtel and co-workers [17] were generated using 20 eV photoionization. The latter generated relative *m/z* peak intensities which were comparable to those observed in TOF studies using 70 eV electron impact ionization [17]. The shortest photolysis wavelengths employed in the current study (235 nm - 225 nm), yield relative peak intensities which are comparable with the previous studies. However, by reducing the UV photon energy we are able to reduce the extent of secondary fragmentation processes, and therefore reveal the primary dissociation processes. These involve N-carbonyl 'peptide' bond fragmentation, as in Channel (B), and N-methyl cleavage, as in Channel (C). The fragment ions resulting from secondary fragmentation processes of the internally excited $CH_3NHCH_2^+$ (*m/z* 44) and $CH_3(NH)CO^+$ (*m/z* 58) ions become more apparent when higher photoylsis energies are employed.

6.3.4 Further insight from velocity-map imaging

Velocity-map images have been acquired for the fragment ions resulting from UV photofragmentation of DMF^+ with 355 nm, 258 nm and 225 nm light. A direct comparison will now be made between the dynamics of the two main primary dissociation channels.

Characteristic energy redistributions

As noted above, photolysis of DMF^+ with shorter wavelength light, e.g. 258 nm or 225 nm, appears to open up a substantial number of secondary fragmentation processes, whereas, photolysis with lower photon energies (in this case 355 nm light) reveals the main primary fragmentation channels, Channel (B) and Channel (C). For these two primary fragmentation channels the translational energy, E_T, distributions obtained from the velocity-map images of the fragment ions have been evaluated as a function of f_T, the fraction of the available energy, E_{av}, which goes into translation. These distributions are shown in Figure 6.7. The available energy has been determined from the energy provided by the photon in excess of that required to form the products:

$$E_{av} = h\nu - \Delta E \tag{6.1}$$

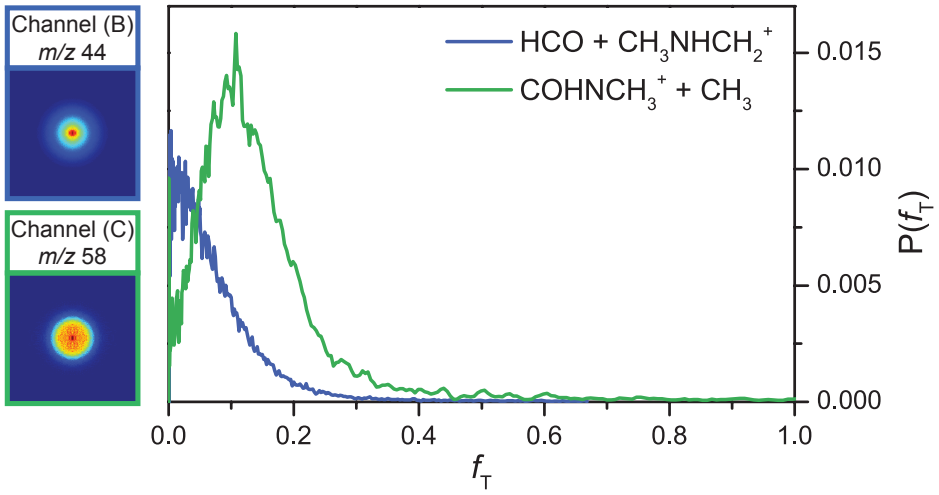

Figure 6.7: Velocity-map images of the *m/z* 44 and *m/z* 58 ions resulting from photolysis of DMF^+ with 355 nm light, along with the $P(f_T)$ distributions obtained from these images.

where

$$\Delta E = E_{\text{products}} - E_{\text{DMF}^+} \tag{6.2}$$

The product energies, E_{products}, have been calculated using the 0 K enthalpies of formation published by Riley and Baer [16]. For the two primary channels of interest, Table 6.3 lists:

1. The photofragments resulting from the product channel.
2. The energy, in excess of the parent ion energy, required to form the products, ΔE.
3. The energy available to the products, E_{av}.
4. The mean values of f_T, $\langle f_T \rangle$.

Table 6.3: Energetic parameters for the two main primary photofragmentation pathways of DMF^+: the product energies relative to the ground state of the DMF^+ ion, ΔE; the energy available to the fragments, E_{av}; and the average fraction of E_{av} which goes into translational energy, $\langle f_T \rangle$.

			355 nm photolysis	
Channel	Fragments	ΔE / eV	E_{av} / eV	$\langle f_T \rangle$
(B)	$HCO + CH_3NHCH_2^+$	0.44	4.49	0.046
(C)	$HCONHCH_2^+ + CH_3$	0.79	4.14	0.109

The primary fragmentation channels proposed here involve 1,2 H-shifts through tight transition states [16]. The rearrangements yield fragments which are much more energetically stable than those that would be formed if the processes proceeded with simple bond cleavage. Such rearrangement processes require a significant amount of energy redistribution, which is reflected in the f_T distributions shown in Figure 6.7. These distributions, which have been quantified in terms of $\langle f_T \rangle$ in Table 6.3, indicate that a significant fraction of the energy available to the products is distributed amongst the internal degrees of the freedom of the photofragments. The time required for such an energy redistribution process is reflected in the isotropic angular distributions, which have been observed in the images of the photofragment ions resulting from both Channel (B) and Channel (C) (see Figure 6.8 (a) and Figure 6.9 (a)). However, despite these general similarities, Channel (B) and Channel (C) do generate different f_T distributions. Channel (C), which yields $HCONCH_2^+ + CH_3$, results in a slightly larger fraction of the available energy being released into translation. Though the barrier heights to rearrangement for Channel (B) and Channel (C) are very similar, 1.60 eV and 1.68 eV, respectively [16], the products from Channel (C) lie $\sim$0.35 eV higher in energy than those that result from Channel (B). However, this energy difference is unlikely to be significant enough to be the source of the distinct f_T distributions observed for these channels.

Such distributions could come about as a result of different dissociation mechanisms. As discussed in Section 6.3.1, initial absorption of the VUV photon produces the DMF^+ cation with a possible internal energy of up to $\sim$1.4 eV. The initially formed DMF^+ does not have enough energy to surmount the barriers to dissociation. However, following absorption of an additional UV photon, DMF^+ is excited to a bound state of the ion, as suggested by Arimura and Yoshikawa [15] and depicted in Figure 6.3. From here we can visualise two different pathways to dissociation:

1. A predissociation mechanism in which the molecule crosses from the bound state to a repulsive state and dissociates along the latter to yield either simple bond cleavage products, or, if the molecule passes through one of the tight transition states, the rearrangement products.

2. An internal conversion mechanism that transfers population from the initially excited bound state to the electronic ground state of the ion. Following further energy redistribution the molecule is able to traverse the barrier to rearrangement, and dissociates to yield the energetically favourable fragmentation products.

Pathway 2 can be expected to allow for significantly more internal energy redistribution than Pathway 1. This would result in an almost statistical type of dissociation, and would generate a f_T distribution peaking very close to zero. In contrast, a predissociation mechanism, as for Pathway 1, would result in a larger fraction of the available energy being released into translation.

Without the aid of high level ab initio calculations and modelling of the fragmentation process, it is not possible to assign the mechanisms for Channel (B) and Channel (C). However, despite this, as a result of the characteristic translational energy distributions observed for Channel (B) and Channel (C), it is possible to clarify further, and in many cases confirm, the origins of the secondary dissociation products, which become more apparent at higher photolysis energies. The processes involving primary N−CO 'peptide' bond dissociation will now be discussed, before considering separately the fragmentation processes that involve initial N−CH_3 cleavage.

Primary N−CO bond fission

As discussed in Section 6.3.3, many of the fragments observed in the TOF spectra of DMF^+ result from an initial N−CO bond cleavage. This implies that a significant number of the fragmentation events which occur on photolysis of DMF^+ occur via a photodissociation mechanism which initially proceeds through Channel (B). In some instances the primary fragmentation products (*m/z* 29 and *m/z* 44) are observed. However, *m/z* 44 ions in particular undergo a range of secondary fragmentation processes. It has been possible to obtain the velocity-map images of all the fragment ions observed, and it is quite straightforward to convert the measured velocities to translational energy. However, it is not so straightforward to convert the individual translational energies of secondary fragmentation products into a total translational energy release, since the mechanism leading to generation of the observed ion is a multi-step process and more than two fragment bodies result. For the case when the secondary dissociation process involves loss of a very light fragment it can be assumed that this low-mass co-fragment removes most of the translational energy released in the secondary dissociation event. Therefore, the translational energy of the observed ion approximately reflects the initial total translational energy release, with a small amount of broadening in the translational energy distribution. With this in mind it is possible to compare the translational energy releases of some of the ions which are considered to result from a primary Channel (B) dissociation.

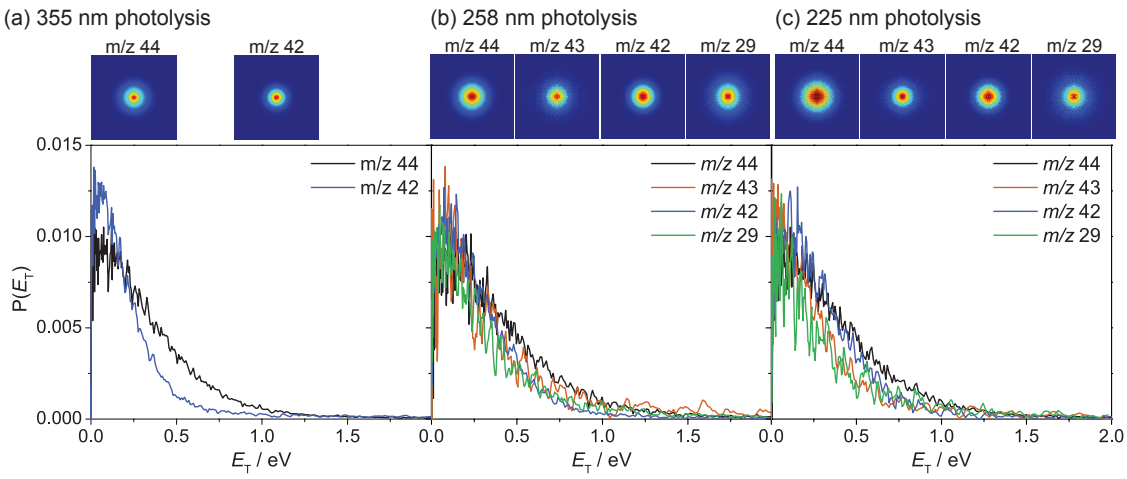

Figure 6.8: (Top) Velocity-map images of the ions (where observed) with *m/z* 44, 43, 42, and 29 resulting from photolysis of DMF^+ with (a) 355 nm, (b) 258 nm, and (c) 225 nm light. (Bottom) The E_T distributions obtained from these images: *m/z* 44 (black), 43 (orange), 42 (blue), and 29 (green).

Figure 6.8 shows the total translational energy, E_T, distributions obtained from the velocity-map images of the fragment ions with *m/z* 44 and *m/z* 42 following photolysis of DMF^+ with (a) 355 nm, (b) 258 nm and (c) 225 nm light. In addition, the E_T distributions obtained from the images of the *m/z* 29 and *m/z* 43 ions are also shown in the latter two panels, since these ions are only observed when the shorter photolysis wavelengths are employed.

m/z 29 results from the photodissociation process complementary to Channel (B), i.e. one in which the resulting positive charge resides on the HCO co-fragment. Since this ion is not observed for photolysis with 355 nm light, this implies that the energy required to access this complementary channel is greater than the energy which can be accessed with this longer wavelength.

In contrast, the *m/z* 44 ion and (at least) one of its secondary fragmentation products, *m/z* 42, are observed on photolysis with 355 nm light. As shown in Figure 6.8 (a), following photolysis of DMF^+ with 355 nm light the total translational energy, E_T, distribution obtained from the velocity-map image of the *m/z* 42 fragment ion (blue trace) is significantly narrower than the corresponding distribution for the *m/z* 44 ion (black trace). This reflects the fact that at this photolysis wavelength, the $NC_2H_6^+$ ions with lower translational energy, and therefore a greater amount of internal excitation, are more likely to undergo a secondary fragmentation process with loss of H_2.

By comparing the E_T distributions obtained from the velocity-map images of *m/z* 44 (black trace) and *m/z* 42 (blue trace) in panels (b) and (c) of Figure 6.8, it can be seen that at

shorter photolysis wavelengths (258 nm and 225 nm) these distributions resemble each other much more closely. The $NC_2H_6^+$ ions are produced with such high internal excitation that, regardless of the E_T, the primary fragment ion is equally likely to lose H_2 and produce $NC_2H_4{}^+$. In fact, when shorter wavelength photolysis light is employed, the resultant $NC_2H_6^+$ ions have enough energy for simple H loss to yield *m/z* 43, which is a less energetically favourable process, and is almost negligible following photolysis of DMF^+ with 355 nm light (see Table 6.1). The *m/z* 43 signal following 258 nm photolysis is quite weak, and produces a noisy E_T distribution. However, by increasing the photolysis energy it can be observed that the signal significantly increases. The E_T distribution obtained from the velocity-map image of the *m/z* 43 ion resulting from 225 nm photolysis of DMF^+, shown as the orange trace in Figure 6.8 (c), appears to have a slightly narrower distribution than that for *m/z* 44, which again most probably indicates that the primary fragment ions with more internal energy are more likely to undergo the secondary fragmentation step to yield $NC_2H_5{}^+$.

At the shorter photolysis wavelengths the channel resulting in *m/z* 29 production can be accessed. As observed for *m/z* 44, the process which results in formation of HCO^+ produces an E_T distribution that peaks near zero. Such distributions are characteristic of statistical dissociation processes, i.e the dissociation is slow enough that there is enough time for the available energy to redistribute itself equally amongst the accessible internal degrees of freedom of the molecule. The isotropic images observed for all fragments resulting from an initial N−CO bond cleavage (see Figure 6.8) are consistent with such a slow mechanism.

N-CH_3 bond fragmentation

Channel (B) involves N−CH_3 bond fragmentation to yield $CH_3(NH)CO^+$. The complementary channel will generate $CH_3{}^+$. As discussed in Section 6.3.3, the TOF-MS data gives evidence in favour of a lower barrier to formation of the CH_3 + $CH_3(NH)CO^+$ (*m/z* 58) products compared to that to formation of $CH_3(NH)CO$ + $CH_3{}^+$ (*m/z* 15). *m/z* 15 is only observed at the shorter photolysis wavelengths (258 nm and 225 nm). In contrast, *m/z* 58 is only observed at the longest photolysis wavelength. The $CH_3(NH)CO^+$ fragment ion is thought to undergo secondary fragmentation processes at higher photolysis energies, to yield $H_2N{=}CH_2{}^+$ (*m/z* 30) and possibly $CNH_2{}^+$ (*m/z* 28). The secondary dissociation processes involve an additional translational energy 'kick', which results in significant broadening in the translational energy distribution. This has been observed for both *m/z* 28 and 30, which aids in confirming the origins of these ions.

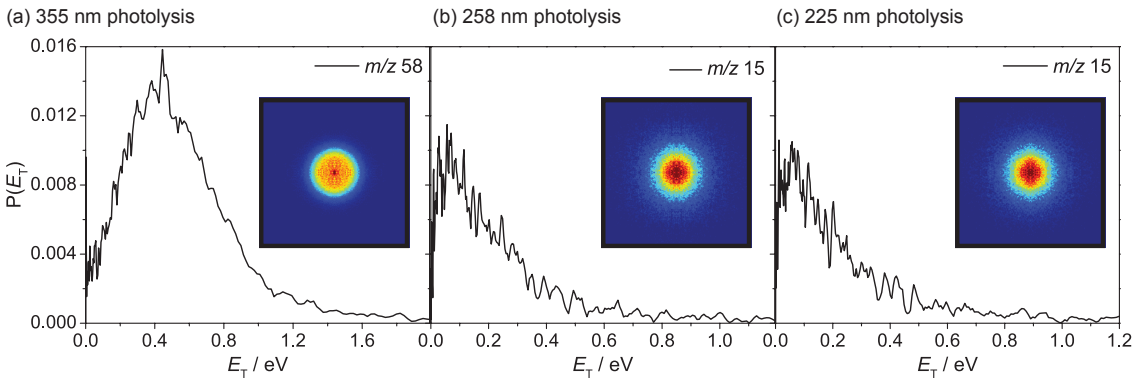

Figure 6.9: E_T distributions obtained from velocity-map images (shown) of the ions resulting from primary N−CH_3 bond fission of DMF^+ following photolysis with (a) 355 nm, (b) 258 nm, and (c) 225 nm light.

The E_T distribution obtained from the velocity-map image of the *m/z* 58 fragment ion produced on photolysis of DMF^+ with 355 nm light, shown in Figure 6.9 (a), clearly peaks away from zero. This distribution is quite different from that for the *m/z* 15 ion resulting from DMF^+ photolysis with 258 nm and 225 nm light, shown in Figure 6.9 (b) and (c). In order to obtain the E_T distributions shown in Figure 6.9, it has been assumed that *m/z* 15 is a primary dissociation fragment, which results from a N−CH_3 bond cleavage, in which the charge remains on the CH_3^+ fragment. Whether this is the case or not, the translational energy distribution peaks at zero. From these distributions it would seem unlikely that there is a contribution to *m/z* 15 from secondary dissociation of *m/z* 58, since the process which yields *m/z* 58 produces fragments with significantly more translational energy. However, it is not possible to rule out a contribution to *m/z* 15 from a process involving initial N−CO bond cleavage.

The *m/z* 58 and *m/z* 15 images, shown in Figure 6.9, display isotropic distributions. From these it is not possible to ascertain the initial excitation which leads to fragmentation. However, it is likely that the processes which yield *m/z* 58 and *m/z* 15 both occur on a slow timescale, as was the case for those involving initial N−CO cleavage.

6.4 Conclusion

The photofragmentation of the DMF^+ cation has been investigated across a range of UV photolysis wavelengths. This study reveals the complexity of the dissociation processes observed for this relatively simple model for a peptide bond. The ion undergoes a number of hydrogen transfer rearrangement processes, and a significant amount of secondary

dissociation also occurs. Performing experiments across a range of photolysis energies has proved particularly useful, since by employing low photolysis energies it is possible to ensure that any secondary dissociation processes are minimised, and the primary fragmentation products are observed. The lowest photolysis energy accesses the primary dissociation channels, which are both thought to involve 1,2 H-shift rearrangement processes to yield energetically favourable products: Channel (B) HCO + $CH_3NHCH_2^+$; and Channel (C) $HCONHCH_2^+$ + CH_3. Both of these primary dissociation channels exhibit isotropic photofragment ion images, implying slow dissociation processes. However, the velocity-map images reveal characteristic energy distributions. Such distributions, along with the TOF-MS of the DMF^+ and DMF-d_7^+ photofragments, allow the clarification of the origins of the observed photofragment ions, especially for those which result from secondary dissociation processes that become particularly evident at higher photolysis energies ($\lambda \leq 258$ nm).

References

[1] Mann, M, Hendrickson, RC, and Pandey, A. *Analysis of Proteins and Proteomes by Mass Spectrometry*. Annual Review of Biochemistry **70**: 437–473 (2001) (cited p. 143, 145).

[2] Aebersold, R and Mann, M. *Mass spectrometry-based proteomics*. Nature **422**: 198–207 (2003) (cited p. 143, 145).

[3] Domon, B. *Mass Spectrometry and Protein Analysis*. Science **312**: 212–217 (2006) (cited p. 143, 145).

[4] Bantscheff, M, Schirle, M, Sweetman, G, Rick, J, and Kuster, B. *Quantitative mass spectrometry in proteomics: a critical review*. Analytical and Bioanalytical Chemistry **389**: 1017–1031 (2007) (cited p. 143, 145).

[5] Wysocki, VH, Resing, KA, Zhang, Q, and Cheng, G. *Mass spectrometry of peptides and proteins*. Methods **35**: 211–222 (2005) (cited p. 143–145).

[6] Brodbelt, JS. *Shedding Light on the Frontier of Photodissociation*. Journal of the American Society for Mass Spectrometry **22**:2 197–206 (2011) (cited p. 143).

[7] Ruotolo, BT, Benesch, JLP, Sandercock, AM, Hyung, SJ, and Robinson, CV. *Ion mobility-mass spectrometry analysis of large protein complexes*. Nature Protocols **3**:7 1139–1152 (2008) (cited p. 144).

[8] Uetrecht, C, Rose, RJ, Duijn, E van, Lorenzen, K, and Heck, AJR. *Ion mobility mass spectrometry of proteins and protein assemblies*. 2010 (cited p. 144).

[9] Jurneczko, E and Barran, PE. *How useful is ion mobility mass spectrometry for structural biology? The relationship between protein crystal structures and their collision cross sections in the gas phase*. 2011 (cited p. 144).

[10] Pritchard, C, O'Connor, G, and Ashcroft, AE. *The Role of Ion Mobility Spectrometry–Mass Spectrometry in the Analysis of Protein Reference Standards*. Analytical Chemistry **85**:15 7205–7212 (2013) (cited p. 144).

[11] Garcia, RA, Pantazatos, D, and Villarreal, FJ. *Hydrogen/Deuterium Exchange Mass Spectrometry for Investigating Protein-Ligand Interactions*. ASSAY and Drug Development Technologies **2**:1 81–91 (2004) (cited p. 144).

[12] Wales, TE and Engen, JR. *Hydrogen exchange mass spectrometry for the analysis of protein dynamics*. Mass Spectrometry Reviews **25**:1 158–170 (2005) (cited p. 144).

[13] Yan, X and Maier, CS. "Hydrogen/Deuterium Exchange Mass Spectrometry". *Mass Spectrometry of Proteins and Peptides*. Totowa, NJ: Humana Press, 2009, 255–271 (cited p. 144).

[14] Hanley, LL and Zimmermann, RR. *Light and Molecular Ions: The Emergence of Vacuum UV Single-Photon Ionization in MS*. Analytical Chemistry **81**:11 4174–4182 (2009) (cited p. 145).

[15] Arimura, M and Yoshikawa, Y. *VUV Photoionization Efficiency Curves and Appearance Energies of N,N-Dimethylformamide Ion and Its Fragment Ions*. Bulletin of the Chemical Society of Japan **64**: 2207–2213 (1991) (cited p. 145–149, 154, 155, 159).

[16] Riley, J and Baer, T. *Unimolecular Decay of Energy-Selected Dimethylformamide Cations: A Combined Molecular Orbital and RRKM Analysis*. The Journal of Physical Chemistry **97**: 385–390 (1993) (cited p. 146, 147, 149–151, 154, 158, 159).

[17] Leach, S, Champion, N, Jochims, HW, and Baumgärtel, H. *Photoionization mass spectrometric studies of N-methyl formamide and N,N'-dimethyl formamide in the 7-18 eV photon energy range*. Chemical Physics **376**: 10–22 (2010) (cited p. 148, 154–157).

[18] Leach, S, Jochims, HW, and Baumgärtel, H. *Photoionization Mass Spectrometric Study of the Prebiotic Species Formamide in the 10-20 eV Photon Energy Range*. The Journal of Physical Chemistry A **114**: 4847–4856 (2010) (cited p. 148).

[19] Leach, S. *Size effects on cation heats of formation. I. Methyl substitutions in nitrogenous compounds*. Chemical Physics **392**: 170–179 (2012) (cited p. 148).

[20] Watanabe, K, Nakayama, T, and Mottl, J. *Ionization potentials of some molecules*. Journal of Quantitative Spectroscopy and Radiative Transfer **2**: 369–382 (1962) (cited p. 149).

[21] Brundle, CR, Turner, DW, Robin, MB, and Basch, H. *Photoelectron spectroscopy of simple amides and carboxylic acids*. Chemical Physics Letters **3**:5 292–296 (1969) (cited p. 149).

[22] Forde, NR, Butler, LJ, and Abrash, SA. *Electronic accessibility of dissociation channels in an amide: N,N-dimethylformamide photodissociation at 193 nm*. The Journal of Chemical Physics **110**:18 8954–8968 (1999) (cited p. 150).

[23] Ohtaki, H, Itoh, S, Yamaguchi, T, Ishiguro, S, and Rode, BM. *Structure of Liquid N,N-Dimethylformamide Studied by Means of X-Ray Diffraction*. Bulletin of the Chemical Society of Japan **56**:11 3406–3409 (1983) (cited p. 150).

[24] Lei, Y, Li, H, Pan, H, and Han, S. *Structures and Hydrogen Bonding Analysis of N, N-Dimethylformamide and N, N-Dimethylformamide-Water Mixtures by Molecular Dynamics Simulations*. The Journal of Physical Chemistry A **107**:10 1574–1583 (2003) (cited p. 150).

[25] Lias, SG. *"Ionization Energy Evaluation" in NIST Chemistry WebBook, NIST Standard Reference Database Number 69, (retrieved June 19, 2013)*. Ed. by Linstrom, PJ and Mallard, WG. National Institute of Standards and Technology, Gaithersburg MD, 20899 (cited p. 156).

7

Rearrangement Reactions of Organic Cations

Contents

7.1 Introduction

A number of exploratory studies will be presented in this chapter and the next. These have been performed in order to establish potential systems for future investigation using the imaging mass spectrometry technique. The studies demonstrate the use of the current velocity-map imaging apparatus for the investigation of gas-phase photochemical processes of organic compounds.

This chapter will discuss work relating to molecular rearrangements of organic cations. The rearrangements of interest, which will be discussed in detail in Sections 7.2 and 7.3, are all

commonly observed in mass spectrometry, in which the ions have typically been generated via electron impact (EI) ionization. In mass spectrometry, the electron energy is usually set to 70 eV, as this energy lies near the maximum in the ionization efficiency curve for most organic molecules [1]. EI ionization with 70 eV electrons generally yields small amounts of the parent ion and significant quantities of simple bond cleavage products. In contrast, low energy ionization, closer to threshold (with, for example, 12 eV electrons) results in fewer fragmentation processes and more rearrangements for certain molecules. With this in mind, Van Bramer and Johnston examined the use of VUV light as a method of soft photoionization for mass spectrometry studies [2]. Their study investigated the effects of 10.5 eV radiation on a range of aliphatic compounds. Generally, VUV photoionization was found to achieve high parent ion abundances and only a few fragment ions, which mainly resulted from low energy rearrangements. Later, de Vries and co-workers investigated the use of laser desorption, with jet-cooling and VUV photoionization to achieve fragment-free mass spectrometric analysis [3]. Their study presents some particularly insightful comparisons between the spectra acquired in a 70 eV electron impact study, and those obtained when employing low energy photoionization. The photoionization spectra result in significantly less fragmentation, and, in their case, when the sample was properly cooled only the parent ion mass was observed in the spectra.

The studies which will be presented in this chapter combine VUV photoionization mass spectrometry with velocity-map imaging. The first study focuses on the molecular rearrangements of aliphatic aldehyde cations. The rearrangements of interest include the McLafferty rearrangement and various related processes, which all involve H-atom transfer to the oxygen of the carbonyl constituent through cyclic transition states. The second study investigates a different type of molecular rearrangement, the retro-Diels-Alder (RDA) reaction of organic cations. The rearrangement, which will be discussed in detail in Section 7.3, is evident in data from mass spectrometry studies of cyclic alkenes. The RDA reaction has also been observed for neutral molecules. The results of a study of the neutral RDA reaction will be presented in Chapter 8.

7.2 Rearrangement Reactions of Organic Cations: (A) Aliphatic Aldehydes

The present study combines velocity-map imaging with time-of-flight mass spectrometry, which can be performed using the same experimental apparatus, in order to investigate the molecular rearrangements and resultant fragmentations of aliphatic aldehyde cations

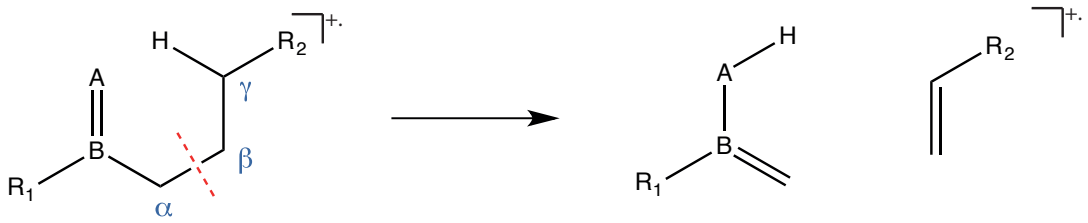

Figure 7.1: The McLafferty rearrangement, which proceeds with transfer of a γ-hydrogen atom through a six-membered transition state to a double bonded atom and results in β-bond cleavage.

in the gas phase. The work focuses on four rearrangement reactions: (i) the McLafferty rearrangement; (ii) the McLafferty rearrangement with double hydrogen transfer; (iii) the rearrangement process resulting in loss of H_2O from the cationic species; and (iv) the McLafferty complement rearrangement.

The McLafferty rearrangement, shown (for the general case) in Figure 7.1, occurs in gas-phase molecular ions containing a double bond. The process involves the transfer of a γ-hydrogen atom through a six-membered transition state to a double bonded atom and results in β-bond cleavage. The rearrangement, which is commonly observed in mass spectrometry studies, takes its name from Professor Fred McLafferty, who discussed the mechanism of the process and emphasised the value of being able to predict, for a certain molecular structure, the rearrangements that could potentially occur during mass spectral analysis [4]. Initially, the name 'McLafferty rearrangement' referred to a process involving a carbonyl functional group, for which the double bond is between a carbon atom and an oxygen atom. However, over time, this terminology has extended to encompass rearrangements involving non-carbonyl systems, such as alkenes, as well as those containing double-bonded sulphur or nitrogen atoms. Bursey and coworkers have compiled a review paper that gives a comprehensive overview of the results of early studies of the McLafferty rearrangement for a wide range of molecules [5].

The McLafferty rearrangement is of particular interest since, in principle, the process can either proceed via a concerted or a stepwise mechanism. Both mechanisms result in the formation of the McLafferty ion with loss of an alkene molecule. Since the McLafferty rearrangement was first revealed, there has been some contention over its true mechanism [5]. Research by Derrick and co-workers [6, 7] favoured the concerted mechanism, shown in Figure 7.2 (a), which proceeds via a six-membered transition state. However, there has always been support for the stepwise process [8–12], shown in Figure 7.2 (b), which involves an initial 1-5 hydrogen atom transfer followed by cleavage of the bond β to the carbonyl

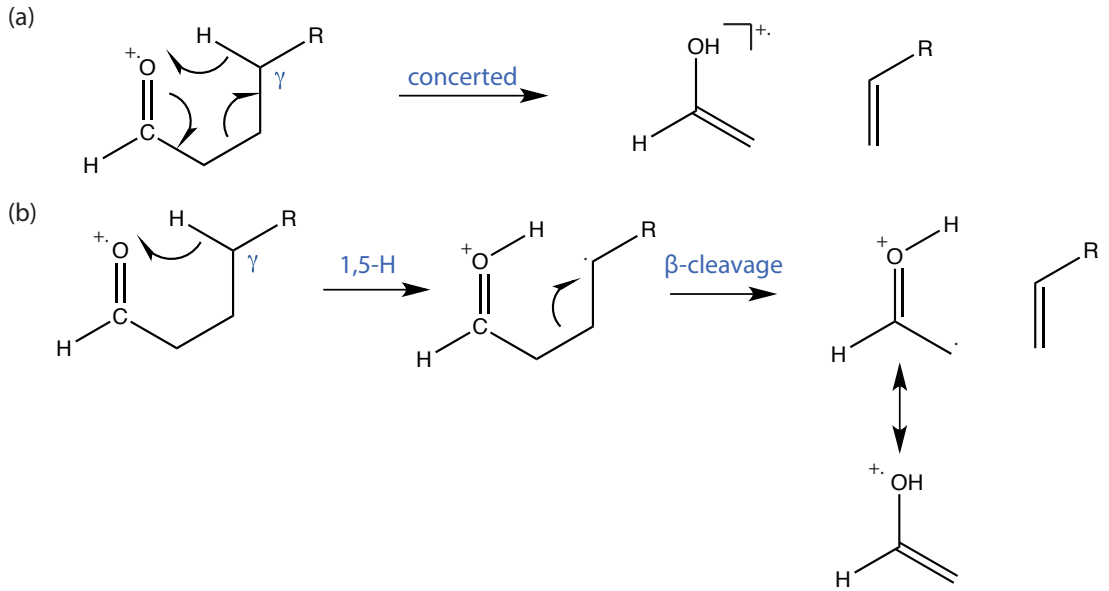

Figure 7.2: The McLafferty rearrangement, which proceeds with charge retention either via (a) a concerted mechanism, or (b) a stepwise mechanism, involving 1,5-H atom transfer and then β-bond cleavage.

group. The current general consensus is that the majority of molecules undergo the rearrangement via a stepwise process, with a select few favouring a concerted mechanism [13, 14].

A recent theoretical study by Norberg *et al.* investigated the McLafferty rearrangement of the radical cations of butanal and 3-fluorobutanal [13]. Their results revealed a transition state for the concerted McLafferty rearrangement of butanal at an energy of 1.635 eV above the ground state of the parent ion. In addition, three different stepwise dissociation pathways were identified. These latter pathways were found to lie at much lower energy, with the highest transition state only 0.624 eV above the ground state of the parent ion. The stepwise pathway is therefore expected to dominate at low internal energies of the parent ion. With the current experimental apparatus we are unable to vary the photon energy across this range to isolate one or other pathway. However, the products of the concerted and stepwise mechanisms are expected to be formed with internal energy distributions characteristic of the two distinct mechanisms, which differ by more than 1 eV in the barrier heights to dissociation. These internal energy distributions will be reflected in the observed translational energy distribution of the fragments.

The second process of interest is the McLafferty rearrangement with double hydrogen transfer, shown in Figure 7.3. The ions that result from this process have been observed in mass spectrometric studies of a range of carbonyl compounds, including esters, aliphatic

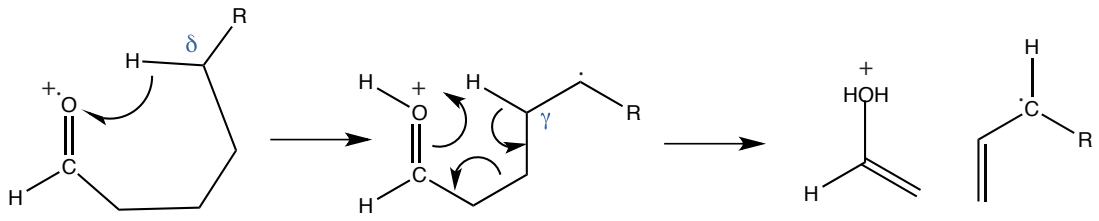

Figure 7.3: The McLafferty rearrangement with double hydrogen transfer. The process is shown here with an initial 1,6-H transfer. No assumption is made as to the ordering of these steps. The final β-bond cleavage may, in principle, occur either in a concerted or a stepwise manner.

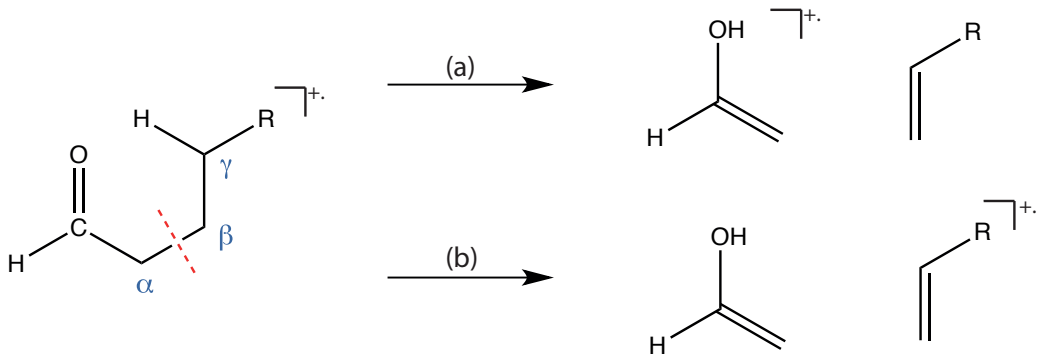

Figure 7.4: Fragmentation of aliphatic aldehydes following hydrogen atom transfer and β-bond cleavage, with (a) the charge remaining on the enolic fragment or (b) the charge residing on the alkene co-fragment. R=H, C_2H_5 and C_3H_7 for butanal, hexanal and heptanal, respectively.

carboxylic acids, aldehydes and ketones (see [2, 5, 15, 16] and references therein). The rearrangement results in the formation of an ion with an additional hydrogen as compared to the product of the McLafferty rearrangement. The resultant ion is therefore referred to as the *McLafferty+1 ion*. The exact mechanism for this process has still not been assigned. However, for the aliphatic chain lengths considered in this work, the process is thought to involve an H-atom transfer via a seven-membered transition state, in addition to the γ-hydrogen transfer of the McLafferty rearrangement (see [5] and references therein).

A different class of rearrangements, which are also considered in this work, are those which result in H_2O loss from the parent cation. These processes are thought to evolve through double hydrogen transfer to the oxygen of a carbonyl group via five, six or seven-membered transition states. H_2O loss proceeds with formation of a diene cation [17].

Rearrangement and fragmentation of an aliphatic aldehyde may result in the formation of an enolic fragment with an alkene co-fragment, as shown in Figure 7.4. Figure 7.4 (a) shows the McLafferty rearrangement itself, which results in the formation of the enolic

fragment ion (termed the *McLafferty ion*). However, generally either of the nascent fragments may retain the positive charge. The alkene ion product, formed as in process (b) in Figure 7.4, is referred to as the *McLafferty complement*. The relative abundance of the enol and alkene ions is determined by their respective ionization energies (IE), with the fragment possessing the lowest IE being the most abundant [18]. The McLafferty complement rearrangement is in fact a different dissociation process to the McLafferty rearrangement, and proceeds via its own fragmentation pathway. Therefore, the fragments that result from these rearrangements will have different translational energy distributions. The fragmentation products that result from the McLafferty complement rearrangement have also been considered in this study.

The three aldehydes considered in the present work are butanal, hexanal and heptanal. The McLafferty rearrangement with double hydrogen transfer is not observed for the butanal cation, and the fragment ions resulting from H_2O loss following MS studies of butanal are not particularly abundant [17]. However, it is the smallest aldehyde that fulfils the structural requirements that make the McLafferty rearrangement possible, i.e. it has a hydrogen γ to the carbonyl group. For this reason, this species has been chosen as the model compound for theoretical studies of the McLafferty rearrangement on multiple occasions [9, 10, 13]. In addition, a number of mass spectrometry studies have been performed on butanal [2, 17, 19, 20]. Therefore, it was appropriate to select butanal for investigation in the present study. For the relatively short chain aldehydes, the experimentally observed prevalence of the McLafferty rearrangement increases with chain length [2, 19, 20], and the McLafferty rearrangement with double hydrogen transfer and H_2O loss are also observed, with this in mind, hexanal and heptanal have also been investigated in the present study. To our knowledge, the reaction products of the aldehydic cations chosen have not previously been investigated by means of VMI.

Some of the rearrangements of interest have previously been observed in the VUV photoionization mass spectrometry study of Van Bramer and Johnston [2]. The current study, which expands on the previous work, aims to reveal the extent to which VMI can further our understanding of molecular rearrangements, particularly those of aliphatic aldehydes. In addition, in order to quantify the observed translational energies of the fragmentation products, some preliminary ab initio calculations have been carried out to determine the product energies for those channels for which the structures of the fragments are known. The mechanism for the McLafferty+1 rearrangement has not been strictly assigned and, therefore, the co-fragment which accompanies the McLafferty+1 ion may have a number of different structures. This is also the case for the ion which results from H_2O loss. For a

full treatment of the rearrangements of interest the product energies should be determined for every possible co-fragment and ion structure for the McLafferty+1 and H_2O loss processes, respectively. However, for this initial study, the ab initio calculations have been carried out to determine the energies of the products that result from the McLafferty rearrangement and McLafferty complement rearrangement of butanal, hexanal and heptanal. These proceed with γ-hydrogen transfer and, therefore, the structures of the resultant fragments are known, as shown in Figure 7.4.

7.2.1 Methods

Experiment

The photofragmentation of the three cationic species of interest, butanal, hexanal and heptanal, has been investigated experimentally using the VMI spectrometer, which has already been described in detail in Chapter 2. The molecular masses, vapour pressures, and ionization energies (IE) of the molecules are shown in Table 7.1. All samples were sourced from Sigma Aldrich and have a purity of >95%. For the experiments carried out here, the molecular beam comprised a small percentage of the sample seeded in 2 bar He (BOC, $>$ 99.9%). The seeding ratios employed for each species are also included in Table 7.1. Under the seeding conditions employed, no cluster formation was observed. Within the ion optics assembly, the molecular beam was intersected orthogonally by the co-propagating 118 nm and 355 nm beams, the 355 nm laser having been used to generate the 118 nm light. In all cases, the laser beams were linearly polarised parallel to the plane of the imaging detector. The parent and nascent fragment ions were velocity-mapped on to the 2D imaging detector.

Table 7.1: Molecular masses, vapour pressures, sample percentages and ionization energies (IEs) of butanal, hexanal and heptanal.

Name	Chemical Formula	Molecular Mass / u	Vapour Pressure / mbar (20 °C)	Approx. Seeding Ratio / %	IE / eV	Refs
butanal	$HC(O)C_3H_7$	72	120	0.5	9.83	[21]
hexanal	$HC(O)C_5H_{11}$	100	13	0.5	9.62	[22]
heptanal	$HC(O)C_6H_{13}$	114	4	0.1	9.65	[22]

Computational calculations

All calculations were performed using the Gaussian 09 [23] electronic structure package. To obtain the ground state optimised geometries of the neutral and cation alkyl aldehyde molecules, along with those of the products of their McLafferty and McLafferty complement rearrangements, Møller-Plesset second order perturbation theory (MP2) was employed, in conjunction with the 6-311+G(d,p) basis set, assigned to all atoms. Energies for all species in their MP2 optimised geometry were determined using the coupled-cluster singles and doubles (CCSD) method. Zero-point vibrational energy (ZPE) corrections have been computed from the unscaled frequencies at the MP2/6-311G+(d,p) level of theory.

7.2.2 Results & Discussion

Computational Results

Table 7.2 shows the calculated adiabatic and vertical ionization energies for butanal, hexanal and heptanal and the neutral forms of their McLafferty rearrangement and McLafferty complement rearrangement products. The adiabatic ionization energy is the energy difference between the ZPE corrected energies of the optimised geometries of the neutral ground state and ion ground state. The vertical ionization energy is the energy difference between the ZPE corrected energies of the neutral ground state and the ion ground state, both calculated at the optimised geometry of the neutral ground state. These latter values are comparable with the experimentally measured ionization energies, which have also been included in Table 7.2.

Figure 7.5 shows the energies of the various neutral and ionic species of interest when considering the McLafferty and McLafferty complement rearrangements of butanal, hexanal and heptanal. The product energies are listed in Table 7.3.

The horizontal purple dashed lines in Figure 7.5 indicate the maximum energy to which the parent molecules are excited on absorption of one photon of 118 nm light, i.e. for the case when all of the excess energy is released into internal excitation of the ion rather than into kinetic energy of the departing electron. The horizontal dotted blue lines indicate the maximum energy accessed on absorption of an additional 355 nm photon. It is clear that the sum of these two photon energies greatly exceeds the energies of the fragmentation products of interest. Therefore, unless there are significant barriers to rearrangement, we

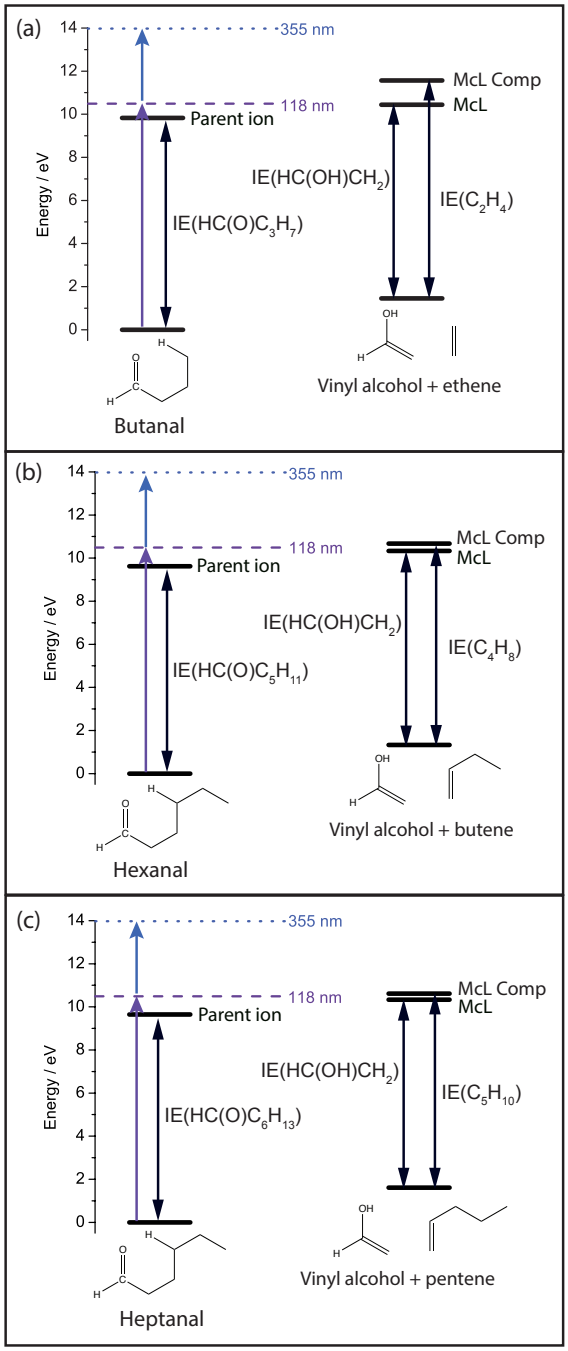

Figure 7.5: Schematic energy diagrams depicting the relationships between the McLafferty (McL) and McLafferty complement (McL comp) product energies and the parent neutral and ionic states, as well as the equivalent neutral pair of co-fragments for (a) butanal, (b) hexanal, and (c) heptanal. The experimental IEs for the parent ions are shown here. The IEs shown for the fragments are the calculated adiabatic ionization energies.

Table 7.2: Calculated and experimental ionization energies (IEs) for butanal, hexanal and heptanal and their McLafferty rearrangement and McLafferty complement rearrangement products: vinyl alcohol, ethene, 1-butene and 1-pentene.

Name	Chemical Formula	Molecular Mass / u	Adiabatic IE / eV	Vertical IE / eV	Experimental IE / eV	Refs
butanal	$HC(O)C_3H_7$	72	9.61	9.71	9.83	[21]
hexanal	$HC(O)C_5H_{11}$	100	9.52	9.60	9.62	[22]
heptanal	$HC(O)C_6H_{13}$	114	9.51	9.59	9.65	[22]
syn-vinyl alcohol	$HC(OH)CH_2$	44	9.00	9.31	9.30	[24]
ethene	C_2H_4	28	10.13	10.31	10.51	[25]
1-butene	C_4H_8	56	9.34	9.56	9.55	[26]
1-pentene	C_5H_{10}	70	9.10	9.17	9.50	[27]

Table 7.3: Energies of the McLafferty (McL) and McLafferty complement (McL comp) products of butanal, hexanal and heptanal, relative to the neutral ground state of the parent molecule.

Parent ion	Rearrangement	Products	Product Energy/ eV
butanal	McL	$HC(OH)CH_2^+ + C_2H_4$	10.44
	McL comp	$C_2H_4^+ + HC(OH)CH_2$	11.57
hexanal	McL	$HC(OH)CH_2^+ + C_4H_8$	10.33
	McL comp	$C_4H_8^+ + HC(OH)CH_2$	10.67
heptanal	McL	$HC(OH)CH_2^+ + C_5H_{10}$	10.33
	McL comp	$C_5H_{10}^+ + HC(OH)CH_2$	10.61

would expect the McLafferty and McLafferty complement ions to result from 118 nm and 355 nm irradiation of butanal, hexanal and heptanal. The time-of-flight mass spectra, which will now be presented, reveal the ions that are in fact observed.

Time-of-Flight Mass Spectra

The time-of-flight mass spectra of the ions produced from the molecules of interest following irradiation with 118 nm and 355 nm light are shown in Figure 7.6. The parent ion appears as the most intense (base) peak in each spectrum. It is clear from the multitude of mass peaks present within the spectra that photofragmentation yields a large number of

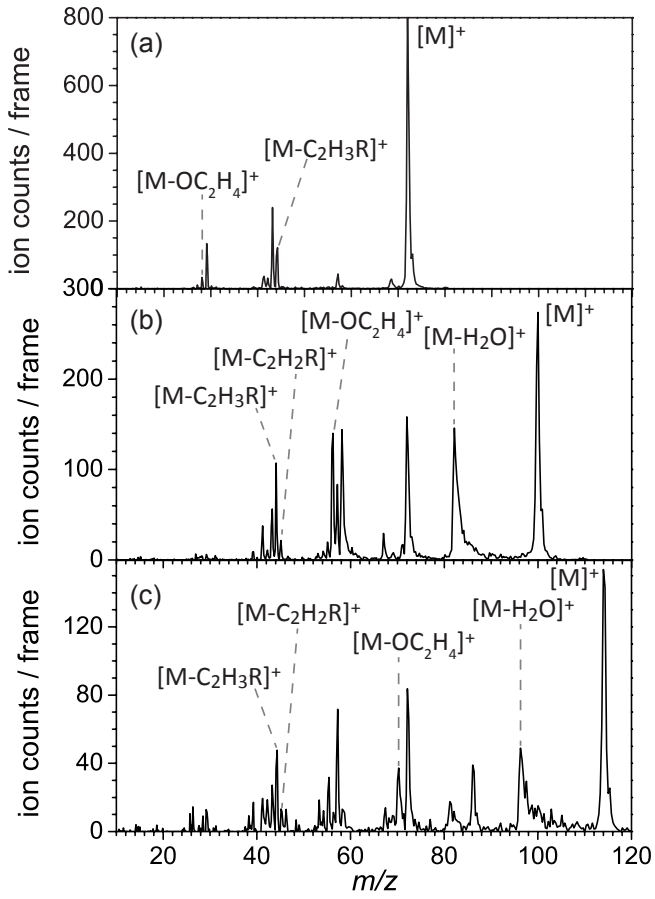

Figure 7.6: Time-of-flight mass spectra for (a) butanal, (b) hexanal, and (c) heptanal following irradiation with 118 nm and 355 nm light. The McLafferty ion, $[M - C_2H_3R]^+$, the McLafferty complement ion, $[M - OC_2H_4]^+$, the ion from H_2O loss, $[M - H_2O]^+$, the McLafferty+1 ion, $[M - C_2H_2R]^+$, and the parent ion, $[M]^+$, are labelled. R = H, C_2H_5 and C_3H_7 for butanal, hexanal and heptanal, respectively.

fragment ions. The intensities of these peaks, relative to the base peak, have been evaluated, and from these is it possible to obtain an idea of the relative probability of the different processes which lead to production of the observed ions.[1] The *m/z* peaks observed in the TOF-MS of butanal, hexanal and heptanal are tabulated along with their relative intensities in Tables 7.4 to 7.6.

In the following, we focus on the masses resulting from the four rearrangement processes of interest. The McLafferty ion produced from the aliphatic aldehydes (the vinyl alcohol cation, $[M - C_2H_3R]^+$) appears at *m/z* 44, and its complement appears at $m/z = (M - 44)$, where M is the mass of the parent ion, $[M]^+$. The McLafferty rearrangement with double

[1]The relative intensities presented here are not necessarily synonymous with branching ratios. No assumption is made as to the origin of the ions.

Table 7.4: *m/z* peaks observed in the TOF-MS of butanal, along with their relative intensities and chemical formulae of their likely ion identities.

m/z	27	28	29	41	42
Chemical Formula	C_2H_3	C_2H_4	C_2H_5 / HCO	C_3H_5	C_3H_6
Relative Intensity	0.41	1.45	7.16	3.79	1.95
m/z	43	44	57	72	
Chemical Formula	$HCOCH_2$ / C_3H_7	$HC(OH)CH_2$	$HCOC_2H_4$	$HCOC_3H_7$	
Relative Intensity	14.37	7.40	3.31	100	

Table 7.5: *m/z* peaks observed in the TOF-MS of hexanal, along with their relative intensities.

m/z	39	41	42	43	44	45	53	54	55
Relative Intensity	1.18	5.12	1.57	10.92	14.4	3.00	1.52	1.92	2.59
m/z	56	57	58	67	69	71	72	82	100
Relative Intensity	35.86	16.74	44.68	5.15	1.72	3.56	63.02	98.55	100.00

hydrogen transfer produces the McLafferty+1 ion, $[M - C_2H_2R]^+$, with *m/z* 45. H_2O loss from the parent cation results in $[M - H_2O]^+$ ions with $m/z = (M - 18)$.

Butanal, $HC(O)C_3H_7$, produces relatively few fragmentation products (see Figure 7.6 (a) and Table 7.4), and those fragment ions that are observed have low intensities relative to the strong parent ion signal, which appears as the base peak at *m/z* 72. The McLafferty ion is observed at *m/z* 44, with a relative intensity of 7.4%. Its complement, $C_2H_4{}^+$, appears at *m/z* 28, with a much reduced relative intensity of 1.45%. Butanal does not undergo

Table 7.6: *m/z* peaks observed in the TOF-MS of heptanal, along with their relative intensities.

m/z	25	26	27	28	29	31	40	41
Relative Intensity	1.02	1.55	0.11	0.96	2.67	0.36	0.00	5.03
m/z	42	43	44	45	46	54	55	56
Relative Intensity	5.59	6.81	11.36	3.25	2.53	2.28	8.55	3.18
m/z	57	58	67	68	69	70	72	74
Relative Intensity	19.36	5.49	4.12	2.55	3.45	19.36	34.11	1.96
m/z	75	81	82	86	96	100	103	114
Relative Intensity	0.42	8.86	7.26	19.82	45.56	14.79	5.79	100

the McLafferty+1 rearrangement, and therefore no ions are observed at *m/z* 45. The H_2O loss channel is not evident either. The remaining peaks in the spectrum can be assigned to bond cleavages and secondary fragmentations. There are a number of rearrangements and secondary fragmentation processes that can come into play. Since these fragment ions are not the key focus of this study, the identities of the peaks have only been assigned tentatively. $HCOC_2H_4^+$ (*m/z* 57) is the product of γ-bond cleavage. $C_2H_5^+$ (*m/z* 29) and $HCOCH_2^+$ (*m/z* 43) may result from simple β-bond cleavage. However, α-bond cleavage produces fragments of the same *m/z*: $C_3H_7^+$ (*m/z* 43) and HCO^+ (*m/z* 29). Signals at *m/z* 27 (C_2H_3), *m/z* 41 (C_3H_5) and *m/z* 42 (C_3H_6) are minor peaks, which most likely result from secondary fragmentations.

As the chain length increases by two CH_2 units from butanal to hexanal, a larger number of photofragmentation channels become available. This is evident in the increased number of peaks in the TOF-MS (see Figure 7.6 (b)), the relative intensities of which are listed in Table 7.5. In contrast to butanal, the McLafferty complement (*m/z* 56) peak is now significantly more intense than the McLafferty peak (*m/z* 44). In addition, the McLafferty+1 ion is observed at *m/z* 45. Furthermore, a metastable peak, the area of which is almost equal to that of the parent, is observed at *m/z* 82, which corresponds to loss of H_2O from the parent ion.

The TOF-MS of heptanal, Figure 7.6 (c), reflects that of hexanal, with yet more fragment ions being produced. The observed ions and their intensities relative to the parent ion are listed in Table 7.6. Again, the McLafferty and McLafferty+1 ions (*m/z* 44 and 45) are evident, as is the McLafferty complement, which appears at *m/z* 70. The peak resulting from H_2O loss appears at *m/z* 96.

Since both 118 nm and 355 nm photons are present simultaneously within the interaction region, there are a number of mechanisms by which photofragment ions could be produced. However, the absorption cross-section at 118 nm is much greater than at 355 nm for the molecules considered in this study, and so it is more likely that an initial absorption of a 118 nm photon occurs [28, 29]. Therefore, only those pathways that involve initial absorption of a VUV photon will be considered here. Since the photon energy of 118 nm light exceeds the IEs of the parent molecules, absorption of a VUV photon results in ionization. This process is evident in the presence of the intense parent ion peaks within the TOF-MS, shown in Figure 7.6. Absorption of one photon of 118 nm light can also result in dissociative ionization, since there are a number of fragment ions with appearance ener-

gies[2] below the 10.49 eV available from a single photon of VUV light. Fragmentation can also occur when a parent ion, formed following absorption of a 118 nm photon, absorbs a photon of 355 nm light. The additional energy provided by the 355 nm photon surpasses the dissociation limits to a number of fragmentation channels, leading to production of additional fragment ions. It would be a lengthy process to confirm the individual dissociation mechanisms that lead to production of all of the observed fragment ions from each of the parent molecules. Instead, in the case of hexanal, a qualitative power dependence study has been undertaken. From the dependence of the various signal intensities on the laser power, the product ions resulting from one-photon dissociative ionization have been distinguished from those whose formation requires an additional photon of 355 nm light.

Figure 7.7 displays the TOF-MS of hexanal acquired at two different 355 nm laser powers (pulse energies). The peaks with known appearance energies (AEs) are indicated. It can be observed that those peaks with AEs below the 10.49 eV available from the VUV photon are not as strongly dependent on the pulse energy of the 355nm laser. For example, *m/z* 82, which corresponds to loss of H_2O from the parent ion, has an AE of 9.80 eV, and the signal intensity varies significantly less with laser pulse energy than either the McLafferty ion, *m/z* 44, which has an AE of 11.60 eV, or the McLafferty complement ion, *m/z* 56, which has an AE of 10.70 eV. The appearance energies for the ions resulting from the rearrangements of interest are listed in Table 7.7. Although the AE of the McLafferty+1 ion, *m/z* 45, is not known, from the variation in signal intensity with laser energy we predict an AE greater than 10.49 eV. From the varying dependencies of the signal intensity on laser pulse energy it is possible to conclude that of the rearrangements of interest, only H_2O loss results from 118 nm dissociative ionization of the hexanal parent ion. The formation of the McLafferty, the McLafferty complement and the McLafferty+1 ions requires that the parent ions absorb at least one additional 355 nm photon.

The appearance energies of the fragment ions of interest formed from butanal are also listed in Table 7.7. The AE for the McLafferty complement might be expected to be greater than that observed for the McLafferty ion, since its ionization energy is higher (10.51 eV as compared to 9.30 eV [24, 25]). If this is the case, then, as for hexanal, the McLafferty and McLafferty complement ions both have AEs above the VUV photon energy, and, therefore, must result from absorption of an additional 355 nm photon by the parent ion.

[2]In the discussion of the TOF spectra, the fragment ion appearance energies are considered, since these take into account any barriers to dissociation, which are likely to exist for the rearrangement processes considered here. The calculated product energies will be called upon when the translational energies of the products are discussed.

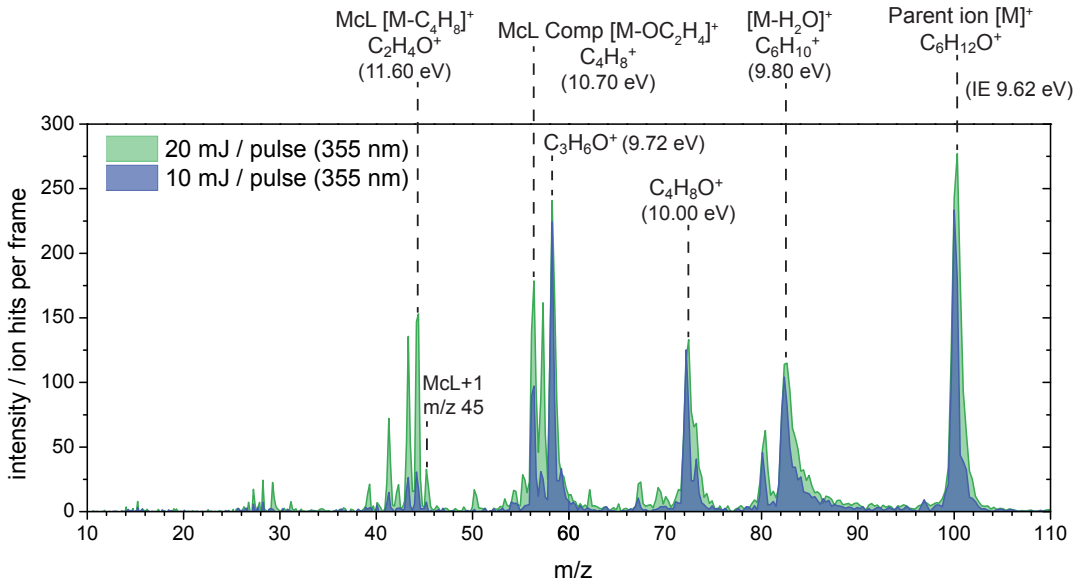

Figure 7.7: TOF-MS of hexanal acquired with two different 355 nm laser pulse energies. The known appearance energies for a number of ions are shown in brackets along with their chemical formula.

Table 7.7: The appearance energies (AE) in eV of the ions produced through the rearrangmenets of interest of butanal, hexanal and heptanal. Also shown are the ionization energies of the parent molecules.

	Fragment ion	Parent ion		Refs
		butanal	hexanal	
		AE / eV	AE / eV	
McLafferty	$[M - C_2H_3R]^+$	10.52	11.60	[30]
McLafferty complement	$[M - OC_2H_4]^+$	-	10.70	[30]
McLafferty +1	$[M - C_2H_2R]^+$	N/A	-	
H_2O loss	$[M - H_2O]^+$	N/A	9.80	[30]
Parent molecule IEs	$[M]^+$	9.83	9.62	[21, 22]

In the work of Van Bramer and Johnston, for which the VUV light was generated in a similar fashion to this work, the experimentalists made every attempt to minimise the effect of the 355 nm laser [2]. For this reason, in the TOF-MS produced from that work only those peaks with AEs below 10.49 eV, i.e. those ions which result from dissociative ionization, appear as major peaks. The peaks resulting from 355 nm involvement are, in that case, minor. By comparing the TOF-MS for butanal and heptanal from the current work with

those reported in the previous work, it is possible to confirm the photon dependence of the mass peaks of interest. In the previous TOF-MS of butanal, the McLafferty and McLafferty complement ions appear with very low signal intensity, and can only just be observed above the baseline, whereas in Figure 7.6 (a), these ions are observed at *m/z* 44 and *m/z* 28, respectively, with significant intensity. This confirms that, as in the case of hexanal, the production of these fragment ions involves both a 118 nm photon and a 355 nm photon. This is also the case for the McLafferty ion and the McLafferty+1 ion in the TOF-MS of heptanal. However, the McLafferty complement from heptanal results from one-photon dissociative ionization at 118 nm.

With reference to the previous VUV photoionization study of Van Bramer and Johnston [2] and our qualitative power dependence study, we can conclude that in each case production of the McLafferty ion requires that the parent ion absorbs an additional 355 nm photon. The McLafferty complement ions from butanal and hexanal follow a similar pattern, as do the McLafferty+1 ions produced from hexanal and heptanal. Generation of the McLafferty complement from heptanal and H_2O loss from hexanal and heptanal are the only processes of interest which result from dissociative ionization of the parent molecule. These photon dependencies are summarised in Figure 7.8. Many of the rearrangements of interest require the parent cation to have a greater energy than that generated from a single VUV photon. Although the involvement of the 355 nm light presents some complications within the experiment, absorption of an additional photon of 355 nm enables ions with AEs of up to 14 eV to be generated, therefore revealing fragmentation channels which would otherwise be inaccessible to the current experiment.

From this discussion of the origins of the ions, as illustrated in Figure 7.8, it is clear that care must be taken when comparing the relative intensities of the fragment ion signals. Only those ions with the same photon dependence can truly be compared. Table 7.8 lists peak intensities for the fragment ions resulting from the rearrangements of interest, relative to the intensity of the parent ion signal. The relative intensities (RIs) shown in bold are for the parent ions and those fragment ions that result from single-photon dissociative ionization mechanisms. The McLafferty rearrangement is the dominant rearrangement for butanal. However, for this molecule very little fragmentation occurs. As the carbon chain lengthens, as for hexanal, the McLafferty rearrangement product becomes more prevalent compared to the parent ion, but it is overshadowed by the McLafferty complement, which has a lower appearance energy. For heptanal there are significantly more competing fragmentation processes, as reflected in the number of fragment ions observed in the TOF-MS (see Figure 7.6 (c) and Table 7.6). However, despite this, the McLafferty and McLafferty+1

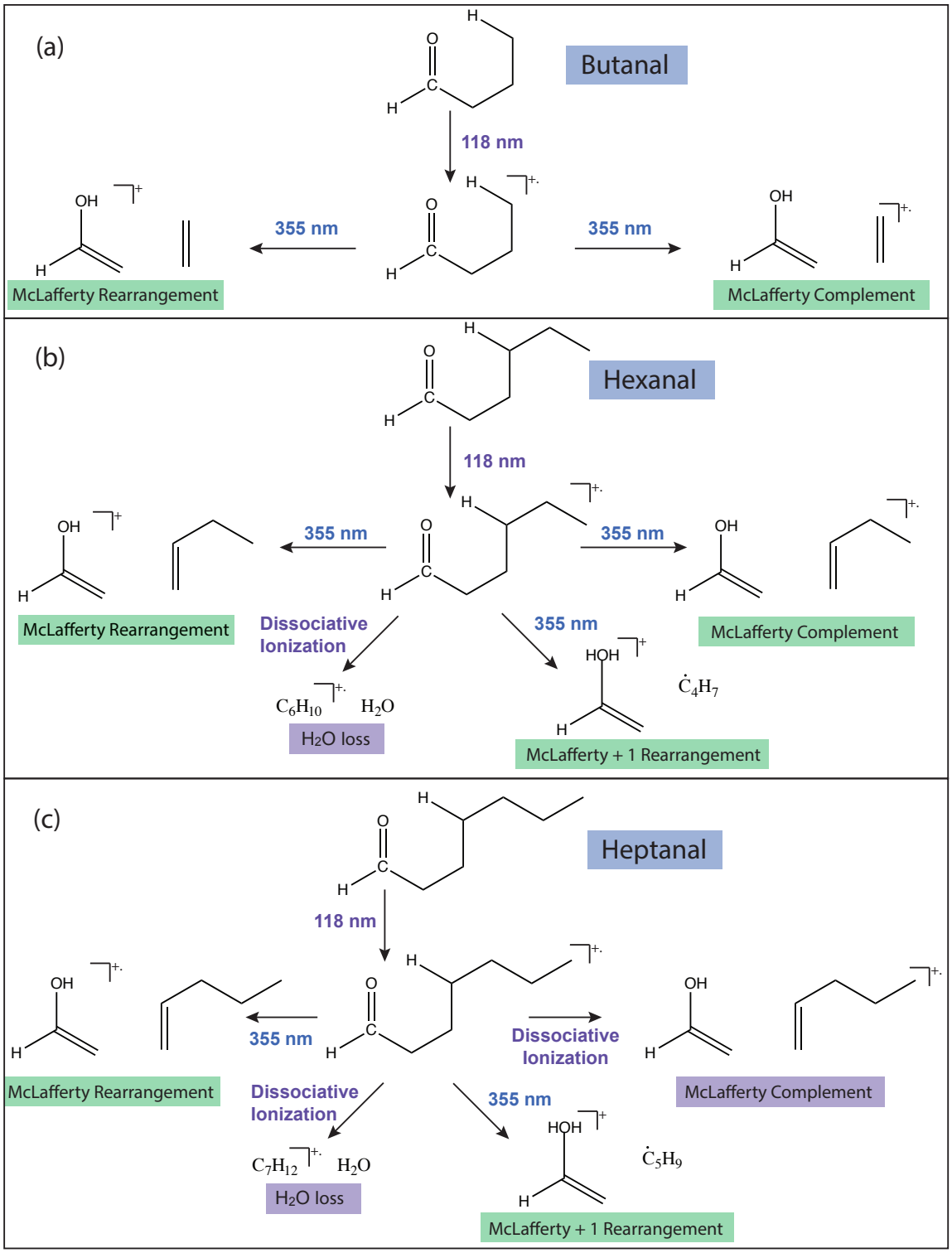

Figure 7.8: The observed rearrangements of interest and their photon dependence are summarised for (a) butanal, (b) hexanal, and (c) heptanal. In each case the initial step involves VUV photoionization of the parent molecule. The observed ions are then formed either as a result of dissociation ionization or absorption of an additional photon of 355 nm light.

Table 7.8: The relative intensities of the McLafferty ($[M-C_2H_3R]^+$) McLafferty complement ($[M-OC_2H_4]^+$), McLafferty+1 ($[M-C_2H_2R]^+$), $[M-H_2O]^+$ and parent ($[M]^+$) ions observed in the TOF-Ms of butanal, hexanal and heptanal.

Fragment ion	Intensity relative to parent ion		
	butanal	hexanal	heptanal
$[M-C_2H_3R]^+$ (McL)	7.40	14.4	11.36
$[M-OC_2H_4]^+$ (McL complement)	1.45	35.86	**19.36**
$[M-C_2H_2R]^+$ (McL+1)	-	3.00	3.25
$[M-H_2O]^+$	-	**98.55**	**45.56**
$[M]^+$	**100**	**100**	**100**

ions produced from heptanal have similar RIs as compared with those of the ions produced from hexanal.

The $[M-H_2O]^+$ fragment ions, which result from single-photon dissociative ionization with loss of H_2O, are observed to be the most intense fragment ion peaks in the TOF-MS of hexanal and heptanal. These ions are unstable with respect to methyl loss. If the secondary fragmentation occurs in the time-of-flight tube this will result in a broadening of the mass peak. This is the case for both hexanal and heptanal, and the fragment ions appear as metastable peaks in the TOF-MS. Some secondary fragmentation must also occur before the ions pass out of the ion optics region, since the secondary fragmentation ions are also observed at their appropriate mass; signal is observed at *m/z* 67 and *m/z* 81 in the TOF-MS of hexanal and heptanal, respectively, which corresponds to CH_3 loss from $[M-H_2O]^+$. The secondary fragmentation also results in loss of intensity at the primary fragment ion mass.

In summary, a wide range of dissociation processes occur following irradiation of the aliphatic aldehydes with 118 nm and 355 nm light. The velocity-map images recorded for the McLafferty, McLafferty complement, McLafferty+1 and $[M-H_2O]^+$ ions (where observed), will now be presented and discussed.

Velocity-Map Imaging

The velocity-map images and the translational energy distributions extracted from the images are shown in Figures 7.9, 7.11, 7.13 and 7.14. As shown in Figure 7.9, the E_T distributions for the McLafferty rearrangement products of (a) butanal, (b) hexanal, and (c)

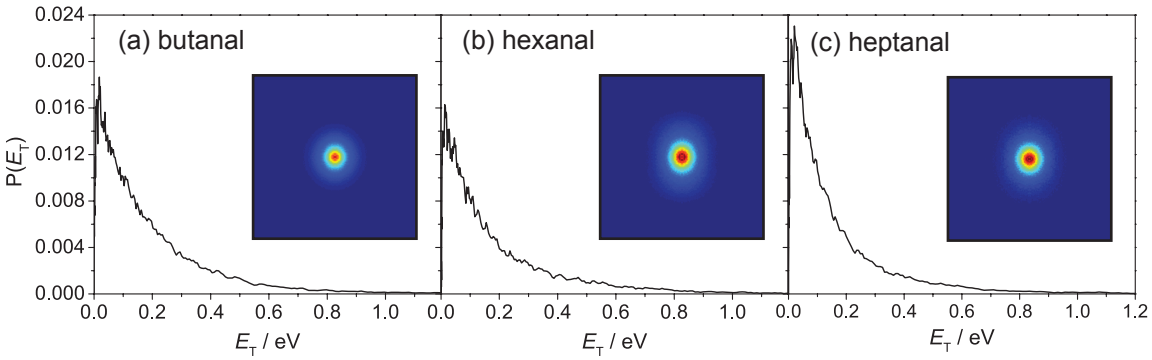

Figure 7.9: Translational energy distributions for the products of the McLafferty rearrangements of (a) butanal, (b) hexanal, and (c) heptanal. In each case, the P(E_T) distribution has been obtained from a velocity-map image of the McLafftery ion, *m/z* 44 (inset).

heptanal all peak at low translational energy (∼0.015 eV) and tail off at around 1 eV. Even though the appearance energy of the McLafferty ion from hexanal lies more than 1 eV higher in energy than that of butanal, the E_T distributions obtained from the velocity-map images of these ions appear to be similar.

To obtain a clearer picture of the energy partitioning, the translational energy, E_T, can be expressed as a fraction, f_T, of the energy available to the fragments, E_{av}.

$$f_T = E_T/E_{av} \tag{7.1}$$

Figure 7.10 shows the distribution of f_T for the products of the McLafferty rearrangement of butanal, hexanal and heptanal. The available energies, E_{av}, and the average fraction of this energy which goes into translation, $\langle f_T \rangle$, are listed in Table 7.9. The products of the McLafferty rearrangement of the parent ions of interest appear to show a signature f_T distribution, with $\langle f_T \rangle$ of around 0.03. This implies that around 97% of the energy available to the products is distributed amongst the internal degrees of freedom of the fragmentation products. The similarities in the distributions reflect the similarities in the dissociation processes which yield them. Such f_T distributions are characteristic of statistical dissociation processes. On absorption of a photon of 355 nm light the aliphatic aldehyde parent ion has enough energy to traverse the transition state barrier for the McLafferty rearrangement. The mechanism likely involves an initial excitation followed by relaxation back down to the ion electronic ground state. The slow dissociation process allows for significant internal energy redistribution. As reflected in the f_T distributions, the most internally excited fragments are the most likely to surmount the activation barrier to reach the transition state.

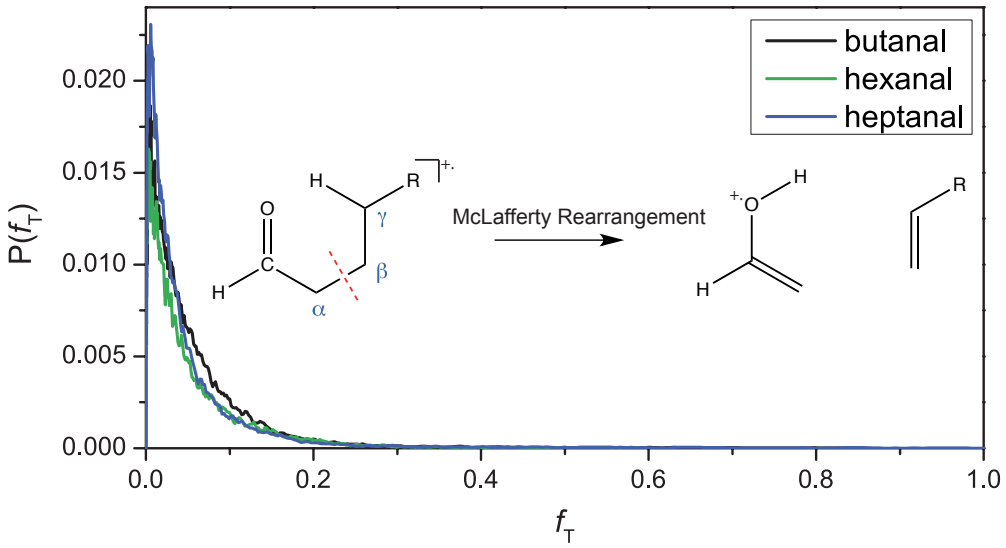

Figure 7.10: f_T distributions for the products of the McLafferty rearrangements of butanal (black), hexanal (green), and heptanal (blue). The McLafferty rearrangement is illustrated, R = H, C_2H_5 and C_3H_7 for butanal, hexanal, and heptanal, respectively.

Table 7.9: Energies available to the McLafferty and McLafferty complement products of butanal, hexanal and heptanal. ‡Calculated product energy exceeds energy of single VUV photon.

Parent ion	Rearrangement	E_{av} / eV	$\langle f_T \rangle$
butanal	McLafferty	3.543	0.032
	McLafferty complement	2.413	0.072
hexanal	McLafferty	3.653	0.030
	McLafferty complement	3.313	0.086
heptanal	McLafferty	3.653	0.026
	McLafferty complement	- ‡	-

The distributions in Figure 7.10 do not display any bimodal structure, as may be expected if the McLafferty ion were produced via stepwise and concerted mechanisms. As discussed, the work of Norberg *et al.* revealed that in the case of butanal, the concerted mechanism has a barrier height more than 1 eV higher in energy than for any of the three stepwise process that were identified [13]. It is therefore expected that the stepwise processes dominate here. However, without a tuneable VUV source it is not possible to distinguish clearly between these.

Formation of the McLafferty complement ion involves fragmentation of the parent ion

through a different dissociation channel than for the case when the McLafferty ion is formed. Therefore, the observed ions cannot be momentum matched, as they are not formed from the same fragmentation event. This is exemplified in the case of heptanal, for which the TOF-MS data has revealed that the McLafferty complement ion results from single-photon dissociative ionization, whereas the formation of the McLafferty ion requires the energy from a 355 nm photon, in addition to the initially absorbed VUV photon, to proceed.

The E_T distribution obtained from the McLafferty complement ion of heptanal is shown in Figure 7.11 (c). The distribution peaks at a translational energy of 0.015 eV, and tails off at around 0.4 eV. This rearrangement yields a much narrower distribution of translational energies than observed for the McLafferty rearrangement of heptanal. This follows since the latter process, which involves an additional 355 nm photon, is likely to have significantly more energy available to the fragmentation products.

Although the TOF-MS data indicate that the McLafferty complement products result from single-photon dissociative ionization of heptanal, the product energy for this process, obtained from the electronic structure calculations, exceeds the energy available from one photon of 118 nm. Therefore, the f_T distribution could not be assessed for this dissociation channel, as has been done for the McLafferty rearrangement of heptanal. Since the 1-pentene ion (*m/z* 70, the McLafferty complement ion of heptanal) is observed, the dissociation of the heptanal cation must result in a stable 1-pentene cation. A number of minimum energy geometries have been located for 1-pentene. However, only one structure, which yields the product energies presented here, formed a stable 1-pentene cation. This can mean one of two things: either this structure is that which is formed as a result of the McLafferty complement rearrangement, but the calculations overestimate the product energy; or there exists a lower energy structure of the 1-pentene cation. Either way, further electronic structure calculations need to be undertaken in order to form a clearer picture of this channel.

In the case of butanal and hexanal, in order to form their McLafferty complement ions, the parent ions absorb an additional photon of 355 nm light. The E_T distributions for the McLafferty complement ions of butanal and hexanal are shown in Figure 7.11 (a) and (b), respectively. These more closely resemble the McLafferty rearrangement distributions, which also result from additional absorption of a 355 nm photon. The f_T distributions for McLafferty complement rearrangement products of butanal and hexanal are shown in Figure 7.12 and their corresponding $\langle f_T \rangle$, along with E_{av}, are listed in Table 7.9. Just as the McLafferty rearrangement of the aliphatic aldehyde ions generates a signature f_T

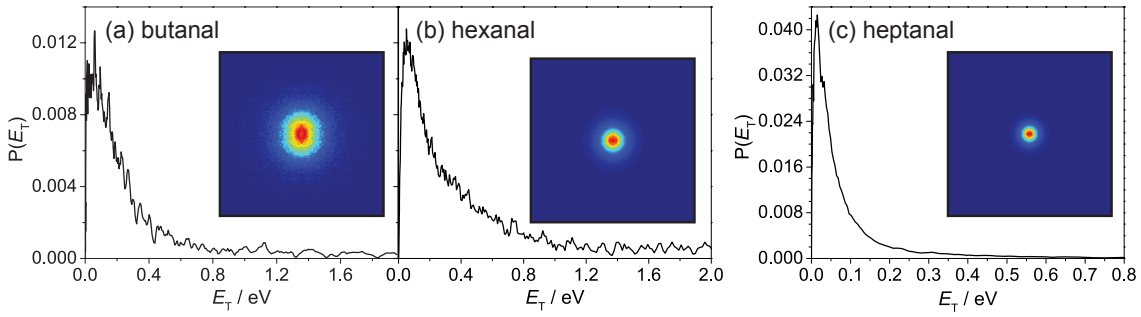

Figure 7.11: Total translational energy releases for the McLafferty complement products (neutral enol and alkene cation) from (a) butanal, (b) hexanal and (c) heptanal, obtained from the velocity-map images of the McLafferty complement ions shown.

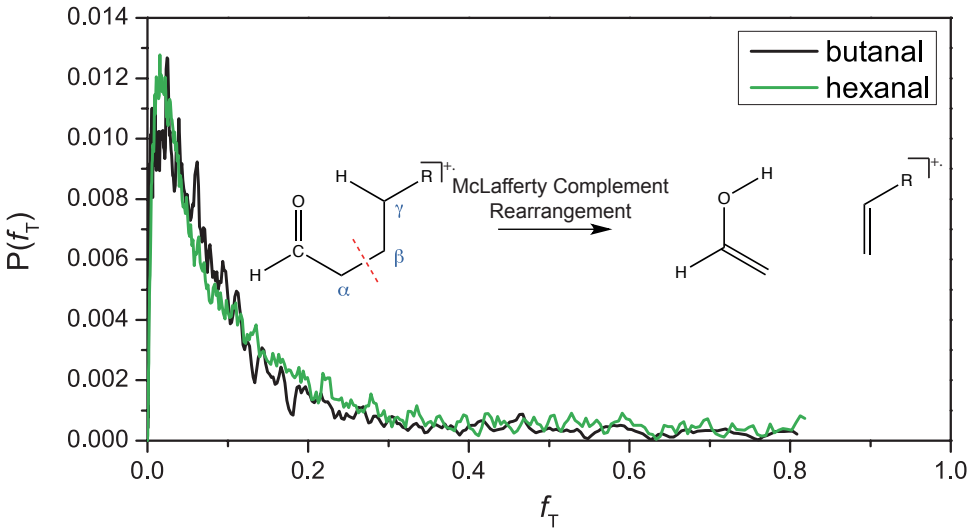

Figure 7.12: f_T distributions for the products of the McLafferty complement rearrangements of butanal (black), and hexanal (green). The McLafferty complement rearrangement is illustrated, R = H, and C_2H_5 for butanal, and hexanal, respectively.

distribution, so does the McLafferty complement rearrangement of the butanal and hexanal ions. The $\langle f_T \rangle$ of the McLafferty complement rearrangement indicate that this process results in slightly more of the energy available to the products being released as translation, compared with the McLafferty rearrangement; however the fragments are still born with a significant degree of internal excitation.

The McLafferty+1 rearrangements of hexanal and heptanal also result in products with low translational energy. As shown in Figure 7.13, the product E_T distributions peak at 0.010 eV for (a) hexanal and (b) heptanal. Both distributions tail off at around 0.6 eV. As compared to the E_T distributions from the McLafferty rearrangement, the products of the McLafferty+1

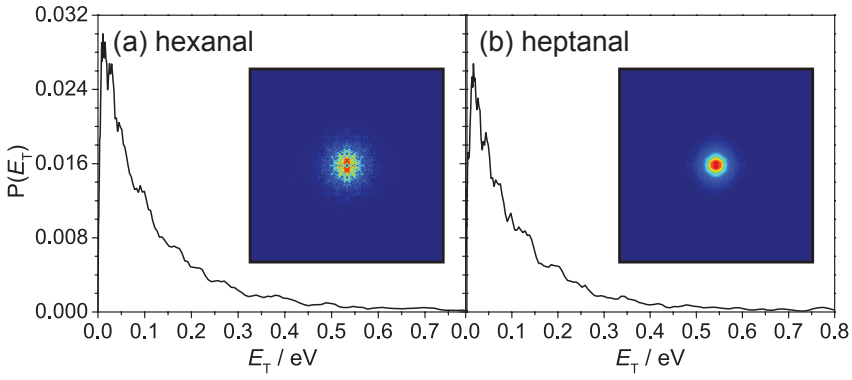

Figure 7.13: P(E_T) distributions for the products of the McLafferty+1 rearrangements of (a) hexanal and (b) heptanal. The images of the McLafferty+1 ion from which these distributions have been obtained are shown.

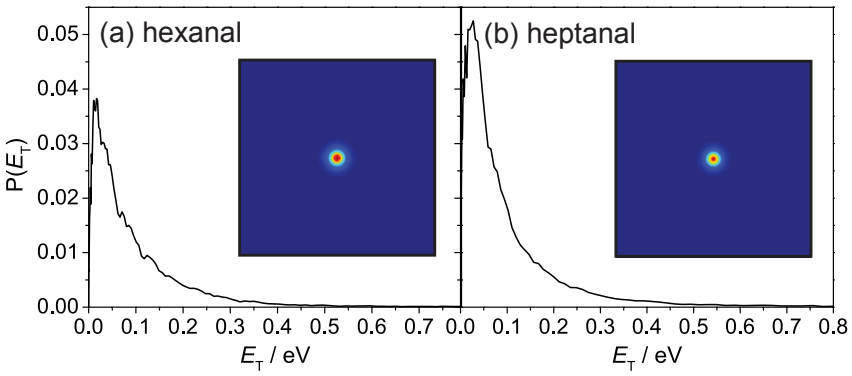

Figure 7.14: P(E_T) distributions of the $[M - H_2O]^+$ and H_2O fragmentation products of (a) hexanal and (b) heptanal, obtained from velocity-map images of the $[M - H_2O]^+$ ion (inset).

rearrangement are formed with a larger percentage of the population possessing very low translation energy. A considerable amount of internal energy redistribution is required in order to ensure the energy is in the correct degrees of freedom to surmount the barriers to the transition states involved in the McLafferty+1 rearrangement; the ion in this case is quite long lived, and eventually finds its way to the correct region of the potential energy surface to allow dissociation.

The product ions resulting from H_2O loss in hexanal and heptanal yield the E_T distributions shown in Figure 7.14 (a) and (b), respectively. As in the case of the McLafferty complement process in heptanal, which also results from single-photon dissociative ionization, these E_T distributions appear narrow with peaks at low translational energy, 0.016 eV and 0.028 eV for hexanal and heptanal, respectively. It should be noted, however, that the translational

energy distribution resulting from H_2O loss from the hexanal and heptanal ions may in fact peak at lower translational energy than is observed here. As discussed, the $[M-H_2O]^+$ ions are unstable with respect to methyl loss. A portion of the most highly internally excited (lowest E_T) fragment ions most probably undergo secondary fragmentations in the interaction region. Furthermore, the appearance of the metastable $[M-H_2O]^+$ peaks in the TOF spectra, Figure 7.6, indicate that the images shown in Figure 7.14 may include contributions from ions formed in secondary fragmentation of $[M-H_2O]^+$ that occur in the flight tube region, which therefore arrive at the same TOF. When undertaking imaging mass spectrometry studies, metastable peaks should be treated with care.

The velocity-map images presented here all display isotropic angular distributions, with E_T distributions that peak close to zero and resemble exponential decays. Such translational energy distributions are often characteristic of statistical dissociation processes. These distributions are typical of two mechanisms: (1) a mechanism involving dissociative ionization on the electronic ground state of the parent ion, and (2) a mechanism in which an initial excitation of the parent ion is followed by internal conversion to the ground state with dissociation resulting from this internally excited ground state parent ion.

Laskin and Lifshitz, who have compiled a review of kinetic (translational) energy release distributions in mass spectrometry, have discussed a number of different ways in which the translational energy distributions resulting from statistical distributions can be modelled [31]. The methods range from Phase Space Theory (PST) to the model free approach (MFA) (see [31] and references therein). The former method works on the assumption that the complete phase space of the species is sampled, so that the E_T distribution reflects the density of states. To implement such a model, ab initio calculations generally have to be performed in order to obtain the vibrational and rotational frequencies of the molecule of interest. In contrast, no prior knowledge, either of the internal degrees of freedom or of the potential energy surface of the fragmentation process, is required for the latter method. For this reason, MFA is a very simple method for the analysis of E_T distributions. The experimentally obtained E_T distributions are fit to an equation for an exponential decay. Through this fitting process, it is possible to obtain the binding energy and an estimate of any centrifugal barrier. However, these statistical models assume that there is no barrier to dissociation, and only work well for cases in which the reverse activation energy is negligible. In the case of the McLafferty-type rearrangement processes, the reactions must proceed over a barrier since they involve tight transition states. From the observed E_T distributions, which peak at very low translational energy, it is clear that these barriers

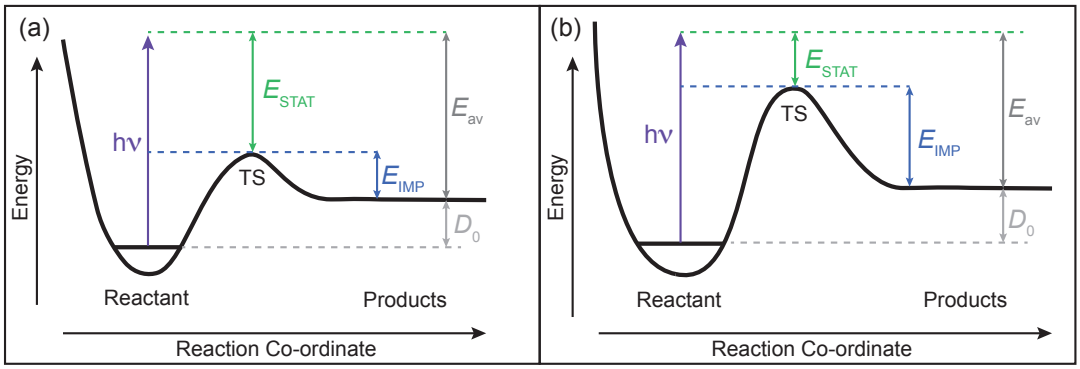

Figure 7.15: Schematic examples of two cuts through potential energy surfaces, showing very different barrier heights. (a) shows the case of a lower transition state (TS) energy, whereas (b) shows a higher barrier height. E_{STAT} and E_{IMP} are illustrated for each case. (Adapted from Fig. 1 from reference [32].)

are low. However, a true fitting of the E_T distributions requires that they are taken into account.

Neumark and co-workers have put forward a method to characterise non-statistical unimolecular dissociation over a barrier [32]. The statistical adiabatic impulsive (SAI) model portions the available energy, E_{av}, into E_{STAT} and E_{IMP}, as illustrated in Figure 7.15, where the former is the energy in excess of the barrier to dissociation, and the latter is the equivalent of the reverse activation barrier. These two energy reservoirs are treated separately in order to model the system. The treatment of E_{STAT} considers direct projections of a vibrational microcanonical ensemble at the transition state onto product quantum states, whereas, for E_{IMP}, the sudden dissociation of the transition state is considered. In order to apply the SAI model, the energy of the reactant, products and transition state (TS) should be known, so that the interaction potential for the unimolecular dissociation is well described. Future ab initio calculations will enable characterisation of the parent ion, fragmentation products and transition states for the rearrangements of interest. The results of such calculations and the fitting of the experimental E_T distributions with the SAI method will grant further understanding of the dynamics involved in the dissociation of aliphatic aldehyde cations.

7.2.3 Conclusion

The McLafferty rearrangement, the McLafferty complement rearrangement, the McLafferty+1 rearrangement, and H_2O loss from the parent ion have been the focus of this preliminary study into the fragmentation processes of the aliphatic aldehyde cations. Butanal,

hexanal and heptanal have been used as model systems. It has been observed experimentally that the rearrangements of interest result from either one-photon dissociative ionization, following absorption of a VUV photon, or following absorption of an additional photon of 355 nm light. By employing the 355 nm light, it is possible to investigate channels which would otherwise be inaccessible. The rearrangements all result in translational energy distributions peaking at very low energies, with a significant portion of the available energy going into the internal degrees of freedom of the fragment ions, as would be expected from either a mechanism involving dissociative ionization of the electronic ground state of the parent ion, or a mechanism in which an initial excitation of the ion is followed by internal conversion to the electronic ground state of the parent ion and dissociation on this state.

Ab initio calculations of the product energies have enabled the observed E_T distributions to be quantified as a fraction, f_T, of the available energy. The f_T plots reveal the signature distributions of the McLafferty and McLafferty complement rearrangements. Further ab initio calculations and fitting of the experimentally determined E_T distributions would aid in extending our understanding of the dissociation mechanisms involved in the rearrangements of the aliphatic aldehyde ions.

Although with the current experimental setup it has not been possible to make a formal conclusion as to whether the McLafferty rearrangement proceeds in a stepwise or concerted manner, within the energy range investigated, it is expected that one or more stepwise processes evolve on the ground state potential energy surface of the parent ion. The use of tuneable VUV radiation with VMI may allow the concerted and stepwise mechanisms to be observed independently. Such an investigation would benefit from extensive ab initio calculations on the McLafferty rearrangements of hexanal and heptanal, along the lines of those performed for butanal by Norberg *et al.* [13].

7.3 Rearrangement Reactions of Organic Cations: (B) Retro-Diels-Alder Reaction

The work that has been described in this chapter so far has discussed a number of rearrangements of cationic species, specifically those of aliphatic aldehyde cations. The focus now shifts to a different process, which is also commonly observed in mass spectrometry studies, namely the retro-Diels-Alder (RDA) reaction of cyclic mono-alkene cations. RDA reactions of cyclic mono-alkenes, which yield conjugated di-alkene (diene) and mono-alkene (ene) products, have also been observed to occur for neutral species, in both the gas and liquid phase. These neutral reactions will be discussed in Chapter 8.

Mass spectrometry studies of RDA reactions from the period 1965-1982 were reviewed by Tureček and Hanuš [33], and prior to that by Djerassi and co-workers [34]. Since then, in a number of mass spectrometry studies, substantially larger molecules, than those that have been investigated here, have been observed to undergo the RDA reaction (see, for example, [35–38]). Furthermore, a number of gas-phase experimental and theoretical studies have investigated the Diels-Alder reaction in the forward direction [39–42]. Bouchoux et al. [43] have undertaken a theoretical investigation into the low energy dissociation processes of cyclohexene, which is the simplest cyclic alkene which undergoes the retro-Diels-Alder reaction. However, to our knowledge, the preliminary study presented here constitutes the first experimental imaging study of a number of cyclic mono-alkenes.

For this velocity-map imaging study, four species, all of which have been observed to undergo the RDA reaction in mass spectrometry studies, have been chosen as the model systems, namely cyclohexene, and three of its derivatives, 1-methyl and 4-methyl-cyclohexene, and limonene. In mass spectrometry studies of alkene species, a number of different processes compete with the RDA reaction [33]. These include H_2-loss, H-loss, and other simple bond fragmentation processes. When these competing reactions present themselves as low energy pathways they often dominate, and the RDA reaction is suppressed [34]. As a consequence, two different cyclohexene derivatives may dissociate via very different pathways. For example, 1-acetyl and 4-acetylcyclohexene exhibit both CH_3 loss and cleavage of the ring-$COCH_3$ bond, but the RDA reaction is not observed; whereas 1- and 4-methylcyclohexene undergo the RDA reaction [34]. Furthermore, it has been observed that a limited internal energy range of the parent ion will optimise the RDA reaction [44], which probably comes about since a certain amount of energy is required to surpass any barrier to dissociation for the RDA pathway, however, at significantly higher energies than this other dissociation processes might dominate over the RDA reaction. Therefore, one of

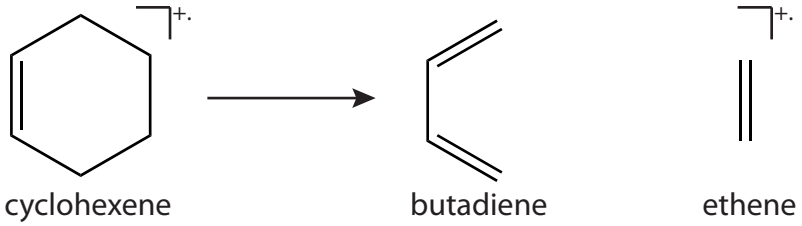

Figure 7.16: The retro-Diels-Alder reaction of the cyclohexene cation to form butadiene and ethene.

the aims of this work is to determine whether the model systems undergo the RDA reaction as a result of either single-photon dissociative ionization, which accesses low energy internal states of the molecular ion, or following additional UV photoexcitation, which accesses higher internal states of the parent ion.

The simplest example of an RDA reaction, that of the cyclohexene cation, results in the formation of butadiene and ethene, as shown in Figure 7.16. The RDA reactions of the cyclohexene derivatives are shown in Figure 7.17. The RDA reaction of the 1-methylcyclohexene cation, Figure 7.17 (a), produces isoprene with an ethene co-fragment. The 4-methylcyclohexene cation yields butadiene and propene, as shown in Figure 7.17 (b). The third derivative cation of interest, limonene, undergoes an RDA reaction, Figure 7.17 (c), which yields two isoprene fragments. The RDA reactions may yield products with the charge on either the diene or the ene fragmentation product (the general case has been shown here), representing two distinct fragmentation pathways. Both will be considered in this study. For clarity, in the text that follows, the channel which leads to production of the ene cation will often be referred to as the 'complementary RDA reaction'.

As shown in Figure 7.18, the RDA reactions of cyclic alkene cations can either proceed via (a) concerted or (b) stepwise mechanisms. The effective mechanism is observed to be dependent on the ring substituents and constituents, in principle, if the energy required for each process is comparable, both mechanisms could be active [33]. The concerted mechanism, Figure 7.18 (a), involves a six membered transition state. In contrast, the stepwise process, Figure 7.18 (b), proceeds initially via a simple bond cleavage step, which leads to formation of an intermediate species. A second bond cleavage yields the diene and ene products. Velocity-map imaging experiments have the potential to reveal which mechanism is active in a particular case.

In the present study, time-of-flight mass-spectra of the cyclic alkene cations, and velocity-map images of the RDA product ions are analysed in light of the fragment ion appearance

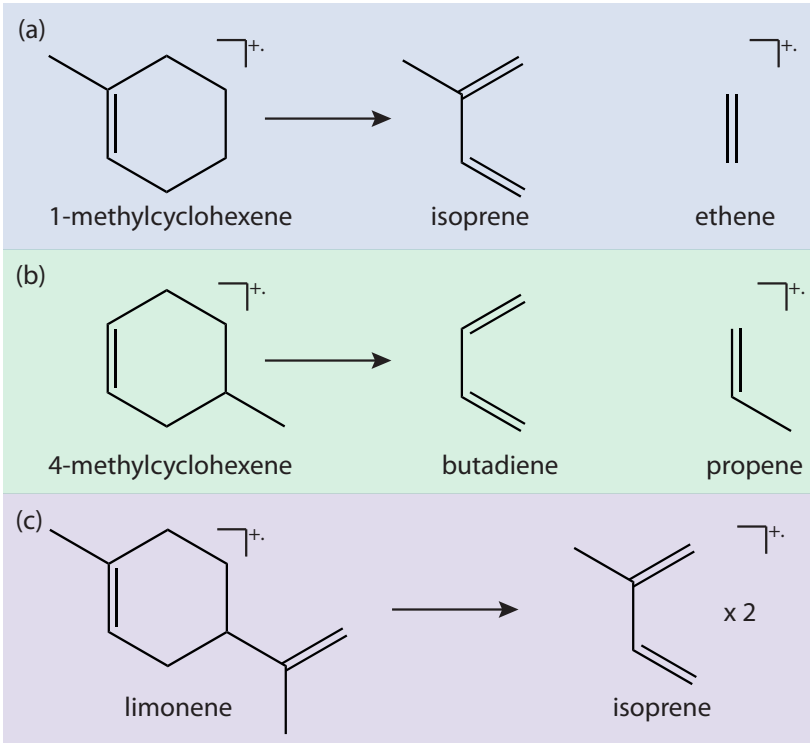

Figure 7.17: The retro-Diels-Alder reactions for the cationic forms of (a) 1-methylcyclohexene, (b) 4-methylcyclohexene and (c) limonene.

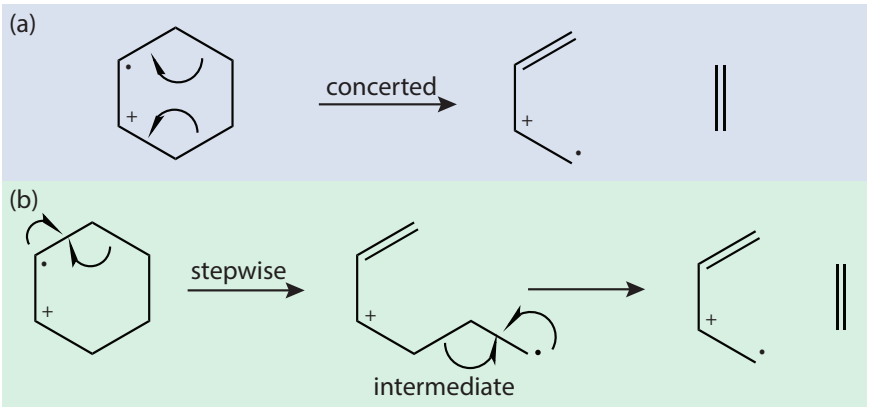

Figure 7.18: (a) concerted RDA reaction mechanism; (b) stepwise mechanism, which proceeds via two alpha bond cleavage steps. Only the RDA reactions that yield the diene cation with a neutral ene co-fragment are illustrated.

Table 7.10: Vapour pressures, sample percentages and ionization energies (IEs) of the cyclic alkenes of interest. †Under these seeding conditions no cluster formation was observed.

Name	Chemical Formula	Vapour Pressure / mbar (20 °C)	Approx. Seeding Ratio / % †	IE / eV	Refs
cyclohexene	C_6H_{10}	100	0.25	8.95	[45]
1-methyl-1-cyclohexene	C_7H_{12}	40	0.25	8.67	[30]
4-methyl-1-cyclohexene	C_7H_{12}	36	0.25	8.91	[30]
limonene	$C_{10}H_{16}$	2	0.1	8.3	[46]

energies available from the literature, and product energies obtained from ab initio calculations.

7.3.1 Methods

Experiment

The VMI spectrometer was described in Chapter 2. The compounds of interest were obtained from Sigma Aldrich, and all have purities $> 97\%$. The molecular beam was formed of a gas mixture comprising a small percentage of sample seeded in 2 bar He (BOC, $> 99.9\%$). The seeding ratios employed are shown in Table 7.10, along with the vapour pressures of the molecules of interest. Within the ion optics assembly, the molecular beam was intersected orthogonally by the co-propagating 118 nm and 355 nm laser beams. In all cases, the laser beams were linearly polarised parallel to the plane of the imaging detector. The parent ions and nascent fragment ions were velocity-mapped on to the 2D imaging detector.

Calculations

All calculations were performed using the Gaussian 09 [23] electronic structure package. The calculations which have been undertaken for this work are similar to those described in Section 7.2.1. The ground state optimised geometries of the neutral and cationic forms of cyclohexene, the cyclohexene derivatives of interest, and the relevant retro-Diels-Alder reaction products, were calculated using Møller-Plesset second order perturbation theory (MP2) in conjunction with the 6-311+G(d,p) basis set, assigned to all atoms. Energies for all species in their MP2 optimised geometry were determined using the coupled-cluster

Table 7.11: Calculated and experimental ionization energies (IEs) of cyclohexene, 1-methylcyclohexene, 4-methylcyclohexene and limonene.

Name	Chemical Formula	Adiabatic IE / eV	Vertical IE/ eV	Experimental IE / eV	Refs
cyclohexene	C_6H_{10}	8.71	8.94	8.95	[45]
1-methyl-1-cyclohexene	C_7H_{12}	8.31	8.55	8.67	[30]
4-methyl-1-cyclohexene	C_7H_{12}	8.67	8.91	8.91	[30]
limonene	$C_{10}H_{16}$	8.29	8.54	8.3	[46]

singles and doubles (CCSD) method. Zero-point vibrational energy (ZPE) corrections have been computed from the unscaled frequencies at the MP2/6-311G+(d,p) level of theory.

7.3.2 Results & Discussion

Computational Results

Table 7.11 lists the calculated adiabatic and vertical ionization energies, together with the experimentally determined values, for cyclohexene and the three derivatives of interest. The energies of the retro-Diels-Alder products relative to the ground state of the parent ion are listed in Table 7.12, and illustrated on an energy level diagram in Figure 7.19. Relevant ionization energies (IEs) [30, 45, 46] and appearance energies [46, 47] are also shown in the figure. The product energies, calculated here with ab initio methods, compare with the values of the heats of formation of the products obtained from thermochemical data, IEs and AEs [33, 34]. In the case of cyclohexene, and 1-methyl and 4-methylcyclohexene, the diene cation and neutral ene products lie lower in energy than the products from the complementary RDA reaction, i.e. the ene cation and neutral diene co-fragment. This reflects the relative ionization energies of the neutral forms of the RDA products.

Whether the RDA reaction proceeds via a concerted mechanism or a stepwise mechanism, we do not expect to observe a direct dissociation process, since in the former the system passes through a single transition state, and the latter involves more than one transition state, and one or more intermediate species. The measured AEs of the diene cations support this well established idea that the the RDA reaction pathways involve one or more barriers to dissociation.

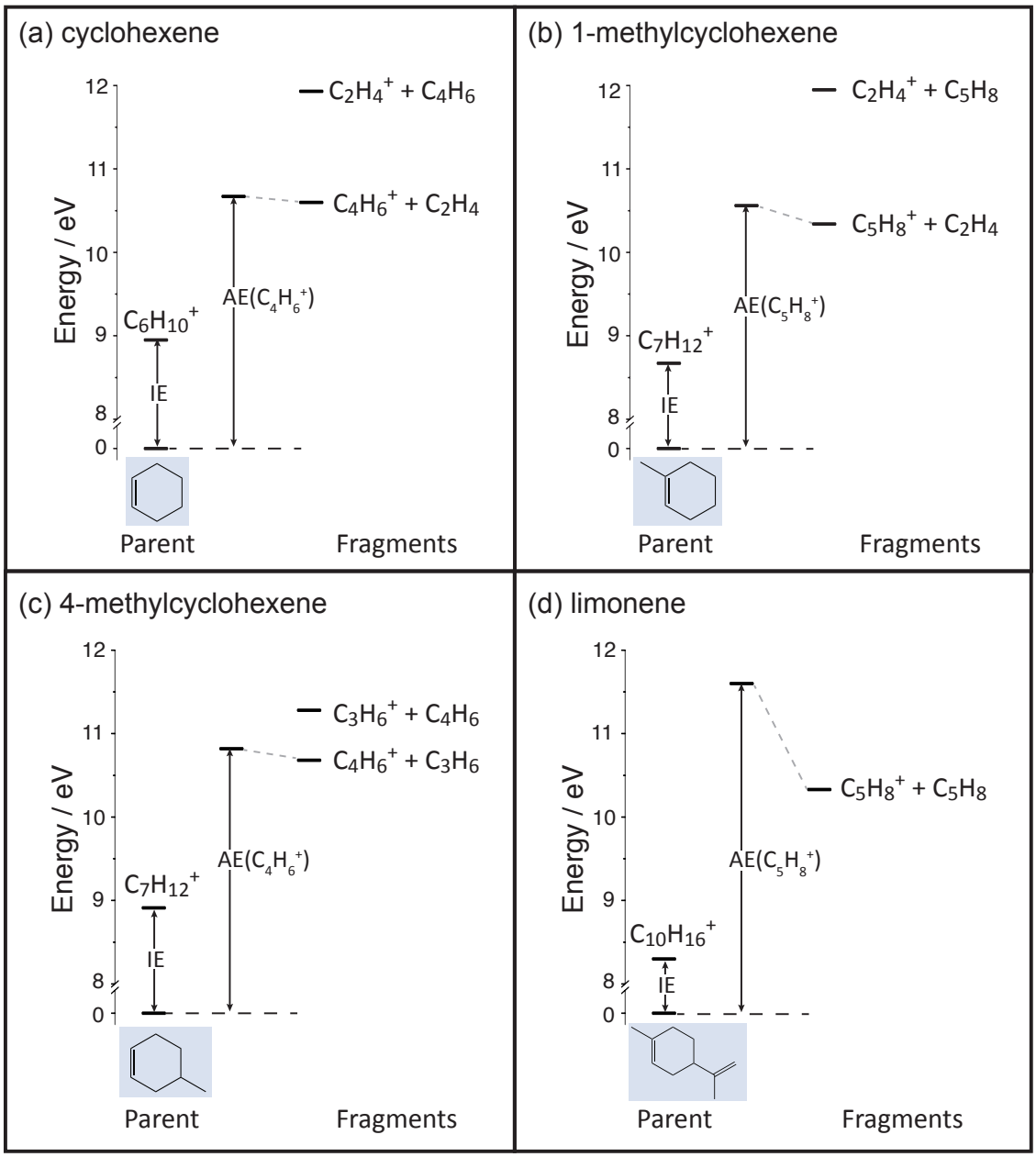

Figure 7.19: The energies of the species involved in the retro-Diels-Alder reactions of the cationic forms of (a) cyclohexene, (b) 1-methylcyclohexene, (c) 4-methylcyclohexene and (d) limonene. See text for details.

Table 7.12: Calculated product energies relative to the parent ion ground state, ΔE, for the retro-Diels-Alder reaction products of cyclohexene and cyclohexene derivative cations.

	Ion		Neutral		
Parent	Name	Formula	Name	Formula	ΔE / eV
cyclohexene	ethene	$C_2H_4^+$	butadiene	C_4H_6	3.22
	butadiene	$C_4H_6^+$	ethene	C_2H_4	1.90
1-methyl-1-cyclohexene	ethene	$C_2H_4^+$	isoprene	C_5H_8	3.65
	isoprene	$C_5H_8^+$	ethene	C_2H_4	2.06
4-methyl-1-cyclohexene	propene	$C_3H_6^+$	butadiene	C_4H_6	2.62
	butadiene	$C_4H_6^+$	propene	C_3H_6	2.01
limonene	isoprene	$C_5H_8^+$	isoprene	C_5H_8	2.04

Time-of-flight mass spectra

Time-of-flight mass-spectra (TOF-MS) resulting from 118nm and 355 nm irradiation of the four molecules of interest are shown in Figure 7.20. In each of the TOF-MS a large number of fragment ion peaks can be observed, indicating that a wide range of fragmentation processes have occurred. As in the case of the aliphatic aldehyde cation study, for the experiments described here, both 118 nm and 355 nm are present simultaneously within the interaction region. The absorption cross-sections of the molecules investigated are much greater at 118 nm than at 355 nm [48, 49]. In addition, as shown in Table 7.10, all of the parent molecules have ionization energies below the 10.49 eV available from the VUV photon. Therefore, for the fragment ions observed here, the initial step to formation involves VUV photoionization. Single-photon dissociative ionization could yield some of the fragment ions observed. However, as shown in Table 7.13, the appearance energies of the RDA products, which are of particular interest here, are above the 10.49 eV available from the VUV photon [46, 47]. Therefore, we conclude that the RDA reactions of the parent species considered here occur following absorption of an additional 355 nm photon.

The masses corresponding to both ene and diene cationic products, which result from the complementary retro-Diels-Alder reactions, have been observed in the TOF-MS of cyclohexene and each of its derivatives. The relative intensities (RIs) of the complementary RDA fragment ions, listed in Table 7.14, indicate that the RDA channel to diene cation production is dominant, and that the appearance energies of the ene cations lie higher in energy than those of the butadiene cations, given in Table 7.13.

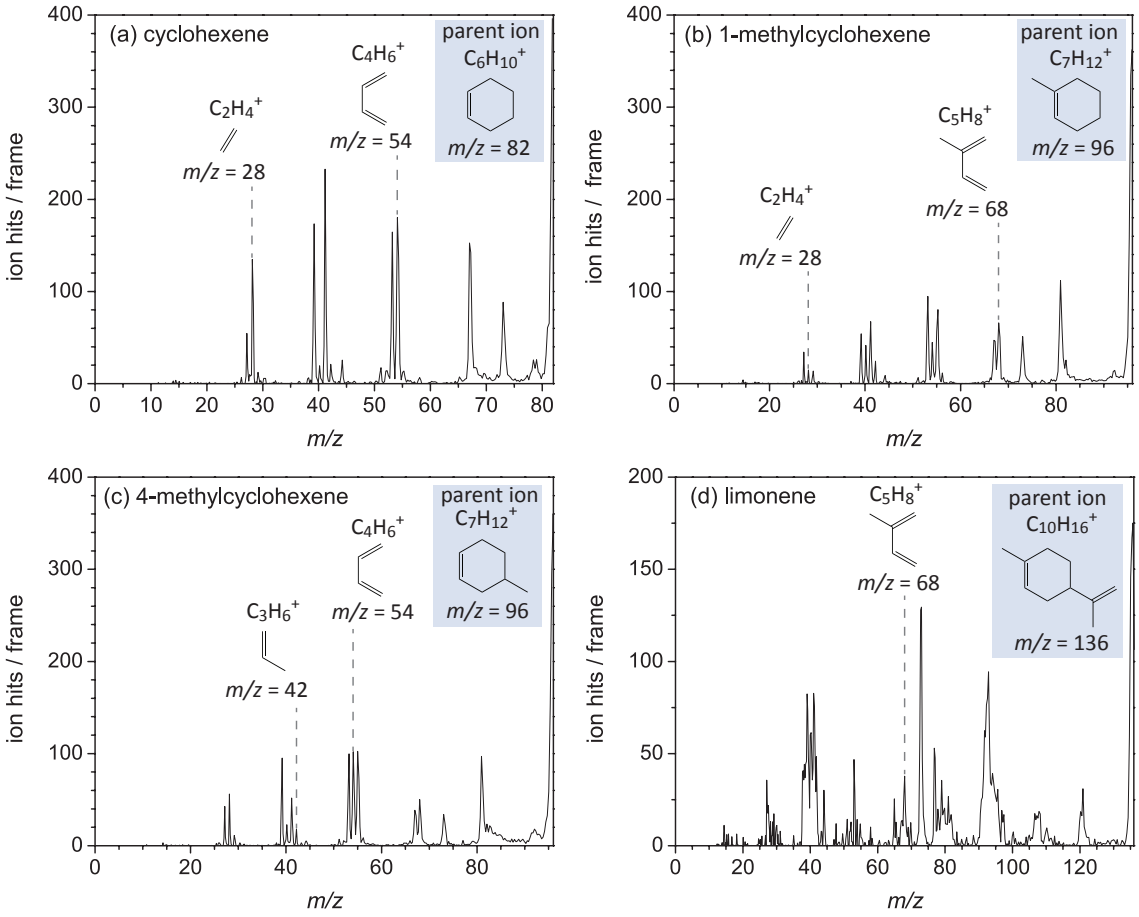

Figure 7.20: Time-of-flight mass spectra for (a) cyclohexene, (b) 1-methylcyclohexene, (c) 4-methylcyclohexene, and (d) limonene following radiation with 118 nm and 355 nm light.

Table 7.13: The appearance energies of the RDA reaction products of cyclohexene and three of its derivatives. The AEs of the ene cations, from the complementary RDA reactions, are expected to be higher than those for the butadiene cations, shown here.

Parent ion	Fragment ion	Chemical Formula	AE / eV	Refs
cyclohexene	butadiene	C_4H_6	10.67	[47]
1-methyl-1-cyclohexene	isoprene	C_5H_8	10.56	[47]
4-methyl-1-cyclohexene	butadiene	C_4H_6	10.82	[47]
limonene	isoprene	C_5H_8	11.6	[46]

Table 7.14: The relative intensities (RI) of the RDA products obtained from the TOF-MS. The limonene RDA product RI is shown relative to the parent ion. The ionization energies (IE) of the products are displayed for reference, these have been obtained from [45].

Parent ion	Fragment ion	*m/z*	Relative Intensity	IE / eV
cyclohexene	ethene	28	0.44	10.51
	butadiene	54	1	9.07
1-methyl-1-cyclohexene	ethene	28	0.07	10.51
	isoprene	68	1	8.86
4-methyl-1-cyclohexene	propene	42	0.11	9.73
	butadiene	54	1	9.07
limonene		136	1	
	isoprene	68	0.13	8.86

The observed RI data are in line with Stevenson's rule.[3] However, in this case, this is only because the relative AEs of the fragment ions from the complementary RDA reactions reflect their relative ionization energies. Stevenson's rule assumes that the processes involved do not proceed over a barrier, and, as shown in Figure 7.19, this is not the case for the reactions considered here.

In the following, the RDA reactions of the cyclic alkene cations that result in production of the diene cation with neutral ene co-fragment, will be considered. The diene ions formed from these reactions are less likely to have contributions from secondary fragmentation processes.

Velocity-map imaging

The velocity-map images acquired for the four diene product ions are shown in Figure 7.21, along with the fractional translational distributions, $P(f_T)$. The $P(f_T)$ distributions all peak close to zero, which may be an indication that parent ions formed with a high degree of internal excitation are most likely to undergo the RDA reaction, with the internal excitation being retained in the products.

All of the images in Figure 7.21 display isotropic angular distributions, indicating that the RDA reaction proceeds over a relatively long timescale. The images and $P(f_T)$ distributions

[3] Stevenson's rule states that the product pair that maintains the charge on the species with the lowest ionization energy will be more stable, and therefore the more abundant in the TOF-MS [50].

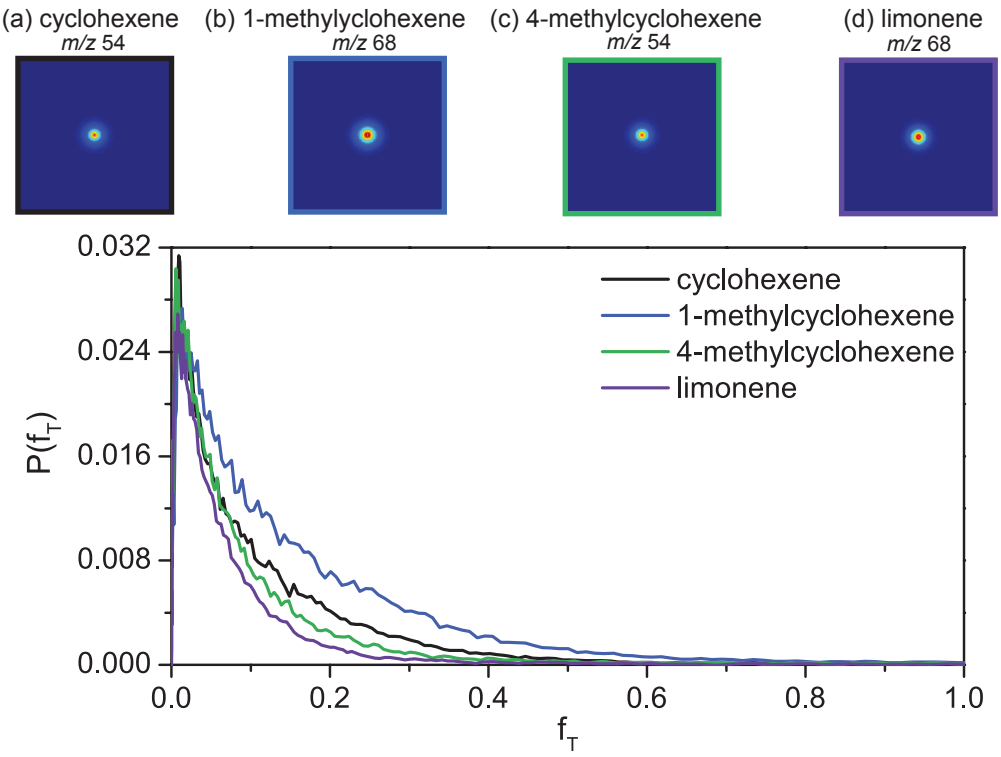

Figure 7.21: Top: images of the diene cations formed in the RDA reactions of (a) cyclohexene (butadiene cation, *m/z* 54), (b) 1-methylcyclohexene (isoprene cation, *m/z* 68), (c) 4-methylcyclohexene (butadiene cation, *m/z* 54), and (d) limonene (isoprene cation, *m/z* 68). Bottom: $P(f_T)$ distributions obtained from the images shown.

are reminiscent of those seen for the rearrangement reactions of the aliphatic aldehydes (see Section 7.2.2). Obviously the dissociation pathways of the aliphatic aldehydes and the cyclic alkenes are different; however, the observed f_T distributions indicate similarities in the dissociation dynamics. As in the case of the aliphatic aldehydes, the isotropic images most likely indicate a dissociation process occurring on a timescale that is slow compared to the rotational time period of the parent ion. This is consistent with a mechanism requiring sufficient time for substantial energy redistribution within the parent ion before the reaction proceeds. Such $P(f_T)$ distributions most probably indicate a mechanism involving internal conversion from an initially excited state of the parent ion back down to the ground state (or lower-lying state) of the ion. Dissociation proceeds on the lower-lying state if the system has sufficient energy to overcome the transition state barrier(s).

Comparing the four $P(f_T)$ distributions in Figure 7.21, we note that the distribution for the RDA reaction of 1-methylcyclohexene, which yields the isoprene ion, $C_5H_8^+$ (*m/z* 68), and a neutral ethene co-fragment, tails off at noticeably higher f_T than the other distributions, with up to 60% of the available energy being released as translation. In contrast, the

distributions for 4-methylcyclohexene and limonene tail off at around $f_T = 0.4$. From this preliminary analysis of the data it appears that cyclohexene derivatives substituted at the C_1 position perhaps result in a broader distribution of translational energies when compared with those substituted at the C_4 carbon. Further investigation of cyclohexene derivatives would reveal whether this is a general trend. In addition, a more complete understanding of this observation could be aided by modelling of the photodissociation process, with such methods as the statistical adiabatic impulsive (SAI) model put forward by Neumark and co-workers for non-statistical dissociation over a barrier [32] (Section 7.2.2). High-level ab initio calculations of these cyclic alkene systems would enable characterisation of their interaction potentials, and, therefore, allow the experimentally determined $P(f_T)$ distributions to be modelled in such a way.

7.3.3 Conclusion

In summary, VUV photoionization of the four precursor molecules yields the cyclic alkene cations. The RDA reactions of these species result from further excitation of the nascent cations with 355 nm light. The velocity-map images of the diene product ions display isotropic angular distributions. This, along with the $P(f_T)$ distributions, which reveal highly internally excited fragmentation products, likely indicate that the RDA reaction in each case involves a mechanism in which, following an initial electronic excitation, the molecule relaxes back down to a lower-lying state, and dissociates over one or more barrier(s). The work presented here only pricks the surface of the complicated dissociation dynamics of these cyclohexene derivatives. As will be discussed in Section 7.3.4, imaging studies have the potential to reveal much more about the photofragmentation of such species.

7.3.4 Futher investigations

The investigation of the rearrangement reactions, and also various other photodissociation processes, of the cyclic alkene cations would benefit from a study of the photon dependence. Any discussion based on relative intensities of TOF peaks without an understanding of the photon dependence of the processes that yield these peaks is only qualitative. For a quantitative assessment it is also necessary to fully understand the behaviour of metastable peaks, and the contribution to any of the masses of interest from secondary fragmentation processes. For example, low mass peaks, such as *m/z* 28, could be produced from secondary fragmentation of larger masses. For this, at least a qualitative understanding of the photon dependencies of the peaks, as we have for the aliphatic aldehyde cation study,

would be beneficial. From this, the identity of the fragment masses could most likely be assigned with more certainty, and the VMI study could be extended to investigate not only the RDA reaction of these species but also their other fragmentation processes.

Imaging has the potential to discern whether particular RDA reactions proceed via a stepwise or a concerted mechanism. Fragments resulting from such different mechanisms would be expected to display differing distributions of internal and translational energy. For example, the ene product resulting from a stepwise mechanism may be expected to have significantly more rotational energy than if it were produced via a concerted mechanism, due to the considerable torque likely to be imparted to the fragments on cleavage of the second bond. Therefore, in principle, VMI could distinguish between the products of these mechanisms.

Another channel of investigation lies in the fact that the 1-methyl-cyclohexene and 4-methyl-cyclohexene ions can potentially interconvert through movement of the double-bond as a result of hydrogen transfer processes, which commonly occur within organic ions. For this reason the masses corresponding to the RDA fragmentation products from both 1-methyl- and 4-methyl-cyclohexene may appear in the mass spectra of 1-methyl- or 4-methyl-cyclohexene [34, 51]. However, from this observation it is not possible to conclude that the structures do interconvert, since the 'unexpected RDA products', i.e. those masses which correspond to the RDA products following structural interconversion from 1-methyl-cyclohexene to 4-methyl-cyclohexene (or vice versa), may result from pathways other than an RDA reaction.

For practical reasons, in the current study, images have been acquired for the fragment ions resulting from the 'expected' RDA reactions of the parent ions, i.e. those reactions shown in Figures 7.16 and 7.17, which occur without any structural interconversion. An extension of this study would be to velocity-map image all of the fragment ions resulting from 1-methylcyclohexene, then to do the same for 4-methylcyclohexene. By comparing the energy distributions of fragmentation products of the same mass (from the different parent ions) it may be possible to determine whether the 'unexpected RDA products' do in fact result from an RDA reaction following structural interconversion. Attempts have been made to confirm the origins of the 'unexpected RDA products' using mass spectrometry, by comparing the relative intensities of the RDA masses for all the methyl-substituted cyclohexene parent ions [34]. However, such studies could not account for potentially metastable ions or secondary fragmentation contributions to the masses of interest. Imaging, however, has access to another dimension of information. Furthermore, such an imaging study, one

in which *all* the fragment ions are imaged, would give insight into the dynamics of the dissociation channels which compete with the RDA reactions.

High-level ab initio calculations would allow the RDA reactions and other photodissociation processes of the cyclic alkenes to be modelled, which would assist in the data interpretation of the future imaging studies described here.

7.4 Rearrangement Reactions of Organic Cations: a summary

Two preliminary gas-phase organic photochemistry studies have been presented in this chapter. The first has investigated the McLafferty-type rearrangement reactions of aliphatic aldehyde cations. The second study has focused on the retro-Diels-Alder reactions of a number of cyclic mono-alkene cations. From both of these studies it is clear that even molecules of the relatively modest size investigated (10+ atoms) can have very complex dissociation dynamics. However, imaging has the potential to unravel the photofragmentation processes.

As discussed, such studies would benefit greatly from high-level ab initio calculations and modelling of the photodissociation processes. In addition, a few experimental enhancements could considerably improve the scope of such studies. In the current work, the 355 nm and 118 nm laser beams have not been separated. The 355 nm light has often been required to dissociate the cations resulting from VUV photoionization. However, if these two laser beams were separated before entering the interaction region, the technique could become much more flexible. Separation of the 355 nm laser beam would allow for a more straightforward use of a separate tuneable UV light source to achieve dissociation following VUV photoionization. One of the strengths of the 118 nm light as the VUV photoionization source is it simplicity. However, ideally, for the study of ion dissociation, a tuneable VUV light source would be employed [52].

As mentioned in Section 1.5, the work included in this thesis is part of a much larger imaging mass spectrometry study. In the work presented here, only a select few dissociation processes of the aliphatic aldehydes, and only the retro-Diels-Alder reaction of the cyclohexene derivatives, have been considered. The photofragmentation studies of these species could well be extended, particularly with the use of a multi-mass detection technique, such as Pixel-Imaging Mass Spectrometry (PImMS), which will be discussed further in Chapter 9. Multi-mass imaging, in which multiple fragments are imaged in one time-of-flight cycle, would increase the rate of data collection, and therefore make it viable to investigate all the dissociation processes of a particular system, since the photofragment ion images could be acquired on a relatively short timescale.

References

[1] Gross, JH. *Mass Spectrometry: A Textbook*. 2nd ed. Springer, 2011 (cited p. 168).

[2] Van Bramer, SE and Johnston, MV. *10.5 eV Photoionization Mass Spectrometry of Aliphatic Compounds*. American Society for Mass Spectrometry **1**: 419–426 (1990) (cited p. 168, 171, 172, 181, 182).

[3] Nir, E, Hunziker, HE, and Vries, MS de. *Fragment-Free Mass Spectrometric Analysis with Jet Cooling/VUV Photoionization.* Analytical Chemistry **71**:9 1674–1678 (1999) (cited p. 168).

[4] McLafferty, FW. *Mass Spectrometric Analysis Broad Applicability to Chemical Research*. Analytical Chemistry **28**:3 306–316 (1956) (cited p. 169).

[5] Kingston, DGI, Bursey, JT, and Bursey, MM. *Intramolecular Hydrogen Transfer in Mass Spectra. II. McLafferty Rearrangement and Related Reactions*. Chemical Reviews **74**:2 215–242 (1974) (cited p. 169, 171).

[6] Stone, DJ, Bowie, JH, Underwood, DJ, Donchi, KF, Allison, CE, and Derrick, PJ. *Mechanistic Studies of Unimolecular Ionic Decompositions by Deuterium and Heavy-Atom Isotope Effects. Concerted Elimination of Acetaldehyde from the Benzyl Ethyl Ether Radical Ration*. Journal of the American Chemical Society **105**: 1688–1689 (1983) (cited p. 169).

[7] Allison, CE, Stringer, MB, Bowie, JH, and Derrick, PJ. *Combined Deuterium and Oxygen-18 Isotope Effects in Support of a Concerted, Synchronous Elimination of Acetaldehyde from a Bis(benzyl ethyl ether) Radical Cation*. Journal of the American Chemical Society **110**:19 6291–6297 (1988) (cited p. 169).

[8] Boer, FP, Shannon, TW, and McLafferty, FW. *Electronic Structure of the Six-Membered Cyclic Transition State in Some γ-Hydrogen Rearrangements*. Journal of the American Chemical Society **90**:26 7239–7248 (1968) (cited p. 169).

[9] Ha, TK, Radloff, C, and Nguyen, MT. *An ab initio Study on the McLafferty-Type Rearrangement in the Butanal Radical Cation ($CHOCH_2CH_2CH_3^+$)*. The Journal of Physical Chemistry **90**:13 2991–2994 (1986) (cited p. 169, 172).

[10] Liu, R and Pulay, P. *Ab Initio Evidence for the Stepwise Mechanism of the Mclafferty Rearrangement of the Butanal Radical Cation*. Journal of Computational Chemistry **13**:2 183–186 (1992) (cited p. 169, 172).

[11] Stringer, MB, Underwood, DJ, Bowie, JH, Allison, CE, Donchi, KF, and Derrick, PJ. *Is the McLafferty Rearrangement of Ketones Concerted or Stepwise? The Application of Kinetic Isotope Effects*. Organic Mass Spectrometry **27**: 270–276 (1992) (cited p. 169).

[12] Tureček, F, Drinkwater, DE, and McLafferty, FW. *The Stepwise Nature of the γ-Hydrogen Rearrangement in Unsaturated Ions*. Journal of the American Chemical Society **112**: 993–997 (1990) (cited p. 169).

[13] Norberg, D and Salhi-Benachenhou, N. *McLafferty Rearrangement of the Radical Cations of Butanal and 3-Fluorobutanal: A Theoretical Investigation of the Concerted and Stepwise Mechanisms*. Journal of Computational Chemistry **29**:3 392–406 (2007) (cited p. 170, 172, 186, 192).

[14] Laulhé, S, Bogdanov, B, Johannes, LM, Gutierrez, O, Harrison, JG, Tantillo, DJ, Zhang, X, and Nantz, MH. *Fragmentation of oxime and silyl oxime ether odd-electron positive ions by the McLafferty rearrangement: new insights on structural factors that promote α,β fragmentation*. Journal of Mass Spectrometry **47**: 676–686 (2012) (cited p. 170).

[15] Carpenter, WR, Duffield, AM, and Djerassi, C. *Mass spectrometry in Structural and Stereochemical Problems. CXLIV. Unusual Fragmentations in the Low-Voltage Spectra of Aliphatic Ketones*. Journal of the American Chemical Society **90**:1 160–164 (1968) (cited p. 171).

[16] Lightner, DA, Steinberg, FS, and Huestis, LD. *On the McLafferty and Double Hydrogen Rearrangements in Cycloalkylacetones*. Journal of the Mass Spectrometry Society of Japan **46**:1 11–16 (1998) (cited p. 171).

[17] Maccoll, A and Mruzek, MN. *Low-energy, Low-temperature Mass Spectra. 5 - Alkanals*. Organic Mass Spectrometry **21**: 251–258 (1986) (cited p. 171, 172).

[18] Harrison, AG, Finney, CD, and Sherk, JA. *Factors Determining Relative Ionic Abundances in Competing Fragmentation Reactions*. Organic Mass Spectrometry **5**: 1313–1320 (1971) (cited p. 172).

[19] Gilpin, JA and McLafferty, FW. *Mass Spectrometric Analysis Aliphatic Aldehydes*. Analytical Chemistry **29**:7 990–994 (1957) (cited p. 172).

[20] Maccoll, A. *Low-energy, Low-temperature Mass Spectra. 8 - The McLafferty Rearrangement*. Organic Mass Spectrometry **23**: 381–387 (1988) (cited p. 172).

[21] Traeger, JC and McAdoo, DJ. *Decomposition Thresholds and Associated Translational Energy Releases for eight $C_4H_8O^{+\cdot}$ Isomers*. International Journal of Mass Spectrometry and Ion Processes **68**: 35–48 (1986) (cited p. 173, 176, 181).

[22] Ashmore, FS and Burgess, AR. *Photoelectron Spectra of the Unbranched C_5–C_7 Alkenes, Aldehydes, and Ketones*. Journal of the Chemical Society, Faraday Transactions 2 **74**: 734–742 (1978) (cited p. 173, 176, 181).

[23] Frisch, MJ, Trucks, GW, Schlegel, HB, Scuseria, GE, Robb, MA, Cheeseman, JR, Scalmani, G, Barone, V, Mennucci, B, Petersson, GA, Nakatsuji, H, Caricato, M, Li, X, Hratchian, HP, Izmaylov, AF, Bloino, J, Zheng, G, Sonnenberg, JL, Hada, M, Ehara, M, Toyota, K, Fukuda, R, Hasegawa, J, Ishida, M, Nakajima, T, Honda, Y,

Kitao, O, Nakai, H, Vreven, T, Montgomery, JA, Peralta, JE, Ogliaro, F, Bearpark, M, Heyd, JJ, Brothers, E, Kudin, KN, Staroverov, VN, Kobayashi, R, Normand, J, Raghavachari, K, Rendell, A, Burant, JC, Iyengar, SS, Tomasi, J, Cossi, M, Rega, N, Millam, JM, Klene, M, Knox, JE, Cross, JB, Bakken, V, Adamo, C, Jaramillo, J, Gomperts, R, Stratmann, RE, Yazyev, O, Austin, AJ, Cammi, R, Pomelli, C, Ochterski, JW, Martin, RL, Morokuma, K, Zakrzewski, VG, Voth, GA, Salvador, P, Dannenberg, JJ, Dapprich, S, Daniels, AD, Farkas, Foresman, JB, Ortiz, JV, Cioslowski, J, and Fox, DJ. *Gaussian 09, Revision B.01*. Tech. rep. 2009 (cited p. 174, 196).

[24] Matti, GY, Osman, OI, Upham, JE, Suffolk, RJ, and Kroto, HW. *Photoelectron Spectroscopic Detection of Vinyl Alcohol, CH_2 =CHOH: Evidence for the syn and anti rotamers*. Journal of Electron Spectroscopy and Related Phenomena **49**: 195–201 (1989) (cited p. 176, 180).

[25] Williams, BA and Cool, TA. *Two-photon spectroscopy of Rydberg states of jet-cooled C_2H_4 and C_2D_4*. The Journal of Chemical Physics **94**:10 6358–6366 (1991) (cited p. 176, 180).

[26] Van der Meij, CE, Van Eck, J, and Niehaus, A. *The Decomposition of $C_4H_8^+$ Complexes at Controlled Internal Energies*. Chemical Physics **130**: 325–334 (1989) (cited p. 176).

[27] Traeger, JC. *Heat of Formation for the 1-Methylallyl Cation by Photoionization Mass Spectrometry*. The Journal of Physical Chemistry **90**: 4114–4118 (1986) (cited p. 176).

[28] Martinez, RD, Buitrago, AA, Howell, NW, Hearn, CH, and Joens, JA. *The Near U.V. Absorption Spectra of Several Aliphatic Aldehydes and Ketones at 300 K*. Atmospheric Environment. Part A. General Topics **26**:5 785–792 (1992) (cited p. 179).

[29] Lucazeau, G and Sandorfy, C. *On the Far-Ultraviolet Spectra of Some Simple Aldehydes*. Journal of Molecular Spectroscopy **35**: 214–231 (1970) (cited p. 179).

[30] Lias, SG, Levin, RD, and Kafafi, SA. *NIST Standard Reference Database Number 69 (retrieved June 19, 2013)*. Ed. by Linstrom, PJ and Mallard, WG. NIST Chemistry WebBook. National Institute of Standards and Technology, Gaithersburg MD, 20899 (cited p. 181, 196, 197).

[31] Laskin, J and Lifshitz, C. *Kinetic energy release distributions in Mass Spectrometry*. Journal of Mass Spectrometry **36**: 459–478 (2001) (cited p. 190).

[32] Mordaunt, DH, Osborn, DL, and Neumark, DM. *Nonstatistical unimolecular dissociation over a barrier*. The Journal of Chemical Physics **108**:6 2448–2457 (1998) (cited p. 191, 203).

[33] Tureček, F and Hanuš, V. *Retro-Diels-Alder reaction in mass spectrometry*. Mass Spectrometry Reviews **3**: 85–152 (1984) (cited p. 193, 194, 197).

[34] Budzikiewicz, H, Brauman, JI, and Djerassi, C. *Massenspektrometrie und IHRE anwendung auf strukturelle und stereochemische probleme—LXVII*. Tetrahedron **21**: 1855–1879 (1965) (cited p. 193, 197, 204).

[35] Himottu, M, Pihlaja, K, Stájer, G, Bernáth, G, and Vainiotalo, P. *Mass Spectrometric Study of Some Cycloalkane/ene-condensed 2-thioxo-2,3,5,6-pyrimidin-4(1H)-ones and Cycloalkane/ene-condensed [l,3] thiazino [3,2-a]-pyrimidinones under electron impact*. Organic Mass Spectrometry **26**:5 493–497 (1991) (cited p. 193).

[36] Pihlaja, K, Himottu, M, Fülöp, F, Huber, I, Bernáth, G, and Ovcharenko, V. *Stereochemical Effects in the Electron Ionization Mass Spectra of Cycloalkane-(alkene)-fused 2,3-Dihydro-5H-thiazolo[3,2-a]pyrimidine-5-ones and 3,4-Dihydro-2H,6H- pyrimido[2,1-b]thiazin-6-ones*. Rapid Communications in Mass Spectrometry **10**:6 721–726 (1996) (cited p. 193).

[37] Pihlaja, K, Himottu, M, Ovcharenko, V, Frimpong-Manso, S, and Stájer, G. *Electron Ionization Mass Spectra of Some Diexo Norbornane- and Norbornene-fused Phenyl-substituted 1,3-Oxazines and Related Systems. Competitive retro-Diels-Alder Fragmentations in 4-Phenyl-4a,5,8,8a-tetrahydro-5,8-methano-4H-benzo[e]1,3-oxazines*. Rapid Communications in Mass Spectrometry **11**:3 249–252 (1997) (cited p. 193).

[38] Lucas, A de, Fernández-Gadea, J, Martin, N, Martinez, R, and Seoane, C. *Mass spectra of new substituted 2-amino-4H-pyrans: a retro-Diels-Alder reaction pattern.* Rapid Communications in Mass Spectrometry **14**:19 1783–1786 (2000) (cited p. 193).

[39] Bouchoux, G, Salpin, JY, and Tureček, F. *Cycloaddition Reactions between 1,3-Butadiene Radical Cations and Ethene in the Gas Phase*. Rapid Communications in Mass Spectrometry **8**:4 325–328 (1994) (cited p. 193).

[40] Haberl, U, Wiest, O, and Steckhan, E. *Ab Initio Studies of the Radical Cation Diels-Alder Reaction*. Journal of the American Chemical Society **121**:28 6730–6736 (1999) (cited p. 193).

[41] Hu, H and Wenthold, PG. *Reaction of the Butadiene Cation with Ethylene in the Gas Phase*. The Journal of Physical Chemistry A **106**:44 10550–10553 (2002) (cited p. 193).

[42] Valley, NA and Wiest, O. *Methyl Substitutent Effects in Radical Cation Diels-Alder Reactions*. The Journal of Organic Chemistry **72**:2 559–566 (2007) (cited p. 193).

[43] Bouchoux, G, Salpin, JY, and Yanez, M. *Low Energy Dissociation Processes of Ionized Cyclohexene: A Theoretical Insight*. The Journal of Physical Chemistry A **108**:45 9853–9862 (2004) (cited p. 193).

[44] Vincenti, M, Horning, SR, and Cooks, RG. *Energetics of Retro-Diels-Alder Fragmentation in Limonene as Characterized by Curface-induced Dissociation, and Energy- and Angle-resolved Mass Spectrometry*. Organic Mass Spectrometry **23**: 585–593 (1988) (cited p. 193).

[45] Lias, SG. *"Ionization Energy Evaluation" in NIST Chemistry WebBook, NIST Standard Reference Database Number 69, (retrieved June 19, 2013)*. Ed. by Linstrom, PJ and Mallard, WG. National Institute of Standards and Technology, Gaithersburg MD, 20899 (cited p. 196, 197, 201).

[46] Harris, D, McKinnon, S, and Boyd, RK. *The Origins of the Base Peak in the Electron Impact Spectrum of Limonene*. Organic Mass Spectrometry **14**:5 265–272 (1979) (cited p. 196, 197, 199, 200).

[47] Rosenstock, HM, Draxl, K, Steiner, BW, and Herron, JT. *"Ion Energetics Data" in NIST Chemistry WebBook, NIST Standard Reference Database Number 69, http://webbook.nist.gov, (retrieved July 4, 2013).* Ed. by Linstrom, PJ and mallard, WG. National Institute of Standards and Technology, Gaithersburg MD, 20899 (cited p. 197, 199, 200).

[48] Pickett, LW, Muntz, M, and McPherson, EM. *Vacuum Ultraviolt Absorption Spectra of Cyclic Compounds. I. Cyclohexane, Cyclohexene, Cycolpentane, Cyclopentene and Benzene*. Journal of the American Chemical Society **73**: 4862–4865 (1951) (cited p. 199).

[49] Smialek, MA, Hubin-Franskin, MJ, Delwiche, J, Duflot, D, Mason, NJ, Vronning-Hoffmann, S, Souza, GGB de, Ferreira-Rodrigues, AM, Rodrigues, FN, and Limao-Vieira, P. *Limonene: electronic state spectroscopy by high-resolution vacuum ultraviolet photoabsorption, electron scattering, He(I) photoelectron spectroscopy and ab initio calculations*. Physical Chemistry Chemical Physics **14**: 2056–2064 (2012) (cited p. 199).

[50] Stevenson, DP. *Ionization and dissociation by electronic impact. The ionization potentials and energies of formation of sec.-propyl and tert.-butyl radicals. Some limitations on the method.* Discussions of the Faraday Society **10**: 35–45 (1951) (cited p. 201).

[51] Kinstle, TH and Stark, RE. *Mass spectra of simple exocyclic and endocyclic olefins*. The Journal of Organic Chemistry **32**:5 1318–1322 (1967) (cited p. 204).

[52] Lipson, R, Dimov, S, Wang, P, Shi, Y, Mao, D, Hu, X, and Vanstone, J. *Vacuum Ultraviolet and Extreme Ultraviolet Lasers: Principles, Instrumentation, and Applications*. Instrumentation Science and Technology **28**:2 85–118 (2000) (cited p. 206).

8

Retro-Diels-Alder Reactions of Neutral Organic Species

Contents

8.1 Introduction

This final gas-phase organic photochemistry study, which may be of greater interest to the wider chemistry community than the cation studies that were presented in the previous chapter, explores the retro-Diels-Alder (RDA) reactions of *neutral* organic compounds. The neutral RDA reaction is formally the reverse of the Diels-Alder (DA) reaction, which is commonly employed in solution-phase synthetic organic chemistry to form C−C bonds and to generate six-membered ring structures [1]. The neutral DA and RDA reactions are often presented as prototypical examples of pericyclic reactions, governed by frontier molecular orbital theory, set out by the Woodward-Hoffmann (WH) rules [1]. The WH rules are orbital symmetry selection rules, which summarise whether pericyclic reactions are thermally or photochemically 'allowed' or 'forbidden'. The WH rules predict different outcomes for thermal and photochemical reactions since the former occur on the ground electronic state, whereas latter occur on an electronically excited PES, with a different

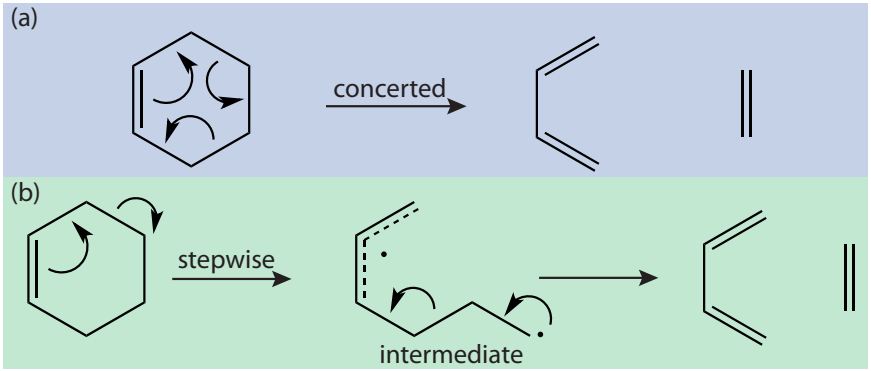

Figure 8.1: (a) concerted RDA reactions vs (b) stepwise RDA reaction, which goes via a diradical intermediate.

symmetry. In reality, the WH rules predict the barrier heights of these reactions, those reactions with low barriers are termed 'allowed', and those with high barrier heights, 'forbidden'. However, even 'forbidden' processes may proceed given enough energy in the system [2]. Furthermore, the WH rules only apply in the case of concerted reaction mechanisms. However, the RDA reactions can also proceed in a stepwise fashion. In the case of the RDA reaction of a cyclic mono-alkene, the concerted mechanism, shown in Figure 8.1 (a), proceeds via a six membered transition state, whereas the stepwise process, as shown in Figure 8.1 (b), involves a diradical intermediate. Both mechanisms yield diene and ene products.

In 1987, Collins and Maré compiled a review of experimental investigations into fragmentation and ring contraction of cyclic mono-alkenes, with the aim of identifying the particular electronic states involved in such processes [3]. Direct photolysis studies of cyclohexene and cyclohexene derivatives were observed to result in a concerted RDA mechanism proceeding on the electronic ground state, populated following internal conversion from the initially generated excited state (see [3, 4] and references therein). In contrast, stepwise mechanisms were observed to proceed via triplet excited states, formed by $Hg(^3P_1)$ photosensitization. In quick succession of this review, Zhao *et al.* published a study on the 193 nm photolysis and infrared multiphoton dissociation (IRMPD) of cyclohexene, which employed the photofragment translation spectroscopy (PTS) technique [5]. The measured translational energy releases of the RDA products formed following 193 nm photolysis and IRMPD were extremely similar. This indicated that following absorption of a 193 nm photon the excited cyclohexene relaxes back down to the ground state through internal conversion and undergoes dissociation along the ground electronic state, as is known to be the case for IRMPD. This study favoured a concerted mechanism, as had been observed for previous direct photolysis experiments [4, 6].

Following this work, a number of femtosecond time-resolved (FTR) mass spectrometry studies of the RDA reaction were undertaken by Zewail and co-workers [2, 7, 8]. These studies suggested that both a concerted and a stepwise mechanism, which take place on a sub-picosecond timescale, were involved in the production of the RDA fragments from mono-alkenes. However, later work by Fuss *et al.* concluded that the products detected in the previous FTR-MS studies were not in fact the final RDA fragmentation products [9]. In this later work, the fragments that were formed on the sub-picosecond timescale were observed to have short lifetimes, indicating that they underwent additional fragmentation processes. The RDA products themselves were only observed on a nanosecond timescale, indicating that these fragments take significantly longer to form than previously suggested.

A number of theoretical studies have examined the Diels-Alder reaction of ethene and butadiene to form cyclohexene, and have also considered the reverse process (RDA), which is of key interest here (see for example [10–13] and [14] for a review of earlier work). These studies have aided in developing our understanding of the dynamics of the (retro-) Diels-Alder reaction. The energetics of the reaction are summarised in Figure 8.2. Two different reaction paths can be observed; the concerted pathway is shown in blue, and the stepwise one in green. In the case of the concerted mechanism, cyclohexene must traverse a single transition state (TS-1) with aromatic character [11], which lies 2.73 eV above the ground state of the cyclohexene parent molecule [10]. In contrast, the stepwise mechanism involves two barriers. The first transition state, TS-3, which lies 3.37 eV above the cyclohexene ground state, corresponds to fragmentation of the C_2-C_3 bond. Unfavourable steric effects then arise between C_3-C_4 and C_5-C_6-C_1-C_2 (the two sections of the molecule which will form the 'ene' and 'diene' fragments). The energy of the system is lowered as the C_3-C_4 section rotates around the C_4-C_5 bond, and out of the plane of the 'diene' section, forming the diradical intermediate [11].[1] The next transition state, TS-2, lies 0.16 eV above TS-3 and corresponds to lengthening of the C_4-C_5 bond [11]. Fragmentation results in the production of the butadiene and ethene fragments, which lie 1.72 eV above the parent cyclohexene [10].[2]

[1] Here we have considered a relatively simple picture for the stepwise mechanism. However, there are a number of additional transition states and intermediates related to rotation around the C_4-C_5 bond. These have been located in the ab initio investigation undertaken by Lischka *et al.* [13].

[2] The enthalpy of reaction, ΔH_{rxn}, illustrated in Figure 8.2, is that recommended by Houk and co-workers, who have established a standard set of reference data for a number of pericyclic reactions, including the Diels-Alder reaction [10]. The barrier height of TS-1 has also been calculated from their recommended values (it is the sum of ΔH_{rxn} and $\Delta H^{\ddagger}_{0K}$, since they have considered the concerted reaction from diene and ene to form cyclohexene). The energies of TS-3 and TS-2 (notation consistent with [11]) are the sum of ΔH_{rxn} and the transition state energies obtained by Sakai, which were given relative to the RDA products in reference [11].

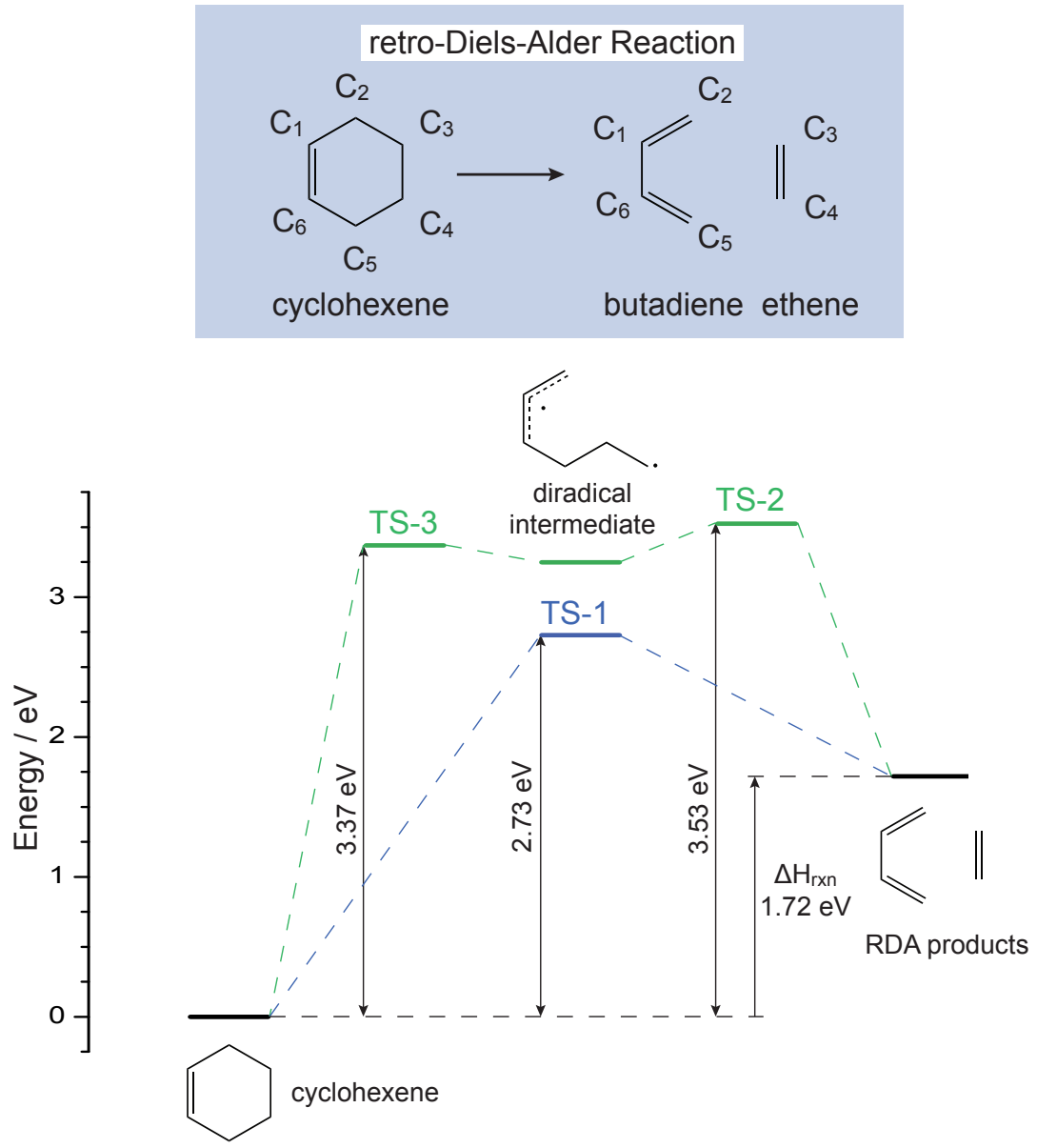

Figure 8.2: Schematic potential energy profiles for the concerted (blue) and stepwise (green) reaction pathways of the retro-Diels-Alder reaction of cyclohexene to form butadiene and ethene. See text for details of transitions states (TS). TS-1 energy has been taken from [10]. TS-2 and TS-3 energies are the sum of ΔH_{rxn} (taken from [10]) and the energies obtain by Sakai [11].

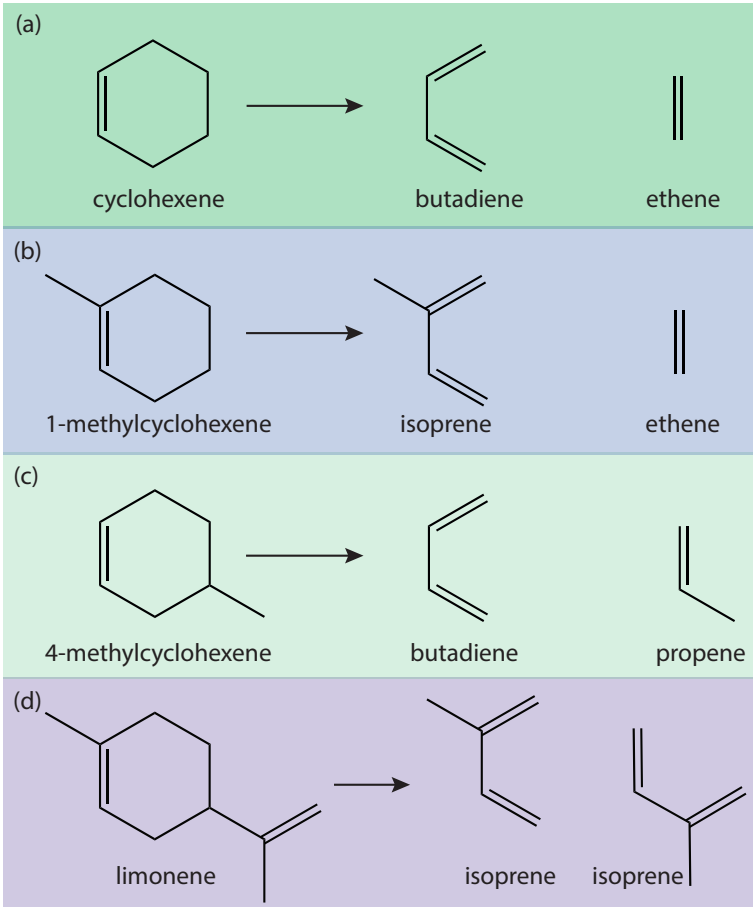

Figure 8.3: The retro-Diels-Alder reactions for (a) cyclohexene, (b) 1-methylcyclohexene, (c) 4-methylcyclohexene, and (d) limonene.

From the discussion above it is clear that cyclohexene has often been employed as the model system for experimental and theoretical studies of RDA reactions, with larger systems being investigated in order to complement the cyclohexene results and to extend the study. In the current work we have followed the same approach, with investigations into the RDA reactions of cyclohexene and three derivatives, namely, 1-methylcyclohexene, 4-methylcyclohexene and limonene. The products of the neutral RDA reactions of these molecules are similar to those resulting from the RDA reactions of the cationic species, discussed in Section 7.3. The RDA reaction of neutral cyclohexene, which forms neutral butadiene and ethene fragments, is shown in Figure 8.3 (a). The RDA reaction of 1-methylcyclohexene, shown in Figure 8.3 (b), generates isoprene with an ethene co-fragment. 4-methylcyclohexene produces butadiene and propene, as shown in Figure 8.3 (c). Limonene, as in the cationic case, undergoes the RDA reaction, Figure 8.3 (d), to yield two isoprene fragments.

This work aims to demonstrate further the use of the VMI apparatus for the study of photofragmentation of larger molecules, this time with a particular focus on the RDA reaction as we attempt to address the question of the concerted vs stepwise mechanism for this process. Since, as discussed, the RDA reaction occurs on a nanosecond timescale our pump-probe experiment is ideal for investigating such a process. In the pump-probe VMI study presented here, a pump pulse of wavelength 193 nm is employed to initiate the rearrangement, then after a period of a few tens of nanoseconds the VUV pump pulse passes through the interaction region, with the aim of universal detection of the parent and all nascent molecules, including the RDA products. Velocity-map images of the RDA products should exhibit distinct differences depending on whether they are produced through a concerted or stepwise process, since the two mechanisms are expected to result in markedly different energy distributions within the fragmentation products.

8.2 Experiment

The sample preparation and experimental details follow those described in Section 7.3.1. The study was carried out on the VMI apparatus described in Chapter 2. For this pump-probe study, the molecular beam was intersected orthogonally by the counter-propagating UV pump and VUV probe laser beams within the ion optics assembly. UV light of wavelength 193 nm photolysed the neutral molecule. Following a delay of 20 ns, VUV light ionized the parent molecule and nascent fragments. For each parent molecule, time-of-flight mass spectra (TOF-MS) were acquired in order to identify the fragmentation products, and velocity-map images were acquired for the fragment ions of interest.

8.3 Results & Discussion

8.3.1 Fragmentation product identification

TOF spectra were recorded following illumination of the sample with the pump laser only, the probe laser only and with both pump and probe lasers. Figure 8.4 (a) shows the TOF spectra recorded for cyclohexene when both the pump and probe lasers passed through the interaction region. From Figure 8.4 (b), which shows the signal from the VUV photoionization (probe) laser only, it is clear that there is significant one-laser dissociative ionization of cyclohexene, leading to the production of fragment ions, which also contributes to the two-laser signal observed in Figure 8.4 (a). The pump-only signal, which has not been

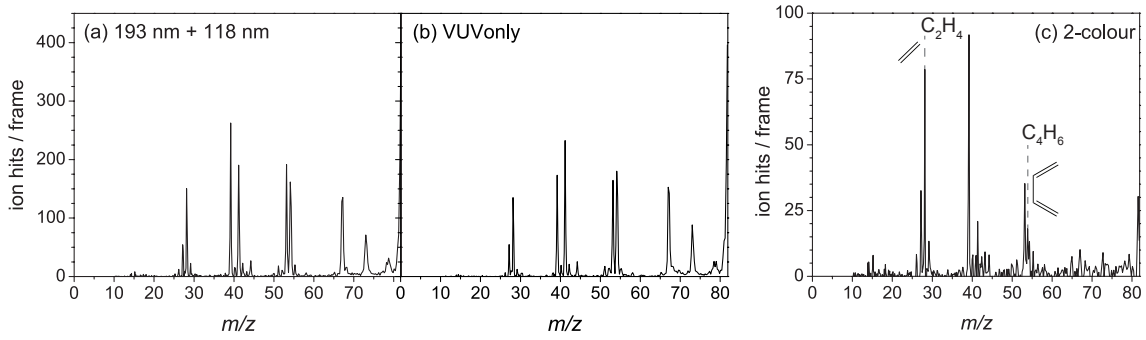

Figure 8.4: Time-of-flight mass spectrum produced following radiation of cyclohexene with (a) 193 nm and 118 nm light (both lasers) and (b) 118 nm light only (single laser contribution). The single laser contribution from 193 nm displays insignificant signal and has not bee display here. (c) is the two-colour TOF-MS which is obtained from subtracting the individual laser contributions from (a).

displayed here, exhibits little to no fragment ion signal. The single-laser signals have been subtracted from the overall signal in order to reveal the two-colour pump-probe signal, which is displayed in Figure 8.4 (c). As discussed in Chapter 2, the TOF spectra are obtained by summing the total number of ion hits as a function of the time-of-flight. Since there may be some fluctuation in the signal intensity over the course of the experimental period, the two-colour TOF-MS, which results from subtracting the individual contributions, may have a significant amount of baseline noise. In these cases, by gating the detector for a certain fragment mass and using the camera in combination with the oscilloscope, it is generally possible to confirm (by eye) whether there is a two-colour contribution to the mass peak of interest. Since the products of the RDA reactions, which result from UV photolysis of cyclohexene and its derivatives, are central to the current study, it was necessary to confirm a two-colour signal for these fragment ions.

Butadiene and ethene result from the RDA reaction of cyclohexene. Signal intensity has been observed at *m/z* 54 and *m/z* 28 in Figure 8.4 (c), which correspond to the molecular masses for butadiene and ethene, respectively. The TOF-MS of the cyclohexene derivatives are displayed in Figure 8.5. As illustrated in Figure 8.5 (a), 1-methylcyclohexene undergoes the RDA reaction to form isoprene (*m/z* 68) and ethene (*m/z* 28). The signal intensities for the *m/z* of the products of the RDA reaction of 4-methylcyclohexene, butadiene (*m/z* 54) and propene (*m/z* 42), both appear to be relatively low in the TOF-MS in Figure 8.5 (b). The products of the RDA reaction of limonene are identical and can be identified as isoprene (*m/z* 68). The signal at *m/z* 68 lies within the baseline noise of the TOF-MS displayed in Figure 8.5 (c), but two-colour signal has been confirmed for this mass. In the case of cyclohexene, and also 1-methylcyclohexene, the *m/z* peak intensities of the RDA products

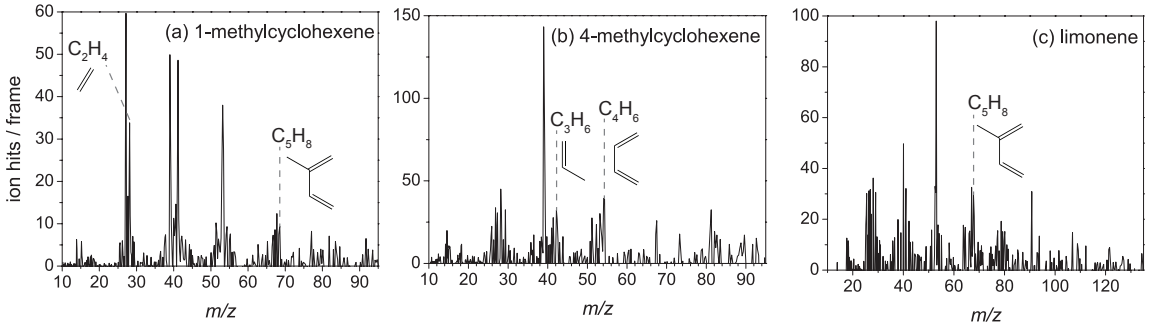

Figure 8.5: Two-colour time-of-flight mass spectra for (a) 1-methyl cyclohexene, (b) 4-methylcyclohexene and (c) limonene following UV photolysis at 193 nm with VUV photoionization of the nascent fragments.

are different. The peak which corresponds to the ene fragment (*m/z* 28) is more intense. This is perhaps surprising, since if the *m/z* peaks, which have been identified as the RDA products, do result from the RDA reaction, it would be expected that they would have equal intensities, as the RDA products should be detected in equal amounts. Such variation could come about to due to fluctuations in signal intensity, or, more likely, as will now be discussed, secondary fragmentation processes could have an effect on the observed signal intensities.

For reference, Table 8.1 lists the four parent molecules of interest and their RDA fragmentation products, along with their chemical formulae, molecular masses and ionization energies (IEs). The ionization energies of the nascent fragments are a key consideration, since these often determine whether a fragment is observed in the TOF spectrum at the corresponding *m/z*. If the IE of a fragment lies higher in energy than the VUV photon energy, then it will not be possible to achieve single-photon ionization and, therefore, the fragment may not be detected at all. Conversely, if the IE of a fragment lies significantly lower in energy than that available from the VUV photon, then it is possible that absorption of such a photon could result in dissociative ionization. This secondary fragmentation process would reduce the signal at the *m/z* corresponding to the primary fragmentation product.

The published value for the IE of ethene is 10.51 eV. This is slightly higher than the 10.49 eV available from the VUV photon. Despite this, for each of the cases where ethene is produced as an RDA product, i.e. for cyclohexene and 1-methylcyclohexene, it has been observed in the TOF-MS. Assuming that the published IE is correct, this may indicate that the ethene fragment is born with some internal energy. However, we should also consider a possible alternative origin for this signal intensity at *m/z* 28. This is a low mass, and the signal may have contributions from secondary fragmentation products of dissociative

Table 8.1: Chemical formulae, molecular masses and ionization energies (IEs) of cyclohexene, and the cyclohexene derivatives, along with their RDA fragmentation products. $^{(a),(b),(c),(d)}$ implies RDA product of (a) cyclohexene, (b) 1-methylcyclohexene, (c) 4-methylcyclohexene or (d) limonene.

			Chemical Formula	Molecular Mass / u	IE / eV	Refs
Parents	(a)	cyclohexene	C_6H_{10}	82	8.95	[15]
	(b)	1-methyl-1-cyclohexene	C_7H_{12}	96	8.67	[16]
	(c)	4-methyl-1-cyclohexene	C_7H_{12}	96	8.91	[16]
	(d)	limonene	$C_{10}H_{16}$	136	8.3	[17]
Fragments		butadiene $^{(a),(c)}$	C_4H_6	54	9.07	[15]
		ethene $^{(a),(b)}$	C_2H_4	28	10.51	[15]
		propene $^{(c)}$	C_3H_6	42	9.73	[15]
		isoprene $^{(b),(d)}$	C_5H_8	68	8.86	[15]

ionization of larger species. If this is the case, then it would complicate the analysis of the TOF spectra considerably. However, as discussed in Chapter 1, when a dissociation event occurs, momentum is conserved. If the co-fragment is known (or assumed) then the measured translational energy of a fragment can be related directly to the total energy released into translation. For two fragments generated in the same dissociation event, e.g. the RDA reaction, the distributions of total translation energy obtained from the individual fragment translational energies should match. In these instances, VMI can play a key role, as 'momentum matching' of fragment ions aids in confirming the origins of the fragment ions observed.

The IEs of the other RDA products, shown in Table 8.1, are all lower than the 10.49 eV photon energy of the VUV probe laser. Dissociative ionization could result in cases where the VUV photon energy is sufficient both to ionize the primary RDA fragmentation product, and to break a bond in the resulting ion. Though the bond dissociation energies for neutral molecules are on the order of $\sim$3-4 eV, the RDA fragments will be formed with some internal energy, and ionization is liable to weaken the bonds within the ion as compared to those of the precursor neutral [18]. Therefore, dissociative ionization processes are not unlikely. Complementary ab initio calculations would enable the modelling of the ionization processes, and these could be useful for making predictions about the dissociative ionization behaviour of the RDA fragmentation products.

It is evident from the TOF-MS presented here that the molecular fragmentations and rearrangements of cyclohexene and its derivatives, which result from photolysis with 193 nm light, lead to the production of numerous fragmentation products. In a more extended study of the fragmentation processes of these molecules each of the fragmentation products would be identified and quantified from the TOF-MS. Ideally, velocity-map images of all of the fragmentation ions observed would be analysed with the aid of ab initio calculations in order to form a complete picture of the photofragmentation process. However, in this preliminary study we keep the focus to the RDA reaction products. For each of the molecules of interest, the RDA products have been identified, and, as shown in Figures 8.4 and 8.5, two-colour signal has been observed in the TOF-MS at the corresponding *m/z*. However, as will be discussed further in Section 8.3.2, secondary fragmentation processes, which result from VUV photoionization, may have an effect on the observed signal intensities. The velocity-map images of the primary RDA fragmentation products will now be presented and discussed.

8.3.2 Imaging the products of the RDA reaction

The total translation energy, E_T, distributions obtained for the RDA products of cyclohexene from the velocity-map images of *m/z* 28 and *m/z* 54 are displayed in Figure 8.6 (a) and Figure 8.6 (b), respectively. These distributions were obtained by multiplying the individual translational energy, E_t, distributions of the photofragments by the appropriate mass factor, (82/54) for *m/z* 28, and (82/28) for *m/z* 54. The distributions shown are those obtained from subtraction of the one-laser images from the two-laser image, to obtain the two-colour image, i.e. the E_T distribution of those fragments that result from single photon dissociation of the parent molecule with 193 nm light, and are ionized on absorption of a single VUV photon. However, a significant portion of the *m/z* 28 E_T distribution in Figure 8.6 (a) derives from under-subtraction of the VUV one-laser signal; the E_T distribution plotted in purple in Figure 8.6 (a) gives an idea of the 'VUV contribution' as compared to the E_T distribution extracted from the image of the two-colour signal shown in green. The portion of interest of the E_T distribution of *m/z* 28 is that which results from the ethene fragments produced following UV photolysis of cyclohexene, the envelope of which peaks at around 0.95 eV in Figure 8.6 (a). Fortuitously, the 'VUV contribution' lies at low translational energy, and overlaps very little with the region of the E_T distribution which results from the true pump-probe signal.[3]

[3]It should be noted that effects from both under-subtraction and over-subtraction have been observed in the low E_T range in a number of the E_T distributions that will be discussed here. This comes about since

The two-colour E_T distribution of *m/z* 54, shown in blue in Figure 8.6 (b), has a low signal-to-noise ratio. As was observed by Zhao *et al.* [5], a significant portion of the *m/z* 54 fragments lose a hydrogen to form *m/z* 53. For this reason the E_T distribution of *m/z* 53 has been included (displayed in orange) with that of *m/z* 54 in Figure 8.6 (b).[4] The *m/z* 53 E_T distribution gives a clearer picture of the butadiene distribution.

The total translational energy distributions of the RDA products and the *m/z* 53 daughter fragment of butadiene have been overlaid in Figure 8.6 (c). By doing so the distributions can be directly compared. Since ethene (*m/z* 28) and butadiene (*m/z* 54) result from the same fragmentation process, these fragments should have the same translational energy distribution. In the E_T distributions for each of the fragments, the low E_T rise of the envelopes of interest are obscured by the one-laser contribution from the probe laser. However, the envelopes all peak at around 0.95 eV and, in addition, the distributions all tail off at around 2.2 eV.[5] The observed E_T distribution is comparable with the distribution that Zhao *et. al* used to fit their PTS data, which peaked at $\sim$0.95 eV and tailed off at around 2.1 eV [5]. The consistency in this region of the E_T distributions, around 1 eV, which results from UV photolysis of cyclohexene, provides strong evidence that the observed *m/z* 28 and *m/z* 54 are indeed the RDA co-fragments, with a significant fraction of the butadiene fragments undergoing H-loss to yield *m/z* 53. Due to fluctuations in signal intensity in the TOF-MS it is not possible to make a quantitative assessment. However, the formation of *m/z* 53 accounts, at least in part, to the discrepancy in signal intensities observed for the RDA product peaks in the TOF-MS, shown in Figure 8.4.

Absorption of a UV photon of wavelength 193 nm primarily involves a $\pi \rightarrow \pi^*$ transition in cyclohexene [5, 9]. The photon imparts 6.41 eV of energy to the cyclohexene molecule, while ΔH_{rxn} for the RDA reaction is 1.72 eV [10]. This leaves 4.69 eV available to be distributed amongst the translational and internal degrees of freedom of the RDA fragments. As observed from the E_T distributions (Figure 8.6) the maximum energy released in translation is around 2.2 eV. Therefore, even in the case of some of the fastest ethene and butadiene fragment pairs more than 50% of the available energy is released into product internal energy. In the case of the photofragments released with the most probable E_T (0.95

the two-colour signal is much weaker than the one-colour VUV-only signal. For the sake of fluidity in the discussion, and clarity in the figures, the 'VUV contribution' has only been discussed in detail for *m/z* 28, and illustrated for this one distribution in Figure 8.6 (a).

[4]Since the H atom which is lost has a significantly lower mass than the resultant *m/z* 53 fragment, the H removes the majority of the translational energy released in this secondary fragmentation. Such a process would only result in a slight broadening of the distribution. Therefore, the pixel-to-E_T conversion for *m/z* 53 follows that of *m/z* 54.

[5]The estimate of the cut off has been taken from where the distributions flatten off to a plateau.

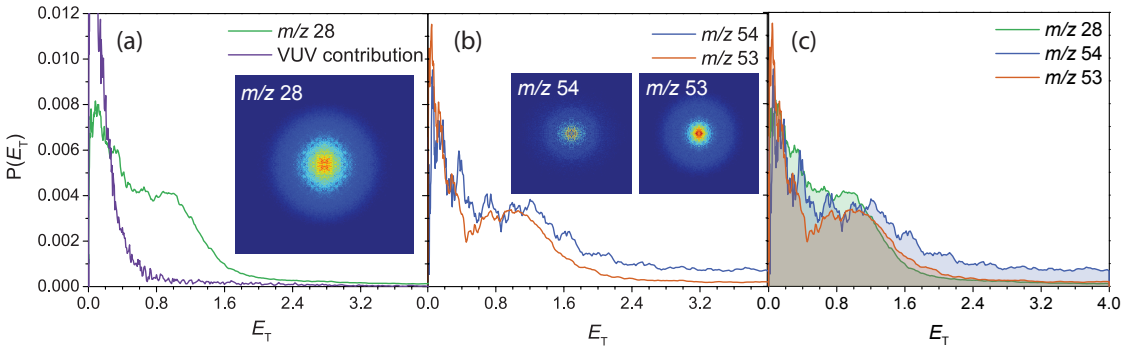

Figure 8.6: Total translational energy distribution obtained from the images (shown) of (a) *m/z* 28 (green), and (b) *m/z* 54 (blue) and *m/z* 53 (orange) ions, which result from the 193 nm photolysis of cyclohexene, followed by VUV photoionization. The 'VUV contribution' to the observed distribution is shown in purple in (a). The E_T distributions have been overlaid in (c).

eV), only ∼20% of the available energy is released into translation, with 3.75 eV being distribution amongst the internal degrees of freedom of the fragmentation products. It is clear that the RDA reaction of cyclohexene results in highly internally excited products. As discussed earlier, this is consistent with the observation of ethene in the TOF spectrum, even though its IE is above the 10.49 eV available from the VUV photoionization photon.

In addition to providing the translation energy distribution of the of the RDA products, from which we can determine the extent of their internal excitation, the velocity-map images also reveal information about the angular distribution of the fragments. The images of the *m/z* 28, 53 and 54 ions, shown in Figure 8.6, all display isotropic angular distributions. This, together with the observation of exceedingly internally excited fragmentation products, is consistent with the generally agreed-upon dynamical processes involved in the RDA reaction [5, 9]: (1) population of the $^1B_2$ electronic excited state of cyclohexene following initial absorption of a 193 nm photon; (2) the molecule then relaxes back down to the ground state through a process of internal conversion, yielding a vibrationally hot parent molecule; (3) the RDA reaction then proceeds, either in a concerted or stepwise fashion, on the ground electronic state.

The E_T distributions obtained from the images of the RDA fragments produced following 193 nm photolysis of 1-methylcyclohexene and 4-methylcyclohexene are shown in Figure 8.7 (a) and Figure 8.7 (b), respectively. As observed for cyclohexene, there is a significant contribution to many of the distributions from the VUV one-laser signal. However, again, the region of most interest lies at higher E_T. By overlaying the E_T distributions obtained from the ene and diene fragments, as has been done for 1-methycyclohexene and

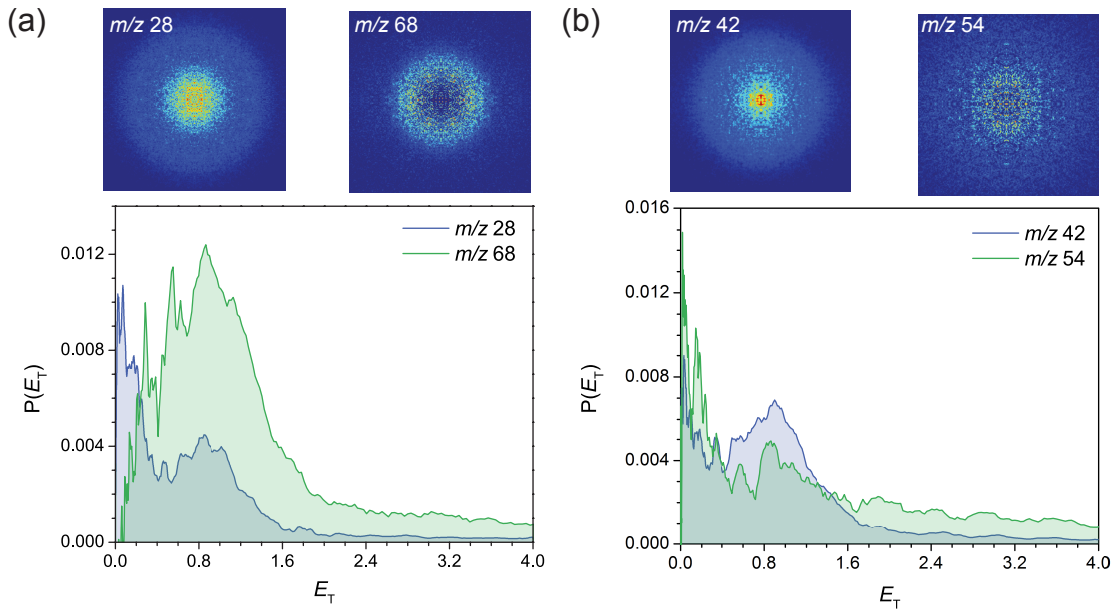

Figure 8.7: Total translational energy distributions obtained from the images (shown) of (a) the *m/z* 28 (blue) and *m/z* 68 (green) ions, and (b) the *m/z* 42 (blue) and *m/z* 54 (green) ion, which result from the 193 nm photolysis of (a) 1-methylcyclohexene, and (b) 4-methylcyclohexene, followed by VUV photoionization.

4-methylcyclohexene in Figure 8.7 (a) and Figure 8.7 (b), respectively, the regions of interest can readily be compared. It can bee seen that the diene E_T distributions, particularly in the case of 4-methylcyclohexene, have poor signal-to-noise (note the raised baseline at high E_T). Despite this, for the portions of the E_T distributions that result from those fragments produced following 193 nm photolysis of the parent molecules, the distibutions are comparable. In the case of 1-methylcyclohexene, the ethene (*m/z* 28) and isoprene (*m/z* 68) distributions both peak at around 0.85 eV and tail off at around 2.1 eV. For 4-methylcyclohexene, the propene (*m/z* 42) and butadiene (*m/z* 54) distributions peak at around 0.87 eV and tail off at around 2.25 eV.

1-methylcyclohexene and 4-methylcyclohexene are derivatives of cyclohexene, with only an additional methyl group at the C_1 position for the former and at the C_4 position for the latter. Therefore, it is expected that the ΔH_{rxn} and dynamical processes for these molecules are very similar to that of cyclohexene. This would explain the remarkable similarity between the E_T distributions observed from the RDA products of the two cyclohexene derivatives, shown in Figure 8.7 (a) and (b), and that observed in the case of cyclohexene itself, shown in Figure 8.6. In contrast, the E_T distribution of the isoprene (*m/z* 68) RDA products of limonene shown in Figure 8.8 (a), appears to be significantly different from those of cyclohexene and the methyl derivatives.

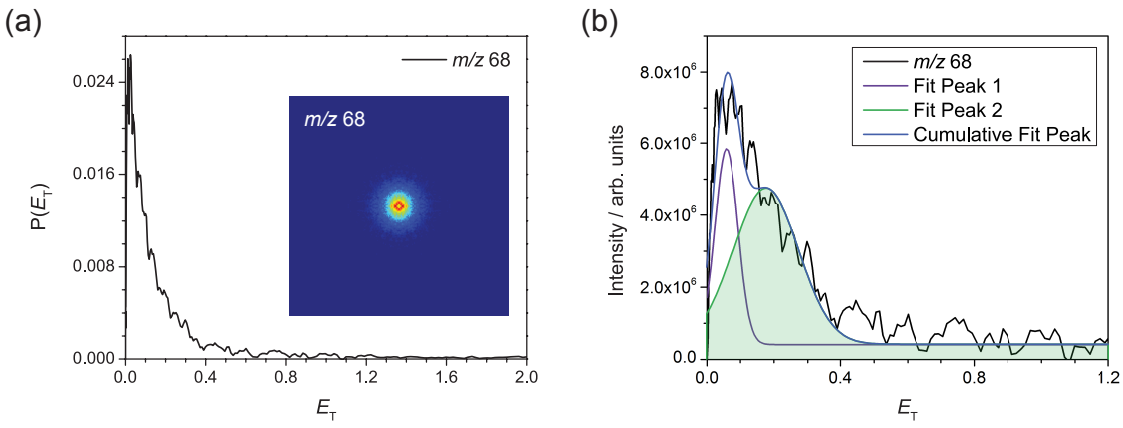

Figure 8.8: (a) Total translational energy distribution obtained from the image of the *m/z* 68 ion (inset), which results from 193 nm photolysis of limonene followed by VUV photoionization. (b) The black line shows same E_T distribution as in (a), but without the Jacobian correction applied to the intensities. This has been fit by the sum of two Gaussians, the purple curve corresponds to the VUV 'contribution' to the signal, the green to the two-colour signal.

From the E_T distribution shown in Figure 8.8 (a), it is difficult to resolve the true pump-probe signal, since this lies at low E_T, and there is significant VUV one-laser signal contamination in this region. However, it has been possible to fit the contributions from the VUV signal and the two-colour signal, each as a Gaussian, and these are shown in Figure 8.8 (b). It is clearest to show this distribution in its form before the Jacobian correction is applied to correct for the re-binning of intensities. The black line shows E_T distribution obtained from the image of *m/z* 68. The VUV and two-colour contributions are shown in purple and green, respectively, with the cumulative fit peak shown in purple. The RDA fragment E_T distribution peaks at 0.18 eV and tails off at around 0.49 eV. As compared to the distributions of cyclohexene and the other derivatives discussed here this distribution is significantly narrower, and shifted to much lower E_T. Limonene, compared to the other cyclohexene derivatives investigated here, is a larger molecule with many more internal degrees of freedom. It can be expected that a mechanism involving internal redistribution of the available energy would result in less energy being released into translation for limonene, than for the other cyclohexenes.

8.4 Conclusion

This study, as with those presented in Chapter 7, has been performed primarily to assess the VMI and VUV photoionization techniques as applied to 'larger' systems. The TOF-MS spectra allowed the identification of the primary fragment ions of interest, but also brought awareness to the possible occurrence of secondary fragmentation processes. The E_T distributions obtained from the velocity-map images confirm that the masses identified are indeed the co-fragments that result from the RDA reactions of the parent molecules of interest. The images also yield the energy distributions of the fragments, and photofragment angular distributions. The highly internally excited fragments, which are produced with isotropic angular distributions, are indicative of a dynamical mechanism involving dissociation of a vibrationally hot ground state, which is formed following internal conversion from an initially excited higher lying state. In this work, the *m/z* 53 ion, which results from secondary fragmentation of butadiene, plays a key role in clarifying the shape of the E_T distribution of the butadiene fragment from the RDA reaction of cyclohexene, and highlights the potential significance of daughter fragments in the imaging studies of these larger organic molecules.

In the current study we have been unable to really tackle the question of the concerted vs stepwise mechanism of the RDA reaction. Zhao *et al.* favoured a concerted mechanism [5], since their study indicated that the RDA reaction of cyclohexene involves a mechanism that results in dissociation of an internally hot ground state parent molecule. However, the time-resolved studies that have been undertaken since then suggest that it is most likely the case that both the concerted and stepwise mechanisms are accessed [7, 9]. It can be expected that the two mechanisms would produce distinct translational and internal energy distributions. Zhao *et al.* [5] discuss how the stepwise fragmentation process would be expected to result in significant rotational and vibrational excitation of the products with a smaller fraction of the energy channeled into translation than they observed experimentally. However, the concerted transition state, as shown in Figure 8.2, lies only 0.64 eV lower in energy than the first TS for the stepwise mechanism. It is possible that a fraction of the hot parent molecules undergo the RDA reaction via a stepwise mechanism, to yield fragments with low E_T. However, we concur with Zhao *et al.* [5] that from our observed experimental data it appears that the concerted mechanism is the more likely.

References

[1] Clayden, G, Warren, S, Greeves, N, and Wothers, P. *Organic Chemistry*. Oxford University Press (2000) (cited p. 213).

[2] Horn, BA, Herek, JL, and Zewail, AH. *Retro-Diels-Alder Femtosecond Reaction Dynamics*. Journal of the American Chemical Society **118**:36 8755–8756 (1996) (cited p. 214, 215).

[3] Collin, GJ and De Maré, GR. *Ring contraction of cyclic olefins: chemical processes specific to electronically excited states?* Journal of photochemistry **38**: 205–215 (1987) (cited p. 214).

[4] Inoue, Y, Takamuku, S, and Sakurai, H. *Direct Photolysis of Cycloalkenes*. Journal of the Chemical Society, Perkin Transactions 2 13 1635–1642 (1977) (cited p. 214).

[5] Zhao, X, Continetti, RE, Yokoyama, A, Hintsa, EJ, and Lee, YT. *Dissociation of cyclohexene and 1,4-cyclohexadiene in a molecular beam*. The Journal of Chemical Physics **91**:7 4118–4127 (1989) (cited p. 214, 223, 224, 227).

[6] Collin, GJ and Deslauriers, H. *The photolysis of gaseous cyclohexene at 184.9 nm*. Canadian Journal of Chemistry **61**:9 1970–1972 (1983) (cited p. 214).

[7] Diau, EWG, De Feyter, S, and Zewail, AH. *Femtosecond dynamics of retro Diels–Alder reactions: the concept of concertedness*. Chemical Physics Letters **304**:3-4 134–144 (1999) (cited p. 215, 227).

[8] Wilsey, S, Houk, KN, and Zewail, AH. *Ground-and excited-state reactions of norbornene and isomers: A CASSCF study and comparison with femtosecond experiments*. Journal of the American Chemical Society **121**:24 5772–5786 (1999) (cited p. 215).

[9] Fuss, W, Schmid, WE, and Trushin, SA. *Ultrafast Dynamics of Cyclohexene and Cyclohexene-d10 Excited at 200 nm*. Journal of the American Chemical Society **123**:29 7101–7108 (2001) (cited p. 215, 223, 224, 227).

[10] Guner, V, Khuong, KS, Leach, AG, Lee, PS, Bartberger, MD, and Houk, KN. *A standard set of pericyclic reactions of hydrocarbons for the benchmarking of computational methods: The performance of ab initio, density functional, CASSCF, CASPT2, and CBS-QB3 methods for the prediction of activation barriers, reaction energetics, and transition state geometries*. Journal of Physical Chemistry A **107**:51 11445–11459 (2003) (cited p. 215, 216, 223).

[11] Sakai, S. *Theoretical Analysis of Concerted and Stepwise Mechanisms of Diels-Alder Reaction between Butadiene and Ethylene*. The Journal of Physical Chemistry A **104**:5 922–927 (2000) (cited p. 215, 216).

[12] Huang, CH, Tsai, LC, and Hu, WP. *Dual-Level Direct Dynamics Study on the Diels-Alder Reaction of Ethylene and 1,3-Butadiene*. The Journal of Physical Chemistry A **105**:43 9945–9953 (2001) (cited p. 215).

[13] Lischka, H, Ventura, E, and Dallos, M. *The Diels-Alder Reaction of Ethene and 1,3-Butadiene: An Extended Multireference ab initio Investigation*. ChemPhysChem **5**:9 1365–1371 (2004) (cited p. 215).

[14] Houk, KN, Gonzalez, J, and Li, Y. *Pericyclic reaction transition states: Passions and punctilios, 1935-1995*. Accounts of Chemical Research (1995) (cited p. 215).

[15] Lias, SG. *"Ionization Energy Evaluation" in NIST Chemistry WebBook, NIST Standard Reference Database Number 69, (retrieved June 19, 2013)*. Ed. by Linstrom, PJ and Mallard, WG. National Institute of Standards and Technology, Gaithersburg MD, 20899 (cited p. 221).

[16] Lias, SG, Levin, RD, and Kafafi, SA. *NIST Standard Reference Database Number 69 (retrieved June 19, 2013)*. Ed. by Linstrom, PJ and Mallard, WG. NIST Chemistry WebBook. National Institute of Standards and Technology, Gaithersburg MD, 20899 (cited p. 221).

[17] Harris, D, McKinnon, S, and Boyd, RK. *The Origins of the Base Peak in the Electron Impact Spectrum of Limonene*. Organic Mass Spectrometry **14**:5 265–272 (1979) (cited p. 221).

[18] Gross, JH. *Mass Spectrometry: A Textbook*. 2nd ed. Springer, 2011 (cited p. 221).

9

Summary and Perspectives

It always seems impossible until it's done.
Nelson Mandela

The work reported in this thesis represents an important 'building block' within a larger project that aims to achieve imaging mass spectrometry by means of multi-mass velocity-map imaging (VMImMS). Velocity-map imaging (VMI) typically involves state-selective detection, and so is often limited to investigating a single dissociation channel. In contrast, the studies presented here have employed VMI in combination with VUV photoionization, which allows the investigation of most, if not all of the different photofragmentation processes occurring for a particular system. As has become apparent from the work presented in this thesis, this capability becomes particularly important when studying large systems, which often display complex dissociation dynamics. Our approach allows us to assess the active photofragmentation pathways, and information from VMI gives an insight into the energy partitioning amongst the fragments, as well as the relative importance of the different dissociation pathways.

The study presented in Chapter 3 demonstrates the first use in our laboratory of 'universal' ionization in combination with the VMI technique; the photodissociation of two neutral alkyl iodide molecules was investigated. Two of the other studies presented in this thesis have also investigated the photofragmentation processes of neutral species. The studies of 193 nm photodissociation of N,N-dimethylformamide and a number of cyclic alkenes were presented in Chapter 5 and Chapter 8, respectively. In all of these studies, the individual fragments that result from UV photolysis of the parent molecule were photoionized by a VUV laser pulse, and then velocity-map imaged. Single-photon ionization with 118 nm

light allows non-resonant detection of all the photofragments resulting from dissociation of a molecule, provided their ionization energies are lower than 10.5 eV.

The study presented in Chapter 3 has investigated specifically the A-band photodissociation of methyl iodide (CH_3I) and ethyl iodide (C_2H_5I). Methyl iodide was chosen since it has become the benchmark molecule for ion imaging studies of photodissociation processes. Since this work aims to investigate 'larger' systems, the natural choice for the second model system was the next in the homologous series of the alkyl iodides, C_2H_5I. A-band photdissociation of the alkyl iodides results in production of C_nH_{2n+1} + I^* and C_nH_{2n+1} + I photoproducts, with the latter yielding a 'hotter' internal energy distribution of the alkyl co-fragment. In the central region of the A-band the $^3Q_0$ transition dominates. The $^3Q_0$ state correlates diabatically with the I^* dissociation channel, and this channel is observed to be the major fragmentation pathway for both alkyl iodides in the wavelength region investigated. The C_nH_{2n+1} + I photoproducts result from a curve-crossing to the $^1Q_1$ state, following initial excitation to the $^3Q_0$ state. The large positive values for the anisotropy parameters observed for all fragments reflect the initial parallel transition.

As discussed in Chapter 5, the photodissociation of N,N-dimethylformamide ($HCON(CH_3)_2$, DMF) has been investigated using 193 nm light. The structure of DMF presents three possible fragmentation pathways leading to formation of radical products. These involve fragmentation of the N−CO and N−CH_3 bonds, and H loss. From the VMI experiment we have been able to estimate a branching ratio for the N−CO and N−CH_3 fragmentation channels. Around 76% of fragmentations yield HCO + $N(CH_3)_2$, whereas only 24% result in formation of $HCONCH_3$ + CH_3. Analysis of the E_T distributions obtained from images of the fragments resulting from primary N−CO 'peptide' bond fission reveals two active dissociation channels, corresponding to formation of HCO^* + $N(CH_3)_2$ and HCO + $N(CH_3)_2{}^*$, with around 90% of all N−CO fragmentation processes yielding the latter. The non-statistical translational energy distributions and large positive anisotropy parameters obtained from all the images of the fragments that result from primary N−CO 'peptide' bond fission indicate that this is a relatively rapid process. The E_T distributions obtained from the HCO and $N(CH_3)_2$ primary photofragments show evidence for bending excitations in these products, which is consistent with an impulsive dissociation. N−CH_3 bond fragmentation yields highly internally excited fragmentation products, which display isotropic angular distributions, in contrast to those observed for the fragments that result from primary N−CO 'peptide' bond fission. We have obtained an overall branching ratio for HCO^* + $N(CH_3)_2$: HCO + $N(CH_3)_2{}^*$: $HCONCH_3$ + CH_3 of 0.06 : 0.74 : 0.24. H

loss from DMF, which has been investigated with H Rydberg atom photofragment translational spectroscopy, most likely results from dissociation of vibrationally 'hot' ground state parent molecules, formed following internal conversion from the excited electronic state(s) that are populated in the initial photon absorption.

Photodissociation of cyclic alkenes can occur via an interesting fragmentation process known as the retro-Diels-Alder (RDA) reaction. There has been significant interest in whether this process proceeds in a stepwise or a concerted fashion. To our knowledge, the work presented in Chapter 8 is the first velocity-map imaging study of cyclic alkene systems. 193 nm photodissociation of the cyclohexenes has been observed to result in the RDA reaction. VUV photoionization allows detection of both photofragments that result from the RDA process, though in several cases the fragments undergo secondary fragmentations, and therefore are not observed with the expected intensity at the appropriate mass-to-charge (*m/z*) ratio. The fragments, which are produced with isotropic angular distributions, are observed to be highly internally excited. The photofragment energy distributions are consistent with a dynamical process involving dissociation of a vibrationally 'hot' ground state parent molecule, which is formed following internal conversion from an initially excited higher-lying state. The photofragment translational spectroscopy study of the 193 nm photodissociation of cyclohexene, performed by Zhao *et al.* [1], concluded that such a process implies that dissociation occurs via the concerted mechanism, which is the lowest lying pathway on the electronic ground state. Furthermore, a stepwise fragmentation process would be expected to result in significant rotational and vibrational excitation of the products, with a smaller fraction of the energy being channeled into translation than they observed experimentally. We concur that from our observed experimental data it appears that the concerted mechanism is the more likely. However, the first stepwise transition state (TS) lies only 0.64 eV higher in energy than the TS for the concerted mechanism. It is possible that a fraction of the internally excited parent molecules undergo the RDA reaction via a stepwise mechanism, with little energy released into fragment translation.

The remaining studies presented in this thesis have investigated the photofragmentation processes of *cationic* species. VUV light has been employed to ionize the parent molecule. In the photodissociation studies of ions, since each dissociation channel necessarily produces one charged species, along with one or more neutral fragments, it is possible to gain an insight into all of the active channels.

The study into the UV photodissociation of the ethyl bromide ($C_2H_5Br^+$) and ethyl iodide ($C_2H_5I^+$) cations, presented in Chapter 4, reveals that these species exhibit several

photofragmentation pathways. In both cases a number of fragment ions have been observed: $C_2H_5^+$, $C_2H_4^+$, $C_2H_3^+$, CH_2X^+, and additionally I^+, in the case of $C_2H_5I^+$. The branching into the various channels that yield the observed photofragment ions has been obtained for both ethyl halide cations following photolysis with 355 nm light. For both species C−X bond fission to yield $C_2H_5^+$ is the major fragmentation pathway. For $C_2H_5Br^+$ photolysis the ratio for $C_2H_5^+$: $C_2H_4^+$: $C_2H_3^+$: CH_2X^+ is 0.41 : 0.38 : 0.20 : 0.01. In the case of $C_2H_5I^+$ photolysis, the ratio for $C_2H_5^+$: $C_2H_4^+$: $C_2H_3^+$: CH_2X^+ : I^+ is 0.62 : 0.19 : 0.06 : 0.02 : 0.12. The $C_2H_5^+$ fragment ion image obtained following UV photolysis of $C_2H_5Br^+$ displays near-limiting parallel recoil anisotropy. Resonantly-enhanced multiphoton ionization (REMPI) detection of the spin-orbit-excited Br^* co-fragments has revealed that prompt C−Br bond fission yields $C_2H_5^+$ + Br^*. Despite the rapid dissociation process, around 80 % of the available energy is partitioned into internal excitation of the products, which is consistent with the very different equilibrium geometry of the ethyl moiety in the ground state parent cation compared with that of the free $C_2H_5^+$ ion. A similar definitive interpretation of the $C_2H_5I^+$ data for the $C_2H_5^+$ dissociation channel is primarily hampered by the significant signal from I^+, formed directly via a competing C−I bond dissociation channel. This competing channel is active at the wavelength required for REMPI detection of the neutral I/I^* fragments. Despite this, the images obtained for the various fragment ions resulting from UV photolysis of $C_2H_5I^+$ suggest many similarities in the fragmentation dynamics of $C_2H_5I^+$ and $C_2H_5Br^+$. In both cases, the dissociation pathways that compete with $C_2H_5^+$ production show the same propensity for partitioning the available energy into product internal excitation as observed in the $C_2H_5^+$ channel. Images acquired for the $C_2H_4^+$, $C_2H_3^+$, CH_2X^+, (and I^+) fragment ions all reveal non-limiting parallel recoil anisotropy. Based on the information to hand, we conclude that most $C_2H_3^+$ fragment ions arise from unimolecular decay (H_2 elimination) of highly internally excited $C_2H_5^+$ cations, which in the case of $C_2H_5Br^+$ are most likely partnered with Br co-fragments, while the $C_2H_4^+$ products most plausibly arise from unimolecular decay (loss of HX) from highly internally excited states of the parent cation. The CH_2X^+ ions are attributable to a minor competing C–C bond fission channel. All of these fragmentation pathways, in contrast to those involving direct C−X bond fission, are thought to occur following radiationless transfer from the initial photoexcited state. Data from detailed high-dimensionality *ab inito* calculations would be required in order to gain a more detailed mechanistic understanding of the various fragmentation pathways.

The remainder of the studies into the photodissociation of cations find their relevance within mass spectrometry. Generally, mass spectrometry studies are performed on cationic species. The study of cations, as opposed to neutrals, has some benefits, mainly regarding

sample input into the apparatus. The sample input method for the VMI apparatus employed here uses the room temperature vapour of a liquid seeded in an inert gas to make up the gas mixture that is used to generate the molecular beam. However, it is often the case that the vapour pressure of the sample will be insufficient to use this method. Therefore, for the investigation of biochemical samples MS employs techniques such as electrospray ionization (ESI), and matrix assisted laser desorption ionization (MALDI), which are able to generate intact gas-phase ions [2, 3]. However, the dissociation processes of cationic species, as compared to their neutral counterparts, can often be much more extensive, since the bond strengths within the former are generally reduced. In addition, ions tend to be highly fluxional, and therefore rearrangement processes can compete strongly with simple bond cleavages. Mass spectrometry studies alone are able to obtain the masses of the fragmentation products, whereas imaging is able to obtain another dimension of information about the dissociation processes.

The study into the UV photodissociation of the N,N-dimethylformamide cation (DMF^+), presented in Chapter 6, reveals the complexity of the dissociation processes observed for this relatively simple model for a peptide bond. The ion undergoes a number of rearrangement processes involving hydrogen transfer, and a significant amount of secondary dissociation also occurs. On photolysis with 355 nm light, which was the longest wavelength employed for this study, the secondary dissociation processes were minimised, and the two primary dissociation channels were accessed. Both channels are thought to involve 1,2 H-shift rearrangement processes to yield energetically favourable products: HCO + $CH_3NHCH_2^+$, and $HCONHCH_2^+$ + CH_3. Both of these primary dissociation channels exhibit isotropic photofragment ion images. The latter process releases a slightly larger fraction of the available energy into photofragment translation. The characteristic energy distributions that result, along with the TOF-MS of the DMF^+ and DMF-d_7^+ photofragments, have provided clarification of the origins of the observed primary and secondary photofragment ions.

The photofragmentation of the aliphatic aldehyde cations displays a number of interesting rearrangement processes. The study presented in Section 7.2, focuses on four rearrangement processes: the McLafferty rearrangement, the McLafferty complement rearrangement, the McLafferty+1 rearrangement, and H_2O loss from the parent ion. For the systems investigated, these rearrangements result from either one-photon dissociative ionization, following absorption of a VUV photon, or from dissociation of the parent cation following absorption of an additional photon of 355 nm light. The translational energy distributions for the fragment ions that result from these processes all peak at low translational energy.

These rearrangements, which all result in a significant portion of the available energy remaining as internal energy of the fragmentation products, are thought to occur via a mechanism involving internal conversion from an initially excited state back down to the ground state of the parent ion. The internally 'hot' parent ions that result are then able to surpass the transition state barriers for the various rearrangements.

A preliminary study of the photodissociation of the cations of cyclohexene and three cyclohexene derivatives has been presented in Section 7.3. These cationic species undergo the retro-Diels-Alder reactions following photolysis with 355 nm light. The velocity-map imaging data from this work bears strong similarities to that of the aldehyde cation photodissociation study. The images of the diene product ions display isotropic angular distributions, and the photofragments are highly internally excited. The RDA reaction most probably occurs via a mechanism involving internal conversion from an initially populated state(s) back down to a lower-lying state, followed by dissociation over one or more barrier(s).

Following photoexcitation, the photofragmentation dynamics are dependent on the electronic state that is initially accessed, the potential energy landscape, and the coupling between different electronic states. We have seen examples of various different types of dynamics, for example, if a dissociative state is initially accessed then direct dissociation proceeds. This has been observed in the case of: the I^* dissociation channel that results following A-band photodissociation of the alkyl iodides; dissociation along the S_2 state of DMF to yield HCO + $N(CH_3)_2^*$ photofragments; and for the C−X bond cleavage following UV photoexcitation of the ethyl halide cation species. It appears, at least from the systems studied in this work, that direct dissociation mechanisms are more prominent for the photodissociation of neutral species, as compared to cations. The fragmentation mechanisms for cations more commonly involve internal conversion from the initially excited state to the electronic ground state, yielding an internally 'hot' ground state parent ion, which subsequently dissociates; such processes are thought to occur for all the cationic species studied here.

The various photodissociation studies presented in this thesis illustrate that velocity-map imaging measurements can provide additional insights into the fragmentation processes of larger molecular systems. Examples of these, which may be of interest to the wider chemical community, include the retro-Diels-Alder reaction, McLafferty-type rearrangements, and 'peptide' bond fragmentation.

Perspectives

While mass spectrometry has proven extremely useful for molecular identification, and methods such as Tandem MS can be employed for peptide sequencing, it is generally not possible to obtain a great deal of dynamical information from MS studies. This thesis has demonstrated that by acquiring the velocity-map images for each ion in the time-of-flight spectrum it is possible to unravel details of the dissociation dynamics of increasingly complex systems. With this in mind, the velocity-map imaging mass spectrometry (VMImMS) project aims to increase the amount of information that can be obtained from a mass-spectrometry-type experiment.

Traditional detection methods for ion imaging studies image only a single mass on each time-of-flight (TOF) cycle. As a result, in order to investigate all of the active fragmentation channels, the different fragmentation products need to be individually imaged. Studies that employ these methods, such as those presented in this thesis, are time consuming. The data acquisition rates that are currently achievable too slow for VMImMS to be employed as a general analytical technique. The ideal detection method for imaging mass spectrometry would involve multi-mass imaging, i.e. multiple (ideally, all) fragment masses would be imaged on each TOF cycle. Since the time-of-flight of the ions is dependent on their mass, a suitable detector would need be able to record multiple images over a period of a few tens to a few hundreds of microseconds, to allow for the lightest fragments through to the heaviest to be imaged in a single TOF cycle. Further, for a typical VMI experiment, a time resolution on the order of nanoseconds would be required to achieve a sufficiently high mass resolution to allow for separation of the individual masses. The PImMS (Pixel Imaging Mass Spectrometry) sensor [4–7] has been designed to meet these requirements. This event triggered detector has been developed through a collaboration between the Chemistry and Physics departments at the University of Oxford and the Rutherford Appleton Laboratory (RAL). The first generation PImMS1 sensor consisted of a 72 x 72 pixel array. The latest PImMS2 sensor benefits from a significantly larger 324 × 324 pixel array. Each pixel is built with four timestamp registers, and is therefore able to record the optical signal generated by four individual particles (separated in time). The statistics of a typical time-of-flight imaging experiment mean that it is unlikely that all four registers will be filled in a given time-of-flight cycle. Simulations showed over 95% detection efficiency even with very large numbers of ions spread across many different masses [7]. The PImMS sensor allows particle events to be imaged with time resolution as high as 12.5 ns, over data acquisition times of more than 50 μs, with longer acquisition times possible at lower time resolution. Such capabilities allow for multi-mass detection, and the sensor has found

applications in a range of fields, including velocity-map imaging, spatial map imaging, and time-resolved imaging of molecular motion [4–9].

In photofragment imaging studies the PImMS sensor allows velocity-map images to be acquired for multiple fragment masses on each TOF cycle [7]. Currently, the PImMS sensors are configured to detect photons, and are employed to image the optical signal generated from an MCP/phosphor screen detector as a result of ion impact on the detector. The data set acquired by the PImMS sensor consists of (x,y,t) data points for each ion hit, from which the velocity-map images can be reconstructed by plotting the (x,y) data points within the TOF window of interest. The results of early proof-of-concept experiments, presented in Figure 9.1, demonstrate the use of PImMS for velocity-map imaging mass spectrometry [7].[1]

Figure 9.1 (b) shows the 3D (x,y,t) data set that results following 446.32 nm photolysis of Br_2, and REMPI detection of the resulting Br atoms. This data comes from an experiment in which fast-switching of the polarity of the velocity-mapping ion lens has been employed to allow for imaging of both the ionized electrons and Br^+ ions on each TOF cycle. The TOF spectrum, shown in Figure 9.1 (a), has been extracted by integrating the signal over x and y. The peaks corresponding to the electrons and to the two isotopes of atomic bromine, ^{79}Br and ^{81}Br, are clearly visible. Their corresponding images have been obtained by plotting (x,y) data for the appropriate arrival time. For the data sets presented here the time-of-flight (and therefore mass) resolution was determined by a combination of the $\sim$100 ns decay lifetime of the P47 phosphor and the 50 ns timing cycle of the PImMS1 sensor used in these experiments. The full time resolution of the PImMS sensor could be exploited in multi-mass imaging measurements by use of faster phosphors, or direct in-vacuum particle detection.

Figure 9.1 (d) shows the (x,y,t) data set for N,N-dimethylformamide following irradiation with 193 nm and 118 nm light.[2] This data set is considerably more complex than that for Br_2. Several fragment ions are observed, showing evidence for multiple fragmentation pathways. The data set shown was acquired under clustering conditions, in which clusters formed within the molecular beam, and therefore also shows evidence for formation and subsequent photolysis of dimers, trimers, and higher clusters within the molecular beam. This data set demonstrates several of the features of VMI, which have also been discussed in this thesis, that may prove useful in imaging mass spectrometry studies of larger

[1] This data was acquired by Edward Wilman, Craig Slater, Jason Lee, and other researchers working on the PImMS project.

[2] The parent ion peak at m/z 73 was extremely intense and was therefore time-gated out of the signal to prevent saturation of and/or damage to the microchannel plate detector.

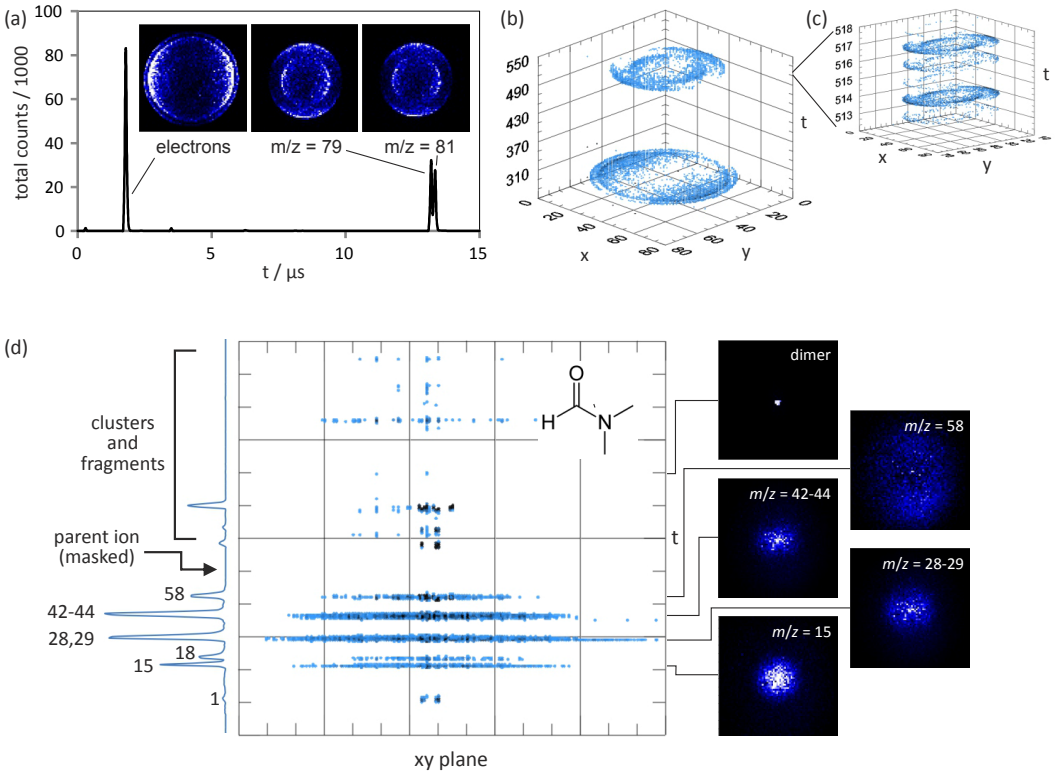

Figure 9.1: The results of early proof-of-concept experiments demonstrating the use of PImMS for velocity-map imaging mass spectrometry taken from reference [7]. (a) TOF spectrum recorded by the PImMS sensor following 446.32 nm photolysis of Br_2, the images of the electrons and ions are inset; (b) 3D (x,y,t) plot of electron and Br^+ ion signals; (c) 'Zoomed in' 3D plot showing the Br^+ ion signals in more detail. In the 3D plots, x and y are labelled in pixel units, and t in timebin units; (d) Data recorded by the PImMS sensor following irradiation of N,N-dimethylformamide with 193 nm and 118 nm light.

molecules. The velocity-map images themselves yield information on the translational energy and angular distributions of the observed ions, which could be used for enhanced molecular fingerprinting, for example. Furthermore, parent ions, for example the dimer in Figure 9.1 (d), may immediately be identified by the fact that they have effectively zero velocity in the image plane, and appear as a small focused spot in the centre of the images. A recent review article [10] has highlighted some of the latest VMImMS work, demonstrating the use of the technique to separate contributions from ions with identical mass-to-charge ratio, and to resolve individual components within mixed samples.

References

[1] Zhao, X, Continetti, RE, Yokoyama, A, Hintsa, EJ, and Lee, YT. *Dissociation of cyclohexene and 1,4-cyclohexadiene in a molecular beam*. The Journal of Chemical Physics **91**:7 4118–4127 (1989) (cited p. 233).

[2] Ashcroft, AE. *Ionization Methods in Organic Mass Spectrometry*. Ed. by Barnett, NW. RSC Analytical Spectroscopy Monographs, 1997 (cited p. 235).

[3] Ashcroft, AE. *An Introduction to Mass Spectrometry* (cited p. 235).

[4] Nomerotski, A, Brouard, M, Campbell, E, Clark, A, Crooks, J, Fopma, J, John, JJ, Johnsen, AJ, Slater, C, Turchetta, R, Vallance, C, Wilman, E, and Yuen, WH. *Pixel Imaging Mass Spectrometry with fast and intelligent Pixel detectors*. Journal of Instrumentation **5**:7 C07007 (2010) (cited p. 237, 238).

[5] John, JJ, Brouard, M, Clark, A, Crooks, J, Halford, E, Hill, L, Lee, JWL, Nomerotski, A, Pisarczyk, R, Sedgwick, I, Slater, CS, Turchetta, R, Vallance, C, Wilman, E, Winter, B, and Yuen, WH. *PImMS, a fast event-triggered monolithic pixel detector with storage of multiple timestamps*. Journal of Instrumentation **7**:8 C08001 (2012) (cited p. 237, 238).

[6] Sedgwick, I, Clark, A, and Crooks, J. *PImMS: A self-triggered, 25ns resolution monolithic CMOS sensor for Time-of-Flight and Imaging Mass Spectrometry*. New Circuits and Systems Conference (2012) (cited p. 237, 238).

[7] Clark, AT, Crooks, JP, Sedgwick, I, Turchetta, R, Lee, JWL, John, JJ, Wilman, ES, Hill, L, Halford, E, Slater, CS, Winter, B, Yuen, WH, Gardiner, SH, Lipciuc, ML, Brouard, M, Nomerotski, A, and Vallance, C. *Multimass Velocity-Map Imaging with the Pixel Imaging Mass Spectrometry (PImMS) sensor: An Ultra-Fast Event-Triggered Camera for Particle Imaging*. The Journal of Physical Chemistry A **116**: 10897–10903 (2012) (cited p. 237–239).

[8] Brouard, M, Johnsen, AJ, Nomerotski, A, Slater, CS, Vallance, C, and Yuen, WH. *Application of fast sensors to microscope mode spatial imaging mass spectrometry*. Journal of Instrumentation **6**:01 C01044 (2011) (cited p. 238).

[9] Kershis, MD, Wilson, DP, White, MG, John, JJ, Nomerotski, A, Brouard, M, Lee, JWL, Vallance, C, and Turchetta, R. *Exploring surface photoreaction dynamics using pixel imaging mass spectrometry (PImMS)*. The Journal of Chemical Physics **139**:8 084202 (2013) (cited p. 238).

[10] Bull, JN, Lee, JWL, Gardiner, SH, and Vallance, C. *Account: An introduction to velocity-map imaging mass spectrometry (VMImMS)*. European Journal of Mass Spectrometry **20**:2 117–129 (2014) (cited p. 239).

Hamba Gahle